

# Seismic Design and Behavior of Steel Braced Frame Buildings with Friction Dampers as Dissipative Floor Connectors

Présentée le 14 octobre 2022

Faculté de l'environnement naturel, architectural et construit  
Laboratoire des structures métalliques résilientes  
Programme doctoral en génie civil et environnement

pour l'obtention du grade de Docteur ès Sciences

par

**Martina PARONESSO**

Acceptée sur proposition du jury

Prof. A. Vassilopoulos, président du jury  
Prof. D. Lignos, directeur de thèse  
Prof. A. Filiatrault, rapporteur  
Prof. M. Latour, rapporteur  
Prof. I. Anastasopoulos, rapporteur





*A mia madre e mio padre, i pilastri della mia vita  
A nonna Maria e nonno Adriano, il porto sicuro dove trovare amore e saggezza  
A nonna Bruna, il mio angelo custode  
A Cristiano, l'essenza del mio universo*



# Abstract

Field observations and comprehensive life-cycle building assessment suggest that buildings designed according to today's seismic standards meet the life-safety requirement. However, they are prone to economic losses due to repairs in the aftermath of earthquakes. In the case of buildings featuring steel concentrically braced frames (CBFs), which form the main focus of this thesis, life-cycle costs are dominated by repairs in acceleration-sensitive non-structural components. This is attributable to the high absolute acceleration demands that arise from the high lateral stiffness of the CBFs and the acceleration amplification caused by the higher mode effects during earthquake shaking. Seismic repairs in steel braces due to flexural buckling is a second contributor to losses in steel CBFs. Due to the highly asymmetric behavior of steel braces, steel CBF buildings are prone to the formation of local story collapse mechanisms. The above suggests that new construction concepts should be exploited to minimize widespread damage in steel CBF buildings.

Within such a context, this doctoral thesis explores the use of sliding friction dampers as dissipative floor connectors for enhancing the seismic performance of steel CBF buildings. The dampers connect each floor of the steel CBF system to the diaphragms of the gravity framing system and they allow for controlled relative movement between them. They are employed as force capping mechanisms in order to (i) limit the magnitude of the absolute floor acceleration demands along the height of the building, (ii) mitigate higher mode effects, and (iii) minimize damage on the structural and non-structural components of the building under earthquake loading.

In the context of this thesis, a full-scale sliding friction damper prototype is first developed and tested physically at EPFL's structures laboratory in order to identify a number of non-metallic composite friction pads that can be potentially used in supplemental damping devices. Subsequently, non-linear static and response history analyses are conducted in order to investigate the benefits of employing sliding friction dampers as dissipative floor connectors within multi-story steel CBF buildings. In this respect, a

design methodology is proposed to determine the activation force of the dampers so as to ensure damage-free seismic performance in the steel CBF and the floor diaphragms of the building. The influence of the gravity framing system and damper activation forces on the seismic behavior of steel CBF buildings is also investigated. To this end, a general nonlinear modelling approach is developed to simulate the hysteretic response of four partially restrained gravity connections, which are commonly used worldwide. Furthermore, a simplified method is proposed to evaluate the effectiveness of the damper activation forces for controlling relevant engineering demand parameters of interest for damage control of steel CBF buildings. The simulation results suggest that the activation forces determined according to the proposed methodology are effective in mitigating higher mode effects and in preventing the CBF and the floor diaphragms from experiencing inelastic behavior under earthquake loading. Moreover, it is shown that the seismic behavior of steel CBF buildings with dissipative floor connectors becomes practically insensitive to record-to-record variability.

## **Keywords**

Steel concentrically braced frames, Dissipative floor connectors, Sliding friction dampers, Non-metallic composite friction pads, Higher mode effects, Design methodology, Gravity framing system, Earthquake engineering, Resilient-based design

# Résumé

Analyses sismiques et observations sur site montrent que les ouvrages dimensionnés selon les normes parasismiques actuelles répondent aux exigences fixées en terme de sécurité structurale. Par contre, ils sont sujettes à pertes économiques importantes à l'issue d'un séisme. Concernant les structures métalliques contreventées (CBFs), qui représentent le sujet principal de cette thèse, ces pertes économiques sont principalement causées par les réparations à effectuer sur leurs éléments non structuraux sensible aux accélérations. Ceci est attribuable aux niveaux élevés d'accélération auxquelles elles sont soumises lors d'un séisme en raison de la grande rigidité latérale des CBFs et des amplifications d'accélération induites par les modes supérieurs. Une deuxième source de perte économique importante est liée aux réparations des contreventements suite à leur flambage. De plus, à cause du comportement fortement asymétrique des contreventements, les CBFs ont la tendance à développer des problèmes de stabilité d'ensemble. Tout cela indique que des nouveaux concepts de construction doivent être exploités afin d'éviter des dommages considérables au sein des CBFs.

Dans un tel contexte, cette thèse de doctorat explore l'utilisation d'amortisseurs sismique à friction (SFDs) comme dissipateurs d'énergie au sol pour améliorer le comportement séismique des CBFs. Ces amortisseurs connectent chaque étage du contreventement aux diaphragmes du système de reprise des charges gravitaires (GFS) et ils permettent un déplacement relative contrôlé entre les deux. Ils sont utilisés comme mécanismes de plafonnement de force afin de (i) limiter l'ampleur des accélérations absolues, (ii) atténuer les effets des modes supérieurs, et (iii) réduire l'endommagement des éléments structuraux et non structuraux du bâtiment lors d'un séisme.

Dans le cadre de cette thèse, un prototype d'amortisseur à friction à grande échelle est développé et testé auprès du laboratoire de structure de l'EPFL afin d'identifier une série de plaquettes de frottement en composite et non-métalliques qui peuvent être potentiellement utilisées dans des dispositifs d'amortissement. Ensuite, analyses statiques et dynamiques non-linéaires sont réalisées dans le but d'examiner les avantages apportés

par l'utilisation d'amortisseurs à friction comme dissipateurs sismiques au sol au sein des CBFs. A cet égard, une méthode de dimensionnement est proposée pour établir les forces d'activation des SFDs de manière à assurer un comportement élastique des contreventements métalliques et des diaphragmes du GFS sous charge sismique. L'influence du GFS et des forces d'activation des SFDs sur le comportement sismique des CBFs est également analysé. Pour ce faire, une méthode de modélisation non-linéaire est développée afin de pouvoir simuler la réponse hystérétique de quatre types de connections semi-rigides couramment utilisé dans la pratique. En outre, une méthode simplifiée est proposée pour évaluer l'efficacité des forces d'activation des SFDs dans le contrôle des accélérations et des déplacements latéraux ressentis par les CBFs lors d'un séisme. Les résultats des simulations numériques indiquent que les forces d'activation déterminées selon la méthode proposée permettent d'atténuer les effets des modes supérieurs et de prévenir le développement d'un comportement inélastique des contreventements métalliques et des diaphragmes du GFS sous charge sismique. De plus, il est démontré que l'utilisation de dissipateurs sismiques au sol permet de réduire considérablement la variabilité issue des évènements sismiques sur les efforts ressentis par les CBFs.

## Mots Clé

Structures métalliques contreventées, Dissipateurs sismiques au sol, Amortisseurs à friction, Plaquettes de frottement en composite et non-métalliques, Modes supérieurs, Méthode de dimensionnement, Système de reprise des charges gravitaires, Génie parasismique, Résilience structurale

# Sommario

Le osservazioni sul campo e la valutazione del ciclo di vita completo degli edifici confermano che strutture progettate secondo gli odierni standard sismici soddisfano i requisiti di sicurezza introdotti a salvaguardia della vita umana. Tuttavia, tali edifici sono comunque esposti al rischio di perdite economiche dovute a interventi di ripristino generalmente necessari dopo un evento sismico. Nel caso di strutture costituite da telai in acciaio a controventatura concentrica (CBF), le quali rappresentano il soggetto principale della presente tesi, i costi del ciclo di vita dell'edificio sono dominati dalle riparazioni di componenti non strutturali sensibili all'accelerazione. Ciò è attribuibile agli importanti livelli di accelerazione assoluta a cui tali componenti sono sottoposti per effetto dell'elevata rigidità laterale dei CBF e delle amplificazioni prodotte dai modi di vibrare di ordine superiore. Le riparazioni dei controventi dovute a fenomeni d'instabilità sono un secondo fattore di perdita economica per edifici CBF in acciaio. A causa del comportamento altamente asimmetrico dei controventi, tali strutture sono soggette alla formazione di meccanismi di collasso localizzati in corrispondenza dei singoli piani. Da quanto precede scaturisce la necessità di individuare nuovi concetti costruttivi capaci di contenere il più possibile la propagazione del danno in edifici CBF in acciaio.

In questo contesto, la presente tesi di dottorato esplora l'uso e l'efficacia di dissipatori scorrevoli ad attrito (SFDs) quali elementi dissipativi di collegamento introdotti in corrispondenza dei diversi piani della struttura capaci di migliorare le prestazioni sismiche di edifici CBF in acciaio. I dissipatori collegano il sistema formato dai CBF in acciaio ai diaframmi rigidi orizzontali del sistema intelaiato a gravità (GFS) in corrispondenza di ogni piano dell'edificio e consentono un movimento relativo controllato fra i due sistemi. Questi dispositivi sono impiegati quali limitatori delle forze scambiate fra i due sistemi al fine di (i) contenere l'intensità delle accelerazioni assolute di piano lungo l'altezza dell'edificio, (ii) mitigare gli effetti dei modi d'ordine superiore e (iii) ridurre al minimo i danni delle componenti strutturali e non strutturali dell'edificio prodotti dall'azione sismica.

Nell'ambito della presente tesi, un prototipo di dissipatore scorrevole ad attrito a grandezza naturale viene dapprima sviluppato e testato fisicamente presso il laboratorio di strutture dell'EPFL al fine di identificare una serie di spessori ad attrito in materiale composito non metallico che possono essere potenzialmente utilizzati in dispositivi di smorzamento. Successivamente, sono condotte analisi non lineari statiche e dinamiche al fine di studiare i vantaggi dell'impiego di SFDs quali elementi dissipativi di collegamento ai piani da utilizzare in seno a edifici multipiano CBF in acciaio. A questo proposito, è proposta una metodologia progettuale che permette di determinare le forze di attivazione dei SFDs in modo tale da garantire prestazioni sismiche esenti da danni tanto nei CBF in acciaio quanto nei diaframmi rigidi che formano gli orizzontamenti dell'edificio. In quest'ambito è inoltre studiata l'influenza del GFS e delle forze di attivazione dei SFDs sul comportamento sismico di edifici CBF in acciaio. A tal fine, viene sviluppato un approccio generale di modellazione non lineare utilizzato per simulare la risposta isteretica di quattro tipi di connessioni di comune impiego nell'ambito di sistemi intelaiati a gravità parzialmente vincolati. Inoltre, viene proposto un metodo semplificato per valutare l'efficacia delle forze di attivazione dei SFDs sui parametri che assumono rilevanza tecnica nel controllo e contenimento dei danni prodotti dall'azione sismica su edifici CBF in acciaio. I risultati delle simulazioni numeriche effettuate confermano che le forze di attivazione determinate secondo la metodologia proposta sono efficaci nel mitigare gli effetti prodotti dai modi di vibrare di ordine superiore e nell'impedire al CBF e ai diaframmi rigidi degli orizzontamenti dell'edificio di sperimentare comportamenti anelastici sotto l'effetto dei carichi sismici. Inoltre, è dimostrato che il comportamento sismico degli edifici CBF in acciaio dotati di elementi dissipativi per collegamento di piano diventa praticamente insensibile alla variabilità delle registrazioni sismografiche considerate nelle simulazioni numeriche.

## Parole Chiave

Telai in acciaio a controventatura concentrica, Elementi dissipativi per collegamenti di piano, Dissipatori scorrevoli ad attrito, Spessori ad attrito in materiale composito non metallico, Effetti Prodotti dai modi di vibrare di ordine superiore, Metodologia di progettazione, Sistema intelaiato a gravità, Ingegneria sismica, Dimensionamento basato sul concetto di resilienza



# Acknowledgments

I would first like to thank my supervisor Prof. Dimitrios G. Lignos for giving me the opportunity to pursue a PhD at RESSLab and for his supervision and guidance during the course of my doctoral studies and master thesis. I would also like to thank the members of my jury, Prof. Anastasios Vassilopoulos, Prof. Ioannis Anastasopoulos, Prof. André Filiatrault and Prof. Massimo Latour for their commitment to reviewing my thesis as well as their insightful comments and suggestions.

I would also like to express my gratitude to Prof. Alain Nussbaumer. It has been a pleasure for me collaborating with him during the time that I spent as scientific assistant at RESSLab. I am also grateful to Prof. Ahmed Elkady for his help and guidance during my master thesis and doctoral studies.

My gratitude extends to the Swiss National Foundation (Project No. 200021\_188476) for its financial support. I would also like to thank the team at GIS for their assistance with the experimental program. I am especially grateful to Lea Frédérique Dubugnon for her tremendous help in constructing the test specimen and to Gilles Guignet who helped me with the instrumentation of the specimen. I am also grateful to Elias Merhi, Nitesh Karmacharya and Cesar Daniel Ramirez Mendoza for their invaluable assistance during the testing program. I would not have been able to conduct the experimental campaign successfully without their support.

I am also grateful to the former secretary of RESSLab, Luisa Proietti, and to the current secretary of RESSLab, Karin Pasche. It was a pleasure for me meeting them. Their encouragement has definitely contributed to the success of my thesis.

I would also like to express my gratitude to all the colleagues that I met at RESSLab for the great time spent together inside and outside the laboratory. I am especially grateful to Dr. Hammad El Jisr for his tremendous support throughout my doctoral studies and to Dr. Gabriele Granello for his encouragement and insightful comments. I am also particularly thankful to Dr. Andronikos Skiadopoulos, Selimcan Ozden, Athina Spinasa and Dr. Konstantinos Bakalis.

I would like to express my sincere gratitude to all the friends that I met at Lausanne during my doctoral studies. In particular, I would like to thank Raffaele, Valentina, Danilo, Valentina, Eva, Kyriaki, Angelinca, Elena and Sarah. The time spent together gave me the energy to get to the end of this journey.

A huge thank also goes to my friends from Ticino, Jean-Paul, Matteo, Cleo, Giorgia, Alice, Enea, Mattia, Paolo and Mattia for their immense support during my studies at EPFL. Special thanks also go to Davide, Giorgia and Sara for being always by my side.

My deep gratitude also goes to Cristiano's family as well as to my family in Italy for their constant support. In particular, I would like to thank my grandparents for their unconditional love.

Finally, I am deeply grateful to my parents. I am what I am because of them. I would not have been able to achieve this goal without their support and love. There are no words to express my gratitude to them.

A huge thank also goes to Cristiano, my better half, for his unconditional love and support and for being always by my side. My journey at EPFL has come to the end, but the one next to you is far from finished.

MARTINA PARONESSO  
LAUSANNE  
JUNE, 2022

# Contents

|   |           |
|---|-----------|
| <b>Introduction</b>   | <b>1</b>  |
| <b>1 Experimental Investigation of Composite Materials for Sliding Friction Dampers in Earthquake Resilient Steel Frames</b>      | <b>13</b> |
| 1.1 Introduction . . . . .  | 14        |
| 1.2 Description of the Experimental Campaign . . . . .  | 16        |
| 1.2.1 Sliding Friction Damper Prototype . . . . .   | 16        |
| 1.2.1.1 Performance Considerations for Selected Friction Pads . .   | 18        |
| 1.2.2 Laboratory Test Setup and Instrumentation . . . . .   | 20        |
| 1.2.3 Loading Protocols . . . . .   | 21        |
| 1.3 Experimental Results . . . . .  | 22        |
| 1.3.1 Results obtained under the Linear Static Loading Protocol . . . .   | 23        |
| 1.3.2 Results obtained under Symmetric Cyclic Loading Protocols . . . .   | 25        |
| 1.3.2.1 Qualitative Performance Evaluation . . . . .  | 26        |
| 1.3.2.2 Quantitative Performance Evaluation . . . . .   | 31        |
| 1.3.3 Performance under Pulse-like and Mainshock-Aftershock Loading Protocols . . . . .   | 34        |
| 1.4 Discussion . . . . .  | 34        |
| 1.4.1 Pressure Dependency . . . . .   | 35        |
| 1.4.2 Effect of Loading Rate, Loading History and Temperature . . . . .   | 36        |
| 1.5 Conclusions . . . . .   | 37        |
| <b>2 Seismic Design and Performance of Steel Concentrically Braced Frame Buildings with Dissipative Floor Connectors</b>          | <b>41</b> |
| 2.1 Introduction . . . . .  | 42        |
| 2.2 Basic Description of a Multi-Story Steel CBF Building with Sliding Friction Dampers as Dissipative Floor Connectors . . . . . | 45        |

|          |   |           |
|----------|---|-----------|
| 2.3      | Design Methodology and Performance Objectives . . . . .   | 47        |
| 2.4      | Case Studies . . . . .  | 51        |
| 2.4.1    | Design of Multi-Story Steel CBF Buildings equipped with Sliding Friction Dampers . . . . .  | 51        |
| 2.4.2    | Nonlinear Building Models . . . . .   | 54        |
| 2.5      | Modal Analysis and Nonlinear Static Analysis . . . . .  | 56        |
| 2.6      | Nonlinear Response History Analysis . . . . .   | 60        |
| 2.6.1    | Peak Story Drift Ratio Demands . . . . .  | 61        |
| 2.6.2    | Peak Absolute Acceleration Demands . . . . .  | 62        |
| 2.6.3    | Peak Story Shear Force Demands . . . . .  | 63        |
| 2.6.4    | Effect of assumed $q$ -factor . . . . .   | 64        |
| 2.6.5    | EDP Hazard Curves . . . . .   | 65        |
| 2.7      | Limitations . . . . .   | 68        |
| 2.8      | Summary and Conclusions . . . . .   | 68        |
| <b>3</b> | <b>Influence of Gravity Connections and Damper Activation Forces on the Seismic Behavior of Steel CBF Buildings with Dissipative Floor Connectors</b> . . . . . | <b>71</b> |
| 3.1      | Introduction . . . . .  | 72        |
| 3.2      | Considered Beam-to-Column Gravity Connections . . . . .   | 74        |
| 3.2.1    | Behavioural Insights . . . . .  | 75        |
| 3.2.2    | Proposed Modelling Approach of Beam-to-Column Gravity Connections . . . . .   | 78        |
| 3.3      | Case Study Building . . . . .   | 83        |
| 3.3.1    | 6-story steel Building with Friction Dampers as Dissipative Floor Connectors . . . . .  | 83        |
| 3.3.2    | Nonlinear Building Model . . . . .  | 86        |
| 3.4      | Nonlinear Response History Analysis . . . . .   | 88        |
| 3.4.1    | Peak Absolute Floor Acceleration Demands . . . . .  | 89        |
| 3.4.2    | Peak Story Drift Ratio Demands . . . . .  | 90        |
| 3.4.3    | Peak Rotation Demands in the Members of the Gravity Framing System . . . . .  | 92        |
| 3.5      | Proposed Simplified Method . . . . .  | 93        |
| 3.5.1    | Equivalent Single Degree of Freedom System . . . . .  | 94        |
| 3.5.2    | Performance Spectra (P-Spectra) . . . . .   | 96        |
| 3.5.3    | Estimated Errors in the Predictions . . . . .   | 97        |

|   |            |
|---|------------|
| 3.6 Conclusions . . . . .   | 98         |
| <b>Conclusions and Future Work</b>                                  | <b>101</b> |
| <b>A Sliding Friction Damper Drawings</b>                           | <b>109</b> |
| <b>B Instrumentation Plan</b>                                       | <b>119</b> |
| <b>C Deduced Quantities</b>   | <b>123</b> |
| C.1 Average Slot Displacement . . . . .                             | 123        |
| C.2 Nominal Bolt Preload . . . . .                                  | 124        |
| C.3 Bolt Preload Variation . . . . .                                | 125        |
| C.4 Bolt Preload . . . . .  | 125        |
| C.5 Total Normal Force . . . . .                                    | 125        |
| C.6 Cumulative Displacement . . . . .                               | 126        |
| C.7 Cumulative Dissipated Energy . . . . .                          | 126        |
| C.8 Tightening Torque . . . . .                                     | 126        |
| <b>D Supplementary Results</b>                                      | <b>129</b> |
| D.1 Friction Pad M1 . . . . .                                       | 129        |
| D.2 Friction Pad M2 . . . . .                                       | 132        |
| D.3 Friction Pad M3 . . . . .                                       | 134        |
| D.4 Friction Pad M4 . . . . .                                       | 136        |
| D.5 Friction Pad M5 . . . . .                                       | 139        |
| <b>E Design Summary</b>   | <b>141</b> |
| E.1 Design standards . . . . .                                      | 141        |
| E.2 Basic Description of the Buildings . . . . .                    | 142        |
| E.2.1 Structural Type and Layout . . . . .                          | 142        |
| E.2.2 Member Cross Sections . . . . .                               | 143        |
| E.2.3 Material Properties . . . . .                                 | 143        |
| E.3 Actions . . . . .   | 147        |
| E.3.1 Permanent Action . . . . .                                    | 147        |
| E.3.2 Variable Actions . . . . .                                    | 147        |
| E.3.3 Seismic Action . . . . .                                      | 148        |
| E.3.3.1 Design Response Spectra . . . . .                           | 148        |
| E.3.3.2 Seismic Mass . . . . .                                      | 149        |
| E.3.4 Combination of Actions at the Ultimate Limit States . . . . . | 150        |

|                        |   |            |
|------------------------|---|------------|
| E.3.4.1                | Persistent or Transient Design Situations . . . . .                 | 150        |
| E.3.4.2                | Seismic Design Situation . . . . .                                  | 151        |
| E.3.5                  | Combination of Actions at the Serviceability Limit States . . . . . | 152        |
| E.4                    | Structural Model . . . . .  | 153        |
| E.4.1                  | Description of the Model . . . . .                                  | 153        |
| E.4.2                  | Modal Response Spectrum Analysis . . . . .                          | 154        |
| E.5                    | Design of the Centrically Braced Frames . . . . .                   | 155        |
| E.5.1                  | Damage Limitation Verification . . . . .                            | 155        |
| E.5.2                  | Second-order Effects . . . . .                                      | 156        |
| E.5.3                  | Design of the Braces . . . . .                                      | 158        |
| E.5.4                  | Design of the Beams . . . . .                                       | 159        |
| E.5.5                  | Design of the Columns . . . . .                                     | 159        |
| <b>References</b>      |   | <b>161</b> |
| <b>Curriculum Vitæ</b> |   | <b>184</b> |

# List of Figures

|   |  |   |
|---|--|---|
| 1 | (a) Axial force-axial displacement hysteretic response of a steel brace, (b)-(e) typical sequence of damage of a steel brace: (b) global buckling, (c) local buckling, (d) fracture initiation, (d) loss of tensile strength (images adopted from Fell et al. [5]) . . . . .   | 2 |
| 2 | (a) Example of soft-story observed in a 2-story steel CBF building in the aftermath of the Tohoku-Oki earthquake (image courtesy of Prof. Dimitrios G. Lignos [15]), (b) concentration of story drifts experienced by a 8-story chevron braced steel frame under the El Centro earthquake record (image adopted from Tremblay and Robert [13]) . . . . .   | 2 |
| 3 | (a) Expected annual losses over 50-year life expectancy of steel CBF buildings normalized with respect to the total replacement cost (image adopted from Hwang and Lignos [20]), (b) drift-based fragility curves associated with brace flexural buckling (image adopted from Lignos and Karamanci [26]) . . . . .   | 3 |
| 4 | Examples of brittle failure modes in bracing connections: (a) fracture of the middle gusset plate and (b) buckling of the corner bracing-end connection in a X-brace (images adopted from Davaran et al. [27]), (c) fractured gusset plates in an inverted V-brace and (d) bending of the middle gusset plate in a X-brace observed in the aftermath of the 2011 Tohoku-Oki earthquake (images adopted from Okazaki et al. [28]) . . . . . | 4 |

|     |  |    |
|-----|--|----|
| 5   | Examples of systems developed to improve the seismic performance of conventional steel braced frames: (a) eccentrically braced frames (image adopted from Dusicka et al. [54]), (b) buckling restrained braced frames (image adopted from Kersting et al. [55]), (c) controlled rocking steel braced frames (image adopted from Eatherton et al. [41]), (d) sliding friction dampers (image adopted from Pall and Pall [56]), (e) slotted bolted connections (image adopted from Pall and Pall [56]), (f) yielding devices (image adopted from Gray et al. [50]) . . . . . | 6  |
| 6   | Absolute floor acceleration demands at the (a) 12 <sup>th</sup> and (b) 6 <sup>th</sup> floor of a 12-story reinforced concrete shear wall building, whose floor diaphragms are connected to the wall through (RE) rigid links, (FD + RB) sliding friction devices and rubber bearings, (BRB + RB) buckling-restrained braces and rubber bearings (images adopted from Tsampras et al. [67]) . . .   | 8  |
| 1.1 | Sliding friction damper prototype: (a)-(b) basic components, (c) main dimensions in millimetres, (d) parameters used to control the slip load $F_s$  | 17 |
| 1.2 | Friction pads: (a) M1, (b) M2, (c) M3, (d) M4, (e) M5, (f) main dimensions in millimetres . . . . .  | 19 |
| 1.3 | (a) Sliding friction damper after installation, (b) instrumentation plan . .   | 20 |
| 1.4 | Employed loading protocols: (a) linear static loading (M), (b) cyclic loading with constant amplitude (CA), (c) cyclic loading with increasing amplitude at low (IA), moderate (IA-H) and high rate (IA-HH), (d) cyclic loading with decreasing amplitude at low rate (DA), (e) pulse-like loading protocol (PL), (f) mainshock-aftershock loading protocol (MS-AS) . . . . .  | 23 |
| 1.5 | Results obtained under the linear static loading protocol for $T_{\text{bolt}} = 200 \text{ Nm/bolt}$ : (a) bolt preload as a function of the total cumulative displacement, (b) axial force-axial displacement response of the damper, (c) friction coefficient as a function of the total cumulative displacement . . . . .  | 24 |
| 1.6 | Cyclic loading protocol with constant amplitude (CA): friction coefficient evolution for (a) M4 and (b) M1, (c) rise in temperature for materials M4 and M1 . . . . .  | 26 |
| 1.7 | Friction coefficient evolution under constant (CA) and increasing amplitude at low rate (IA): (a) M4 for $F_{s,\text{exp}} = 300 \text{ kN}$ , (b) M5 for $F_{s,\text{exp}} = 150 \text{ kN}$  | 27 |
| 1.8 | Results obtained for M5 and $F_{s,\text{exp}} = 150 \text{ kN}$ : (a) friction coefficient evolution, (b) rise in temperature tracked with the thermocouples THbolt inside the bolt holes . . . . .  | 27 |



|      |   |    |
|------|---|----|
| 1.9  | Results obtained under the cyclic loading protocol with decreasing amplitude (DA): friction coefficient evolution for (a) M4 ( $F_{s,exp} = 300$ kN) and (b) M5 ( $F_{s,exp} = 150$ kN), (c) bolt preload . . . . .   | 28 |
| 1.10 | Results obtained for M1 and $F_{s,exp} = 300$ kN: (a)-(b) friction coefficient evolution, (c) rise in temperature at the surface of the inner slotted plate .   | 29 |
| 1.11 | Surface condition of M1 at the end of the cyclic loading protocol (a) IA-HH and (b) IA for $F_{s,exp} = 300$ kN . . . . .   | 29 |
| 1.12 | Results obtained for M3 and $F_{s,exp} = 300$ kN under the cyclic loading protocol with constant amplitude (CA) . . . . .   | 30 |
| 1.13 | Condition of (a),(c) M2 and (b),(d) M3 at the end of the cyclic loading protocol (a),(c) IA ( $F_{s,exp} = 150$ kN) and (b),(d) CA ( $F_{s,exp} = 300$ kN): (a)-(b) surface wearing, (c)-(d) bending deformation . . . . .  | 30 |
| 1.14 | Results obtained for $F_{s,exp} = 300$ kN under the cyclic loading protocol with constant amplitude (CA): (a) M3, (b) and (d) M4, (c) M1 . . . . .  | 31 |
| 1.15 | Fracture patterns of the friction pads (a) M2 and (b) M4 at the end of the loading protocol CA for $F_{s,exp} = 300$ kN . . . . .   | 31 |
| 1.16 | Results obtained for $F_{exp,s} = 300$ kN under the pulse-like (PL) and mainshock-aftershock loading protocol (MS: mainshock, AS1: first aftershock, AS2: second aftershock): (a)-(c) for M1, (d)-(f) for M4 . . . . .  | 35 |
| 1.17 | Mean of $\mu_s$ and $\mu_d$ obtained for different expected slip loads and loading protocols (CA: constant amplitude; DA: decreasing amplitude; IA, IA-H, IA-HH: increasing amplitude at low, moderate and high rate; PL: pulse-like, MS: mainshock; AS1: first aftershock; AS2: second aftershock): (a) for M1, (b) for M4 . . . . . | 36 |
| 1.18 | Friction coefficient obtained for (a)-(c) M1 and (d)-(f) M4 under different loading protocols and $F_{s,exp} = 300$ kN . . . . .  | 37 |
| 2.1  | Configuration of a 6-story steel building equipped with floor SFDs in the N-S direction: (a) plan view, (b) elevation view (section A-A), (c) sliding friction damper, (d) rubber bearing . . . . .   | 46 |
| 2.2  | (a) Idealized behavior of a 6-story steel building equipped with floor SFDs, (b) force distribution along the height of the building . . . . .  | 47 |
| 2.3  | (a) Admissible story shear $V_s$ in a 6-story steel CBF building, (b) $\vec{F}_s$ pattern defined for a 6-story steel CBF building . . . . .  | 50 |

|      |  |    |
|------|--|----|
| 2.4  | (a) Plan view of the 6-story steel buildings, (b)-(c) elevation view of the LD-CBF ( $q = 2.0$ ) and HD-CBF ( $q = 3.0$ ) respectively, (d)-(e) bracing-end connections of the LD-CBF and HD-CBF respectively (details D1 and D2) . . . . .  | 53 |
| 2.5  | (a)-(b) Admissible story shear obtained for the LD-CBF ( $q = 2.0$ ) and HD-CBF ( $q = 3.0$ ) respectively, (c) activation forces selected for the SFDs . . . . .  | 54 |
| 2.6  | (a) 2D numerical model of the 6-story steel building in the N-S direction, (b) axial and rotational springs placed in series in order to model the in-plane and out-of-plane behavior of the bracing-end connections of the LD-CBF and LD-CBF-R (c) truss element used to model both SFD and RBs . . . . . | 55 |
| 2.7  | Pushover curves obtained for the (a) LD-CBF and LD-CBF-R, (b) HD-CBF and HD-CBF-R . . . . .  | 58 |
| 2.8  | Peak SDRs obtained at targeted roof drift ratios for the CBF of the (a) LD-CBF-R and LD-CBF, and (b) HD-CBF-R and HD-CBF . . . . .   | 59 |
| 2.9  | (a)-(b) Acceleration spectra of the ground motion records for the DBE and MCE seismic intensities respectively, (c) $Sa_{avg}$ hazard curve of Sion (Switzerland) . . . . .  | 60 |
| 2.10 | Peak SDRs obtained at DBE (first row) and MCE (second row) for (a),(d) the LD-CBF-R, (b),(e) the CBF of the LD-CBF and (c),(f) the GFS of the LD-CBF . . . . .   | 61 |
| 2.11 | Peak absolute floor acceleration demands obtained at (a)-(b) DBE and (c)-(d) MCE for (a),(c) the LD-CBF-R and (b),(d) the GFS of LD-CBF . . . . .  | 62 |
| 2.12 | 5 % damped floor spectra obtained at the (a) 3 <sup>rd</sup> floor and (b) roof of the LD-CBF-R and LD-CBF under the single record of the 1994 Northridge earthquake recorded at the Jensen Filter Plant station . . . . .   | 63 |
| 2.13 | Normalized peak story shear forces obtained at (a)-(b) DBE and (c)-(d) MCE for (a),(c) the LD-CBF-R and (b),(d) the LD-CBF . . . . .   | 64 |
| 2.14 | (a)-(b) Peak SDRs of the GFS at DBE and MCE, respectively, (c)-(d) peak axial displacements of the SFDs at DBE and MCE, respectively . . . . .   | 65 |
| 2.15 | Exceedance functions for (a) the peak SDRs of the GFS and (b) the peak axial displacement of the SFDs . . . . .  | 66 |
| 2.16 | Hazard curves developed for (a) the peak SDRs of the GFS and (b) the peak axial displacement of the SFDs of the LD-CBF . . . . .   | 67 |

|      |   |    |
|------|---|----|
| 3.1  | Sketch of the investigated beam-to-column gravity connections: (a) shear tab connection, (b) clip angle connection, (c) flush end-plate connection, (d) shear tab connection with bottom T-stub . . . . .   | 75 |
| 3.2  | Calibration of the moment-rotation response of the beam-to-column connections by using the Pinching4 model available in OpenSees: (a) shear tab connection (specimen 6A [159, 198]) (b) clip angle connection (specimen S-HA [202]), (c) flush end-plate connection (specimen CJ4 [208]), (d) shear tab connection with T-stub (east beam [209]) . . . . .  | 77 |
| 3.3  | (a) Definition of the backbone curve of gravity connections ( $M^+, \theta^+$ : values attained under positive bending moment; $M^-, \theta^-$ : values attained under negative bending moment), (b)-(e) sketches of the force distribution considered to determine the flexural capacity $M_{\max}$ of the (b) shear tab connection, (c) clip angle connection, (d) shear tab connection with T-stub, (e) flush end-plate connection . . . . . | 79 |
| 3.4  | Moment-chord rotation backbone curve of the gravity connections normalized with respect to the plastic resisting moment ( $M_p$ ) of the steel IPE 270 beam (i.e., equivalent to W10x26 American wide flange beam) of the GFS under investigation . . . . .   | 82 |
| 3.5  | Configuration of the 6-story steel building equipped with floor SFDs in the N-S direction: (a) plan view, (b) elevation view (section A-A), (c) sliding friction damper, (d) rubber bearing . . . . .   | 84 |
| 3.6  | Beam-to-column connections designed for the GFS of the 6-story steel building: (a) shear tab connection, (b) clip angle connection, (c) flush end-plate connection, (d) shear tab connection with T-stub . . . . .  | 85 |
| 3.7  | (a) Admissible story shear $V_s$ in a 6-story steel CBF building, (b) $\vec{F}_s$ pattern defined for a 6-story steel CBF building . . . . .  | 87 |
| 3.8  | (a) 2D numerical model of the 6-story steel building in the N-S direction, (b) truss element used to model the SFD and the RBs at each story of the building . . . . .  | 88 |
| 3.9  | Acceleration spectra of the ground motions adjusted to the (a) DBE and (b) MCE seismic intensities respectively ( $T_1$ , $T_2$ and $T_3$ are, respectively, the first, second and third fundamental period of the 6-story steel CBF building) . . . . .  | 89 |
| 3.10 | Median peak absolute floor acceleration demands obtained at (a) DBE and (b) MCE for different types of beam-to-column connections . . . . .   | 90 |

|      |  |     |
|------|--|-----|
| 3.11 | Results obtained at the (a)-(b) 2 <sup>nd</sup> and (c)-(d) 7 <sup>th</sup> floor of the 6-story building under the 1999 Chi-Chi earthquake recorded at the CHY086 station and scaled at the MCE seismic intensity: (a),(c) force-displacement response of the SFD, (b),(d) moment-rotation response of the shear tab and flush end-plate connections of the GFS . . . . .         | 91  |
| 3.12 | Median peak story drift ratios of the (a)-(b) CBF and (c)-(d) GFS for different gravity connections: (a),(c) at DBE, (b),(d) at MCE . . . . .  | 91  |
| 3.13 | Median peak rotation demands of the (a)-(b) beams and (c)-(d) columns of the GFS at (a),(c) DBE and (b),(d) MCE . . . . .  | 93  |
| 3.14 | (a) 6-story steel CBF building equipped with floor SFDs transformed into an equivalent single-degree-of-freedom system, (b) moment-rotation response of the spring located at the base of the equivalent single-degree-of-freedom system . . . . .   | 94  |
| 3.15 | Performance spectra constructed for the 6-story CBF building equipped with floor SFDs: (a) median values, (b) 84 <sup>th</sup> percentile . . . . .  | 96  |
| 3.16 | (a) Median values of the peak floor absolute acceleration demands and peak roof displacements of the GFS as predicted with the SDF (unfilled markers) and MDF systems (filled markers); relative error in predicting (b) the peak floor absolute acceleration demand and (c) the peak roof displacement of the GFS of the prototype building . . . . .                             | 97  |
| B.1  | Instrumentation plan . . . . .   | 121 |
| B.2  | Instrumentation of the sliding friction damper . . . . .   | 121 |
| C.1  | Test setup used to define the relationship between the nominal bolt preload and the applied torque . . . . .   | 124 |
| C.2  | Bolt preload as a function of the applied torque ( $R^2 = 0.93$ ) . . . . .  | 125 |
| D.1  | Results obtained for the friction pad M1 under the linear static loading protocol ( $F_{s,exp} = 150$ kN: solid line, $F_{s,exp} = 300$ kN: dotted line): (a) axial force as a function of the average slot displacement, (b) bolt preload as a function of the cumulative dissipated energy, (c) friction coefficient as a function of the cumulative dissipated energy . . . . . | 129 |

- D.2 Results obtained for the friction pad M1 under the cyclic loading protocol with constant amplitude ( $F_{s,exp} = 150$  kN: solid line,  $F_{s,exp} = 300$  kN: dotted line): (a) axial force as a function of the average slot displacement, (b) bolt preload as a function of the cumulative dissipated energy, (c) friction coefficient as a function of the cumulative dissipated energy, (d) temperature as a function of the cumulative dissipated energy . . . . . 130
- D.3 Results obtained for the friction pad M1 under the cyclic loading protocol with increasing amplitude at low rate ( $F_{s,exp} = 150$  kN: solid line,  $F_{s,exp} = 300$  kN: dotted line): (a) axial force as a function of the average slot displacement, (b) bolt preload as a function of the cumulative dissipated energy, (c) friction coefficient as a function of the cumulative dissipated energy, (d) temperature as a function of the cumulative dissipated energy 130
- D.4 Results obtained for the friction pad M1 under the cyclic loading protocol with decreasing amplitude at low rate ( $F_{s,exp} = 150$  kN: solid line,  $F_{s,exp} = 300$  kN: dotted line): (a) axial force as a function of the average slot displacement, (b) bolt preload as a function of the cumulative dissipated energy, (c) friction coefficient as a function of the cumulative dissipated energy, (d) temperature as a function of the cumulative dissipated energy 130
- D.5 Results obtained for the friction pad M1 under the cyclic loading protocol with increasing amplitude at moderate rate ( $F_{s,exp} = 150$  kN: solid line,  $F_{s,exp} = 300$  kN: dotted line): (a) axial force as a function of the average slot displacement, (b) bolt preload as a function of the cumulative dissipated energy, (c) friction coefficient as a function of the cumulative dissipated energy, (d) temperature as a function of the cumulative dissipated energy . . . . . 131
- D.6 Results obtained for the friction pad M1 under the cyclic loading protocol with increasing amplitude at high rate and  $F_{s,exp} = 300$  kN: (a) axial force as a function of the average slot displacement, (b) bolt preload as a function of the cumulative dissipated energy, (c) friction coefficient as a function of the cumulative dissipated energy, (d) temperature as a function of the cumulative dissipated energy . . . . . 131
- D.7 Results obtained for the friction pad M2 under the linear static loading protocol ( $F_{s,exp} = 150$  kN: solid line,  $F_{s,exp} = 300$  kN: dotted line): (a) axial force as a function of the average slot displacement, (b) bolt preload as a function of the cumulative dissipated energy, (c) friction coefficient as a function of the cumulative dissipated energy . . . . . 132

- D.8 Results obtained for the friction pad M2 under the cyclic loading protocol with constant amplitude ( $F_{s,exp} = 150$  kN: solid line,  $F_{s,exp} = 300$  kN: dotted line): (a) axial force as a function of the average slot displacement, (b) bolt preload as a function of the cumulative dissipated energy, (c) friction coefficient as a function of the cumulative dissipated energy, (d) temperature as a function of the cumulative dissipated energy . . . . . 132
- D.9 Results obtained for the friction pad M2 under the cyclic loading protocol with increasing amplitude at low rate ( $F_{s,exp} = 150$  kN: solid line,  $F_{s,exp} = 300$  kN: dotted line): (a) axial force as a function of the average slot displacement, (b) bolt preload as a function of the cumulative dissipated energy, (c) friction coefficient as a function of the cumulative dissipated energy, (d) temperature as a function of the cumulative dissipated energy 133
- D.10 Results obtained for the friction pad M2 under the cyclic loading protocol with decreasing amplitude at low rate and  $F_{s,exp} = 150$  kN: (a) axial force as a function of the average slot displacement, (b) bolt preload as a function of the cumulative dissipated energy, (c) friction coefficient as a function of the cumulative dissipated energy, (d) temperature as a function of the cumulative dissipated energy . . . . . 133
- D.11 Results obtained for the friction pad M2 under the cyclic loading protocol with increasing amplitude at moderate rate ( $F_{s,exp} = 150$  kN: solid line,  $F_{s,exp} = 300$  kN: dotted line): (a) axial force as a function of the average slot displacement, (b) bolt preload as a function of the cumulative dissipated energy, (c) friction coefficient as a function of the cumulative dissipated energy, (d) temperature as a function of the cumulative dissipated energy . . . . . 133
- D.12 Results obtained for the friction pad M3 under the linear static loading protocol ( $F_{s,exp} = 150$  kN: solid line,  $F_{s,exp} = 300$  kN: dotted line): (a) axial force as a function of the average slot displacement, (b) bolt preload as a function of the cumulative dissipated energy, (c) friction coefficient as a function of the cumulative dissipated energy . . . . . 134
- D.13 Results obtained for the friction pad M3 under the cyclic loading protocol with constant amplitude and  $F_{s,exp} = 300$  kN: (a) axial force as a function of the average slot displacement, (b) bolt preload as a function of the cumulative dissipated energy, (c) friction coefficient as a function of the cumulative dissipated energy, (d) temperature as a function of the cumulative dissipated energy . . . . . 134

- D.14 Results obtained for the friction pad M3 under the cyclic loading protocol with increasing amplitude at low rate ( $F_{s,exp} = 150$  kN: solid line,  $F_{s,exp} = 300$  kN: dotted line): (a) axial force as a function of the average slot displacement, (b) bolt preload as a function of the cumulative dissipated energy, (c) friction coefficient as a function of the cumulative dissipated energy, (d) temperature as a function of the cumulative dissipated energy 135
- D.15 Results obtained for the friction pad M3 under the cyclic loading protocol with decreasing amplitude at low rate and  $F_{s,exp} = 150$  kN: (a) axial force as a function of the average slot displacement, (b) bolt preload as a function of the cumulative dissipated energy, (c) friction coefficient as a function of the cumulative dissipated energy, (d) temperature as a function of the cumulative dissipated energy . . . . . 135
- D.16 Results obtained for the friction pad M3 under the cyclic loading protocol with increasing amplitude at moderate rate ( $F_{s,exp} = 150$  kN: solid line,  $F_{s,exp} = 300$  kN: dotted line): (a) axial force as a function of the average slot displacement, (b) bolt preload as a function of the cumulative dissipated energy, (c) friction coefficient as a function of the cumulative dissipated energy, (d) temperature as a function of the cumulative dissipated energy . . . . . 135
- D.17 Results obtained for the friction pad M4 under the linear static loading protocol ( $F_{s,exp} = 150$  kN: solid line,  $F_{s,exp} = 300$  kN: dotted line): (a) axial force as a function of the average slot displacement, (b) bolt preload as a function of the cumulative dissipated energy, (c) friction coefficient as a function of the cumulative dissipated energy . . . . . 136
- D.18 Results obtained for the friction pad M4 under the cyclic loading protocol with constant amplitude ( $F_{s,exp} = 150$  kN: solid line,  $F_{s,exp} = 300$  kN: dotted line): (a) axial force as a function of the average slot displacement, (b) bolt preload as a function of the cumulative dissipated energy, (c) friction coefficient as a function of the cumulative dissipated energy, (d) temperature as a function of the cumulative dissipated energy . . . . . 136
- D.19 Results obtained for the friction pad M4 under the cyclic loading protocol with increasing amplitude at low rate ( $F_{s,exp} = 150$  kN: solid line,  $F_{s,exp} = 300$  kN: dotted line): (a) axial force as a function of the average slot displacement, (b) bolt preload as a function of the cumulative dissipated energy, (c) friction coefficient as a function of the cumulative dissipated energy, (d) temperature as a function of the cumulative dissipated energy 137

|  |     |
|--|-----|
| D.20 Results obtained for the friction pad M4 under the cyclic loading protocol with decreasing amplitude at low rate ( $F_{s,exp} = 150$ kN: solid line, $F_{s,exp} = 300$ kN: dotted line): (a) axial force as a function of the average slot displacement, (b) bolt preload as a function of the cumulative dissipated energy, (c) friction coefficient as a function of the cumulative dissipated energy, (d) temperature as a function of the cumulative dissipated energy      | 137 |
| D.21 Results obtained for the friction pad M4 under the cyclic loading protocol with increasing amplitude at moderate rate ( $F_{s,exp} = 150$ kN: solid line, $F_{s,exp} = 300$ kN: dotted line): (a) axial force as a function of the average slot displacement, (b) bolt preload as a function of the cumulative dissipated energy, (c) friction coefficient as a function of the cumulative dissipated energy, (d) temperature as a function of the cumulative dissipated energy | 137 |
| D.22 Results obtained for the friction pad M4 under the cyclic loading protocol with increasing amplitude at high rate and $F_{s,exp} = 300$ kN: (a) axial force as a function of the average slot displacement, (b) bolt preload as a function of the cumulative dissipated energy, (c) friction coefficient as a function of the cumulative dissipated energy, (d) temperature as a function of the cumulative dissipated energy   | 138 |
| D.23 Results obtained for the friction pad M5 under the linear static loading protocol ( $F_{s,exp} = 150$ kN: solid line, $F_{s,exp} = 300$ kN: dotted line): (a) axial force as a function of the average slot displacement, (b) bolt preload as a function of the cumulative dissipated energy, (c) friction coefficient as a function of the cumulative dissipated energy  | 139 |
| D.24 Results obtained for the friction pad M5 under the cyclic loading protocol with constant amplitude ( $F_{s,exp} = 150$ kN: solid line, $F_{s,exp} = 300$ kN: dotted line): (a) axial force as a function of the average slot displacement, (b) bolt preload as a function of the cumulative dissipated energy, (c) friction coefficient as a function of the cumulative dissipated energy, (d) temperature as a function of the cumulative dissipated energy                    | 139 |
| D.25 Results obtained for the friction pad M5 under the cyclic loading protocol with increasing amplitude at low rate ( $F_{s,exp} = 150$ kN: solid line, $F_{s,exp} = 300$ kN: dotted line): (a) axial force as a function of the average slot displacement, (b) bolt preload as a function of the cumulative dissipated energy, (c) friction coefficient as a function of the cumulative dissipated energy, (d) temperature as a function of the cumulative dissipated energy      | 140 |



|      |   |     |
|------|---|-----|
| D.26 | Results obtained for the friction pad M5 under the cyclic loading protocol with decreasing amplitude at low rate and $F_{s,exp} = 150$ kN: (a) axial force as a function of the average slot displacement, (b) bolt preload as a function of the cumulative dissipated energy, (c) friction coefficient as a function of the cumulative dissipated energy, (d) temperature as a function of the cumulative dissipated energy . . . . .  | 140 |
| D.27 | Results obtained for the friction pad M5 under the cyclic loading protocol with increasing amplitude at moderate rate ( $F_{s,exp} = 150$ kN: solid line, $F_{s,exp} = 300$ kN: dotted line): (a) axial force as a function of the average slot displacement, (b) bolt preload as a function of the cumulative dissipated energy, (c) friction coefficient as a function of the cumulative dissipated energy, (d) temperature as a function of the cumulative dissipated energy . . . . . | 140 |
| E.1  | Plan view of the buildings . . . . .  | 142 |
| E.2  | Elevation view of the building designed for (a) $q = 2$ and (b) $q = 3$ in the E-W direction . . . . .  | 144 |
| E.3  | Elevation view of the building designed for (a) $q = 2$ and (b) $q = 3$ in the N-S direction . . . . .  | 145 |
| E.4  | Design response spectra . . . . .   | 149 |
| E.5  | 3D model developed in SCIA Engineer . . . . .   | 153 |
| E.6  | Modal shapes of the first five periods of vibration of the building designed for $q = 2$ . . . . .  | 155 |
| E.7  | (a) Maximum normalized floor displacements and (b) maximum story drift ratios along the height of the CBFs designed for $q = 2$ and $q = 3$ . . . . .   | 157 |



# List of Tables

|     |   |     |
|-----|---|-----|
| 1.1 | Characteristic properties of the tested friction pad materials . . . . .  | 19  |
| 1.2 | Load protocols used to test the the five friction pads . . . . .  | 22  |
| 1.3 | Data obtained for $F_{s,exp} = 150$ kN and $F_{s,exp} = 300$ kN under the linear static loading protocol . . . . .  | 25  |
| 1.4 | Number of cycles $N_{tot}$ , total cumulative dissipated energy $\sum E_{tot}$ and maximum temperature $T_{max}$ obtained for $F_{s,exp} = 150$ kN and $F_{s,exp} = 300$ kN . . . . . | 32  |
| 1.5 | Mean $\bar{F}$ , mean $\bar{\mu}$ and total loss of pretension $\Delta N_b$ obtained for $F_{s,exp} = 150$ kN and $F_{s,exp} = 300$ kN under the cyclic loading protocols . . . . .   | 33  |
| 1.6 | Data obtained for $F_{s,exp} = 300$ kN under the pulse-like (PL) and mainshock-aftershock loading protocol (MS: mainshock, AS1: first aftershock, AS2: second aftershock) . . . . .   | 36  |
| 2.1 | First-mode periods ( $T_1$ ), mass ratios ( $M/M_{tot}$ ) and stiffness ratios ( $K/K_{tot}$ ) obtained for the four investigated buildings . . . . .                                 | 57  |
| 2.2 | Peak SDRs of the GFS and peak $\delta$ values at different return periods $T$ . .   | 67  |
| 3.1 | Calibrated moment-chord rotation parameters of the backbone curve of the beam-to-column connections illustrated in Fig. 3.1 . . . . .   | 81  |
| 3.2 | Calibrated parameters of the Pinching4 model to simulate the strength and stiffness degradation of the gravity connections illustrated in Fig 3.1 .                                   | 83  |
| B.1 | List of instrumentation type and measurement range . . . . .  | 120 |
| B.2 | List of instrumentation measurements and their notation . . . . .   | 120 |
| B.3 | List of non-functional sensors . . . . .  | 122 |
| E.1 | Member cross sections of the CBFs and MRFs of the building designed for $q = 2$ . . . . .   | 143 |

|      |   |     |
|------|---|-----|
| E.2  | Member cross sections of the CBFs and MRFs of the building designed for $q = 3$ . . . . .   | 145 |
| E.3  | Material properties of the steel members . . . . .  | 146 |
| E.4  | Material properties of the high-strength bolts and diaphragms . . . . .   | 146 |
| E.5  | Summary of the super-imposed dead loads . . . . .   | 147 |
| E.6  | Summary of the variable loads . . . . .   | 148 |
| E.7  | $\varphi$ and $\psi_{2,i}$ values used to compute the combination coefficient $\psi_{E,i}$ . . . . .  | 150 |
| E.8  | Seismic mass acting at each floor of the buildings . . . . .  | 150 |
| E.9  | $\gamma_G$ , $\gamma_{Q,1}$ and $\gamma_{Q,i}$ combination coefficients used for the persistent or transient design situation according to EN 1990, Table A1.2(B) . . . . . | 151 |
| E.10 | $\psi_{0,i}$ factors used for the persistent or transient design situation according to EN 1990, Table A1.1 . . . . .   | 151 |
| E.11 | $\psi_{2,i}$ factors used for the seismic design situation according to EN 1990, Table A1.1 . . . . .   | 152 |
| E.12 | $\psi_{1,1}$ factors defined according to EN 1990, Table A1.1 . . . . .   | 152 |
| E.13 | Periods of vibration and effective modal masses . . . . .   | 154 |
| E.14 | Damage limitation verification computed for the CBFs designed for $q = 2$ and $q = 3$ . . . . .   | 156 |
| E.15 | Second-order effects computed in the N-S direction of the investigated buildings . . . . .  | 157 |
| E.16 | Summary of the design of the braces for $q = 2$ . . . . .   | 158 |
| E.17 | Summary of the design of the braces for $q = 3$ . . . . .   | 158 |
| E.18 | Summary of the design of the primary and secondary beams for $q = 2$ and $q = 3$ . . . . .  | 159 |
| E.19 | Summary of the design of the CBF columns for $q = 2$ . . . . .  | 159 |
| E.20 | Summary of the design of the CBF columns for $q = 3$ . . . . .  | 160 |

*Mutationem motus proportionalem esse vi motrici  
impressae, et fieri secundum lineam rectam qua vis  
illa imprimitur.*

Isaac Newton, Philosophiae Naturalis Principia  
Mathematica

# Introduction

## Research Background

Steel concentrically braced frames (CBFs) are lateral load resisting systems widely used in seismic regions due to their cost-effectiveness and high lateral stiffness. Under seismic action, they dissipate energy primarily through axial yielding and flexural buckling of the braces. In the last forty years, numerous experimental [1–8] and numerical investigations [9–12] have been conducted on the cyclic behavior of these members. The hysteretic response of steel braces is highly asymmetric and it is characterized by degradation in axial stiffness and strength due to inelastic cyclic buckling (see Fig. 1). In closed tubular cross section braces, this is often followed by fracture due to ultra-low-cycle fatigue at the plastic hinge region, which is usually situated at the mid-length of the steel member. The highly asymmetric behavior of these members often leads to concentration of story drifts and the formation of a soft-story [13, 14] as evident from Fig. 2. The above hold true even when capacity design principles are employed as part of the design process of steel CBF buildings.

Field observations from past earthquakes [16–19] have brought to light a second important drawback characterising the steel CBF buildings, i.e. their susceptibility to damage in acceleration-sensitive non-structural components. Indeed, earthquake life-cycle assessment of multi-story CBF buildings [20] have highlighted that, over a 50-year service life, their expected annual losses (EALs) are mostly dominated by the seismic repairs in acceleration-sensitive non-structural components (see Fig. 3a). The above findings are attributable to the high earthquake-induced absolute acceleration demands that arise from (i) the high lateral stiffness of the CBFs and (ii) the acceleration amplification caused by the higher mode effects [21–25] during an earthquake. Referring to Fig. 3a, the second most important contributor to EALs in steel CBF buildings is associated with structural repairs in steel braces due to flexural buckling. This is explained by the fact that steel braces are susceptible to flexural buckling at fairly modest lateral drift

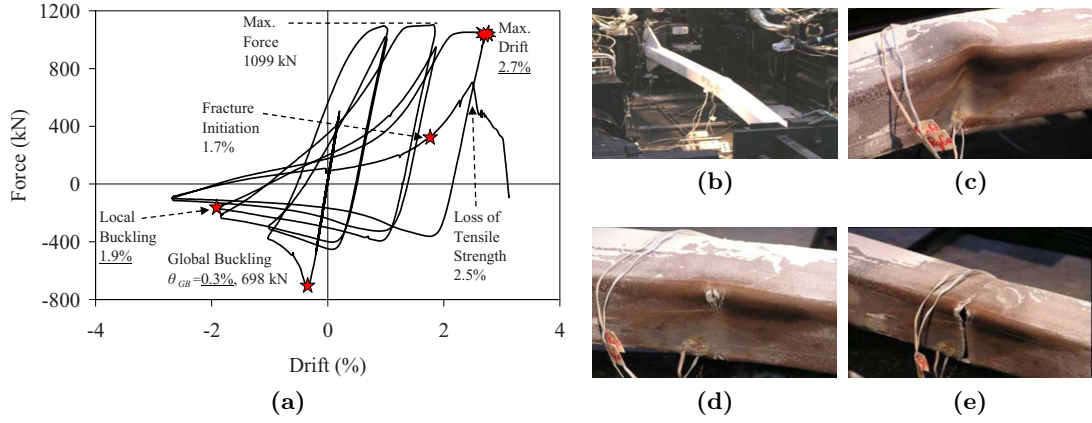


**Figure 1** – (a) Axial force-axial displacement hysteretic response of a steel brace, (b)-(e) typical sequence of damage of a steel brace: (b) global buckling, (c) local buckling, (d) fracture initiation, (e) loss of tensile strength (images adopted from Fell et al. [5])

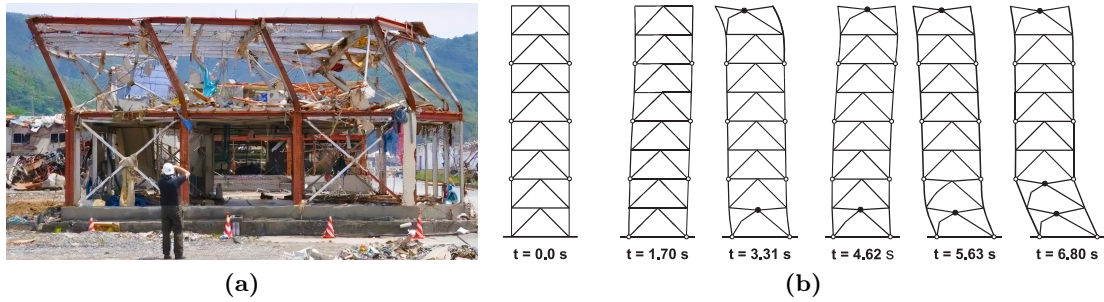


**Figure 2** – (a) Example of soft-story observed in a 2-story steel CBF building in the aftermath of the Tohoku-Oki earthquake (image courtesy of Prof. Dimitrios G. Lignos [15]), (b) concentration of story drifts experienced by a 8-story chevron braced steel frame under the El Centro earthquake record (image adopted from Tremblay and Robert [13])

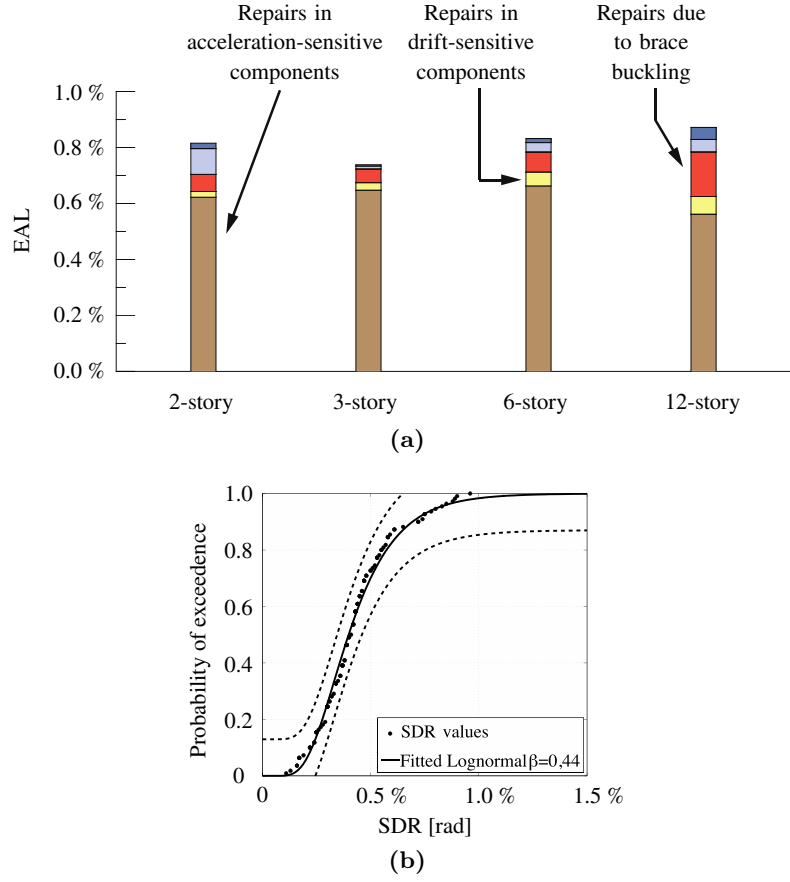


**Figure 3** – (a) Expected annual losses over 50-year life expectancy of steel CBF buildings normalized with respect to the total replacement cost (image adopted from Hwang and Lignos [20]), (b) drift-based fragility curves associated with brace flexural buckling (image adopted from Lignos and Karamanci [26])

demands [26]. Figure 3b shows characteristic fragility functions, which express the probability of a steel brace to experience flexural buckling as a function of the expected story drift ratio (SDR) during an earthquake. Evidently, steel braces are likely to experience, on average, flexural buckling at a SDR of about 0.5 %.

In low-to-moderate seismicity zones, the use of low-ductility steel CBFs is preferred. In this case, due to lack of capacity design principles and the associated bracing connection detailing, inelastic deformations may concentrate into the bracing connections rather than into the bracing member(s) [27]. Referring to Fig. 4, this can lead to unanticipated brittle failure modes during earthquake shaking, which in turn can compromise the seismic performance of the entire building.

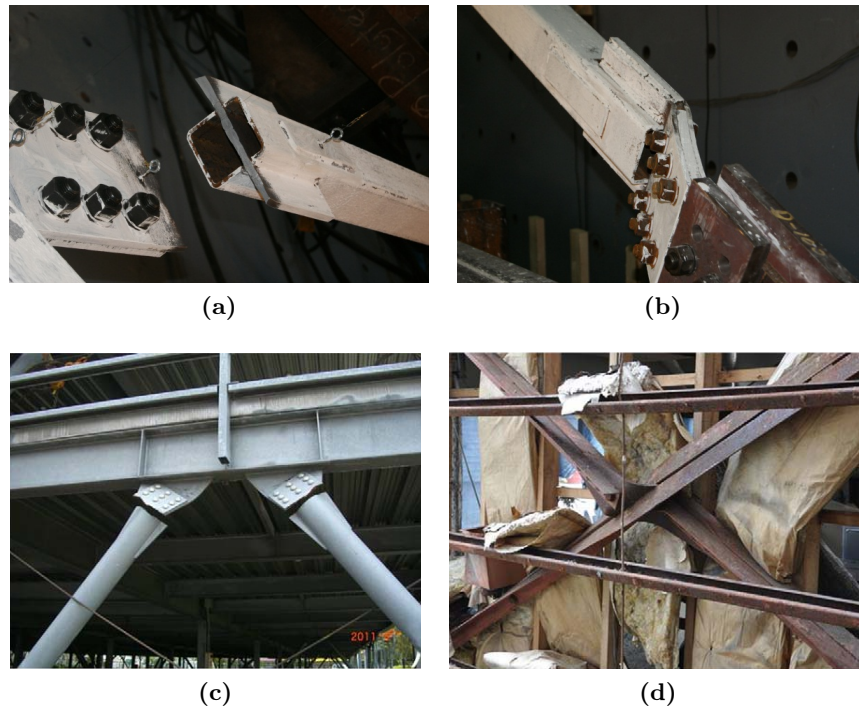


**Figure 4** – Examples of brittle failure modes in bracing connections: (a) fracture of the middle gusset plate and (b) buckling of the corner bracing-end connection in a X-brace (images adopted from Davaran et al. [27]), (c) fractured gusset plates in an inverted V-brace and (d) bending of the middle gusset plate in a X-brace observed in the aftermath of the 2011 Tohoku-Oki earthquake (images adopted from Okazaki et al. [28])



Numerical [13, 14, 29, 30] and experimental investigations [8, 31] conducted on multi-story steel CBF buildings have revealed that it is not feasible to optimally design the steel braces to achieve a uniform demand-to-capacity ratio along the height of the CBFs. This is attributed to the complexity of the hysteretic behavior of these members as well as the seismic force demand variability induced by the higher mode effects [21–25].

Over the years, research focused on improving the seismic performance of conventional steel braced frames through the development of structural systems that are able to provide a stable hysteretic response under cyclic loading. These include, among others, eccentrically braced frames [32–34], buckling restrained braced frames [35–37] and controlled rocking steel braced frames [38–41] (see Figs. 5a-c). Alternatively, passive energy dissipation devices, such as sliding friction dampers [42–44], slotted bolted connections [45–47] and yielding devices [48–50], have been incorporated in steel CBFs in order to enhance their energy dissipation capacity under seismic loading (see Figs. 5d-f). However, studies [51, 52] suggest that, despite these innovations, the challenge on how to control the magnitude of the absolute acceleration demands and their associated variability along the height of steel framed buildings is still an issue to be addressed. Accordingly, the determination of the inertial forces acting on the floor diaphragms of such frames is also challenging [22]. In particular, some of the current design standards do not provide explicit guidelines for the seismic design of the floor diaphragms of buildings [53].

In past studies, the influence of the floor flexibility on the seismic performance of shear wall buildings was investigated [57–60]. Notably, it was demonstrated that the use of flexible diaphragms allow to improve the seismic collapse capacity of the latter as well as their energy dissipation capacity [60]. In particular, it was observed that buildings equipped with flexible diaphragms tend to experience lower absolute floor acceleration demands compared to their rigid diaphragm counterparts when fixed-base condition are considered [61]. However, studies [57, 59, 62] have also highlighted that under earthquake loading, flexible diaphragms can lead to unexpected magnitudes and patterns of force and displacement demands along the building height.

Within such a context, in recent work, the idea of using dissipative floor connectors between the lateral load resisting system and the gravity framing system (GFS) of a building has been proposed [63–70]. Such connectors allow for relative movement between these two systems, thereby controlling the transfer of inertial forces from one system to the other. Figures 6a and 6b show comparisons of the absolute floor acceleration demands attained at the 6<sup>th</sup> and 12<sup>th</sup> floor of a 12-story reinforced concrete shear wall building equipped with dissipative floor connectors [67]. In this case the connectors featured either buckling restrained braces or friction dampers. The simulation results

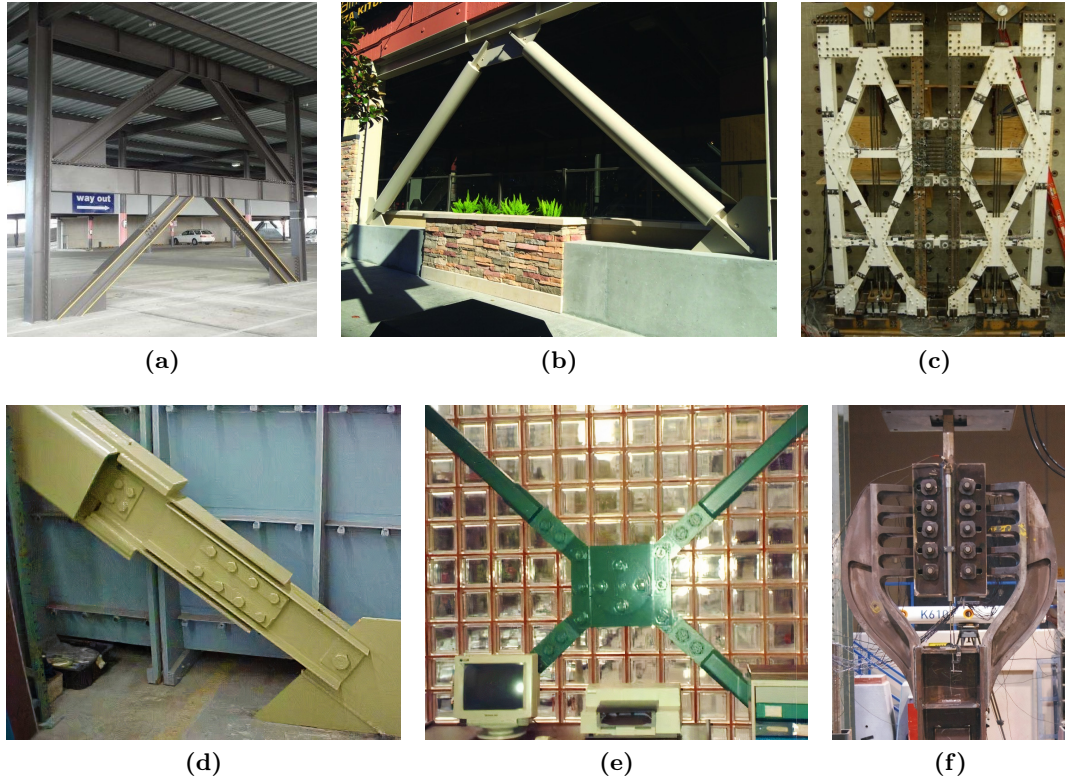


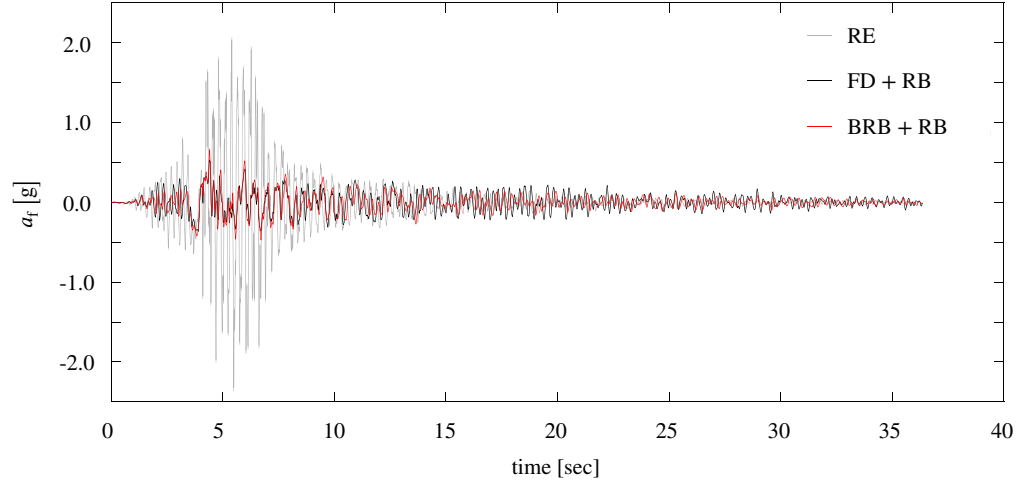
**Figure 5** – Examples of systems developed to improve the seismic performance of conventional steel braced frames: (a) eccentrically braced frames (image adopted from Dusicka et al. [54]), (b) buckling restrained braced frames (image adopted from Kersting et al. [55]), (c) controlled rocking steel braced frames (image adopted from Eatherton et al. [41]), (d) sliding friction dampers (image adopted from Pall and Pall [56]), (e) slotted bolted connections (image adopted from Pall and Pall [56]), (f) yielding devices (image adopted from Gray et al. [50])

demonstrate that the dampers are effective in reducing earthquake-induced floor absolute acceleration demands. Furthermore, it is interesting to notice that, at both floors, the greatest acceleration reduction is achieved in the higher frequency range of the absolute floor acceleration histories. This suggests that dissipative floor connectors are effective in mitigating higher mode effects. However, practice-oriented procedures to determine the activation forces of such connectors are currently missing.

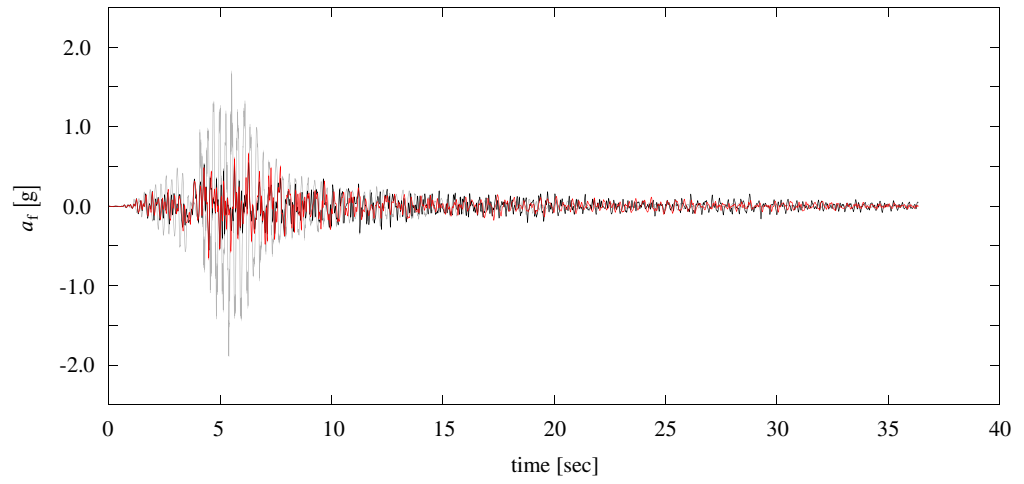
Despite these beneficial aspects, studies [67] have highlighted that, under earthquake loading, the GFS of buildings equipped with dissipative floor connectors is likely to undergo larger peak SDR demands compared to its rigidly connected counterpart. Therefore, the destabilizing effects of gravity may be amplified when dissipative floor connectors are employed within a building. Moreover, buildings with dissipative floor connectors may be more prone to damage in drift-sensitive non-structural components during frequently occurring earthquakes. Therefore, effective engineering solutions should be developed to limit the earthquake-induced lateral displacements of such buildings.

Commonly used dissipative floor connectors include viscous [65], yield [67, 71] and friction dampers [67, 70]. With respect to friction devices, yield dampers such as buckling-restrained braces are less effective in controlling seismic force variability due to the uncertainties associated with the cyclic hardening of their steel core [36, 37, 72]. Furthermore, they require to design different member sizes according to the amplitude of inertial forces to transfer along the height of the building. On the contrary, friction devices allow to easily modify their activation force by adjusting the level of pretension in the bolts. With regard to viscous dampers, their hysteretic response is sensitive to temperature and imposed velocity [73–75]. Therefore, the forces exerted by such dampers vary according to the dynamic load experienced by the building during earthquake shaking. Interestingly, friction dampers are not prone to these issues when they are properly engineered [76, 77].

The energy dissipation capacity of dissipative floor connectors, such as sliding friction dampers, relies on the friction properties of the materials utilized as pads. In this respect, experimental studies conducted on various types of pads [69, 78–83] have highlighted that pads made of non-metallic composite materials exhibit a stable hysteric response under uniaxial cyclic loading. Furthermore, their friction coefficient is practically pressure- and velocity-independent. These findings suggest that sliding friction dampers featuring non-metallic composite pads can be effective in controlling the transfer of inertial forces between the lateral load resisting system and GFS of a building. However, only a handful of studies have explored the use of this type of pads in seismic friction dampers.



(a)



(b)

**Figure 6** – Absolute floor acceleration demands at the (a) 12<sup>th</sup> and (b) 6<sup>th</sup> floor of a 12-story reinforced concrete shear wall building, whose floor diaphragms are connected to the wall through (RE) rigid links, (FD + RB) sliding friction devices and rubber bearings, (BRB + RB) buckling-restrained braces and rubber bearings (images adopted from Tsampras et al. [67])

## Problem Statement and Research Objectives

The previous section suggests that buildings featuring steel CBFs are prone to high absolute acceleration demands and drift concentrations during earthquake shaking due to higher mode effects and the highly asymmetric behavior of the steel braces. Moreover, steel CBF buildings are prone to high economic losses due to seismic repairs in the aftermath of seismic events. Studies conducted on buildings equipped with dissipative floor connectors suggest that the above challenges could be potentially addressed by employing such connectors. While promising, this concept has never been explored in multi-story steel CBF buildings. In light of this, the primary research objectives of the present thesis are summarized as follows:

- conduct a comprehensive experimental program on various types of non-metallic composite materials for potential use in friction pads as part of sliding friction dampers;
- benchmark the seismic performance of multi-story steel CBF buildings equipped with sliding friction dampers as dissipative floor connectors via explicit nonlinear simulations;
- propose a design methodology to determine the activation forces of the sliding friction dampers of multi-story steel CBF buildings; the proposed approach aims to ensure damage-free seismic performance in the steel CBFs and the floor diaphragms;
- investigate solutions on how to limit earthquake-induced lateral drift demands in the gravity framing system of steel CBF buildings with sliding friction dampers as dissipative floor connectors.

## Thesis Outline

This thesis consists of five chapters, three of which are written in the form of journal articles, which have been either published, submitted, or are planned to be submitted to scientific journals. The first and last chapter comprise the introductory and conclusions of this doctoral thesis. At the beginning of each chapter, the contribution of the doctoral candidate is reported as well as the full bibliographic details of the journal article, when published. Furthermore, a set of Appendices are included at the end of this thesis.

**Chapter 1** presents the results from a comprehensive experimental program conducted on a prototype sliding friction damper that was developed in the context of this

thesis. The tests featured five non-metallic friction pads, which have never been explored for potential use in supplemental damping devices. The investigated parameters as part of the experimental program include the applied pressure level to control the activation force of the damper, the imposed loading protocol and the associated loading rate. The static and dynamic friction coefficients of the examined friction pads are quantified in order to evaluate the applicability of such pads in providing supplemental damping in frame structures under earthquake shaking. This chapter is reproduced from the post-print version of the journal article by Paronesso and Lignos [84].

**Chapter 2** investigates the use of sliding friction dampers (SFDs) as dissipative floor connectors to mitigate higher mode effects and absolute acceleration demands on multi-story steel CBF buildings during earthquake loading. A design methodology is proposed to determine the activation forces of the dampers so as to ensure damage-free seismic performance in the steel CBF and the floor diaphragms. The efficiency of the proposed methodology is demonstrated through nonlinear response history analyses on low- and high-ductility 6-story steel CBF buildings. Their seismic performance is contrasted to that of conventional steel CBF buildings with rigid floor diaphragms. Hazard curves of the maximum axial displacement of the SFDs and the peak SDRs of the GFS are also developed to assess the seismic performance of the investigated buildings within the framework of Performance-based Earthquake Engineering. This chapter is reproduced from the pre-print version of the journal article, which is currently under review, by Paronesso and Lignos [85].

**Chapter 3** explores the influence of different types of beam-to-column gravity connections on the seismic demands of steel CBF buildings equipped with floor SFDs. The investigated connections include (i) typical shear tab, (ii) clip angle, (iii) flush end-plate and (iv) shear tab connections with bottom T-stub. A general modelling approach is proposed for simulating their nonlinear hysteretic response. Additionally, a simplified method is developed to explore the effect of the damper activation forces on the seismic performance of such buildings. The structure is first transformed into an equivalent single-degree-of-freedom system. Dual graphics called P-spectra are subsequently generated through nonlinear response history analyses so as to estimate the peak floor absolute acceleration demands and peak/residual roof displacements of the GFS as a function of the activation forces of the SFDs. This chapter is reproduced from the pre-print version of the journal article, which is ready for submission, by Paronesso and Lignos [86].

Finally, the primary conclusions of this thesis are summarized in the last chapter. Limitations as well as suggestions for future work are also discussed. Furthermore, the following five Appendices are included at the end of this document:

**Appendix A** includes the design drawings of the prototype sliding friction damper developed and tested as part of this thesis;

**Appendix B** presents a detailed instrumentation plan and summary of the sensors employed within the experimental campaign described in Chapter 1;

**Appendix C** reports the equations used to compute the experimental results discussed in Chapter 1 as a function of the measurements acquired by the sensors listed in Appendix B;

**Appendix D** provides supplementary results from the experimental campaign, which was summarized in Chapter 1, for each friction pad that was evaluated as part of the present study;

**Appendix E** summarizes the design of the 6-story steel concentrically braced frame buildings investigated in Chapter 2 and 3.





*A gem cannot be polished without friction, nor a man  
perfected without trials.*

Lucius Annaeus Seneca

# 1

## Experimental Investigation of Composite Materials for Sliding Friction Dampers in Earthquake Resilient Steel Frames

### *Bibliographic details*

This chapter presents the post-print version of the article with the following full bibliographic details: Martina Paronesso and Dimitrios G. Lignos. "Experimental study of sliding friction damper with composite materials for earthquake resistant structures". In: *Engineering Structures* 248 (2021), p. 113063. DOI: <https://doi.org/10.1016/j.engstruct.2021.113063>

### *Authors' contribution*

Martina Paronesso, the first author of the above-mentioned submitted paper, designed the specimen, conducted the experimental campaign, analysed the experimental results, visualized the test results, created the figures, wrote the manuscript draft and revised the manuscript. The co-author contributed in developing the methodology presented in this chapter, supervising the

work conducted by Martina Paronesso, funding acquisition, and reviewing and editing the original and final manuscript drafts.

THIS CHAPTER PRESENTS the experimental results from 62 tests on five non-metallic friction pads that could be potentially used in friction dampers for minimizing earthquake-induced damage in buildings. The friction pads are composed of fibres and organic and inorganic fillers bounded together by phenolic resins and have never been explored for potential use in supplemental damping devices. A full-scale sliding friction damper prototype was developed for this purpose. Parameters examined as part of the experimental program include the applied pressure level to control the sliding force, the imposed loading protocol and the associated loading rate. The experimental results reveal that two of the explored friction pads exhibit similar static and dynamic friction coefficients, which are on the order of 0.2 and 0.3 regardless of the examined pressure level and loading protocol. These values are fairly invariant with respect to temperature and to sliding velocity as long as it is larger than 10 mm/sec. While surface wear is the primary damage mechanism of the two most prominent friction pads, their immediate replacement is not imperative in typical earthquake mainshock-aftershock sequences. Moreover, loss of bolt pretension was practically negligible during the same loading sequences.

## 1.1 Introduction

During the past four decades, several passive control devices have been developed to enhance the seismic performance of buildings by providing supplemental damping [87, 88]. Commonly used devices include yield, viscous and friction dampers. Yield dampers, such as buckling-restrained braces, deliver an appreciable energy dissipation capacity [36, 37, 72]. However, the steel core of buckling-restrained braces exhibits cyclic hardening. Therefore, the use of overstrength factors to design the non-dissipative structural elements of a building is imperative. Concerns regarding potential residual deformations and soft-storey mechanisms in the aftermath of earthquakes have also been raised [89, 90]. Viscous dampers are sensitive to temperature and imposed velocity [73–75]. Therefore, they may exert forces that are influenced by the dynamic load imposed on a building.

Friction dampers, if engineered properly, they are not prone to the aforementioned issues [76, 77]. Over the years, numerous types of friction dampers have been developed to enhance the seismic performance of buildings. Pall [78] developed limited slip bolted joints to control the seismic response of structures. Subsequent studies have investigated

the use of friction spring dampers [91] and sliding friction dampers in steel frames with X-bracing [42, 43, 92] as well as chevron bracing [44] configurations. In [93], seven different passive energy dissipation systems were tested on a large-scale 9-storey steel frame. Among the tested devices, Sumitomo friction dampers were effective in providing a stable force-displacement hysteretic response under earthquake shaking. Slotted bolted connections [45–47, 79, 94] and rotational bolted links [95–97] have also been used in steel concentrically braced frames and eccentrically braced frames, respectively. Prior work has also been conducted on the use of friction pads in beam-to-column friction joints of steel moment resisting frames [94, 98–100] as well as reinforced concrete structures [101]. Similarly, friction devices have been employed in self-centering beam-to-column joints [102, 103] and steel column bases [104, 105].

The energy dissipation capacity of a friction damper relies on the friction properties of the materials utilized as pads. In this regard, several experimental investigations have been conducted on different friction pad types. Particularly, prior work has focused on mild-steel pads [78, 79, 82, 83, 106]. Due to surface wear, these may exhibit an unstable force-displacement hysteretic response under cyclic loading. Others have explored the potential use of brass pads [79, 82, 83, 107, 108]. Their hysteretic response is found to be more stable compared to their mild-steel counterparts. However, galvanic corrosion may be a challenge to overcome. Further investigations have been conducted on steel plates coated with sprayed aluminium [80, 83, 109]. This solution could provide a fairly stable force-displacement hysteretic response of the friction device. However, the obtained friction coefficients are somewhat pressure-dependent. Moreover, the application process of the coating may be challenging. Indeed, it usually requires specialized equipment to ensure a high-quality control and performance of the coated steel plates and associated sliding interfaces. As such, the overall cost of the friction pad may be improper. Alternatively, steel plates plated with chemically incompatible metals such as cadmium-aluminium, brass-chromium and cobalt-lead can be also used [110]. Wolff [81] investigated the use of stainless steel plates coated with non-asbestos organic (NAO) materials in base isolation systems. The NAO materials, which exhibit a stable force-displacement hysteretic response, provide friction coefficients lower than 0.2. Similar findings hold true for NAO pads when tested with mild and stainless steel interfaces [102, 111].

In more recent work, the use of Bissaloy steel pads has been explored [82, 106, 112]. Their hysteretic response is fairly stable and repeatable. Surface wear, in this case, is fairly minimal. However, Golondrino et al. [112] found that these materials may provide friction coefficients lower than 0.2 for tightening torques ranging between 350 N m and 500 N m. In more recent works [69, 83, 113], the use of non-metallic materials has been

explored. These studies suggest that a handful of these materials could exhibit a stable hysteretic response under uniaxial cyclic displacement histories. The friction coefficient of these materials, which is both pressure- and velocity-independent, assumes values close to 0.2 [83]. A potential benefit of non-metallic friction pads is that they are not susceptible to galvanic corrosion. Although promising, only a few experimental studies have explored the use of these pad types in sliding friction dampers.

In light of these findings, this study characterizes the behavior of a broad range of non-metallic composite materials. The selected materials are readily available on the market at a fairly minimal cost. Their performance is investigated through a sliding friction damper prototype, which was designed and developed by the authors. The experimental program is conducted under two pressure levels. Monotonic and cyclic tests are conducted at different loading rates aiming to investigate their effect on the force-displacement response of the sliding friction damper. Furthermore, pulse-like and mainshock-aftershock loading protocols are carried out in order to test the sliding friction damper under conditions similar to those occurring during a seismic event. The evolution of the static and dynamic friction coefficients is examined by monitoring both the sliding force and bolt preload. Similarly, temperature variations are tracked close to the sliding interface in order to investigate the effect of the latter on the friction properties of the pads. Limitations as well as suggestions for future work are discussed.

## 1.2 Description of the Experimental Campaign

### 1.2.1 Sliding Friction Damper Prototype

Figure 1.1 illustrates the main components of the sliding friction damper. It consists of four types of metal plates made of S355 J2 steel (nominal yield stress,  $f_y = 355$  MPa) and standard manufacturing tolerances. These types include (i) end steel plates ( $t = 40$  mm), which are positioned at the damper ends and are equipped with ball joints; (ii) an inner slotted steel plate ( $t = 40$  mm); (iii) fixed outer steel plates ( $t = 20$  mm), which connect one of the end plates to the inner slotted plate; and (iv) sliding outer plates ( $t = 20$  mm). These connect one of the end plates to the slotted holes of the inner plate. Each plate has a width of 220 mm and standard 26 mm diameter holes. The sliding motion occurs between two friction pads and the inner slotted plate. At this location, the clamping force is applied with six preloaded high-strength M24 bolts HR 10.9 class (nominal ultimate stress,  $f_{ub} = 1000$  MPa). Disc spring washers (SCHNORR,  $\Phi_i = 25$  mm,  $\Phi_e = 56$  mm,  $h = 7.75$  mm,  $t = 6$  mm) are used to minimize pretension variations during the sliding

motion as suggested in [83] and [113]. A further six preloaded high-strength M24 bolts HR 10.9 class ( $f_{ub} = 1000$  MPa) are utilized to joint the fixed outer plates to the inner slotted plate. A pinned connection is realized at the damper ends through two high-strength steel pins (ETG 100,  $f_y \geq 865$  MPa, 0.2 mm tolerance). A ball joint SKF GE 50 ESX-2LS ( $\Phi_i = 50$  mm,  $\Phi_e = 75$  mm) is placed around each pin in order to accommodate potential relative movements between the latter and the steel plates (see Fig. 1.1b).

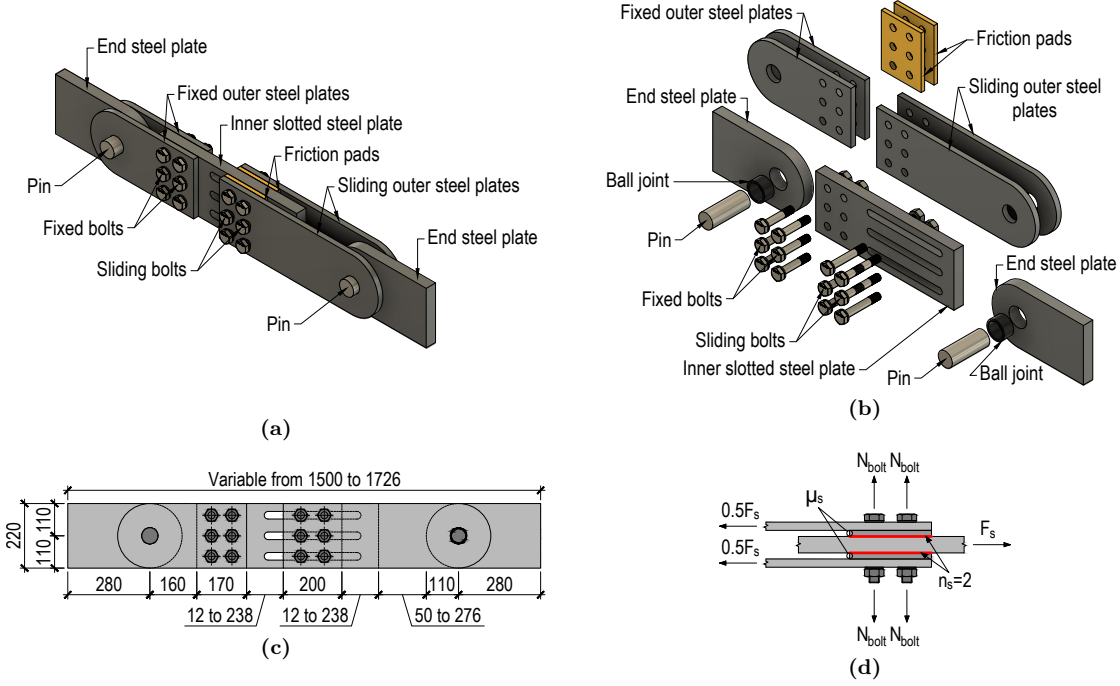


**Figure 1.1** – Sliding friction damper prototype: (a)-(b) basic components, (c) main dimensions in millimetres, (d) parameters used to control the slip load  $F_s$

The damper is designed according to [114, 115] for a maximum axial force of 450 kN and a maximum axial displacement of  $\pm 100$  mm. Referring to Fig. 1.1c, its total length varies from 1500 mm to 1726 mm. The expected slip load is estimated by using Coulomb's law of friction [116]:

$$F_s = n_s \cdot \mu_s \cdot N_{tot} \quad (1.1)$$

Referring to Figure 1.1d,  $F_s$  is the slip load (i.e., static friction force),  $n_s$  is the number of slip interfaces (i.e.,  $n_s = 2$ ),  $\mu_s$  is the static friction coefficient characterising the friction pad and  $N_{tot}$  is the total applied normal force through the preloaded bolts (i.e.,  $N_{tot} = 6 \cdot N_{bolt}$ ).

### 1.2.1.1 Performance Considerations for Selected Friction Pads

The selection of the friction pad materials was based on the following performance criteria, which were established as part of a broader research project with emphasis on the enhanced seismic behavior of steel braced frame buildings equipped with friction dampers:

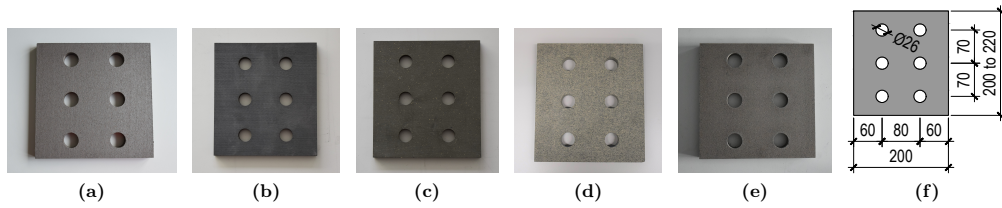
- The static friction coefficient  $\mu_s$  of the pads should ideally be between 0.20 and 0.30 in order to limit wear on the friction pads under cyclic loading. It is noteworthy that  $\mu_s$  values larger than 0.3 are endorsed if minor variations of the friction coefficient are attained due to wear under cyclic loading.
- During sliding, the steel plates in contact with the friction pads should experience minimal damage due to wear. For this purpose, the hardness of the friction pads shall be lower than the one of the steel plates [110]. This requirement aims at concentrating damage in the replaceable components of the damper in the aftermath of earthquakes.
- Under cyclic loading, the friction damper should exhibit a stable hysteretic response without slip force variations under cyclic loading. For this purpose, the static ( $\mu_s$ ) and dynamic ( $\mu_d$ ) friction coefficients of the pads should be similar [110]. Furthermore, in order to limit surface wear, the hardness of the pads should be lower compared to that of the S355 steel plates [110], which generally ranges between 146 HB and 187 HB.
- Galvanic corrosion at the slip interfaces shall be avoided; therefore, non-metallic composite friction pads are preferable.
- Ideally, the selected friction pads should be readily available on the market and obtainable at minimal costs.

Figure 1.2 illustrates the five selected friction pads for the experimental program. According to the manufacturer specifications, they are composed of fibres and organic and inorganic fillers bounded together by phenolic resins. Furthermore, they provide a friction coefficient larger than 0.30 under a maximum operation pressure of 1 MPa. Additional information regarding pertinent material properties is summarized in Table 1.1. Interestingly, the hardness of M2 and M3 is expressed in the Shore D scale, whereas the Rockwell scale is adopted for the other pads. The Shore hardness method is typically used to measure the hardness of soft materials (e.g. rubbers, elastomers and soft plastics such as

polypropylene). On the contrary, the Rockwell hardness method is commonly utilized to determine the hardness of harder plastics such as polycarbonate. This indicates that M2 and M3 are softer materials compared to M1, M4 and M5. Furthermore, the largest values of tensile/flexural strength are observed for the materials M1 and M3.

The recommended operating limits for M4 are 1.7 MPa of pressure and 17.8 m/s of rubber speed, whereas this information was not provided for the rest of the friction pads by the manufacturers. The above limits are only recommended for the intended use and they are far different from those expected in seismic applications (e.g. pressure levels larger than 2.0 MPa). Therefore, an experimental campaign was conducted in order to characterize the behavior of the selected pads under the operation conditions of interest after coordination with the manufacturers of the pads.

Each pad is 15 mm thick and 200 mm wide. The corresponding height ranges from 200 mm for M1 and M5 to 220 mm for the rest (see Fig. 1.2f). For materials M2 and M3, the 26 mm diameter holes were drilled at the EPFL's Structures Laboratory with a water jet cutting machine as recommended by the manufacturer, whereas the other pads were directly provided with the holes by the manufacturers.



**Figure 1.2** – Friction pads: (a) M1, (b) M2, (c) M3, (d) M4, (e) M5, (f) main dimensions in millimetres

**Table 1.1** – Characteristic properties of the tested friction pad materials

| Material ID | Original application | Friction coefficient <sup>a</sup> |         |         |                    |                   | Hardness     | Wear rate<br>[10 <sup>-5</sup> mm <sup>3</sup> /J] | Tensile stress <sup>e</sup><br>[MPa] | Compressive stress <sup>e</sup><br>[MPa] | Normal stress due to flexure <sup>e</sup><br>[MPa] |
|-------------|----------------------|-----------------------------------|---------|---------|--------------------|-------------------|--------------|--|--------------------------------------|--|--|
|             |                      | $\mu^b$                           | $\mu_s$ | $\mu_d$ | $P_{ref}$<br>[MPa] | $T_{ref}$<br>[°C] |              |  |                                      |  |  |
| M1          | SID <sup>c</sup>     | –                                 | 0.36    | 0.32    | 1.0                | 100               | 73 HR        | 1.0  | –                                    | 100                                      | 67   |
| M2          | BA <sup>d</sup>      | 0.3                               | –       | –       | 1.0                | 50                | 60/70 ShoreD | 0.60 mm  | 13.7–17.7                            | 28.4–36.8                                | –  |
| M3          | BA <sup>d</sup>      | 0.28                              | –       | –       | 1.0                | 25                | 65/75 ShoreD | 0.46 mm  | 171.7                                | –  | –  |
| M4          | BA <sup>d</sup>      | 0.59                              | –       | –       | 1.0                | –                 | 104 HR       | 2.3  | 14.8                                 | 73.1                                     | 28.3   |
| M5          | BA <sup>d</sup>      | –                                 | 0.67    | 0.42    | 1.0                | 100               | 97 HR        | 4.5  | –                                    | 100                                      | 52   |

<sup>a</sup> Friction coefficients obtained under the reference pressure  $P_{ref}$  and at the reference temperature  $T_{ref}$

<sup>b</sup> Average friction coefficient

<sup>c</sup> Seismic isolation devices

<sup>d</sup> Braking applications

<sup>e</sup> The tensile stress, compressive stress and normal stress due to flexure of the materials were determined according to [117], [118] and [119] respectively





the in-plane and out-of-plane movements of the damper (LVDTh-WE, LVDTh-W-NS, LVDTh-E-NS), whereas two inclinometers (INCs) were utilized to measure the in-plane and out-of-plane rotations (INC-WE, INC-NS) of the damper. Thermocouples (THs) were used to track temperature variations at the surface of the inner slotted plate (THout) as well as close to the sliding interfaces (THbolt). Furthermore, a washer load cell (WLC) was used to verify if pretension variations occur during the sliding motion and to get a sense of the applied bolt preload prior to testing.

### 1.2.3 Loading Protocols

The experimental program is described in Table 1.2. Monotonic (M) and cyclic tests with constant (CA), increasing (IA, IA-H, IA-HH) and decreasing (DA) amplitudes were conducted at different loading rates (i.e., 0.025 Hz, 0.05 Hz and 0.15 Hz) (see Fig. 1.4a-1.4d). Furthermore, loading protocols idealizing a pulse (PL) and a mainshock-aftershock (MS-AS) series were carried out in order to test the friction damper under conditions similar to those occurring during a seismic event (see Figures 1.4e-1.4f). For these tests, the maximum sliding velocity (i.e., 27 mm/s) and the excursion associated to it were constrained by the maximum capacity of the available servo-hydraulic equipment. It is noteworthy that the loading protocols reported in Table 1.2 are more severe compared to those proposed in the EN 15129 [120] provisions. Indeed, the purpose of the experimental campaign was to investigate the performance of the sliding friction damper prototype under extreme loading conditions.

In order to examine the response of the friction damper to conditions potentially similar to earthquake loading, of interest are ground motions representing ground shaking in the forward directivity region of a fault rupture. These records are usually characterized by a large high-velocity pulse early on in the ground motion history. Due to limitations of the employed servo-hydraulic equipment and to maximize the input pulse velocity to further evaluate the effects of loading rate on the behavior of the friction pads, the concept of pulse idealization was employed, which was introduced by [121] to represent near-fault ground motions with reasonable accuracy. The pulse duration herein was tuned to represent the local seismicity characteristics of pulse-like ground motions in Sion (Switzerland). Moreover, other records with similar characteristics were reviewed from historic earthquake data [122].

Referring to Table 1.2, the loading protocols M, CA, IA, DA and IA-H were run for an expected slip load of 150 kN (i.e., pressure of 5.5 N/mm<sup>2</sup>–10 N/mm<sup>2</sup>) and 300 kN (i.e., pressure of 7.0 N/mm<sup>2</sup>–21 N/mm<sup>2</sup>) in order to verify if the friction coefficient  $\mu$  of

the pads is pressure-dependent. The remaining tests (i.e., IA-HH, PL and MS-AS) were performed merely on M1 and M4 for  $F_{s,\text{exp}} = 300 \text{ kN}$ . The target  $F_{s,\text{exp}}$  values were achieved by calibrating the bolt preload through a conventional torque wrench.

**Table 1.2** – Load protocols used to test the the five friction pads

| Loading protocol ID   | Disp. amp.<br>[mm]         | Frequency $f$<br>[Hz] | Number of cycles | Sliding velocity $v_s$<br>[mm/s] |
|---|----------------------------|-----------------------|------------------|----------------------------------|
| Linear static loading (M)   | $\pm 70$                   | 0.0025                | 0.5              | 0.7                              |
| Cyclic loading with constant amplitude (CA)                           | $\pm 50$                   | 0.025                 | 20               | 5                                |
| Cyclic loading with increasing amp. at low rate (IA)                  | $\pm 5, 10, 15, \dots, 50$ | 0.025                 | 20               | 0.5, 1.0, 1.5, $\dots$ , 5.0     |
| Cyclic loading with decreasing amp. at low rate (DA)                  | $\pm 50, 45, 40, \dots, 5$ | 0.025                 | 20               | 5.0, 4.5, 4.0, $\dots$ , 0.5     |
| Cyclic loading with increasing amp. at moderate rate (IA-H)           | $\pm 5, 10, 15, \dots, 50$ | 0.05                  | 20               | 1.0, 2.0, 3.0, $\dots$ , 10      |
| Cyclic loading with increasing amp. at high rate <sup>a</sup> (IA-HH) | $\pm 5, 10, 15, \dots, 50$ | 0.15                  | 20               | 3.0, 6.0, 9.0, $\dots$ , 30      |
| Pulse-like loading protocol <sup>a</sup> (PL)                         | 50 <sup>b</sup>            | —                     | —                | 27 <sup>c</sup>                  |
| Mainshock-aftershock protocol <sup>a</sup> (MS-AS):                   |                            |                       |                  |                                  |
| - Mainshock (MS)  | 40 <sup>b</sup>            | —                     | —                | 27 <sup>c</sup>                  |
| - First aftershock (AS1)  | 30 <sup>b</sup>            | —                     | —                | 27 <sup>c</sup>                  |
| - Second aftershock (AS2)   | 24 <sup>b</sup>            | —                     | —                | 27 <sup>c</sup>                  |

<sup>a</sup> Load protocol used to test exclusively the friction pads M1 and M4

<sup>b</sup> Excursion associated to the maximum sliding velocity applied during the load protocol

<sup>c</sup> Maximum sliding velocity applied during the load protocol

### 1.3 Experimental Results

The experimental results are summarized in three sub-sections. First, the data obtained under the linear loading protocol are reported for  $F_{s,\text{exp}} = 150 \text{ kN}$  and  $F_{s,\text{exp}} = 300 \text{ kN}$ . Notably, the performance of the friction damper is evaluated in terms of axial force-axial displacement ( $F$ - $\delta$ ), whereas the bolt preload  $N_{\text{bolt}}$  and the friction coefficient  $\mu$  of the pads are reported as a function of the total cumulative displacement  $\sum \delta_i$ . The second and third sub-sections include a qualitative and quantitative discussion of the experimental results, respectively.

The friction coefficients reported in the following sections were determined as follows:

$$\mu = \frac{F}{n_s \cdot n_{\text{bolt}} \cdot N_{\text{nom,bolt}} \cdot (1 - r_{\text{bolt}})} \quad (1.2)$$

Where,  $n_{\text{bolt}}$  is the number of preloaded bolts (i.e.,  $n_{\text{bolt}} = 6$ ),  $N_{\text{nom,bolt}}$  is the bolt preload applied with the wrench torque before each test and  $r_{\text{bolt}}$  is the loss of pretension measured with the washer load cell. It is noteworthy that  $\mu$  assumes negative/positive values when the axial force  $F$  induces tension/compression on the damper. Such a force

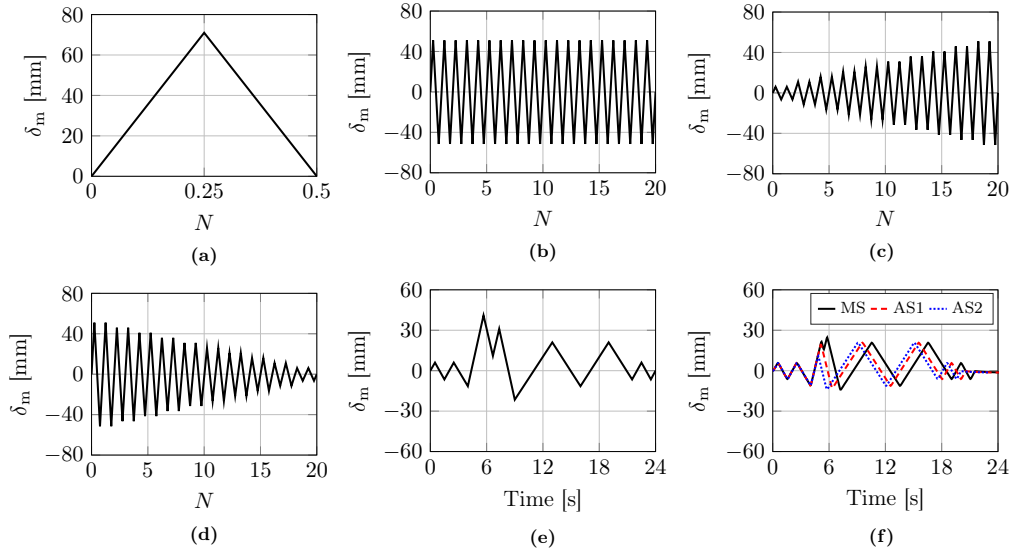


**Figure 1.4** – Employed loading protocols: (a) linear static loading (M), (b) cyclic loading with constant amplitude (CA), (c) cyclic loading with increasing amplitude at low (IA), moderate (IA-H) and high rate (IA-HH), (d) cyclic loading with decreasing amplitude at low rate (DA), (e) pulse-like loading protocol (PL), (f) mainshock-aftershock loading protocol (MS-AS)

was not corrected for the inertial force that arise from the moving components of the sliding friction damper because the accelerations experienced by the specimen during each loading protocol were nearly zero. Furthermore, prior to testing, several calibrations were conducted with the torque wrench in order to ensure that all bolts were equally preloaded. This also included calibration of the washer load cell. Because disc spring washers were employed, variations in bolt pretension were minimized, thus enabling the use of only one washer load cell to trace potential bolt relaxations.

### 1.3.1 Results obtained under the Linear Static Loading Protocol

The normal pressure levels applied on the friction pads range between 5.5 MPa and 21 MPa. In order to examine the effect of pressure on the friction properties of the pads, a preliminary test was conducted by applying a tightening torque  $T_{\text{bolt}}$  of 200 Nm/bolt and the loading protocol shown in Fig. 1.4a. For pads M1, M4 and M5, it was found that the damper started sliding for an axial force  $F_s$  smaller than the expected one (i.e.,  $F_s/F_{s,\text{exp}} \leq 0.88$ ) because their static friction coefficient was smaller than the nominal value ( $0.28 \leq \mu_{s1}/\mu_{\text{exp}}^* \leq 0.61$ ). This did not hold true for M2 and M3. Indeed, in

---

\*Ratio between the static friction coefficient obtained at the beginning of the 1st loading excursion and the static or average friction coefficient provided by the manufacturer under a pressure of 1 MPa

such a case,  $F_s/F_{s,\text{exp}} < 1.0$  because the bolt preload sharply decreased during the first loading cycle as depicted in Fig. 1.5a. This could be attributed to a through-thickness deformation of the pads caused by a pore water migration, which occurred in their matrix. Notably, the bolt holes for M2 and M3 were drilled with a water jet cutting machine. Subsequently, the drying phase was performed at a temperature of 40 to 50 °C as recommended by the manufacturer. Nevertheless, appreciable water was trapped in the pads' matrix. Part of the initial bolt preload was transferred to the pore water, i.e. the effective stress experienced by the pads' matrix was smaller compared to the applied one. Once the pretension was applied and the pads started sliding, the pore water migrated towards the edges of the pads. This caused a decrease of  $N_{\text{bolt}}$ . Referring to Fig. 1.5a, a slight increase of pretension was observed mainly when the applied force  $F$  was reversed from tension to compression. Under compression, the sliding outer steel plates moved out-of-plane; this increased the normal stress in the bolts. The preliminary test conducted for  $T_{\text{bolt}} = 200 \text{ Nm/bolt}$  assisted in adjusting the estimated friction coefficients of the five friction pads in order to conduct the rest of the loading protocols shown in Fig. 1.4 for  $F_{s,\text{exp}} = 150 \text{ kN}$  and  $F_{s,\text{exp}} = 300 \text{ kN}$ .

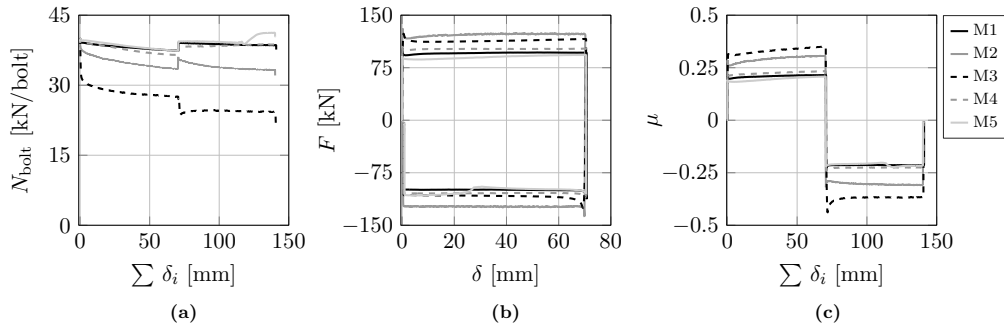


**Figure 1.5** – Results obtained under the linear static loading protocol for  $T_{\text{bolt}} = 200 \text{ Nm/bolt}$ : (a) bolt preload as a function of the total cumulative displacement, (b) axial force-axial displacement response of the damper, (c) friction coefficient as a function of the total cumulative displacement

Referring to Table 1.3, the largest static friction coefficients were obtained for M2 and M3. For  $F_{s,\text{exp}} = 150 \text{ kN}$ , these were equal to 0.35 and 0.30, respectively. The other materials featured  $\mu_{s1}^\dagger$  values between 0.19 and 0.23. A comparison of the  $\mu_{s1}$  values obtained for  $F_{s,\text{exp}} = 150 \text{ kN}$  and  $F_{s,\text{exp}} = 300 \text{ kN}$  reveals that  $\mu_{s1}$  decreased when the pressure at the sliding interface increased. The effect of the clamping force on  $\mu$  is further discussed in Section 1.4.1. In accordance with previous findings, a sharp loss of pretension was observed merely for M2 and M3 (i.e.,  $\Delta N_b > 35\%$  for  $F_{s,\text{exp}} = 300 \text{ kN}$ ).

<sup>†</sup>Static friction coefficient obtained at the beginning of the 1st loading excursion

Furthermore, minor variations of  $F$  were observed for M4. Indeed, in such a case,  $N_{\text{bolt}}$  and  $\mu$  featured a relatively constant value throughout the experiment (i.e.,  $\Delta N_{\text{b}} = 2\%$  and  $\Delta\mu_i \leq 9\%$ ). Conversely, a major variation of  $F$  was observed for M1 and M5 during the first loading excursion for  $F_{\text{s,exp}} = 300\text{ kN}$  (i.e.,  $\Delta F_1 > 20\%$ ). This was due to the progressive increase of  $\mu$  as depicted in Table 1.3 (i.e.,  $\Delta\mu_i > 20\%$ ). This relates to the pre-sliding surface conditions of the friction pads. Notably, during the second loading excursion (i.e., once the surface layer of the pads was partially removed),  $\mu$  slightly varied with the increase of  $\sum \delta_i$  (i.e.,  $\Delta\mu_2 \leq 7\%$ ). Similarly,  $\mu$  featured relatively constant values for  $F_{\text{s,exp}} = 150\text{ kN}$ . This is justified by the fact that the pads utilized for this test were previously tested under two monotonic tests, i.e. at the beginning of the experiment their surface was partially smoothed. Therefore, M1 and M5 provide fairly constant  $\mu$  values when their surfaces are preliminary scraped.

**Table 1.3** – Data obtained for  $F_{\text{s,exp}} = 150\text{ kN}$  and  $F_{\text{s,exp}} = 300\text{ kN}$  under the linear static loading protocol

| Material ID                        |    | Axial force   |                                |                     | Loss of pretension | Friction coefficient         |                                 |                      |
|------------------------------------|----|---|--------------------------------|---------------------|--------------------|------------------------------|---------------------------------|----------------------|
|                                    |    | $\frac{F_{\text{s}}^{\text{a}}}{F_{\text{s,exp}}^{\text{b}}}$ | $\Delta F_1^{\text{c}}$<br>[%] | $\Delta F_2$<br>[%] |                    | $\mu_{\text{s}1}^{\text{e}}$ | $\Delta\mu_1^{\text{f}}$<br>[%] | $\Delta\mu_2$<br>[%] |
| $F_{\text{s,exp}} = 150\text{ kN}$ | M1 | 0.87  | 2                              | 13                  | 2                  | 0.19                         | 3                               | 13                   |
|                                    | M2 | 1.16  | 5                              | 9                   | 22                 | 0.35                         | 10                              | 5                    |
|                                    | M3 | 0.81  | 7                              | 12                  | 33                 | 0.30                         | 10                              | 9                    |
|                                    | M4 | 0.97  | 3                              | 6                   | 2                  | 0.23                         | 9                               | 4                    |
|                                    | M5 | 1.12  | 5                              | 4                   | 2                  | 0.22                         | 7                               | 2                    |
| $F_{\text{s,exp}} = 300\text{ kN}$ | M1 | 0.91  | 21                             | 6                   | 4                  | 0.17                         | 24                              | 6                    |
|                                    | M2 | 0.64  | 8                              | 6                   | 36                 | 0.18                         | 33                              | 13                   |
|                                    | M3 | 0.57  | 4                              | 13                  | 41                 | 0.23                         | 13                              | 5                    |
|                                    | M4 | 0.79  | 3                              | 4                   | 2                  | 0.18                         | 6                               | 3                    |
|                                    | M5 | 0.86  | 33                             | 5                   | 1                  | 0.21                         | 38                              | 7                    |

<sup>a</sup> Slip load for  $\sum \delta_i = 0\text{ mm}$

<sup>b</sup> Expected slip load estimated with the Coulomb's law of friction and the static friction coefficient provided by the manufacturer (the average friction coefficient is utilized when the static one is not provided)

<sup>c</sup>  $\Delta F_i$ : maximum axial force variation recorded during the  $i$ th loading excursion (estimated compared to the slip load obtained at the beginning of the  $i$ th loading excursion)

<sup>d</sup> Total loss of pretension obtained at the end of the test

<sup>e</sup>  $\mu_{\text{s}i}$ : static friction coefficient obtained at the beginning of the  $i$ th loading excursion

<sup>f</sup>  $\Delta\mu_i$ : maximum friction coefficient variation obtained during the  $i$ th loading excursion (estimated compared to  $\mu_{\text{s}i}$ )

### 1.3.2 Results obtained under Symmetric Cyclic Loading Protocols

This section begins with a qualitative description of the typical friction coefficient evolution and  $F - \delta$  response observed under constant/variable pressure and sliding velocity. Pertinent observations regarding temperature are also made. This is followed by a quantitative examination of key experimental data.

### 1.3.2.1 Qualitative Performance Evaluation

Figures 1.6a and 1.6b illustrate the typical friction coefficient evolution under constant displacement amplitude for the two examined pressure levels. For materials whose properties were not particularly affected by the operating temperature (e.g. M4),  $\mu$  progressively increased with respect to the cumulative displacement due to surface wear [83] (see Fig. 1.6a). However, under continuous sliding motion, the surface of the pads smoothed; hence,  $\mu$  stabilized. This process was generally accelerated under high normal pressures, i.e. during most of the tests conducted for  $F_{s,exp} = 150$  kN, the stable phase was achieved after a larger number of cycles compared to  $F_{s,exp} = 300$  kN.

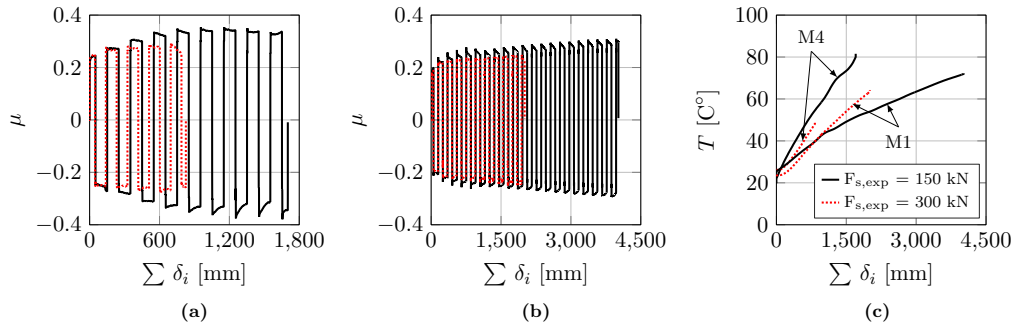


**Figure 1.6** – Cyclic loading protocol with constant amplitude (CA): friction coefficient evolution for (a) M4 and (b) M1, (c) rise in temperature for materials M4 and M1

Referring to Fig. 1.6b, material M1 exhibited a friction coefficient  $\mu$ , which increased with respect to the cumulative displacement. Notably, the increase observed during the initial loading cycles was attributed to the wearing process. Subsequently, the temperature at the sliding interface progressively increased, thereby causing a steady increase of  $\mu$  (see Fig. 1.6b and 1.6c). This is discussed in detail in Section 1.4.2.

Figure 1.7 depicts the evolution of the friction coefficient of M4 and M5 under the loading protocols CA and IA. The results suggest that  $\mu$  is somewhat dependent on the sliding velocity. Notably, during both tests,  $\mu$  progressively increased during the initial loading cycles and subsequently, stabilized around a relatively constant value (i.e., around 0.28 for M4 and 0.5 for M5 under IA). However, the increased rate was more pronounced for the incremental amplitude protocol. This was in part related to the wearing process, i.e. fragments of the pads piled up at the ends of the grooves and got into the sliding interface once the displacement amplitude was widened. This enhanced the wearing process resulting in an increase of  $\mu$  at larger displacements [106]. Secondly, the friction coefficient  $\mu$  may assume larger values at higher loading rates due to visco-plastic phenomena [123]. Referring to Fig. 1.4c, during the loading protocol with increasing

amplitude ( $f = 0.025$  Hz), the sliding velocity  $v_s$  is increased by approximately 0.5 mm/s every two loading cycles. Therefore, the observed increase of  $\mu$  during the first two loading cycles of the experiment was merely due to the wearing process. After the hardening phase,  $\mu$  became fairly constant regardless of the applied sliding velocity. Therefore, the examined friction pads can provide constant  $\mu$  values when they operate at  $v_s$  values exceeding a given threshold (e.g. around 3 mm/s for M5), i.e. above certain loading rates, the visco-plastic effect becomes negligible.

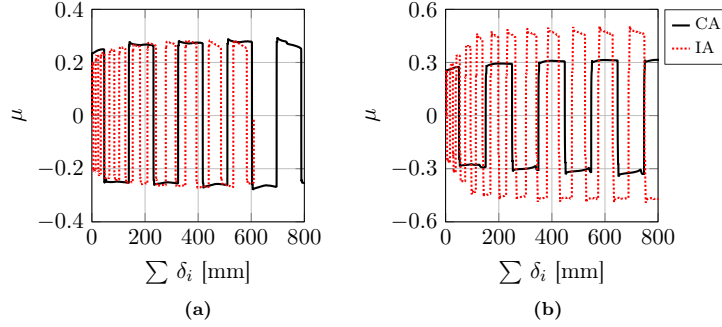


**Figure 1.7** – Friction coefficient evolution under constant (CA) and increasing amplitude at low rate (IA): (a) M4 for  $F_{s,exp} = 300$  kN, (b) M5 for  $F_{s,exp} = 150$  kN

In cases where the temperature at the sliding interface exceeded  $60^\circ\text{C}$  (e.g. see M5), the stable phase was followed by a progressive decrease of  $\mu$  under consecutive loading cycles (see Fig. 1.8). Both this and the loading rate effects are further investigated in Section 1.4.2.

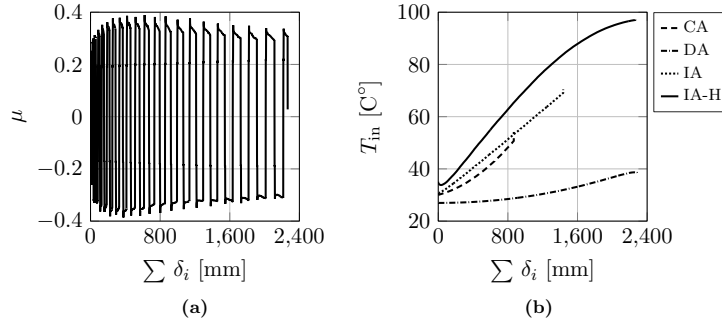


**Figure 1.8** – Results obtained for M5 and  $F_{s,exp} = 150$  kN: (a) friction coefficient evolution, (b) rise in temperature tracked with the thermocouples THbolt inside the bolt holes

Under constant pressure and decreasing sliding velocity (loading protocol DA), the friction coefficient of the materials whose properties were somewhat velocity-dependent evolved as shown in Fig. 1.9. Notably, for M4,  $\mu$  progressively increased under decreasing loading velocities for  $\sum \delta_i \leq 1000$  mm (see Fig. 1.9a). This suggests that at this

stage (i.e., for sliding velocities higher than 4.5 mm/s) the wearing process prevails over the visco-plastic effect leading to an increase of  $\mu$ . With the progressive decrease of the loading rate, the visco-plastic effect acquires significance, whereas the effects of the wearing process diminish. The combination of these two phenomena leads to a decrease of  $\mu$ . However, this trend was not observed for M5 in Fig. 1.9b. Indeed, in this case,  $\mu$  experienced a sharp increase for  $\sum \delta_i > 1500$  mm although decreasing sliding velocities were applied. This was due to the decrease of the bolt preload observed in Fig. 1.9c up to about 30 %, i.e. a pressure decrease occurred at the sliding interface and a consequent increase of  $\mu$  was observed. Referring to Fig. 1.10, for friction pads not exhibiting velocity dependency (e.g. M1),  $\mu$  progressively increased under increasing and decreasing sliding velocities. In such a case, the increase rate, which was comparable to that from constant displacement amplitudes, was attributed to the wearing process and the rise in temperature at the sliding interface. The hardening phase was followed by a stable stage and a softening trend when the heat generated at the sliding interface caused alterations of the pads' surfaces as illustrated in Fig. 1.11a for M1 and IA-HH. Notably, some coppery areas were clearly visible near the bolt holes. Referring to Fig. 1.11b, this phenomenon was not observed in other cases due to the gradual increase of  $T_{\text{surf}}$  (see Fig. 1.10c).

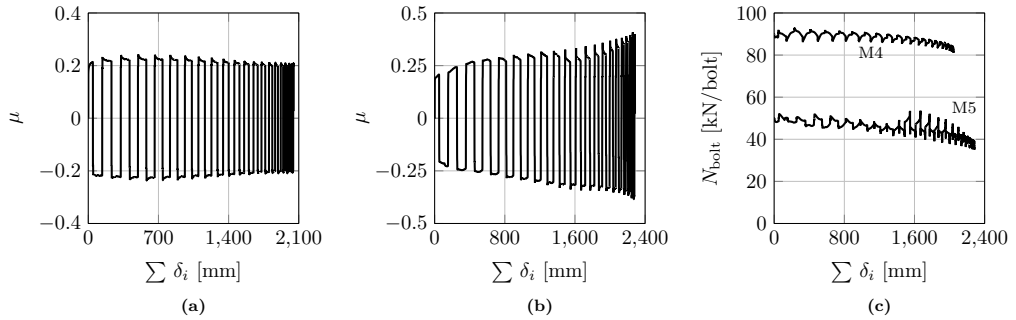


**Figure 1.9** – Results obtained under the cyclic loading protocol with decreasing amplitude (DA): friction coefficient evolution for (a) M4 ( $F_{s,\text{exp}} = 300$  kN) and (b) M5 ( $F_{s,\text{exp}} = 150$  kN), (c) bolt preload



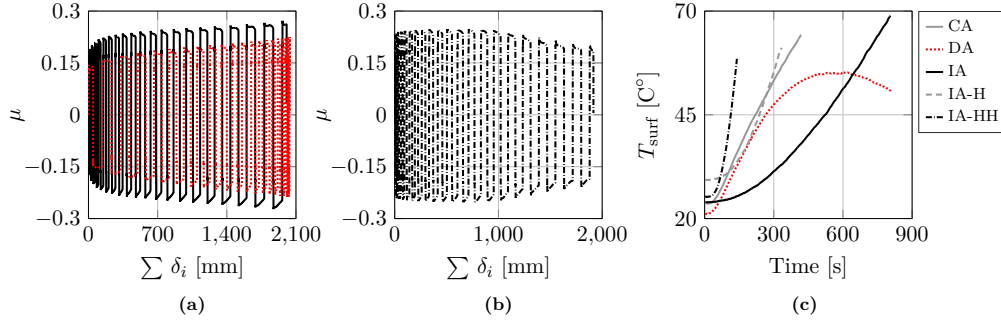


**Figure 1.10** – Results obtained for M1 and  $F_{s,exp} = 300$  kN: (a)-(b) friction coefficient evolution, (c) rise in temperature at the surface of the inner slotted plate



**Figure 1.11** – Surface condition of M1 at the end of the cyclic loading protocol (a) IA-HH and (b) IA for  $F_{s,exp} = 300$  kN

The data collected for M2 and M3 were obtained under variable pressure. Indeed, consistent with Section 1.3.1, a sharp loss of pretension was observed during each test performed with M2 and M3 (see Fig. 1.12a). During the sliding motion, M2 featured a fairly constant  $\mu$  value because (i) the static and dynamic friction coefficient of M2 were relatively similar [78] and (ii) the contact between the pads' surface and the inner slotted plate slightly varied under consecutive loading cycles. As a result, the pads experienced fairly uniform wear (see Fig. 1.13a).

Referring to Fig. 1.13b and 1.13d, the pads M3 experienced nonuniform wear and residual bending deformation under the loading protocol CA. This is why the friction coefficient of M3 strongly varied during the sliding motion (see Fig. 1.12c) and  $F$  varies once the slip load was exceeded (see Fig. 1.14a). Conversely, the damper slid under a relatively constant axial force throughout the tests conducted with M4 (see Fig. 1.14b). Indeed, as illustrated in Fig. 1.14d, M4 is characterized by similar  $\mu_s$  and  $\mu_d$  values. As regards M1 and M5,  $F$  mainly varied during the first loading excursion as shown in Fig. 1.14c. This is consistent with the results obtained under the linear loading protocol (see Fig. 1.5f) and it corroborates the hypothesis that this relates to the pre-sliding surface conditions of the pads. Indeed, during the second loading excursion (i.e., once

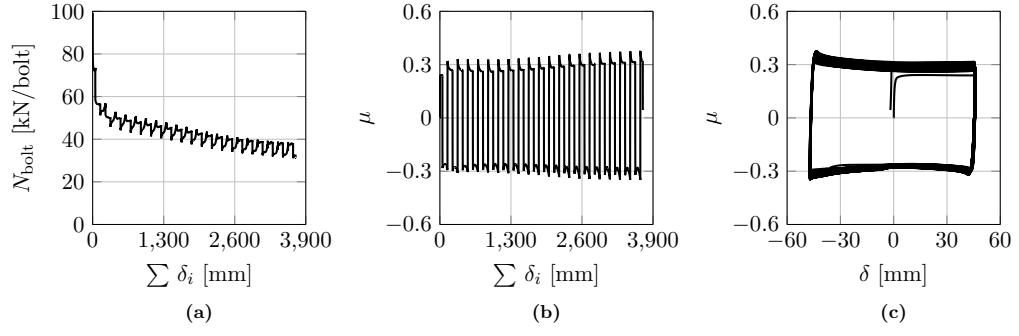


**Figure 1.12** – Results obtained for M3 and  $F_{s,exp} = 300$  kN under the cyclic loading protocol with constant amplitude (CA)

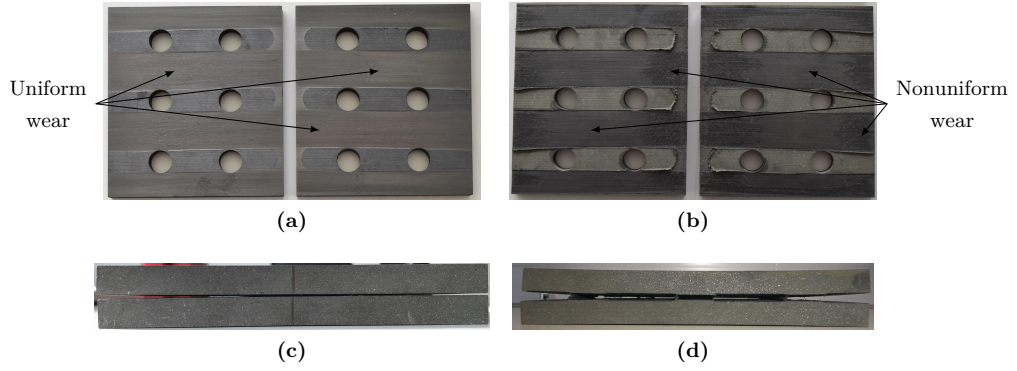


**Figure 1.13** – Condition of (a),(c) M2 and (b),(d) M3 at the end of the cyclic loading protocol (a),(c) IA ( $F_{s,exp} = 150$  kN) and (b),(d) CA ( $F_{s,exp} = 300$  kN): (a)-(b) surface wearing, (c)-(d) bending deformation

the surface layer of the pads was partially removed),  $\mu$  experienced only slight variations during the sliding motion and the discrepancy between  $\mu_s$  and  $\mu_d$  was fairly minor.

Most of the tests carried out with M2, M4 and M5 were terminated due to fracture of at least one friction pad. Figure 1.15 shows that fracture extends within the net section normal to the loading direction. During the tests, the thickness of the pads progressively reduced due to the wearing process acting at the sliding interface. Concurrently, the damper axial force remained constant or increased with the number of loading cycles. As a result, the tensile stress demand, which was amplified by stress concentration near the bolt hole, exceeded the tensile stress resistance of the friction pad. Fracture occurred instantaneously in this case.

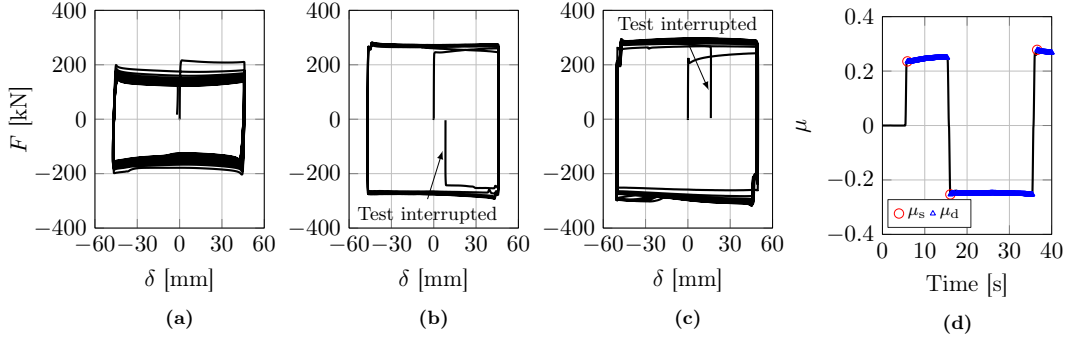


**Figure 1.14** – Results obtained for  $F_{s,exp} = 300$  kN under the cyclic loading protocol with constant amplitude (CA): (a) M3, (b) and (d) M4, (c) M1



**Figure 1.15** – Fracture patterns of the friction pads (a) M2 and (b) M4 at the end of the loading protocol CA for  $F_{s,exp} = 300$  kN

### 1.3.2.2 Quantitative Performance Evaluation

The experimental results obtained under the symmetric cyclic loading protocols for  $F_{s,exp} = 150$  kN and  $F_{s,exp} = 300$  kN are summarized in Tables 1.4 and 1.5. Particularly, Table 1.4 includes (i) the classification of the state of the pads when each test was terminated, (ii) the number of cycles ( $N_{tot}$ ) and the total cumulative dissipated energy ( $\sum E_{tot}$ ) up to fracture of the friction pad(s), (iii) the maximum measured temperature ( $T_{max}$ ). On the other hand, Table 1.5 provides the mean values of  $F$  ( $\bar{F}$ ) and  $\mu$  ( $\bar{\mu}$ ) as well as the total loss of pretension ( $\Delta N_b$ ).

Referring to Table 1.4, all the tests conducted with M3 were completed. Similarly, for M1, pad's fracture occurred merely during the loading protocol CA for  $F_s = 300$  kN. This represents an isolated case likely caused by the presence of defects arisen during the manufacturing process in the matrix of the composite material M1. The reason why M3 and M1 did not experience fracture under the considered loading protocols is related to the fact that, among all, such pads are characterized by (i) the largest values of tensile/flexural strength and (ii) the smallest values of wear rate.

**Table 1.4** – Number of cycles  $N_{\text{tot}}$ , total cumulative dissipated energy  $\sum E_{\text{tot}}$  and maximum temperature  $T_{\text{max}}$  obtained for  $F_{\text{s,exp}} = 150 \text{ kN}$  and  $F_{\text{s,exp}} = 300 \text{ kN}$ 

| Protocol ID <sup>a</sup> | Material M1      |                  |                       |                  | Material M2 |                  |                       |                  | Material M3 |                  |                       |                  | Material M4 |                  |                       |                  | Material M5 |                  |                       |                  |
|--------------------------|------------------|------------------|-----------------------|------------------|-------------|------------------|-----------------------|------------------|-------------|------------------|-----------------------|------------------|-------------|------------------|-----------------------|------------------|-------------|------------------|-----------------------|------------------|
|                          | St. <sup>b</sup> | $N_{\text{tot}}$ | $\sum E_{\text{tot}}$ | $T_{\text{max}}$ | St.         | $N_{\text{tot}}$ | $\sum E_{\text{tot}}$ | $T_{\text{max}}$ | St.         | $N_{\text{tot}}$ | $\sum E_{\text{tot}}$ | $T_{\text{max}}$ | St.         | $N_{\text{tot}}$ | $\sum E_{\text{tot}}$ | $T_{\text{max}}$ | St.         | $N_{\text{tot}}$ | $\sum E_{\text{tot}}$ | $T_{\text{max}}$ |
|                          |                  |                  | [kJ]                  | [°C]             |             |                  | [kJ]                  | [°C]             |             |                  | [kJ]                  | [°C]             |             |                  | [kJ]                  | [°C]             |             |                  | [kJ]                  | [°C]             |
| CA                       | ·                | 20               | 680                   | 72               | x           | 19               | 555                   | 58               | ·           | 20               | 475                   | 56               | x           | 9                | 325                   | 79               | x           | 5                | 175                   | 50               |
|                          | x                | 11               | 565                   | 64               | xx          | 1                | 10                    | 32               | ·           | 20               | 465                   | 62               | x           | 5                | 215                   | 47               | xx          | 3                | 110                   | 35               |
| IA                       | ·                | 20               | 320                   | 50               | ·           | 20               | 305                   | 39               | ·           | 20               | 240                   | 35               | xx          | 15               | 195                   | 36               | x           | 15               | 280                   | 63               |
|                          | ·                | 20               | 575                   | 68               | x           | 5                | 30                    | 24               | ·           | 20               | 335                   | 50               | x           | 10               | 120                   | 40               | xx          | 5                | 35                    | 25               |
| DA                       | ·                | 20               | 310                   | 42               | ·           | 20               | 250                   | 30               | ·           | 20               | 220                   | 34               | x           | 7                | 180                   | 34               | ·           | 20               | 350                   | 39               |
|                          | ·                | 20               | 475                   | 55               | ·           | 20               | 330                   | 45               | ·           | 20               | 285                   | 58               | xx          | 19               | 310                   | 79               | ·           | 20               | 450                   | 97               |
| IA-H                     | ·                | 20               | 340                   | 43               | ·           | 20               | 330                   | 45               | ·           | 20               | 285                   | 58               | xx          | 19               | 310                   | 79               | ·           | 20               | 450                   | 97               |
|                          | ·                | 16 <sup>c</sup>  | 270                   | 57               | xx          | 3                | 15                    | 32               | ·           | 20               | 335                   | 52               | ·           | 20               | 455                   | 68               | xx          | 4                | 30                    | 31               |
| IA-HH                    | ·                | 20               | 560                   | 55               | ·           | 20               | 330                   | 45               | ·           | 20               | 285                   | 58               | x           | 8                | 85                    | 34               | ·           | 20               | 350                   | 39               |

<sup>a</sup> The values reported in the gray rows represent the data obtained for  $F_{\text{s,exp}} = 300 \text{ kN}$ <sup>b</sup> State of the pads at the moment of the test termination (·: none of the pads fractured, [x]: one pad fractured, [xx]: both pads fractured)<sup>c</sup> Test terminated due to a oil flow issue with the hydraulic pumps

Conversely, as discussed in Section 1.3.2.1, most of the tests carried out with M2, M4 and M5 were terminated due to fracture of at least one pad. This phenomenon can be explained by analysing the characteristics of the pads reported in Table 1.1. Notably, the flexural strength of M5 is approximately 1.3 times lower than the one of M1, whereas its wear rate is 4.5 larger. Similar considerations hold true when the properties of M2 are compared with those of M3. This suggests that M2 and M5 experienced early fracture compared to M3 and M1 due to their high wear rate and low tensile/flexure strength. With regards to M4, its wear rate is approximately half of the one of M5. As a result, M4 fractured after a larger number of cycles compared to M5 although its flexural strength is about 1.8 times smaller.

In most cases, under a constant displacement amplitude (CA), the pads fractured several cycles before those tested under other loading protocols (e.g. IA or DA). This is attributed to the relatively large cumulative energy dissipation demand during CA relative to that of other protocols. For instance,  $\sum E_{\text{tot}}$  of pad M1 is equal to 680 kJ under CA, whereas it ranges between 310 kJ and 575 kJ for the rest of the loading protocols.

Under continuous sliding, part of the dissipated energy was transformed into heat at the sliding interface [124]. Notably, thermocouples installed close to this zone (see Fig. 1.3b) recorded  $T_{\text{max}}$  values above 70 °C for M1, M4 and M5, and around 60 °C for M2 and M3.

Referring to Table 1.5, M1 and M4 provide  $\bar{\mu}$  values ranging between 0.2 and 0.3, whereas  $\bar{\mu} \geq 0.30$  is obtained for the rest of the materials. This is explained by the

**Table 1.5** – Mean  $\bar{F}$ , mean  $\bar{\mu}$  and total loss of pretension  $\Delta N_b$  obtained for  $F_{s,\text{exp}} = 150$  kN and  $F_{s,\text{exp}} = 300$  kN under the cyclic loading protocols

| Protocol ID <sup>a</sup> | Material M1                        |               |                     | Material M2                        |             |                     | Material M3                        |             |                     | Material M4                        |             |                     | Material M5                        |             |                     |
|--------------------------|------------------------------------|---------------|---------------------|------------------------------------|-------------|---------------------|------------------------------------|-------------|---------------------|------------------------------------|-------------|---------------------|------------------------------------|-------------|---------------------|
|                          | $\frac{\bar{F}}{F_{s,\text{exp}}}$ | $\bar{\mu}^b$ | $\Delta N_b$<br>[%] | $\frac{\bar{F}}{F_{s,\text{exp}}}$ | $\bar{\mu}$ | $\Delta N_b$<br>[%] | $\frac{\bar{F}}{F_{s,\text{exp}}}$ | $\bar{\mu}$ | $\Delta N_b$<br>[%] | $\frac{\bar{F}}{F_{s,\text{exp}}}$ | $\bar{\mu}$ | $\Delta N_b$<br>[%] | $\frac{\bar{F}}{F_{s,\text{exp}}}$ | $\bar{\mu}$ | $\Delta N_b$<br>[%] |
| CA                       | 1.15                               | 0.26          | 4                   | 0.98                               | 0.42        | 42                  | 0.80                               |             |                     | 1.28                               | 0.32        | 18                  | 1.4                                | 0.30        | 15                  |
|                          | 0.95                               | 0.23          | 11                  | 0.62                               | 0.25        | 32                  | 0.39                               | 0.26        | 65                  | 0.90                               | 0.26        | 9                   | 0.90                               | 0.38        | 6                   |
| IA                       | 0.95                               | 0.19          | 7                   | 0.94                               | 0.53        | 53                  | 0.75                               | 0.53        | 59                  | 1.05                               | 0.25        | 4                   | 1.54                               | 0.44        | 17                  |
|                          | 0.96                               | 0.23          | 16                  | 0.71                               | 0.31        | 48                  | 0.59                               | 0.35        | 62                  | 0.82                               | 0.25        | 13                  | 1.00                               | 0.37        | 2                   |
| DA                       | 0.97                               | 0.19          | 3                   | 0.75                               | 0.35        | 42                  | 0.64                               | 0.34        | 38                  | 1.03                               | 0.24        | 6                   | 1.08                               | 0.30        | 22                  |
|                          | 0.81                               | 0.20          | 17                  |                                    |             |                     |                                    |             |                     | 0.75                               | 0.21        | 7                   |                                    |             |                     |
| IA-H                     | 1.01                               | 0.20          | 0                   | 1.03                               | 0.50        | 47                  | 0.91                               | 0.44        | 42                  | 1.12                               | 0.27        | 9                   | 1.42                               | 0.33        | 0                   |
|                          | 0.91                               | 0.21          | 7                   | 0.89                               | 0.36        | 41                  | 0.60                               | 0.30        | 46                  | 0.77                               | 0.23        | 16                  | 1.22                               | 0.43        | 1                   |
| IA-HH                    | 1.03                               | 0.23          | 4                   |                                    |             |                     |                                    |             |                     | 0.94                               | 0.27        | 7                   |                                    |             |                     |

<sup>a</sup> The values reported in the gray rows represent the data obtained for  $F_{s,\text{exp}} = 300$  kN<sup>b</sup> Mean friction coefficient computed by considering both static and dynamic friction coefficients

fact that M1 and M4 are characterized by a low wear rate compared to the rest, i.e. the volume of pad's fragments generated at the sliding interfaces is modest. This leads to moderate  $\mu$  values. However, M1 provides similar  $\bar{\mu}$  values under different  $F_s$  values and loading rates ( $0.19 \leq \bar{\mu} \leq 0.26$ ). Moreover, the pretension losses were  $\Delta N_b \leq 17\%$ , thereby yielding to  $\bar{F}/F_{s,\text{exp}}$  ratios close to 1.0. While pad M4 enjoys comparable  $\bar{\mu}$  values with pad M1 ( $0.21 \leq \bar{\mu} \leq 0.32$ ), several tests were terminated due to early fracture of the pads. As a result, the  $\bar{\mu}$  and  $\bar{F}$  values of M4 varies within a larger range compared to those of M1. This consideration also applies to M5. However, in such a case, the data set collected for  $F_s = 300$  kN is limited compared to the one obtained for  $F_s = 150$  kN due to the early fracture of the pads (see Table 1.4). Similarly, each test performed on M2 for  $F_s = 300$  kN was terminated within the first five loading cycles due to the early fracture of the pads. Conversely, the  $\bar{\mu}$  values obtained for M3 suggest that the friction coefficient of M3 is pressure dependent. Indeed,  $\bar{\mu}$  shows a reduction of nearly 60% when the clamping force is doubled. Furthermore, most of the  $\bar{F}/F_{s,\text{exp}}$  ratios obtained for M2 and M3 are well below 1.0. This was attributed to the significant loss of pretension for both M2 ( $\Delta N_b > 30\%$ ) and M3 ( $\Delta N_b > 40\%$ ), which in turn led to major variations of  $\bar{\mu}$ . As regards M2, noise emissions above 80 dB were recorded throughout the experimental campaign.

Overall, both M1 and M4 demonstrated a satisfactory performance under the employed symmetric cyclic loading protocols. Therefore, further investigations were carried out merely on these two materials with pulse-like and mainshock-aftershock loading protocols. The results are discussed in the following section.

### 1.3.3 Performance under Pulse-like and Mainshock-Aftershock Loading Protocols

This section focuses on tests conducted for  $F_{s,exp} = 300 \text{ kN}$  under the pulse-like (PL) and mainshock-aftershock loading protocols (MS-AS) for M1 and M4 pads. Referring to Fig. 1.16a and 1.16d, M1 and M4 provided fairly similar  $F - \delta$  responses regardless of the employed loading protocol. Notably, cyclic hardening was observed during the first two loading cycles of PL and MS due to the initial conditions of the friction pad surfaces. Subsequently,  $F$  achieved a relatively constant value, which was maintained throughout the loading history. The maximum axial force variation ( $\Delta F_{max}$ ) varied within 15 % and 23 % for PL and MS and within 6 % and 8 % for AS1 and AS2. Similar percentages were obtained for  $\Delta \mu_{max}$  (i.e., maximum friction coefficient variation). The bolt preload  $N_{bolt}$  was fairly constant during each test, thereby indicating no loss of pretension (see Fig. 1.16b and 1.16e). Referring back to Fig. 1.16c and 1.16f, for both M1 and M4,  $\mu$  progressively increased during the first two loading cycles of PL and MS. This phenomenon was caused by the wearing process on the sliding interfaces. Indeed, it occurred when a relatively constant sliding velocity  $v_s$  was applied (i.e., around 10 mm/s) and minor temperature variations were observed. Subsequently,  $v_s$  was varied between 27 mm/s and 10 mm/s. Notwithstanding this variation in sliding velocity,  $\mu$  achieved a constant value for both M1 and M4, which was maintained up to the end of the test; hence, at  $v_s > 10 \text{ mm/s}$  the visco-plastic effect became negligible for M4. Similarly, the friction coefficient of M1 did not increase during PL and MS because minor temperature variations occurred during these tests (i.e., less than 1 °C).

Referring to Table 1.6, the static and dynamic friction coefficients of M1 and M4 were fairly similar ( $0.97 \leq \bar{\mu}_d/\bar{\mu}_s \leq 1.03$ ). Furthermore, Table 1.6 reveals that M1 and M4 provide similar  $\bar{\mu}$  values during consecutive events. Therefore, under conditions potentially similar to those occurring during a seismic event, the examined friction pads may be suitable for providing supplemental damping in earthquake engineering applications.

## 1.4 Discussion

This section provides a discussion on the pressure-dependency of the friction coefficient of M1 and M4. The effect of loading rate, loading history and temperature on  $\mu$  for M1 and M4 is also debated.

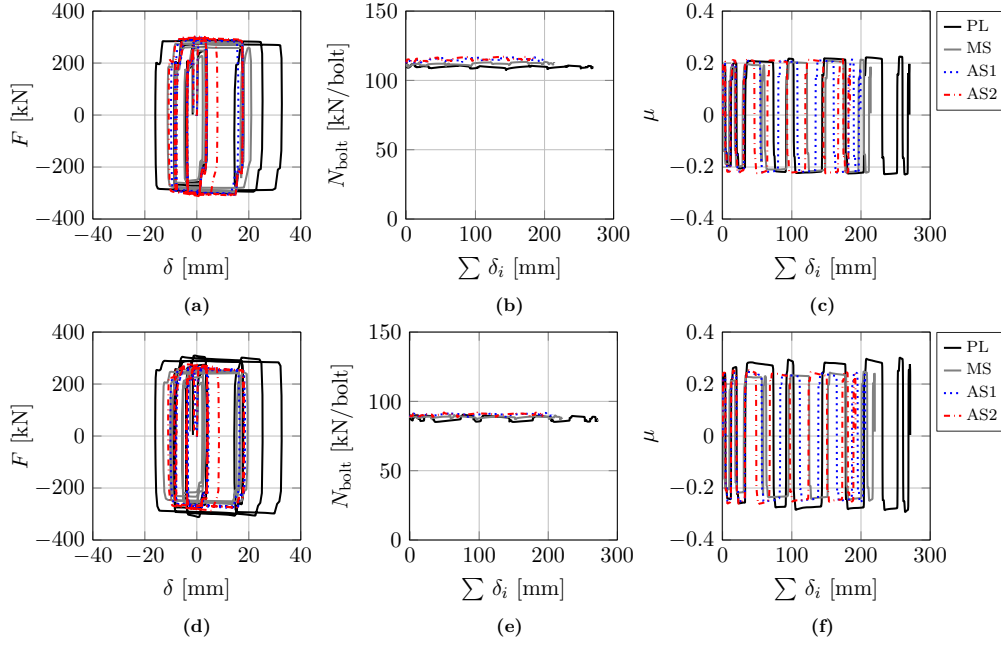


**Figure 1.16** – Results obtained for  $F_{\text{exp},s} = 300$  kN under the pulse-like (PL) and mainshock-aftershock loading protocol (MS: mainshock, AS1: first aftershock, AS2: second aftershock): (a)-(c) for M1, (d)-(f) for M4

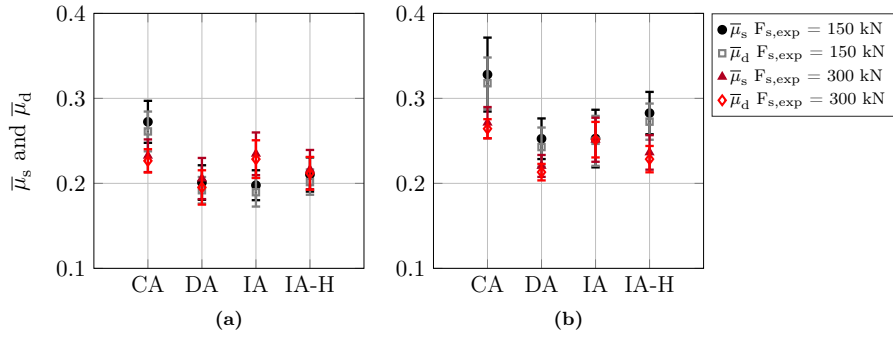
#### 1.4.1 Pressure Dependency

The mean ( $\bar{\mu}$ ) and standard deviation ( $\sigma$ ) of  $\mu$  are computed for different slip loads and loading protocols as depicted in Fig. 1.17, where the static and dynamic friction coefficients of the friction pads M1 and M4 are separated. It is apparent that when the clamping force is doubled,  $\bar{\mu}_s$  and  $\bar{\mu}_d$  experience a maximum variation of approximately 15% for both M1 and M4. Furthermore, the discrepancy between  $\bar{\mu}_s$  and  $\bar{\mu}_d$  is practically negligible (i.e.,  $0.95 \leq \bar{\mu}_d/\bar{\mu}_s \leq 1.00$  for both materials). Therefore, although  $\mu$  is somewhat pressure dependent, the corresponding percentage reductions of  $\bar{\mu}$  are fairly modest at pressures higher than 7 MPa–8 MPa. Referring to Fig. 1.17,  $\sigma$  assumes values smaller than 0.05 regardless of the employed loading protocol and pressure level. Noteworthy stating that part of this variability is due to the surface damage of the the inner steel plate. Indeed, while it was designed with a higher hardness than that of the friction pads, the surface of the steel plate exhibited some damage due to wear after numerous cyclic loading tests. However, this source of variability is deemed negligible.



**Table 1.6** – Data obtained for  $F_{s,exp} = 300$  kN under the pulse-like (PL) and mainshock-aftershock loading protocol (MS: mainshock, AS1: first aftershock, AS2: second aftershock)

| Protocol ID | Material M1                   |                           |               |                            |                                   | Material M4                 |                         |             |                          |                                   |
|-------------|-------------------------------|---------------------------|---------------|----------------------------|-----------------------------------|-----------------------------|-------------------------|-------------|--------------------------|-----------------------------------|
|             | $\frac{\bar{F}^a}{F_{s,exp}}$ | $\Delta F_{max}^b$<br>[%] | $\bar{\mu}^c$ | $\Delta\mu_{max}^d$<br>[%] | $\frac{\bar{\mu}_d}{\bar{\mu}_s}$ | $\frac{\bar{F}}{F_{s,exp}}$ | $\Delta F_{max}$<br>[%] | $\bar{\mu}$ | $\Delta\mu_{max}$<br>[%] | $\frac{\bar{\mu}_d}{\bar{\mu}_s}$ |
| PL          | 0.95                          | 15                        | 0.22          | 15                         | 1.01                              | 0.97                        | 20                      | 0.28        | 19                       | 1.01                              |
| MS          | 0.92                          | 21                        | 0.21          | 19                         | 1.03                              | 0.82                        | 23                      | 0.23        | 22                       | 1.02                              |
| AS1         | 0.98                          | 8                         | 0.21          | 7                          | 0.99                              | 0.87                        | 6                       | 0.24        | 6                        | 0.97                              |
| AS2         | 0.99                          | 6                         | 0.21          | 5                          | 0.99                              | 0.89                        | 8                       | 0.24        | 8                        | 0.97                              |

<sup>a</sup> Mean of the axial force  $F$ <sup>b</sup> Maximum axial force variation recorded during the experiment (estimated compared to  $\bar{F}$ )<sup>c</sup> Mean friction coefficient computed by considering both static and dynamic friction coefficients<sup>d</sup> Maximum friction coefficient variation recorded during the experiment (estimated compared to  $\bar{\mu}$ )**Figure 1.17** – Mean of  $\mu_s$  and  $\mu_d$  obtained for different expected slip loads and loading protocols (CA: constant amplitude; DA: decreasing amplitude; IA, IA-H, IA-HH: increasing amplitude at low, moderate and high rate; PL: pulse-like, MS: mainshock; AS1: first aftershock; AS2: second aftershock): (a) for M1, (b) for M4

#### 1.4.2 Effect of Loading Rate, Loading History and Temperature

Figures 1.18a and 1.18d illustrate the friction coefficients obtained under different loading protocols and sliding velocities  $v_s$  for  $F_{s,exp} = 300$  kN. For M1, it is apparent that  $\mu$  is not particularly affected by the imposed sliding velocity. For M4, while  $\mu$  attains a small increase up to  $v_s < 10$  mm/s, this is not statistically significant. According to [125], it is reasonable to assume that M4 is characterized by a visco-plastic shear strength; hence its stress-strain response varies according to the imposed deformation rate [126]. While the friction coefficient of M4 turns out to be somewhat loading-rate dependent [123], this dependency vanishes at sliding velocities  $v_s > 10$  mm/s. Therefore, under conditions potentially similar to those occurring during a seismic event, M4 can provide relatively stable  $\mu$  values.



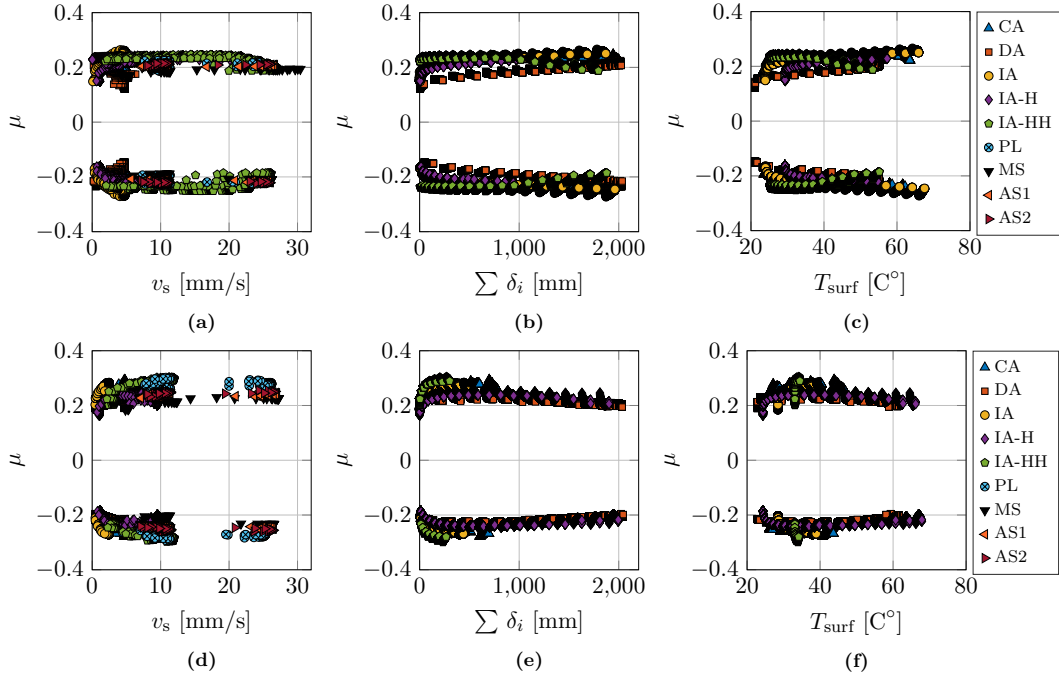


**Figure 1.18** – Friction coefficient obtained for (a)-(c) M1 and (d)-(f) M4 under different loading protocols and  $F_{s,\text{exp}} = 300 \text{ kN}$

With regard to the temperature effect, Fig. 1.18c and 1.18f illustrate the friction coefficients of M1 and M4 as a function of the temperature tracked at the surface of the inner slotted plate ( $T_{\text{surf}}$ ) for  $F_s = 300 \text{ kN}$  and the examined loading protocols. It is likely that the  $T_{\text{surf}}$  values associated to  $\mu$  in Fig. 1.18c and 1.18f are somewhat lower compared to the effective temperature experienced by the pads at the sliding interface. Referring to Fig. 1.18c, the rise from room temperature to  $40^\circ\text{C}$  causes a modest increase of  $\mu$ . However, under IA-HH,  $\mu$  progressively decreases for  $T_{\text{surf}} > 40^\circ\text{C}$ . As discussed in Section 1.3.2.1, this phenomenon is attributable to the surface alteration of the pads caused by the heat generated at the sliding interface (see Figure 1.11). Conversely, the experimental results obtained for M4 suggest that its friction coefficient is practically insensitive to the increase of  $T_{\text{surf}}$ .

## 1.5 Conclusions

This chapter presents findings from a comprehensive experimental program conducted on a prototype sliding friction damper. The tests featured five non-metallic composite friction pads (termed M1 to M5 herein) at two different pressure levels through bolt

pretension and under monotonic and cyclic loading protocols. Their static and dynamic friction coefficients were properly quantified in order to evaluate the applicability of the examined friction pads in providing supplemental damping in frame structures during earthquake shaking.

A number of shortcomings have been encountered with materials M2, M3 and M5. Particularly, pads made of M2 exhibited noise emissions above 80 dB. Moreover, at a sliding force of  $F_{s,exp} = 300$  kN most of the tests were terminated after a few cycles due to net section fracture of the pads near their bolt holes. Same limitations hold true for M5. Conversely, the friction coefficient of M3 proved to be pressure dependent.

Cyclic tests with pads made of M2 and M3 demonstrated a significant loss of bolt pretension. This caused variation in contact between the pads and the inner slotted plate. As a result, pads M3 usually experienced nonuniform wear and an irreversible bending deformation. The observed loss of pretension was mainly attributable to the inadequate dry treatment carried out on pads made of M2 and M3 after drilling the bolt holes with a water jet machine. Therefore, the performance of these two materials may be re-evaluated provided that a different manufacturing technique is employed.

In contrast, the prototype friction damper performed satisfactory when the friction pads featured materials M1 and M4. Particularly, both materials were characterized by similar static and dynamic friction coefficients (i.e.,  $0.95 \leq \bar{\mu}_d/\bar{\mu}_s \leq 1.00$ ). Consequently, the friction damper exhibited a fairly stable axial force-axial displacement hysteretic response without variations in axial force demands.

The experimental results suggest that the friction coefficient of pads M1 and M4 was fairly invariant at pressures higher than 7 to 8 MPa. These are typical for the range of slip loads to be achieved with friction dampers in seismic applications.

A comprehensive assessment of the  $\mu$  values obtained for pads M1 and M4 under various loading histories reveals that both materials provide fairly consistent  $\mu$  values when they operate at sliding velocities larger than 10 mm/s. Furthermore, the friction coefficient of pads M4 is practically insensitive to temperature variations measured during tests (i.e., roughly between 20 °C and 70 °C). On the contrary, the friction coefficient of M1 tends to slightly increase with the rise in temperature at the sliding interface. However, the experimental results obtained under the pulse-like and mainshock-aftershock loading protocols suggest that under conditions somewhat similar to those occurring during a seismic event, the temperature at the sliding interface does not increase sufficiently to cause major variations of  $\mu$ . Furthermore,  $\mu$  assumes similar values under consecutive events for both materials.

The pad surfaces were fairly damaged due to surface wear regardless of the imposed loading history. While surface wear often caused net section fracture to the pads during loading histories imposing cumulative energies of more than 85 kJ, this issue can be easily addressed by simply using thicker friction pads.

In conclusion, the results suggest that friction pads M1 and M4 are promising for further exploitation in sliding friction dampers for earthquake-induced vibration control of buildings.

Finally, the experimental program summarized in this chapter features a number of limitations. First, the pressure- and velocity-dependency of the pads' friction coefficient was investigated for a maximum pressure level of approximately 20 MPa and a maximum sliding velocity of 30 mm/s. These limits were imposed by the capacity of the existing laboratory equipment. Future experiments should be conducted with emphasis at larger input velocities characteristic of near-fault earthquake sequences. Moreover, time-dependent phenomena associated with force relaxations should also be carefully evaluated with the examined materials.

## Data availability statement

Some or all data generated or used during the study are available in a repository or online in accordance with funder data retention policies. Some or all data that support the findings of this study can be publicly accessed from Zenodo data repository [10.5281/zenodo.4544314](https://doi.org/10.5281/zenodo.4544314) or can be made available from the corresponding author upon reasonable request.



*Instead of trying to capture the variability of structural response, we should be designing structures that are less sensitive to uncertainty.*

Professor Edward L. Wilson of the University of  
California at Berkeley

# 2

## Seismic Design and Performance of Steel Concentrically Braced Frame Buildings with Dissipative Floor Connectors

### *Bibliographic details*

This chapter presents the pre-print (submitted) version of the article with the following full bibliographic details: Martina Paronesso and Dimitrios G. Lignos. "Seismic design and performance of steel concentrically braced frame buildings with dissipative floor connectors". In: *Earthquake Engineering & Structural Dynamics* (under review)

### *Authors' contribution*

Martina Paronesso, the first author of the above-mentioned paper, developed the proposed design methodology, construct the finite element models, carried out the nonlinear response history analysis, analysed and visualized the simulations results, created the figures, wrote the manuscript draft and revised the manuscript. The co-author contributed in developing the methodology presented in this chapter, supervising the work conducted by Martina

Paronesso, funding acquisition, and reviewing and editing the original and final manuscript drafts.

THIS CHAPTER EXPLORES the use of sliding friction dampers as dissipative floor connectors to mitigate higher mode effects and earthquake-induced absolute acceleration demands on steel concentrically braced frame (CBF) buildings. The dampers connect each floor of the steel CBF system to the diaphragms of the gravity framing system (GFS) and they allow for a relative in-plane movement between the two systems. For this purpose, a design methodology is first proposed to define the activation forces in the sliding friction dampers so as to ensure damage-free seismic performance in the steel CBF and the diaphragms of the GFS. The efficiency of the design methodology is demonstrated through nonlinear response history analyses on a low- and high-ductility 6-story steel CBF building. The simulation results suggest that (a) the determined activation forces of the sliding friction dampers are effective in mitigating higher mode effects and in preventing story drift concentrations regardless if capacity design is employed for the CBF system; (b) the absolute acceleration demands are reduced by approximately 50 % relative to those in the rigid diaphragm counterpart. Similar reductions are achieved in the lateral drift demands of the GFS at seismic intensities with return periods of 475 and 2475 years. The reduction in the variability of seismic response, both in terms of absolute floor acceleration demands and story drift ratios in the CBF system, is noteworthy. Limitations as well as suggestions for future work are discussed.

## 2.1 Introduction

Steel concentrically braced frames (CBFs) are widely used in seismic regions. Under seismic action, they dissipate energy primarily through yielding and flexural buckling of the braces. Experimental [3, 5] and numerical [9, 12] studies have shown that the hysteretic behavior of such members is highly asymmetric. This often leads to the formation of soft stories due to drift concentrations [13, 14]. Field observations from past earthquakes [16, 19] and studies conducted on earthquake life-cycle assessment [20] of CBF buildings have revealed that they are prone to damage in acceleration-sensitive non-structural components. This is attributable to the high earthquake-induced absolute acceleration demands that arise from (i) the high lateral stiffness of CBFs and (ii) the acceleration amplification caused by the higher mode effects [22, 24, 25].

Prior research focused on improving the seismic performance of steel braced frames through structural systems able to provide stable hysteretic response under cyclic loading. These include, among others, eccentrically braced frames [32–34], buckling restrained braced frames [35–37] and controlled rocking steel braced frames [38, 39, 41]. Others have suggested to enhance the energy dissipation capacity of steel CBFs by incorporating in the frame passive energy dissipation devices such as sliding friction dampers [42–44], slotted bolted connections [45–47] and yielding devices [48–50]. Hsiao et al. [127] proposed the concept of the naturally buckling brace that combines high-strength and low-yield steels within a steel brace with a specified initial eccentricity. More recently, strong-back systems have been promoted to prevent the formation of soft-story mechanisms [128, 129].

Despite the above-mentioned innovations, the challenge on how to control the magnitude of the absolute acceleration demands and their associated variability along the CBF height is still an issue to be addressed. Accordingly, the determination of the inertial forces acting on the floor diaphragms of such frames is deemed equally challenging. Indeed, higher mode effects can induce significant amplifications and fluctuations in the inertial force distribution [22, 24, 25]. In this regard, field observations from past earthquakes [18, 130] suggest that an inaccurate quantification of the inertial forces in the design phase can lead to severe damage of the structural and non-structural components of a building. In particular, it was observed that the integrity of several multi-story buildings was compromised due to the extensive damage undergone by their floor diaphragms [130].

In light of these findings, the development of new systems enables the protection of structural and non-structural components of a building during earthquake loading. In this respect, promising outcomes have been obtained by using dissipative floor connectors, which allow for relative in-plane movement between the floor diaphragms and the lateral load resisting system of a building. Notably, in the early seventies, Kelly et al. [71] and Skinner et al. [131] developed hysteretic floor devices for reinforced concrete buildings. Key [63] explored these connections to link a moment-resisting frame to a shear wall. This study revealed that such connectors improve the energy dissipation capacity of the building. Similarly, Priestley et al. [132] developed X-plate mechanical connectors to mitigate damage on the floor diaphragms of precast lateral load resisting systems (PRESSSS). Amaris et al. [133] proposed a non-tearing floor solution in which sliders/shear devices are used to connect the floor diaphragms to the lateral load resisting system of PRESSSS. Vides and Pampanin [66] pointed out that such connectors contribute in reducing the hysteretic energy demand in the structure and they reduce damage on the non-structural

components. Luco and de Barros [64] explored the possibility of improving the seismic performance of tall buildings by connecting a rigid perimeter frame to a flexible interior structure through damping devices located along the height of the building. This study demonstrated that dissipative floor connectors greatly reduce the peak absolute floor acceleration and story drift demands of the buildings under seismic action. Mar & Tipping [65] developed a building system that allowed the relative motion between the lateral and the gravity framing systems (GFS) through an assembly of springs and viscous dampers. In controlled rocking steel buildings, Eatherton and Hajjar [134] utilized shear plates to accommodate the uplift of the rocking frame relative to the floor diaphragms. Others investigated the use of friction [135, 136], hysteretic [137, 138] and viscous [139–142] floor devices to prevent pounding between adjacent multi-story structures. In an analogous manner, innovative details have been developed in order to isolate the non-structural components from the primary structural system/gravity framing of a building [143–145]. Recently, experiments including shake table testing have been conducted on reinforced concrete shear wall structures equipped with dissipative floor connectors [67–70]. Such connectors consist of either friction dampers or buckling restrained braces coupled with rubber bearings. These tests highlighted that these devices are effective in reducing earthquake-induced acceleration demands, mitigating higher mode effects and minimizing structural damage during a seismic event. While promising, the use of dissipative floor connectors within steel CBF buildings has never been explored. Accordingly, a practice-orientated methodology to design steel CBF buildings equipped with dissipative floor connectors does not currently exist.

In this thesis chapter, the seismic performance of multi-story steel CBF buildings equipped with floor sliding friction dampers (SFDs) is investigated. The dampers control the transfer of inertial forces between the GFS and the CBF. A risk-targeted design approach is proposed for steel CBF buildings equipped with floor SFDs. This comprises a methodology for selecting the activation forces of the SFDs. The benefits from the use of the floor SFDs are explored by evaluating the seismic performance of two 6-story steel CBF buildings. The first one features a low ductility braced frame, whereas the second one is capacity-designed. The seismic performance of the CBF buildings is evaluated in a probabilistic manner by assessing a number of engineering demand parameters (EDPs). Furthermore, EDP hazard curves of the maximum axial displacement of the SFDs and the peak story drift ratios (SDRs) of the GFS are developed to assess the seismic performance of the two buildings in a probabilistic manner. Finally, limitations as well as suggestions for future studies are discussed.



## 2.2 Basic Description of a Multi-Story Steel CBF Building with Sliding Friction Dampers as Dissipative Floor Connectors

Figure 2.1a illustrates the plan view of a 6-story steel building, which consists of 3-bay space steel moment resisting frames (MRFs) in the East-West direction and two steel CBFs in the North-South (N-S) direction. Motivated by Tsampras et al. [67, 69], in the N-S direction, the diaphragms of the GFS are connected to the steel columns of the CBFs through SFDs. Referring to Fig. 2.1b, the dampers are located at the individual floors of the building and they are connected to the CBF and GFS via clevises with spherical bearings. As illustrated in Fig. 2.1c, the SFDs are bolted to the steel column of the CBF and connected to the concrete floor slab of the GFS through anchor bolts. Each SFD slides and dissipates energy when it experiences an axial force that equals its activation force  $F_s$ . Referring to Fig. 2.1a, in addition to the SFDs, laminated rubber bearings (RBs) are installed between the columns of the CBF and the primary beams of the GFS. These components are bolted to the column of the CBF and anchored to a perimeter concrete ring beam that spans the opening around the CBFs. The RBs are installed so as to provide out-of-plane stability to the CBF in a similar fashion with those used by Tsampras et al. [67, 69]. In fact, the axial stiffness of the RBs is significantly higher than their shear stiffness ( $K_{RB}$ ). Hence, they enable in-plane relative movement between the CBF and the GFS. In particular, under shear deformation, the RBs exhibit a linear elastic response as schematically shown in Fig. 2.1d.

Figure 2.2a depicts the idealized behavior of a 6-story steel CBF building equipped with floor SFDs and RBs. The horizontal loads  $F_i$  correspond to the inertial forces generated during a seismic event at floor  $i$ . Under  $\vec{F} < \vec{F}_s$ , the SFDs act as rigid links between the CBF and the GFS. Therefore, in this case, the CBF and GFS experience identical lateral drift demands as in a conventional steel CBF building. Conversely, for  $\vec{F} = \vec{F}_s$ , the SFDs start sliding by allowing a relative in-plane movement between the CBF and GFS. At this instant, each damper transfers to the  $i^{\text{th}}$  floor of the CBF a horizontal force  $F_i$  equal to  $F_{s,i}$  (see Fig. 2.1c). Concurrently, the RBs experience shear deformation by transferring a horizontal force equal to  $\Delta F_{RB,i} = n_{RB} \cdot K_{RB,i} \cdot \delta_i$ , where  $n_{RB}$  is the number of RBs per floor and  $\delta_i$  is the horizontal displacement undergone by the latter (see Fig. 2.1d). As a result, under seismic action, the SFDs along with the RBs limit the inertial forces to (see Fig. 2.2a):

$$\vec{F} = \vec{F}_s + \Delta \vec{F}_{RB} \quad (2.1)$$

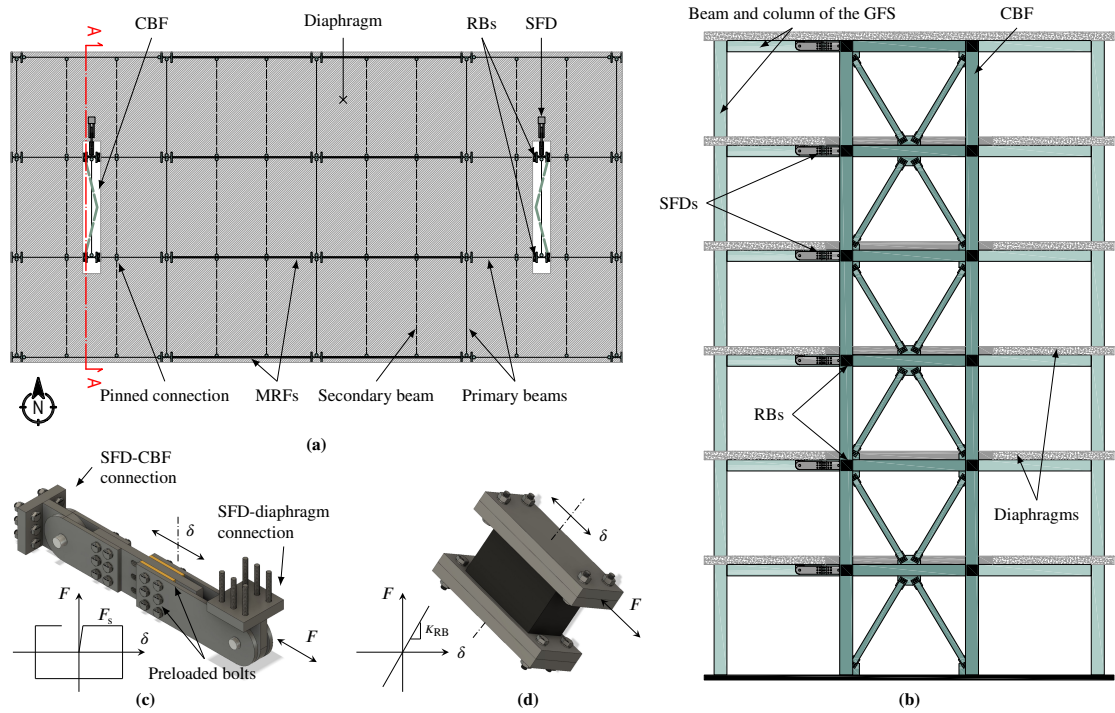


**Figure 2.1** – Configuration of a 6-story steel building equipped with floor SFDs in the N-S direction: (a) plan view, (b) elevation view (section A-A), (c) sliding friction damper, (d) rubber bearing



means of nonlinear response history analysis (NRHA), where elastic response of the CBF should be observed at the 84<sup>th</sup> percentile of the seismic demands. Additionally, the floor diaphragms of the GFS should remain elastic at both DBE and MCE. Conversely, under rare seismic events (i.e. probability of exceedance over 50 years building life expectancy smaller than 2%), damage of the structural components of the building may be accepted.

Firstly, the building is designed by considering that the GFS is rigidly connected to the CBFs. The ultimate and serviceability limit states are verified according to the design provisions of the design location. In particular, the seismic design forces can be determined through the equivalent lateral force method or the modal response spectrum analysis as discussed in EN 1998-1-1 [53] or ASCE/SEI 7-16 [146]. A discussion about the behavior factor  $q$  (i.e., strength reduction factor in ASCE/SEI standards) to be used for the design of the lateral load resisting system of the building is presented in Section 2.6.4.

Once the main structural components of the building are designed, the activation forces of the SFDs are selected so that (i) the diaphragms of the GFS do not experience damage prior to sliding of the SFDs and (ii) the CBF remains elastic under  $\vec{F} = \vec{F}_s + \Delta\vec{F}_{RB}$ . As first approach,  $\Delta\vec{F}_{RB}$  is assumed to be equal to  $\alpha\vec{F}_s$ , where  $\alpha$  may be initially taken equal to 15 %. In order to satisfy the requirement (i), the story shear induced by the activation forces at each story  $i$  of the CBF ( $V_{s,i}$ ) should be smaller than the one caused by the design diaphragm forces ( $V_{d,i}$ ):

$$V_{s,i} = \sum_i^{N \geq i} F_{s,i} \leq (1 - \alpha) \cdot V_{d,i} = (1 - \alpha) \cdot \sum_i^{N \geq i} F_{d,i} \quad (2.2)$$

where  $N$  is the number of stories and  $F_{s,i}$  and  $F_{d,i}$  are, respectively, the activation and design diaphragm force at story  $i$ . Due to a lack of guidelines in the current European provisions [53] for the seismic design of diaphragms, the lateral load pattern  $\vec{F}_d$  is determined according to ASCE/SEI 7-16 [146], Clause 12.10.1.1, as follows:

$$F_{d,i} = \frac{\sum_{x=i}^N F_x}{\sum_{x=i}^N w_x} \cdot w_i \quad (2.3)$$

where  $F_x$  is the design seismic force at story  $x$ , and  $w_x$  and  $w_i$  are the seismic weight tributary at story  $x$  and  $i$  respectively. It is noteworthy that at each story  $i$ ,  $F_{d,i}/w_i$  should be within  $0.2 \cdot S_d \cdot \gamma_I$  and  $0.4 \cdot S_d \cdot \gamma_I$ , where  $S_d$  is the 5% damped design spectral

acceleration at the corner periods  $T_B \leq T \leq T_C$  and  $\gamma_I$  is the building importance factor according to EN 1998-1-1 [53].

With regards to the requirement (ii), the latter is satisfied as long as  $V_{s,i}$  is smaller than the story shear causing inelastic deformations in the CBF ( $V_{CBF,i}$ ) at story  $i$ :

$$V_{s,i} = \sum_i^{N \geq i} F_{s,i} \leq (1 - \alpha) \cdot V_{CBF,i} = (1 - \alpha) \cdot \sum_i^{N \geq i} F_{CBF,i} \quad (2.4)$$

where  $F_{CBF}$  is the horizontal load pattern causing inelasticity in the CBF. Notably, under seismic action, CBFs designed according to capacity design (e.g. for a behavior factor  $q > 2.0$  according to EN 1998-1-1 [53]) may become inelastic due to brace buckling. Therefore, the load pattern  $\vec{F}_{CBF}$  is conservatively defined as a function of the 90 % of the buckling resistance of these members:

$$\vec{F}_{CBF} = M_{IL}^{-1} \cdot 0.90 \cdot \vec{N}_b \quad (2.5)$$

where  $\vec{N}_b$  is a vector, whose indices are the buckling resistance of the braces, and  $M_{IL}$  is an  $N \times N$  influence matrix. The index  $a_{ij}$  of  $M_{IL}$  represents the maximum absolute axial force experienced by the braces located at story  $i$  when a unit force is applied at  $j^{\text{th}}$  floor of the CBF. When CBFs are designed with limited ductility (i.e.,  $1.0 \leq q \leq 2.0$ ), brace buckling is not necessarily the first limit state achieved by the latter under seismic action. Notably, fracture of the bracing-end connections can potentially occur prior to brace buckling because, in such a case, no specific rules for capacity design and detailing are imperative for the bracing-end connections. Therefore, in this case,  $\vec{F}_{CBF}$  is defined as follows:

$$\vec{F}_{CBF} = M_{IL}^{-1} \cdot \vec{N}_{Ed} \quad (2.6)$$

where  $\vec{N}_{Ed}$  is a vector, whose indices are the maximum axial forces experienced by the braces under combinations of actions determined for the seismic design situation.

In summary, the activation forces of the SFDs should be selected so that both Eq. 2.2 and 2.4 are satisfied:

$$V_{s,i} = \sum_i^{N \geq i} F_{s,i} \leq (1 - \alpha) \cdot \min\{V_{d,i}, V_{CBF,i}\} \quad (2.7)$$

Referring to Fig. 2.3a, several  $\vec{F}_s$  patterns may be selected so that Eq. 2.7 is fulfilled. The methodology presented in this chapter suggests to select the largest  $F_s$  values through which the requirements (i) and (ii) can be satisfied at each story of the building. In

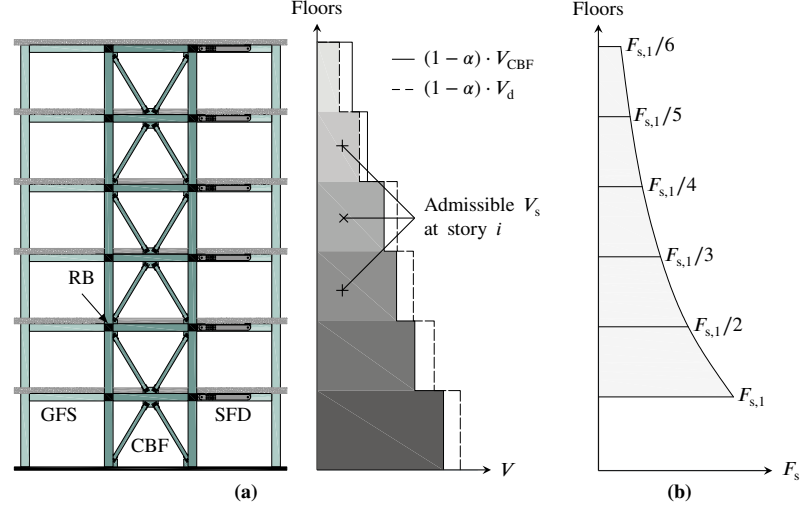


**Figure 2.3** – (a) Admissible story shear  $V_s$  in a 6-story steel CBF building, (b)  $\vec{F}_s$  pattern defined for a 6-story steel CBF building

particular, given that the admissible story shear decreases along the height of the building (see Fig. 2.3a), it is recommended to use a decreasing  $F_s$  distribution along the height of the building, whose maximum value is located at the 1<sup>st</sup> story of the CBF (see Fig. 2.3b):

$$F_{s,1} = \frac{(1 - \alpha) \cdot \min\{V_{d,1}, V_{CBF,1}\}}{\sum_{i=1}^N 1/i} \quad (2.8)$$

$$F_{s,i} = \frac{F_{s,1}}{i} \quad (2.9)$$

Once the  $\vec{F}_s$  pattern is defined, the selected activation forces should be carefully evaluated in order to verify whether it is feasible to effectively achieve such levels of force in the SFDs. Subsequently, the main components of the SFDs (e.g. steel plates and preloaded bolts) can be designed. Notably, in order to define the total normal force ( $N_{tot}$ ) to apply at the sliding interfaces with the preloaded bolts (see Fig. 2.1c), the activation force of each damper may be approximated by using the Coulomb's law of friction [116]:

$$F_s = n_s \cdot \mu_s \cdot N_{tot} \quad (2.10)$$

where  $n_s$  is the number of slip interfaces and  $\mu_s$  is the static friction coefficient characterising the selected friction pads.

As discussed in Section 2.2, in addition to the SFDs, laminated RBs are installed at each floor of the building. Their  $K_{RB}$  should be the smallest possible so that the

horizontal forces experienced by the CBF exhibit minor variations once the SFDs start sliding (i.e.,  $\Delta \vec{F}_{RB}$  attains minor values).

Finally, NRHA should be conducted in order to verify that the design performance objectives set at DBE and MCE are satisfied. If not, the activation forces of the dampers should be re-defined by using a reduced  $\alpha$  factor in Eq. 2.8. In addition to this, the maximum horizontal displacement demands ( $\delta_{\max}$ ) of both SFDs and RBs should be quantified. Notably, at MCE, the displacement capacity ( $\delta_{RB}$ ) of the selected RBs should be larger than  $\delta_{\max}$  in order to prevent their fracture under seismic action. Similarly, the slot of the SFDs (see Fig. 2.1c) should be sized so that the preloaded bolts do not exceed the allowable displacement demands enabled by the slotted holes at MCE (i.e. slot  $> \delta_{\max}$ ). Furthermore, the earthquake-induced acceleration demands and SDRs of the building should be quantified at both DBE and MCE in order to evaluate the extent of damage in non-structural components. Potential variations of the activation force of the SFDs due to the uncertainties in the properties of the friction pads should also be considered according to the lower/upper bound analysis procedures available in design standards for buildings and bridges incorporating seismic isolation and passive energy dissipation systems [147, 148].

Alternatively, the activation forces of the SFDs can be selected so as a targeted absolute floor acceleration demand ( $a_{\text{target}}$ ) is not exceeded along the height of the building under seismic action. Notably, at each floor  $i$ , the SFDs should start sliding for an axial force equal to  $F_{s,i} = a_{\text{target}} \cdot m_i$ , where  $m_i$  is the total mass applied at the floor  $i$  of the building. Subsequently, the building is sized for the selected  $F_s$  distribution. Nevertheless, this approach can lead to fairly small  $F_s$  values in the case that low  $a_{\text{target}}$  values are selected (e.g. 0.2g). Therefore, in such a case, a more flexible building can be obtained compared to the case in which it is designed according to the procedure illustrated in Fig. 2.3. As discussed in Section 2.6.4, this can make the floor SFDs less effective in controlling the SDR demands experienced by the GFS under seismic loading.

## 2.4 Case Studies

### 2.4.1 Design of Multi-Story Steel CBF Buildings equipped with Sliding Friction Dampers

For illustration purposes, the proposed methodology is applied to two 6-story steel buildings of importance class II designed for  $q = 2.0$  and  $q = 3.0$  according to the European provisions [53, 149]. Such buildings are of particular interest to illustrate the efficiency

of the proposed methodology in mitigating higher mode effects because their seismic response is affected by the second and third modes of vibration when dissipative floor connectors are not employed.

The design location of the two buildings is situated in Sion (Switzerland), in a region characterized by a soil type D and a reference peak ground acceleration ( $a_{gR}$ ) of 0.22 g. Referring to Fig. 2.4a, both buildings consist of 3-bay space steel MRFs in the E-W direction and two perimeter CBFs in the N-S direction. Each CBF is connected to the diaphragm of the GFS through a SFD and two RBs per floor. Columns are oriented around their weak axis in the N-S direction and they are spliced at stories 3 and 5. In the E-W direction, the primary beams are connected to the columns with stiffened end-plate connections, whereas those in the N-S direction are pin-jointed at their ends. In addition, secondary beams with pin-jointed ends span in the N-S direction. All the structural steel members are made of S355 steel (nominal yield stress,  $f_y = 355$  MPa), whereas the diaphragms consist of profiled steel decks. The seismic design forces of each building are determined through modal response spectrum analysis. Figures 2.4b and 2.4c illustrate the elevation view along with the member sizes of the CBFs designed for  $q = 2.0$  and  $q = 3.0$ , respectively. In the former, capacity design principles are not employed contrary to the latter. Therefore, the CBF designed for  $q = 2.0$  (denoted hereinafter as LD-CBF) has a limited ductility compared to the one designed for  $q = 3.0$  (denoted hereinafter as HD-CBF). A sketch of the bracing-end connections of the LD-CBF and HD-CBF is depicted in Figs. 2.4d and 2.4e. The connection shown in Fig. 2.4d consists of a gusset plate welded to the flange of the steel beam. The brace is connected to the gusset plate through bolts. The design of each bracing-end connection is accomplished according to the EN 1993-1-8 [150] provisions in order to prevent (i) net section fracture of the gusset plate or brace, (ii) shear fracture of the bolts, (iii) bearing failure of the bolt holes on the gusset plate or brace, (iv) block tearing, and (v) local buckling of the gusset plate. Referring to Fig. 2.4e, the bracing-end connections of the HD-CBF are designed as discussed by Roeder et al. [151]. In particular, a clearance distance of eight times the thickness of the gusset plate is adopted to obtain compact gusset plates and accommodate the out-of-plate rotation of the brace in compression [152].

Laminated RBs with  $K_{RB} = 0.8$  kN/mm and  $\delta_{RB} = 380$  mm are located at each floor of the LD-CBF and HD-CBF. According to the manufacturer specifications, these components consist of an elastomeric block made of natural rubber, which is reinforced with steel sheets bonded by vulcanising. Each RB has a diameter of 650 mm and a thickness of approximately 300 mm.



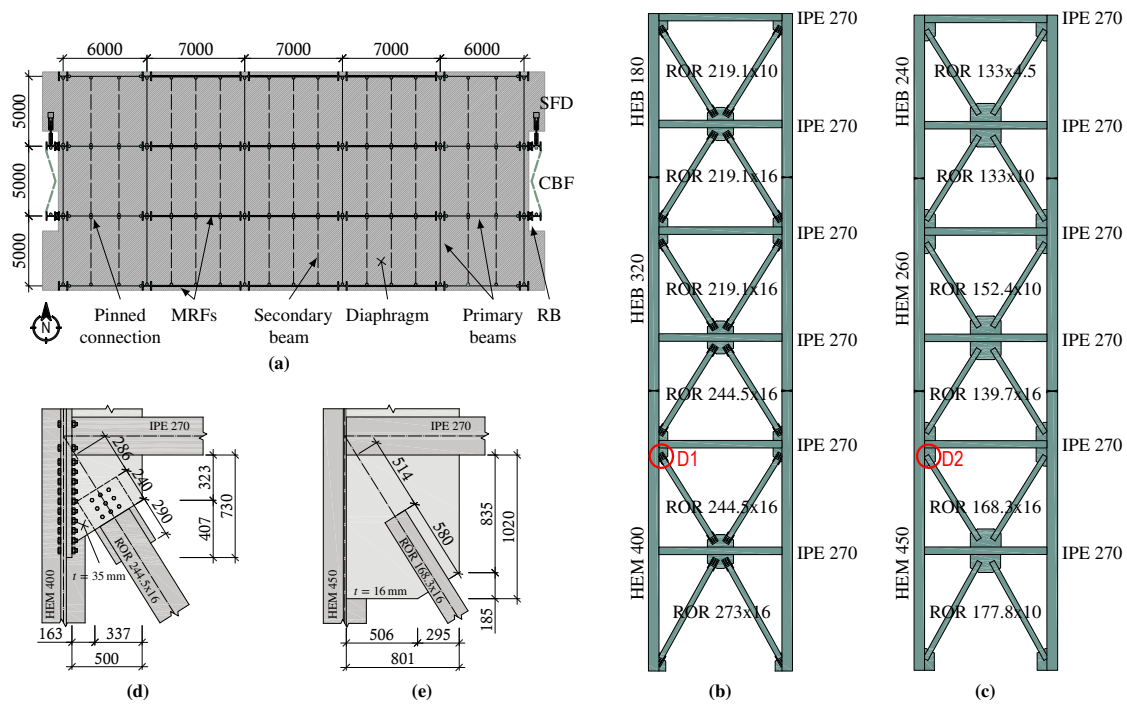


**Figure 2.4** – (a) Plan view of the 6-story steel buildings, (b)-(c) elevation view of the LD-CBF ( $q = 2.0$ ) and HD-CBF ( $q = 3.0$ ) respectively, (d)-(e) bracing-end connections of the LD-CBF and HD-CBF respectively (details D1 and D2)

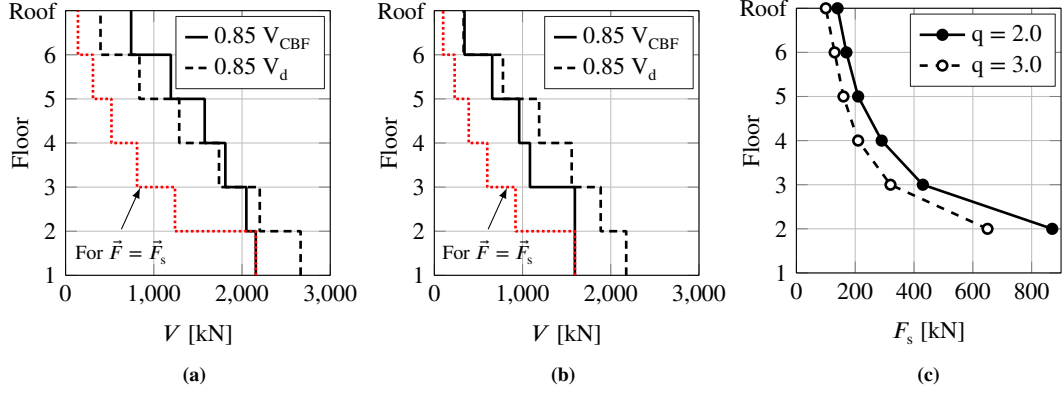


**Figure 2.5** – (a)-(b) Admissible story shear obtained for the LD-CBF ( $q = 2.0$ ) and HD-CBF ( $q = 3.0$ ) respectively, (c) activation forces selected for the SFDs

The activation forces of the SFDs are defined as discussed in Section 2.3. Notably, the diaphragm forces are determined considering  $S_d = 0.74 g$  and  $\gamma_I = 1.0$ . With regards to  $\vec{F}_{CBF}$ , the latter is defined according to Eq. 2.5 for the HD-CBF and according to Eq. 2.6 for the LD-CBF. Figures 2.5a and 2.5b illustrate the admissible story shear  $\vec{V}_s$  obtained for the two buildings. In both cases,  $\vec{V}_s$  is limited by  $\vec{V}_{CBF}$  expect at the top stories. Furthermore, it is noteworthy that the LD-CBF is characterized by higher  $V_d$  and  $V_{CBF}$  values compared to the HD-CBF. This is because the members of the LD-CBF have been sized for seismic forces larger than those used to design the HD-CBF. As a result, the activation forces of the SFDs of the LD-CBF turn out to be about 1.3 higher than those obtained for the HD-CBF (see Fig. 2.5c). Notably,  $F_s$  values between 870 kN and 140 kN are found for the LD-CBF.

## 2.4.2 Nonlinear Building Models

Two-dimensional (2D) numerical models of the 6-story steel buildings in the N-S direction are developed in the Open System for Earthquake Engineering Simulation (OpenSees) Platform [153] (release version 2.5.0). Figure 2.6a illustrates the main features of such models. The CBF columns and beams are modelled using force-based beam-column elements with 10 Gauss-Lobatto integration points along the member's length [154]. A 4x1 mesh is used to discretize the flange and web of each cross section as proposed by Kostic et al. [155]. The Voce-Chaboche material model [156, 157] is adopted to simulate the stress-strain response of each fiber. The input model parameters assigned to the latter are based on the work of de Castro e Sousa et al. [158] for S355 steel. At the beams' ends, the shear tab connections are modelled with a zero-length spring, whose hysteretic

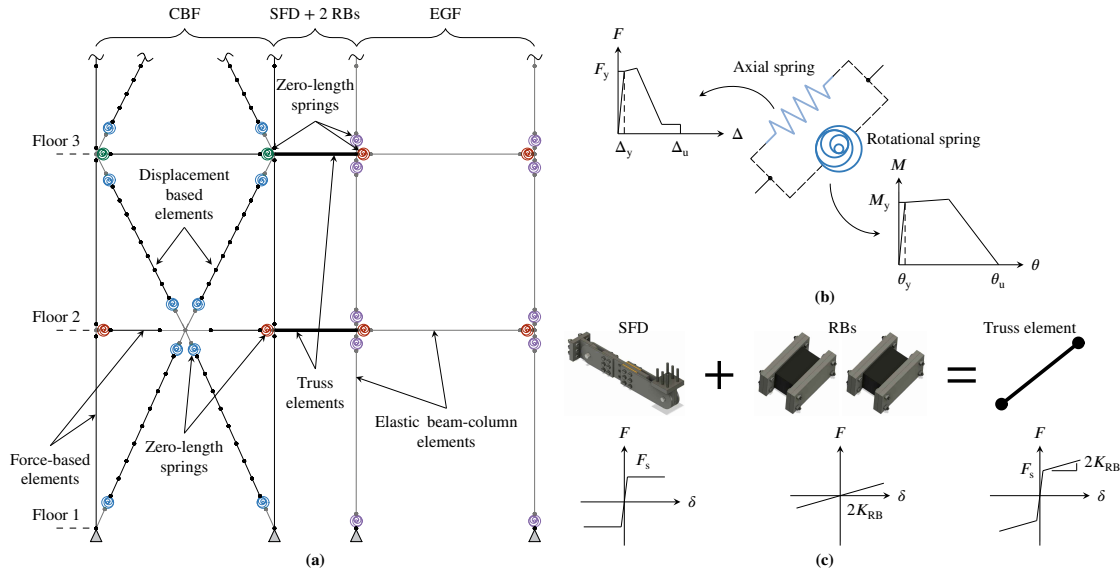


**Figure 2.6** – (a) 2D numerical model of the 6-story steel building in the N-S direction, (b) axial and rotational springs placed in series in order to model the in-plane and out-of-plane behavior of the bracing-end connections of the LD-CBF and LD-CBF-R (c) truss element used to model both SFD and RBs

moment-rotation response is defined according to Elkady and Lignos [159] at the even-numbered floors and as suggested by Stoakes et al. [160] at the odd-numbered floors. Steel braces are modelled according to Karamanci and Lignos [12], including brace buckling and fracture initiation due to ultra low-cycle fatigue. The gusset plate connections of the HD-CBF are modelled as suggested by Hsiao et al. [11]. With regards to the LD-CBF, an axial and rotational spring are placed in series as illustrated in Fig. 2.6b in order to model the in-plane and out-of-plane behavior of the bracing-end connections, respectively. The response of both springs is simulated with the modified Ibarra-Medina-Krawinkler (IMK) deterioration model [161]. In particular, the parameters of the rotational spring are defined based on the experimental study conducted by Davaran et al. [27]. With regards to the axial spring, its maximum axial force corresponds to the minimum force reached by the connection at a critical limit state (e.g. failure of bolts in shear, fracture of the net section of the gusset plate, buckling of the gusset plate,...). Once this force demand is reached, the bracing-end connection is assumed to fracture (i.e., a zero plastic deformation capacity is reached).

The GFS of the buildings is modelled through an equivalent 1-bay frame denoted by Elkady and Lignos [159] as "equivalent gravity frame" (EGF). At each story, the beams and columns of the EGF are modelled with an elastic element, whose proper-

ties are equivalent to half of the sum of those of the members that compose the GFS in the N-S direction. At the EGF columns' ends, plastic hinges are idealized with a zero-length spring based on the modified IMK deterioration model with input model parameters according to Lignos et al. [162]. Similarly, at the EGF beams' extremities, shear tab connections are modelled through rotational springs as discussed in Elkady and Lignos [159].

Referring to Fig. 2.6a, each floor of the EGF is linked to the CBF through a truss element. Such element has a bilinear force-displacement response and it is employed to model both SFD and RBs as illustrated in Fig. 2.6c. Notably, at a given floor  $i$ , the truss element becomes inelastic when it experiences an axial force  $F_i$  equal to the activation force  $F_{s,i}$  of the SFD located at that floor. Once the SFD starts sliding, the RBs experience shear deformation, thereby providing a post-elastic stiffness of  $2K_{RB}$  to the truss element. It is noteworthy that the RBs investigated in this study are modelled by assuming that their hysteretic force-displacement response is velocity-independent as suggested by their manufacturer. Alternatively, a velocity-dependent hysteretic response of the RBs can be considered by employed the Kelvin solid model as discussed in Christopoulos and Filiatrault [163]. With regards to the elastic stiffness of the truss element, this parameter corresponds to the elastic stiffness of the SFD. In this study, the latter is set to 1000 kN/mm, which corresponds to the elastic stiffness of the SFD, which was derived by Paronesso and Lignos [84] based on experiments on SFDs.

The base supports of the CBF and EGF are assumed pinned. The gravity loads and seismic masses acting on the building are determined according to the EN 1990-1-1 [164] and EN 1991-1-1 [165] provisions. Half of them are applied to the EGF columns as discussed by Gupta and Krawinkler [166] and Elkady and Lignos [159]. Indeed, the CBF does not carry any seismic mass because it is disconnected to the GFS. Second-order effects are considered through the corotational transformation. Furthermore, 2% damping ratio is assigned to the first and third vibration periods of each numerical model.

## 2.5 Modal Analysis and Nonlinear Static Analysis

In this section, modal analysis and nonlinear static analysis based on the first mode lateral load pattern are conducted in order to evaluate the performance of the LD-CBF and HD-CBF. The case study in which the GFS is rigidly connected to the CBF is also investigated (denoted hereinafter as LD-CBF-R for  $q = 2.0$  and HD-CBF-R for  $q = 3.0$ ). For the LD-CBF-R and the HD-CBF-R, the truss elements illustrated in Fig. 2.6a were replaced by rigid links in order to simulate the rigid diaphragm action.

**Table 2.1** – First-mode periods ( $T_1$ ), mass ratios ( $M/M_{\text{tot}}$ ) and stiffness ratios ( $K/K_{\text{tot}}$ ) obtained for the four investigated buildings

| Building | System   | $K/K_{\text{tot}}^{\text{a}}$ | $M/M_{\text{tot}}$ | $T_1$<br>[sec] |
|----------|----------|-------------------------------|--------------------|----------------|
| LD-CBF-R | CBF      | 0.92                          | 0.1                | 0.4            |
|          | EGF      | 0.08                          | 0.9                | 8.9            |
|          | LD-CBF-R | 1.00                          | 1.0                | 1.0            |
| HD-CBF-R | CBF      | 0.98                          | 0.1                | 0.4            |
|          | EGF      | 0.02                          | 0.9                | 8.4            |
|          | HD-CBF-R | 1.00                          | 1.0                | 1.1            |
| LD-CBF   | CBF      | 0.92                          | 0.0                | -              |
|          | EGF      | 0.08                          | 1.0                | 8.9            |
|          | LD-CBF   | 1.00                          | 1.0                | 1.0            |
| HD-CBF   | CBF      | 0.98                          | 0.0                | -              |
|          | EGF      | 0.02                          | 1.0                | 8.4            |
|          | HD-CBF   | 1.00                          | 1.0                | 1.1            |

<sup>a</sup> Elastic lateral stiffness of the investigated building<sup>b</sup> Total mass acting on the investigated building

Table 2.1 summarizes the stiffness ratios ( $K/K_{\text{tot}}$ ), mass ratios ( $M/M_{\text{tot}}$ ) and first-mode periods ( $T_1$ ) obtained for the four investigated buildings. Notably,  $K/K_{\text{tot}}$  values larger than 0.90 are obtained for the CBF regardless of the case study considered. Furthermore, mass ratios close to unit are obtained for the GFS when dissipative floor connectors are employed. This suggests that, under seismic action, the inertial forces generate on the floor diaphragms of the GFS and they are merely resisted by the CBF. With regards to the first-mode periods, LD-CBF-R and HD-CBF-R are characterized by a  $T_1$  value of about 1.0sec and 1.1sec, respectively. Similar values are also obtained for the LD-CBF and HD-CBF. Indeed, the elastic lateral stiffness of the building is not affected by the use of the dissipative floor connectors. Furthermore,  $T_1$  values larger than 8.0sec are obtained for the GFS of the four investigated case studies. This confirms that the GFS is flexible compared to the CBF.

Figure 2.7 depicts the pushover curves obtained for the four analysed cases. In this figure, the total base shear ( $V_{\text{tot}}$ ) is normalized with respect to the seismic weight ( $W$ ), whereas the roof drift ratio ( $\Delta_{\text{roof}}/H$ ) is the roof displacement ( $\Delta_{\text{roof}}$ ) normalized with respect to the total height ( $H$ ) of the building. In the same figure, the normalized design base shear ( $V_{\text{design}}/W$ ) of each building is superimposed. Notably, the LD-CBF-R and HD-CBF-R are designed for  $V_{\text{design}}/W = 0.27$  and  $V_{\text{design}}/W = 0.15$ , respectively. The results shown in Fig. 2.7 demonstrate that, as expected, the two CBF buildings are mostly force-controlled. Notably, a static overstrength factor (i.e., ratio of the maximum total

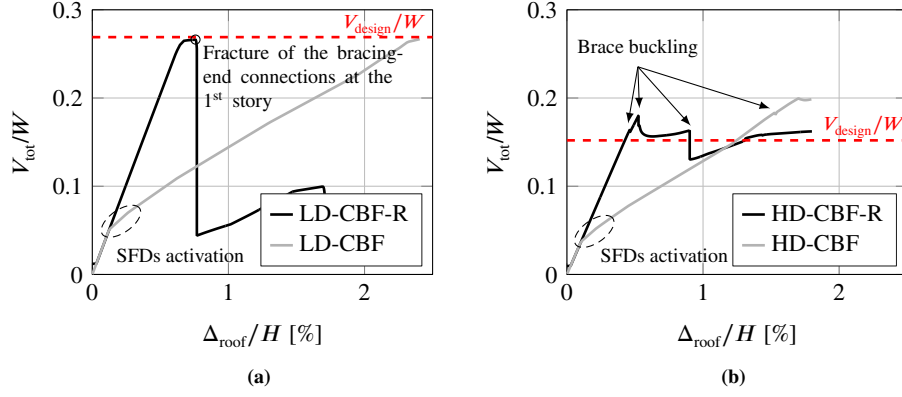


**Figure 2.7** – Pushover curves obtained for the (a) LD-CBF and LD-CBF-R, (b) HD-CBF and HD-CBF-R

base shear resisted by the building to  $V_{\text{design}}$ ) close to unity is obtained in both cases, unlike steel MRFs, which are usually drift controlled; thus, the system overstrength may be appreciable in this case [159, 167].

The simulation results for the LD-CBF-R and HD-CBF-R reveal that the CBFs become inelastic at  $\Delta_{\text{roof}}/H = 0.65\%$  and  $\Delta_{\text{roof}}/H = 0.46\%$ , respectively. Notably, the LD-CBF-R experiences fracture of the bracing-end connections in the 1<sup>st</sup> story for  $V_{\text{tot}}/W = V_{\text{design}}/W$ . This causes a sharp decrease of  $V_{\text{tot}}$  of approximately 80%. Conversely, brace buckling occurs at the 6<sup>th</sup> and 3<sup>rd</sup> story of the HD-CBF-R for  $\Delta_{\text{roof}}/H = 0.46\%$  and  $\Delta_{\text{roof}}/H = 0.53\%$ , respectively. This phenomenon leads to a minor variation of  $V_{\text{tot}}$  because after brace buckling, the internal forces redistribute within the CBF and the unbuckled braces in the other stories further resist to the applied load pattern. This confirms the fact that the HD-CBF-R is characterized by a higher ductility compared to the LD-CBF-R. In addition, a further variation of  $V_{\text{tot}}$  is observed for  $\Delta_{\text{roof}}/H = 0.90\%$  when brace buckling occurs at the 5<sup>th</sup> story of the HD-CBF-R.

Referring to Fig. 2.7, for  $\Delta_{\text{roof}}/H < 0.1\%$ , the results obtained for the LD-CBF and HD-CBF match those found for the LD-CBF-R and HD-CBF-R, respectively. Indeed, up to this lateral drift demand, all the SFDs experience an axial force lower than  $F_s$ . For  $\Delta_{\text{roof}}/H \geq 0.1\%$ , the SFDs activate by controlling the transfer of horizontal forces between the CBF and the GFS. Whenever a SFD starts sliding, the pushover curve of the LD-CBF and HD-CBF experiences a decrease in lateral stiffness as shown in Fig. 2.7. For the LD-CBF, a slight increment of slope is observed for  $\Delta_{\text{roof}}/H = 2.0\%$  when the GFS starts resisting part of the applied load (i.e., less than 3% of the total). Referring to Fig. 2.7b, the HD-CBF becomes inelastic when brace buckling occurs in the 6<sup>th</sup> story for  $\Delta_{\text{roof}}/H = 1.5\%$ . This corresponds to a roof drift ratio at least 3 times larger than

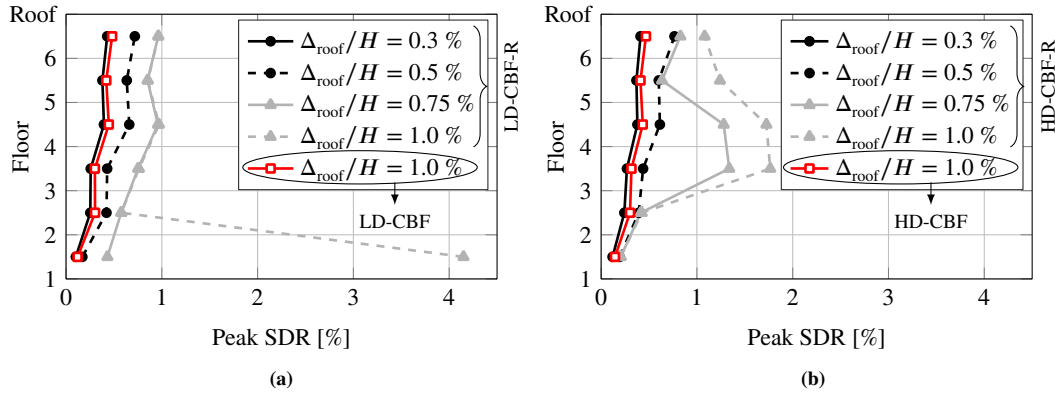


**Figure 2.8** – Peak SDRs obtained at targeted roof drift ratios for the CBF of the (a) LD-CBF-R and LD-CBF, and (b) HD-CBF-R and HD-CBF

the one at which a similar event is observed in the HD-CBF-R (i.e.,  $\Delta_{\text{roof}}/H = 0.46\%$ ). Similarly, the LD-CBF behaves elastically up to about  $\Delta_{\text{roof}}/H = 2.5\%$ .

Figure 2.8 depicts the progression of the peak SDRs in the steel CBFs of the four investigated buildings. Referring to Fig. 2.8a, the LD-CBF-R develops a soft-story mechanism at its 1<sup>st</sup> story for  $\Delta_{\text{roof}}/H > 0.75\%$ . This is due to fracture of the bracing-end connections located in this story. Similarly, for  $\Delta_{\text{roof}}/H > 0.5\%$ , drift concentration occurs in the 3<sup>rd</sup> and 4<sup>th</sup> story of the HD-CBF-R subsequent to brace buckling (see Fig. 2.8b). Conversely, uniform peak SDR lower than 0.5% are observed along the height of the CBF of the LD-CBF and HD-CBF for  $\Delta_{\text{roof}}/H = 1.0\%$ . This suggests that under a first-mode lateral load pattern, the SFDs are effective in delaying structural damage in both HD-CBF and LD-CBF. Furthermore, cyclic pushover analysis is conducted in order to indicatively quantifying the equivalent viscous damping ratio  $\xi_{\text{hyst}}$  of each building as discussed by Jacobsen [168]. To this end, the maximum horizontal displacement applied at the roof of each building corresponds to the one determined according to the design displacement spectrum for the MCE seismic intensity. It is found that both LD-CBF-R and HD-CBF-R are characterized by a  $\xi_{\text{hyst}}$  value between 2% and 3%, whereas  $\xi_{\text{hyst}}$  values larger than 15% are achieved when dissipative floor connectors are employed. On the other hand, further analyses should be conducted in order to investigate the impact of higher mode effects on the response of the examined buildings and to further validate the proposed design methodology discussed in Section 2.3.

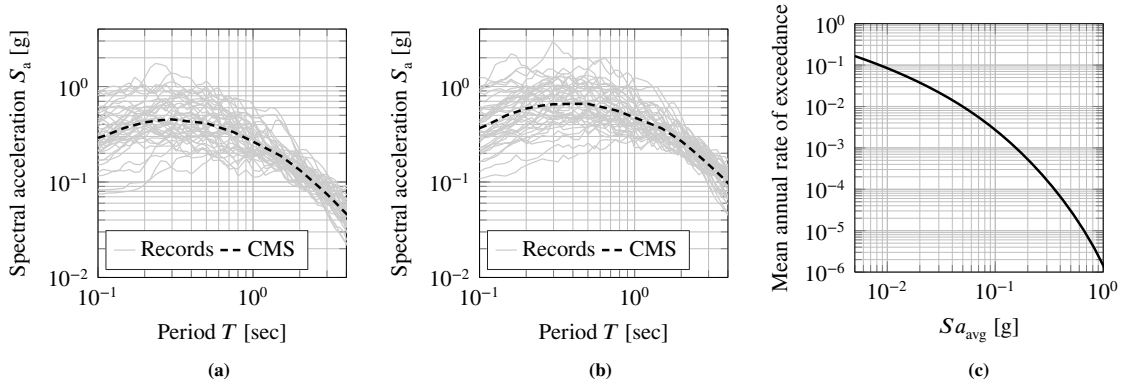


**Figure 2.9** – (a)-(b) Acceleration spectra of the ground motion records for the DBE and MCE seismic intensities respectively, (c)  $Sa_{avg}$  hazard curve of Sion (Switzerland)

## 2.6 Nonlinear Response History Analysis

In this section, the seismic performance of the LD-CBF is investigated through NRHA. The comparison between the LD-CBF and LD-CBF-R is established in terms of SDRs, peak absolute floor acceleration (PFA) demands and story shear force demands. Similarly, the performance of the LD-CBF and HD-CBF is compared in order to investigate the influence of the assumed behavior factor  $q$  on the SDRs of the GFS. Finally, EDP hazard curves are developed for the maximum axial displacement of the SFDs and the peak SDRs of the GFS in order to interpret the performance of the LD-CBF within the framework of performance-based earthquake engineering (PBEE).

The NRHA is conducted by using two sets of 40 ground motions, which are selected from the PEER NGA-West database [169] after conducting probabilistic seismic hazard analysis for the design site. The first set is adjusted to the DBE intensity (i.e., 10% probability of exceedance in 50 years), whereas the second one is adjusted to the MCE intensity (i.e., 2% probability of exceedance in 50 years) based on the conditional mean spectrum [170–172] (CMS) of Sion (see Figs. 2.9a and 2.9b). Such a spectrum is computed through probabilistic seismic hazard analysis by using the average spectral acceleration  $Sa_{avg}$  as an intensity measure [173] (IM). Notably, the area source model of SHARE [174] is adopted and all the fault sources within 200 km from the site location are accounted for. OpenQuake (version 3.7.1) [175] is utilized to perform hazard and disaggregation analyses. In such analyses,  $Sa_{avg}$  is defined as the geometric mean of spectral acceleration values discretized in increments of 0.1 sec within the period range of 0.4 to 4.4 sec. The  $Sa_{avg}$  hazard curve of Sion is illustrated in Fig. 2.9c for reference.



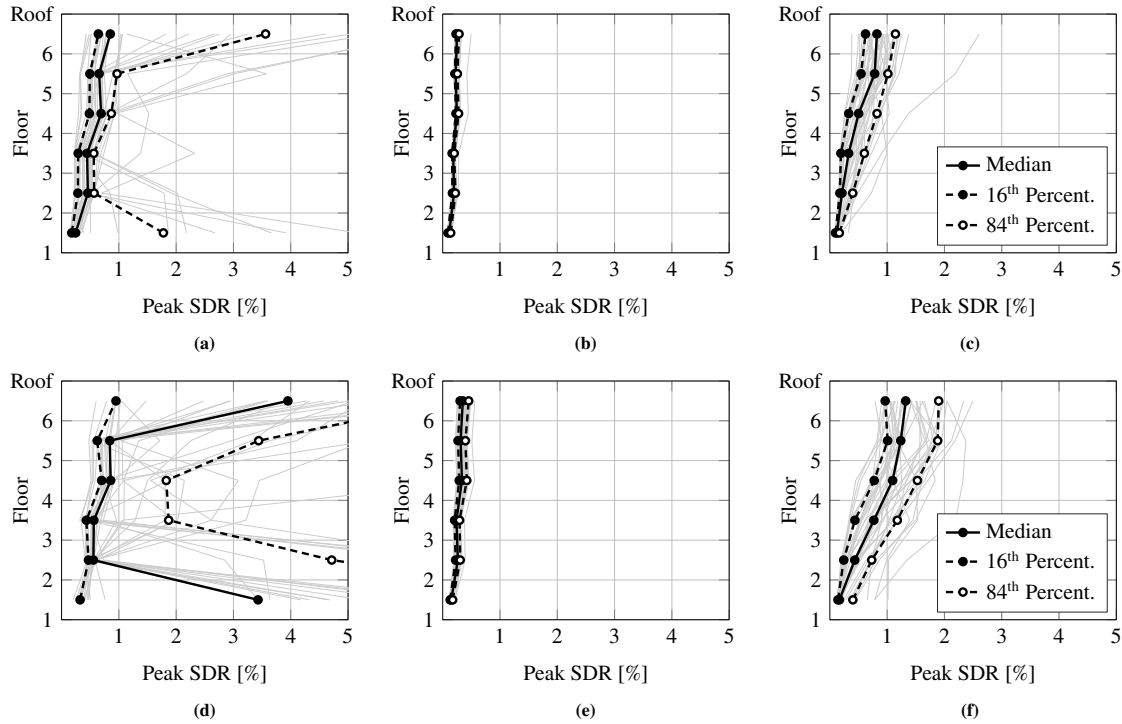


**Figure 2.10** – Peak SDRs obtained at DBE (first row) and MCE (second row) for (a),(d) the LD-CBF-R, (b),(e) the CBF of the LD-CBF and (c),(f) the GFS of the LD-CBF

### 2.6.1 Peak Story Drift Ratio Demands

Figure 2.10 illustrates the peak SDRs obtained for the LD-CBF-R and LD-CBF at DBE and MCE. It is noteworthy that for the LD-CBF-R, the CBF and GFS undergo the same peak SDRs because they are rigidly connected to each other. Referring to Fig. 2.10a, at DBE, the LD-CBF-R experiences a fairly uniform SDR median profile, which ranges within 0.25 % and 0.85 %. However, the large variability in the SDR demands observed in the 1<sup>st</sup> story suggests that the LD-CBF-R is prone to the formation of a soft story. A considerable variability in the SDR demands is also observed in the 6<sup>th</sup> story. This is due to the higher mode effects, which amplify the seismic force demands in the top stories, thereby causing damage in the CBF (e.g. fracture of the bracing-end connections). From the same figure, drift concentration within the 6<sup>th</sup> story is evident for a considerable number of ground motion records. Similar results hold true for the MCE seismic intensity (see Fig. 2.10d). However, in such a case, the SDR median profile varies within 0.55 % and 4.0 % and a significant SDR variability is observed in the seismic demands of each story.

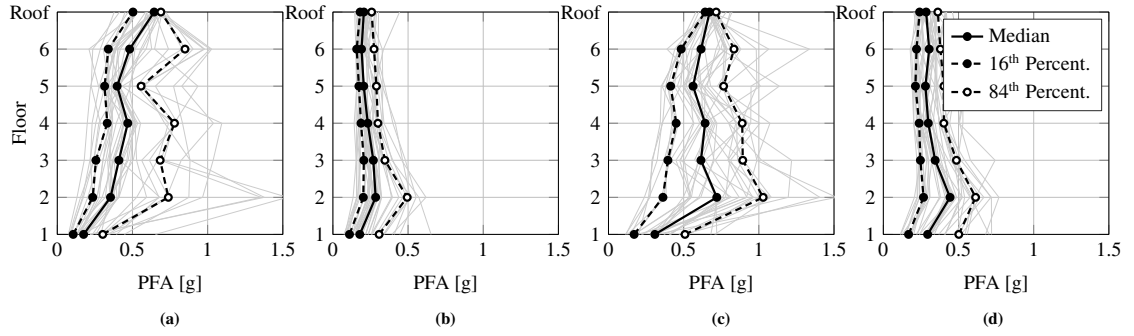


**Figure 2.11** – Peak absolute floor acceleration demands obtained at (a)-(b) DBE and (c)-(d) MCE for (a),(c) the LD-CBF-R and (b),(d) the GFS of LD-CBF

With regards to the LD-CBF, Figs. 2.10b and 2.10e depict the peak SDRs along the CBF height at DBE and MCE, respectively. At both seismic intensities, uniform peak SDRs lower than 0.5% are observed. Furthermore, the associated variability in the SDR demands is nearly zero. These results suggest that the activation forces based on the proposed methodology of Section 2.3 are effective in mitigating the higher mode effects. Moreover, the CBF remains elastic regardless of the employed q-factor. Referring to Figs. 2.10c and 2.10f, the SDR median profile of the GFS assumes values smaller than 0.80% and 1.3% at DBE and MCE, respectively. Moreover, in most of the stories, the variability of the SDR demands is fairly small compared to that of the LD-CBF-R. Additionally, no story drift concentrations are observed. Nevertheless, it is noteworthy that SDRs larger than 0.5% can damage the partition walls of a building during an earthquake [176]. Interestingly, this shortcoming can be overcome by using deformable partition walls [143–145]. In such a case, SDRs of about 1.5% can be accommodated without severely damaging the drift-sensitive non-structural components of the building [144].

## 2.6.2 Peak Absolute Acceleration Demands

Figure 2.11 depicts the PFA demands along the height of the LD-CBF-R and LD-CBF at DBE and MCE. It is noteworthy that the PFAs experienced by the CBF of the LD-CBF are negligible because most of its seismic mass is supported by the GFS. The PFA demands of the latter are depicted in Figs. 2.11b and 2.11d for the DBE and MCE seismic intensities, respectively.

At both DBE and MCE, the LD-CBF-R experiences PFA median values between 0.35 g to 0.75 g (see Figs. 2.11a and 2.11c). According to FEMA P-58-1 [177], these acceleration demands can severely damage the acceleration-sensitive non-structural compo-

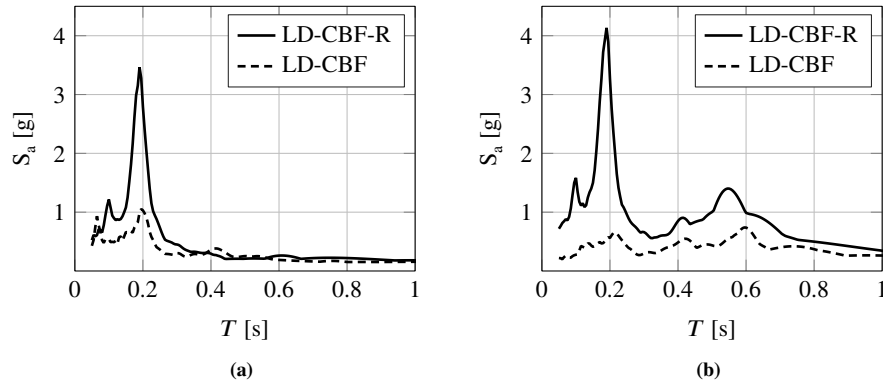


**Figure 2.12** – 5 % damped floor spectra obtained at the (a) 3<sup>rd</sup> floor and (b) roof of the LD-CBF-R and LD-CBF under the single record of the 1994 Northridge earthquake recorded at the Jensen Filter Plant station

nents of a building, thereby leading to significant earthquake-induced economic losses [20]. Interestingly, such values are reduced by more than 50 % for the LD-CBF (see Figs. 2.11b and 2.11d). The variability of the PFA demands observed at each floor of the LD-CBF-R is reduced when floor SFDs are installed between the CBF and GFS. This suggests that the SFDs allow for controlling the higher mode effects and reduce the earthquake-induced acceleration demands along the building height during earthquake shaking. In order to better illustrate this phenomenon, Fig. 2.12 shows the 5 % damped floor spectra obtained at the 3<sup>rd</sup> floor and roof of the LD-CBF-R and LD-CBF under the single record of the 1994 Northridge earthquake recorded at the Jensen Filter Plant station and scaled to the DBE seismic intensity for the design site of interest. Interestingly, the spectral acceleration demands reduce significantly near the second- (i.e.  $T = 0.55$  sec) and third-mode periods (i.e.  $T = 0.2$  sec) of the investigated buildings. This demonstrates the efficiency of the dissipative floor connectors in mitigate higher mode effects along the height of the LD-CBF-R.

### 2.6.3 Peak Story Shear Force Demands

Figure 2.13 depicts the peak story shear forces ( $V$ ) along the height of the LD-CBF-R and LD-CBF at DBE and MCE. Such values are normalized with respect to the total seismic weight ( $W$ ) of the buildings. In the same figure, it is superimposed the maximum admissible story shear ( $V_{s,max}$ ) that the LD-CBF can experience so as both the CBF and the floor diaphragms remain elastic. This limit is computed according to Eq. 2.7 by assuming  $\alpha = 0.0$ , as discussed earlier.

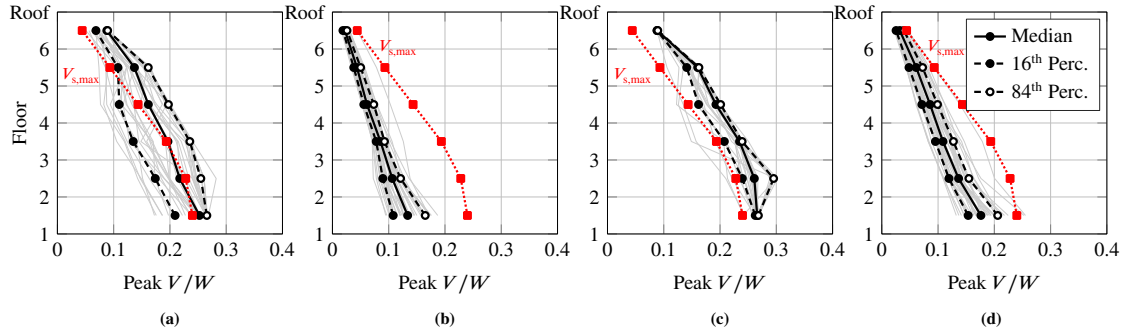


**Figure 2.13** – Normalized peak story shear forces obtained at (a)-(b) DBE and (c)-(d) MCE for (a),(c) the LD-CBF-R and (b),(d) the LD-CBF

Referring to Figs. 2.13a and 2.13c, the  $V/W$  median profile obtained for the LD-CBF-R decreases progressively along the building height by following a concave-shape pattern. This is indicative of dynamic amplifications due to higher mode effects [178, 179]. Furthermore, the peak  $V/W$  values in the LD-CBF-R exceed  $V_{s,max}$  at both seismic intensities of interest. This confirms that the LD-CBF-R exhibits inelastic behaviour during the ground motion shaking. Conversely, peak  $V/W$  values lower than  $V_{s,max}$  are obtained for the LD-CBF at DBE and MCE (see Figs. 2.13b and 2.13d), i.e. the activation forces defined according to Section 2.3 (see Fig. 2.5c) are adequate to prevent damage of the GFS diaphragms as well as the CBF. Interestingly, the median  $V/W$  profile of the LD-CBF decreases linearly along its height. This shape is characteristic to a first mode-dominant seismic behaviour. This suggests that, in the pre-design phase of the building, the seismic design forces can actually be determined through the equivalent lateral force method as discussed in EN 1998-1-1 [53] or ASCE/SEI 7-16 [146] by assuming a first mode lateral force pattern, which can generally simplify the overall seismic design process.

#### 2.6.4 Effect of assumed $q$ -factor

This section examines the peak SDR demands of the GFS as part of the LD-CBF and HD-CBF. Referring to Figs. 2.14a and 2.14b, the GFS of the HD-CBF experiences larger or equal story drift demands than those of the GFS in the LD-CBF. In particular, a maximum SDR median value of about 0.8% and 1.3% is observed for both buildings at DBE and MCE, respectively. This relates to the magnitude of the SFD activation forces. Notably, as discussed in Section 2.4.1, the LD-CBF is characterized by higher  $V_d$  and  $V_{CBF}$  values compared to the HD-CBF. As such, the activation forces  $F_s$  of the LD-CBF are about 1.3 times larger than those of the HD-CBF (see Fig. 2.5c). Figures 2.14c

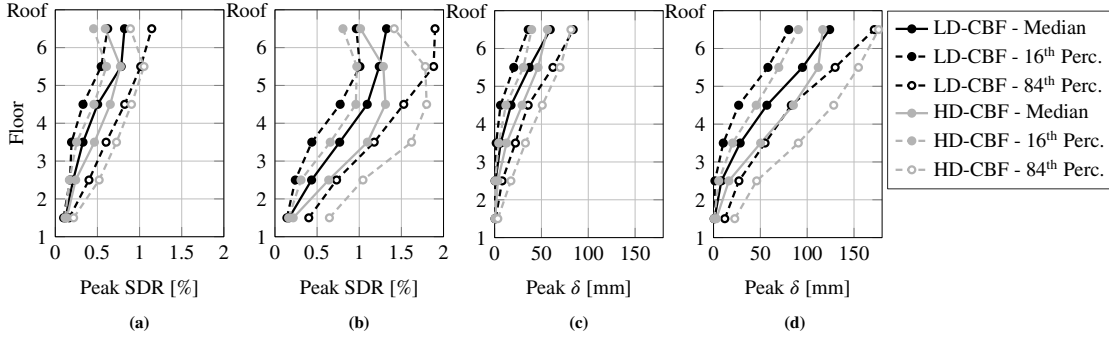


**Figure 2.14** – (a)-(b) Peak SDRs of the GFS at DBE and MCE, respectively, (c)-(d) peak axial displacements of the SFDs at DBE and MCE, respectively

and 2.14d suggest that this results in smaller axial displacements  $\delta$  for the SFDs of the LD-CBF, i.e. the GFS of the LD-CBF deflects less compared to its HD-CBF counterpart. Consequently, in the former the drift-sensitive non-structural components are less likely to experience damage (e.g. infill walls and exterior glazing) compared to the latter. Hence, the use of SFDs is more effective with low-ductility CBFs where capacity design rules are not considered. Finally, referring to Figs. 2.14c and 2.14d, the displacement capacity  $\delta_{RB}$  of the selected RBs (i.e.,  $\delta_{RB} = 380$  mm) is not exceeded in any of the studied cases.

### 2.6.5 EDP Hazard Curves

This section presents the development of characteristic EDP hazard curves to quantify the annualized maximum slot demand of the SFDs and the peak SDRs of the GFS at selected return periods of interest. Such curves are generated according to Jalayer et al. [180] by using the results obtained from the two stripe NRHA discussed earlier. Notably, a log-normal distribution is employed to represent the simulated data. A power function is utilized to describe the relationship between the median of the EDPs and the intensity measure  $Sa_{avg}$ . The corresponding EDP hazard curves are then obtained based on Eq. 2.11:

$$\lambda_{EDP}(y) = \int_x P[EDP \geq y \mid IM = x] \cdot d\lambda_{IM}(x) = \sum_x P[EDP \geq y \mid IM = x] \cdot \Delta\lambda_{IM}(x) \quad (2.11)$$

Where  $P[EDP \geq y \mid IM = x]$  is the probability that EDP exceeds  $y$  given that  $IM = Sa_{avg}$  equals  $x$ , and  $\lambda_{IM}(x)$  is the IM hazard curve of Sion (see Fig. 2.9c). It is noteworthy that the probability of exceedance  $P[EDP \geq y \mid IM = x]$  is computed by assuming that

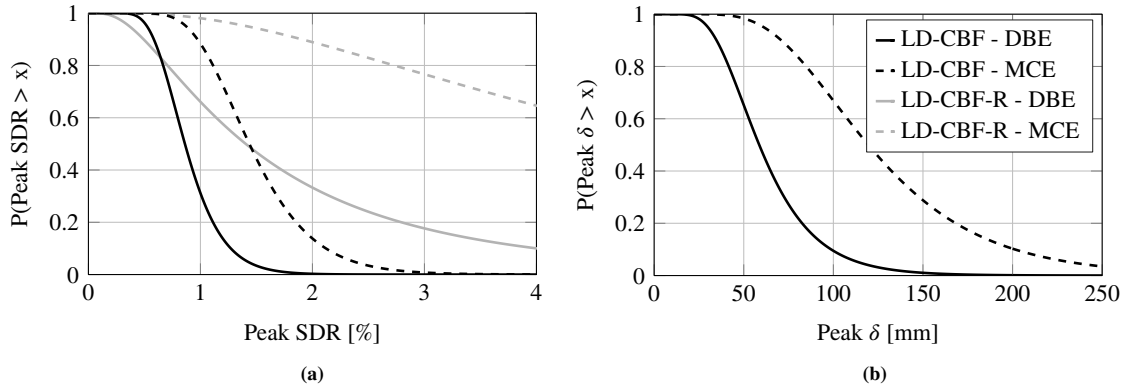


**Figure 2.15** – Exceedance functions for (a) the peak SDRs of the GFS and (b) the peak axial displacement of the SFDs

the standard deviation of each EDP is constant and equal to the average of the standard deviation obtained at DBE and MCE [181].

Figure 2.15 illustrates the probabilities of exceedance of each EDP of interest for the LD-CBF and LD-CBF-R. Referring to Fig. 2.15a, at the MCE seismic intensity, the GFS of the LD-CBF is less likely to experience a targeted peak SDR compared to the LD-CBF-R. Notably, there is a 95 % chance that the LD-CBF-R experiences a lateral drift demand of 1.5 % at MCE, whereas there is only a 45 % chance for the LD-CBF to reach this SDR demand for the same return period. At return periods corresponding to a design-basis earthquake, the results suggest that the expected SDR demands in the LD-CBF are nearly half of those with a rigid diaphragm. On the other hand, for frequently occurring seismic events (i.e., return periods of 72 years), the GFS of the LD-CBF is more likely to experience higher drift demands than its rigid diaphragm counterpart. This is attributed to the SFDs that allow for relative movement between the CBF and the GFS prior to brace buckling, which, on average, occurs at about 0.5 % for conventional CBF buildings.

Similarly, Fig. 2.15b depicts the exceedance functions of the peak  $\delta$  values. As expected, the probability that the SFDs experience a targeted  $\delta$  value is larger at MCE than at DBE. Notably, there is 10 % change that  $\delta \geq 100$  mm at DBE, whereas there is a 65 % chance to reach the same demand at MCE.

The developed EDP hazard curves are illustrated in Fig. 2.16. In the same figure, the annual rates of exceedance corresponding to three different return periods (i.e., 72, 475 and 2475 years) are superimposed. The latter have been computed by assuming that earthquakes follow a Poisson distribution over time. Table 2.2 summarizes the EDP values obtained at the three return periods of interest.

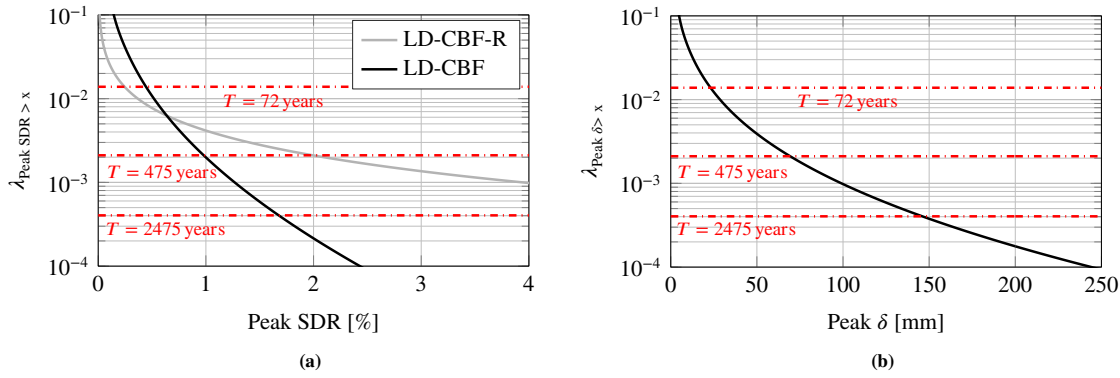


**Figure 2.16** – Hazard curves developed for (a) the peak SDRs of the GFS and (b) the peak axial displacement of the SFDs of the LD-CBF

As depicted in Fig. 2.16a, for seismic events characterized by  $\lambda_{\text{Peak SDR}} < 0.006$ , the GFS of the LD-CBF experiences smaller peak SDRs compared to those in the LD-CBF-R. In particular, Table 2.2 shows that for seismic events with a 475-years return period, the GFS of the LD-CBF deflects by 1.0 %, whereas peak SDRs of 2.0 % are observed for the rigid diaphragm case. Similar results hold true for a return period of 2475 year. Conversely, under frequent seismic events (i.e.,  $\lambda_{\text{Peak SDR}} > 0.006$ ), the GFS of the LD-CBF is prone to higher drift demands compared to the rigid diaphragm case. Restrepo and Bersofsky [176] found that partition walls are susceptible to damage at these drift levels (i.e., peak SDRs close to 0.65 %). However, this shortcoming can be overcome by enabling deformable partition walls [143–145]. On the other hand, structural damage in bracing-end connections and steel braces, which is likely to be observed at these drift amplitudes, is prevented.

Referring to Fig. 2.16b and Table 2.2, the hazard curves developed for  $\delta$  suggest that for seismic events with a return period of 475-years, a slot size of about  $2 \times 70 = 140$  mm is required. The same design parameter should be approximately doubled for a seismic event with a return period of 2475 year.

**Table 2.2** – Peak SDRs of the GFS and peak  $\delta$  values at different return periods  $T$

| Return period<br>(POE in 50 years) <sup>a</sup> | Annual rate | Peak SDRs of the GFS [%] |          | Peak $\delta$ [mm] |
|---|-------------|--------------------------|----------|--------------------|
|   |             | LD-CBF                   | LD-CBF-R | LD-CBF             |
| 72 (50 %)                                       | 0.0139      | 0.45                     | 0.25     | 23                 |
| 475 (10 %)                                      | 0.0021      | 1.0                      | 2.0      | 70                 |
| 2475 (2 %)                                      | 0.0004      | 1.7                      | > 4.0    | 150                |

<sup>a</sup> Probability of exceedance in 50 year building life expectancy

## 2.7 Limitations

The present study features a number of limitations. Notably, three-dimensional effects (both on nonlinear modeling and seismic action) were not examined. Similarly, the collapse risk assessment of mid- to high-rise steel CBF buildings equipped with floor SFDs should be examined within the framework of FEMA P695 [182] in order to identify the range of applicability of the proposed design methodology for determining the damper activation forces. In the 2D numerical models presented in this paper, the SFDs have been modelled with truss elements, whose axial force-axial displacement response is defined based on the assumption that the slot size of the SFD is sufficiently long and the preloaded bolts do not reach the limits of the slotted holes of the friction damper. It is recommended that future work addresses this issue. In that respect, the EDP hazard curves developed for the slot demands may be an effective tool to pre-design the required slotted holes of the sliding friction dampers.

With regards to the SFDs, the axial force-axial displacement response of the truss elements was defined by ignoring the variations/uncertainties in the properties of the assumed friction pads. While prior studies [69, 83, 84] have demonstrated that materials composed of fibers bounded together by phenolic resins can provide consistent friction coefficients under different operating conditions, lower/upper bound analyses may be conducted to examine this issue.

Steel CBF buildings with dissipative floor connections allow for the relative movement between the GFS and the CBF. This movement is strongly dependent to the activation forces of the SFDs and may be allowed even at frequency occurring seismic events. Within such a context, the destabilizing effects of the GFS should be further investigated. Because of differences in the construction practice of steel frame buildings and their GFS around the world, such a study should consider alternative gravity framing connections so as the influence of different strength and stiffness combinations on the dynamic response of the GFS could be comprehended.

## 2.8 Summary and Conclusions

This paper proposes a design methodology for multi-story steel CBF buildings with dissipative floor connectors between the CBF and GFS systems. In this study, sliding friction dampers were considered as dissipative floor connectors. The dampers allow for a relative in-plane displacement between the GFS and CBF systems, thereby controlling (a) the absolute floor acceleration demands, and (b) the corresponding story shear forces



along the building height so as to minimize the inelastic deformations both in the steel CBF and floor diaphragms. The seismic demand predictions were evaluated using two 6-story steel frame buildings with a low ductility and a capacity-designed CBF system, and a set of 40 ground motions that represent the seismic hazard at the design site. The results suggest that the activation forces of the sliding friction dampers determined according to the proposed methodology are effective in mitigating higher mode effects and in preventing the CBF and the floor diaphragms from experiencing inelastic behaviour regardless of the CBF-type employed. The seismic performance evaluation of the steel CBF buildings with dissipative floor connectors is contrasted with that of steel CBFs with rigid floor diaphragms. The primary findings of the paper are summarized as follows:

- The examined steel CBF buildings with rigid floor diaphragms are susceptible to drift concentrations either in their bottom or upper stories due to the highly asymmetric response of the steel braces and the challenge of the lateral load resisting system to redistribute the seismic loads. The seismic response of the same CBF buildings is characterized by high variability in the story drift ratios and peak absolute floor acceleration demands due to the strong influence of higher mode effects.
- The simulation results suggest that the SDR demands in the steel CBF buildings equipped with dissipative floor connectors remain uniform and smaller than 0.5 % even at seismic events with a return period of 2475 years. Notably, for the set of 40 seismic records, the associated variability in the SDR demands of the steel CBFs is nearly zero. As such, the primary performance objective of the proposed design methodology to minimize the inelastic demands in the steel CBF is satisfied. Moreover, capacity design in the steel CBF system is not imperative, which is an important finding.
- Nonlinear response history analyses reveal that the SDR demands in the GFS of the examined 6-story steel buildings equipped with dissipative floor connectors are, on average, 0.75 % or less at a design basis earthquake. This generally increases to about 1 % or less at seismic events with a 2475-year return period. At both seismic intensities, the maximum SDR demands occur in the upper stories, whereas in the bottom ones, the SDR demands do not exceed, on average, 0.5 %.
- Dissipative floor connectors are more effective in reducing the SDR demands in the GFS when the steel CBF system is designed with low strength reduction factors (i.e.,  $q = 2$  in this case). The reason is that the magnitudes of the activation forces in

the sliding friction dampers can be higher than those achieved in capacity-designed steel CBF systems, thereby allowing for smaller relative movement of the GFS at seismic events with return periods of 475 and 2475 years. This is an important finding for controlling damage in drift-sensitive non-structural elements.

- Unlike steel CBF buildings with rigid diaphragms, those with dissipative floor connectors enjoy a convex story shear force demand distribution along their height, which is characteristic of first-mode dominant seismic response. This suggests that, in the pre-design phase of the building, the seismic design forces can be accurately estimated through the equivalent lateral force method by assuming a first mode lateral force pattern.
- Absolute floor acceleration demands reduce by a factor of two in steel CBF buildings both at a design basis and maximum considered seismic event when dissipative floor connectors are employed. Moreover, the results demonstrate that the absolute floor acceleration demands do not exceed, on average, 0.3 g, thereby minimizing damage in acceleration-sensitive non-structural elements.

Future research should be undertaken in order to explore the implications of the lateral drift demands in the GFS so as to ensure limited damage in the drift-sensitive non-structural elements as well as the destabilizing effects of gravity loads, which are mostly carried by the GFS.

*Before the effect one believes in different causes than  
one does after the effect.*

Friedrich Nietzsche

# 3

## Influence of Gravity Connections and Damper Activation Forces on the Seismic Behavior of Steel CBF Buildings with Dissipative Floor Connectors

### *Bibliographic details*

This chapter presents the pre-print version of the article with the following full bibliographic details: Martina Paronesso and Dimitrios G. Lignos. "Influence of Gravity Connections and Damper Activation Forces on the Seismic Behavior of Steel CBF Buildings with Dissipative Floor Connectors". In: *Earthquake Engineering & Structural Dynamics* (ready for submission)

### *Authors' contribution*

Martina Paronesso, the first author of the above-mentioned paper, designed the investigated building, developed the proposed modelling approach and the simplified assessment method, construct the finite element models, carried out the nonlinear response history analysis, analysed and visualized the

simulations results, created the figures, wrote the manuscript draft and revised the manuscript. The co-author contributed in developing the methodology presented in this chapter, supervising the work conducted by Martina Paronesso, funding acquisition, and reviewing and editing the original and final manuscript drafts.

THIS CHAPTER INVESTIGATES the influence of typical gravity connections on the seismic demands of steel concentrically braced frame (CBF) buildings with friction dampers as dissipative floor connectors. The investigated connections include (i) typical shear tab, (ii) clip angle, (iii) flush end-plate and (iv) shear tab connections with bottom T-stub. It is shown that the seismic behavior of the gravity framing system (GFS) is practically insensitive to the gravity connection type because the supplemental damping provided by the dissipative floor connectors dominates the seismic response of the GFS. While flush end-plate and shear tab connections with bottom T-stub generally exhibit smaller rotational demands than more flexible gravity connections, the resultant lateral drift demands in the GFS are more-or-less identical in all cases due to the elastic contribution of the gravity columns. A simplified method is also proposed to evaluate the influence of the damper activation forces on the seismic response of multi-story CBF buildings equipped with floor sliding friction dampers. First, the building is transformed into an equivalent single-degree-of-freedom system. Subsequently, dual graphics called P-spectra are generated through nonlinear response history analysis. These graphics allow to estimate the peak floor absolute acceleration demands and peak/residual roof displacements of the GFS as a function of the activation forces of the sliding friction dampers. An application example demonstrates that the proposed method can be reliably employed in a pre-design phase to identify the range of damper activation forces through which an optimal performance of the steel CBF building may be anticipated.

### 3.1 Introduction

Dissipative floor connectors in frame buildings allow for relative movement between the lateral load resisting system and the gravity framing system (GFS). Such connectors can feature hysteretic devices [71, 131], steel plate connections [132, 134], non-tearing systems with re-centering properties [133], buckling restrained braces [68] as well as viscous [64, 65] and sliding friction dampers [69, 85]. Experimental [68, 69] and numerical [65, 85] studies have revealed that the dissipative floor connectors are effective in (i) reducing

floor absolute acceleration demands, (ii) preventing story drift concentrations and (iii) mitigating higher mode effects during earthquake loading. In a recent study, Paronesso and Lignos [85] found that the story drift demands in the GFS of steel concentrically braced frame (CBF) buildings with dissipative floor connectors are higher than those in the rigid diaphragm counterparts for frequently occurring earthquake events. This suggests that the destabilizing effects of gravity may be increased in this case. Furthermore, damage in the drift-sensitive non-structural components of the building may be a critical consideration during frequently occurring earthquake events.

The role of the GFS on the seismic performance of steel frame buildings has been mostly explored in cases where it is rigidly connected to the lateral load resisting system. Notably, prior numerical studies carried out on steel moment resisting frame [159, 166, 183–186] (MRF) and CBF [20, 187, 188] buildings with conventional shear tab connections suggest that the lateral strength and stiffness of the GFS generally reduces the likelihood of story drift concentrations during seismic events with a low probability of occurrence. Experiments [189] have also revealed that the elastic stiffness of a GFS with conventional shear tab connections is at least twice larger than what is recommended in ASCE 41-17 [190]. This would naturally influence the relative movement of the GFS in buildings with dissipative floor connectors. However, this issue deserves more attention because the beam-to-column connection types and the beam geometries in the GFS could vary.

Comprehensive studies on earthquake life-cycle assessment of steel MRF and CBF buildings [20, 191] have pointed out that expected annual losses due to building demolition may be overestimated even up to 50 % when the GFS is neglected in the nonlinear building models. Furthermore, in prior studies [184, 186] it was shown that the use of partially restrained gravity connections as well as the orientation of the gravity columns increases the system overstrength and deformation capacity of the steel frame buildings. Same findings hold true from field observations conducted after the 1994 Northridge earthquake [192], which revealed that although steel MRF and CBF systems in buildings were severely damaged, these did not collapse due to the reserve capacity provided by the GFS. Nevertheless, to the best of the authors' knowledge, no research has been undertaken to further comprehend the effects of the mechanical characteristics (i.e., strength, stiffness and plastic deformation capacity) of partially restrained gravity connections on the lateral drift demands of buildings equipped with dissipative floor connectors.

In buildings with dissipative floor connectors, the relative movement between the lateral load resisting system and the GFS is strongly influenced by the activation forces of such connectors. To optimally select these forces, parametric studies via nonlinear

response history analysis (NRHA) are required. In this case, several iterations may be necessary to identify the range of connector properties/characteristics that satisfy multiple seismic performance objectives (e.g. targeted limits on peak floor acceleration demands and story drift ratios). Within such a context, Guo and Christopoulos [51, 193] developed a simplified approach called the performance spectra method, which allows for the preliminary damper design in multi-story buildings equipped with hysteretic/viscous devices. A graphical design tool called P-spectra can be used to relate multiple story-based engineering demand parameters (EDPs) (e.g. total base shear force and absolute peak/residual roof drift) to the selected damper properties. Therefore, a comparison between different damping strategies can be performed at a viable computational cost [194]. An analogous approach should be developed for the pre-design of buildings equipped with dissipative floor connectors.

The scope of this study is twofold. Firstly, a general modelling approach is developed for simulating the nonlinear hysteretic response of a broad range of partially restrained gravity connections as part of a typical GFS. The modelling approach is validated to available experimental data on these connection types. It is then used to quantitatively assess the seismic demands of steel CBF buildings with floor sliding friction dampers (SFDs). The GFS is comprised of different types of beam-to-column gravity connections. Emphasis is placed on the effectiveness of the considered connections in limiting the lateral drift demands in the GFS. Secondly, a P-spectra method is developed, which is specifically tailored for steel CBF buildings with SFDs as dissipative floor connectors. The simplified method is employed to identify the range of activation forces up to which the SFDs are effective in minimizing lateral drift demands in the GFS as well as other story-based EDPs of interest for earthquake damage control. The accuracy of the proposed method is verified and discussed through an application example of a 6-story steel CBF building equipped with floor SFDs.

## 3.2 Considered Beam-to-Column Gravity Connections

Referring to Fig. 3.1, typical gravity framing beam-to-column connections feature (a) conventional shear tab, (b) clip angle, (c) flush end-plate, and (d) shear tab connections with a bottom T-stub. While the use of conventional shear tab and clip angle connections is typical in North America, in Europe flush end-plate connections are more common.

The subsequent section provides a summary of the primary behavioural characteristics of the above-mentioned connections with emphasis on their primary failure modes. The proposed approach for modelling their monotonic and cyclic hysteretic behavior in

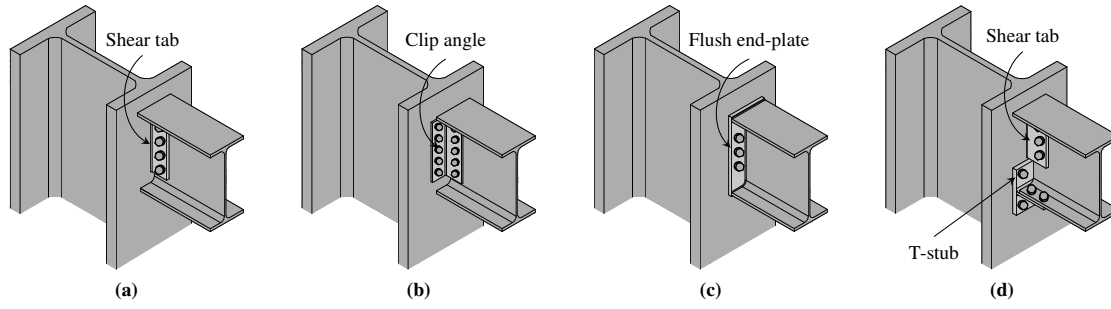


**Figure 3.1** – Sketch of the investigated beam-to-column gravity connections: (a) shear tab connection, (b) clip angle connection, (c) flush end-plate connection, (d) shear tab connection with bottom T-stub

terms of moment-chord rotation (i.e., rotation over the length of the respective member) response is also presented.

### 3.2.1 Behavioural Insights

Referring to Fig. 3.1a, conventional shear tab connections consist of a single steel plate (i.e., shear tab), which is welded to the column profile and bolted to the beam web. In design practice, shear tab connections are generally idealized as pinned. However, prior studies [195–198] have demonstrated that in the presence of a concrete floor slab, such connections can resist bending moments on the order of 30 to 45 % of the plastic resisting moment ( $M_p$ ) of the respective bare steel beam. Liu and Astanekh-Asl [196] demonstrated that the flexural capacity of shear tab connections depends on their geometry as well as on the damage mechanisms controlling their design. Notably, under positive bending moments (i.e. slab in compression), these connections may exhibit (i) net section fracture of the shear tab or beam web, (ii) shear fracture of the bolts or weld, (iii) bearing failure of the bolt holes on the shear tab or beam web, and (iv) crushing of the concrete slab against the column face. Except the latter, the rest of the failure modes are also anticipated under negative bending moments (i.e. slab in tension).

Clip angle connections consist of double steel angles bolted or welded to the column and beam profiles (see Fig. 3.1b). Similarly to the shear tab connections, the clip angle connections are usually assumed to be pinned. Nevertheless, experimental studies conducted on bare clip angle connections [199–202] (i.e. without a concrete floor slab) revealed that the latter can achieve a modest flexural resistance (i.e, between 10 % and 20 % of the plastic resisting moment  $M_p$  of the respective bare steel beam). This value is approximately doubled in the presence of a concrete floor slab [202, 203]. Experiments [200–202] suggest that the typical failure mechanism observed in clip angle

connections is strongly related to the thickness of the steel angles as well as the gage distance (i.e., distance between the bolt line and the heel of the angle). Depending on these two quantities, clip angle connections can experience flexural yielding of the angles [202]. Other failure modes involve concrete crushing of the slab, bolt failure due to combined tension and shear, as well as bearing failure of the bolt holes on the beam web.

Referring to Fig. 3.1c, flush end-plate connections consist of a steel plate welded to the end of the beam and bolted to the column face. Prior experimental studies [204–207] have demonstrated that flush end-plate connections are characterized by a higher elastic rotational stiffness and flexural capacity than those of shear tab and clip angle connections. Notably, bare flush end-plate connections can resist to bending moments larger than 30 % of the plastic resisting moment  $M_p$  of the steel beam [206, 208]. In the presence of a composite floor system, flexural resistances larger than 65 %  $M_p$  may be achieved when deep steel beams (i.e., beam depth larger than 350 mm) and/or high reinforcement ratios (i.e., larger than 1.0 %) are employed [204–206]. Lower values of flexural resistance are generally attained with shallower steel beams and reinforcement ratios lower than 0.5 % [208]. The flexural capacity of these connections is controlled by tensile fracture of the structural bolts, flexural yielding of the steel flush end-plate, crushing of the slab against the column profile and/or reinforcement yielding [204–206, 208].

Figure 3.1d depicts the forth beam-to-column connection investigated in this study. It comprises a shear tab connection with a bottom T-stub. The T-stub connects the bottom flange of the beam to the column profile through bolts. The center of rotation of the bare shear tab connection is therefore moved downwards in the presence of the T-stub. As a result, the moment arm of the connection is increased and higher values of flexural capacity as well as rotational stiffness are attained compared to the one depicted in Fig. 3.1a. In particular, cyclic loading tests conducted on shear tab connections with bottom T-stub [209] have showed that in the presence of a concrete floor slab and deep steel beams (i.e., beam depth larger than 350 mm), these connections are able to achieve bending moments larger than 70 % of the plastic resisting moment  $M_p$  of the bare steel beam. Similar results hold true for connections composed of top and/or seat steel angles [203, 204, 210]. Similarly to flush end-plate connections, smaller values of flexural resistance are generally attained when shallower steel beams and/or reinforcement ratios lower than 0.5 % are employed [204]. Green et al. [209] found that under positive and negative bending moments, the T-stub is subjected to tensile and compressive forces, respectively, which can lead to a plethora of failure modes, including (i) net section fracture of the T-stub web, (ii) yielding of the T-stub, (iii) shear or tensile fracture of



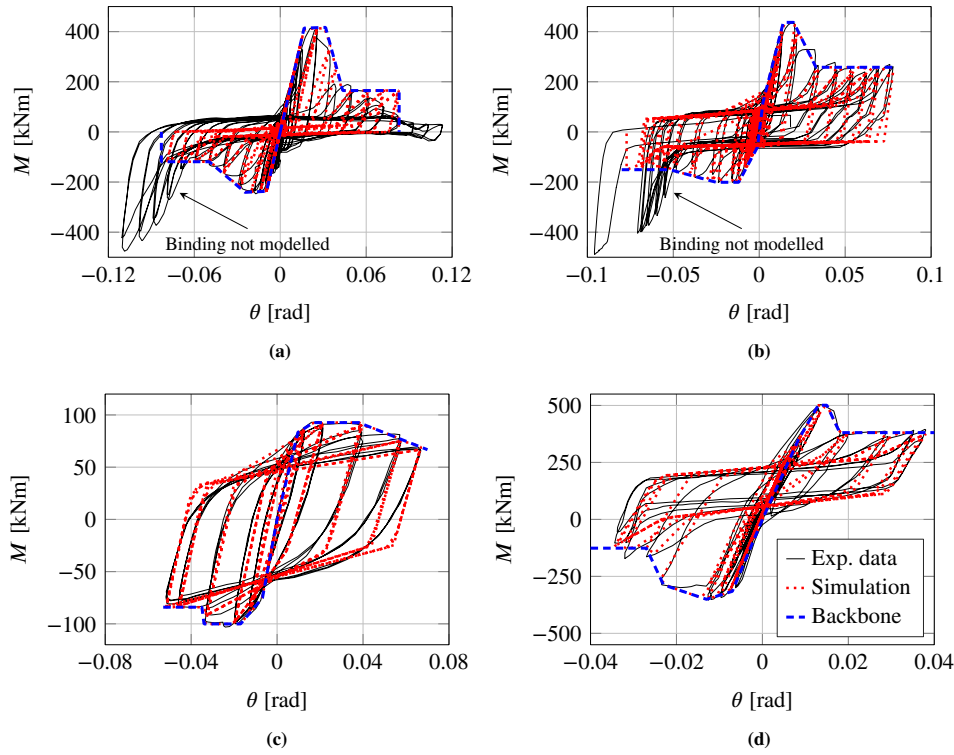


**Figure 3.2** – Calibration of the moment-rotation response of the beam-to-column connections by using the Pinching4 model available in OpenSees: (a) shear tab connection (specimen 6A [159, 198]) (b) clip angle connection (specimen S-HA [202]), (c) flush end-plate connection (specimen CJ4 [208]), (d) shear tab connection with T-stub (east beam [209])

the bolts, and (iv) bearing failure of the bolt holes on the T-stub web or beam flange. Concrete crushing and reinforcement yielding are additional failure mechanisms that can occur in the presence of a concrete floor slab.

The behavioural insights from the four investigated gravity connections suggest that they share some common behavioral characteristics. However, as Fig. 3.2 shows, their hysteretic moment-rotation response exhibits some notable differences. For instance, in the presence of a concrete floor slab, pinching characterizes the cyclic behavior of clip angle and shear tab connections with and without bottom T-stub (see Figs. 3.2a, 3.2b and 3.2d). Conversely, flush end-plate connections exhibit a peak-oriented hysteretic response (see Fig. 3.2c), which generally leads to a higher energy dissipation than the other examined connections.

Referring to Fig. 3.2, the cyclic behavior of each connection is generally controlled by bolt slip at  $\theta \leq 0.01$  rads, concrete cracking and crushing, yielding of the connection components and/or of the reinforcing bars of the slab. In particular, under positive

bending moment, flexural strength degradation as a result of concrete crushing is evident in all cases. Furthermore, an asymmetric cyclic behavior is observed due to the presence of the concrete floor slab. With regards to the shear tab and clip angle connections, connection stiffening due to beam binding can occur under cyclic loading (see Figs. 3.2a and 3.2b). This causes an increase of flexural demands, which in turn can lead to potential plastification in the steel columns of the GFS [159].

Figure 3.2 clearly shows that, depending on the connection type, its rotational stiffness and the flexural resistance may vary considerably with potential implications on the deformation demands of the GFS. In the subsequent section, a modelling approach is proposed for each gravity connection type discussed earlier.

### 3.2.2 Proposed Modelling Approach of Beam-to-Column Gravity Connections

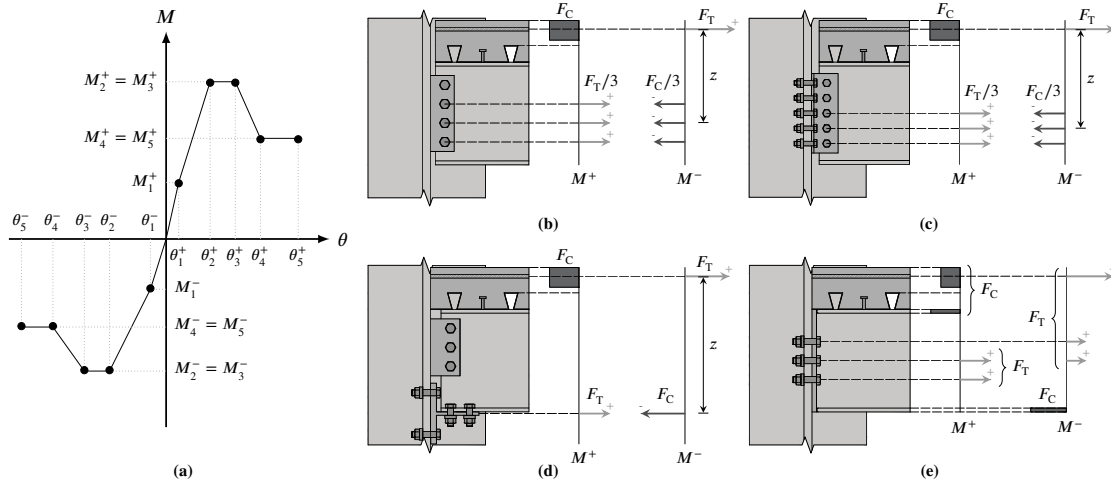
The modelling approach of a typical gravity connection includes (a) its monotonic backbone curve, and (b) its hysteretic relationship under cyclic loading.

Figure 3.3a illustrates the input parameters to define the backbone curve of the four considered connections in terms of their moment-chord rotation ( $M - \theta$ ) in the presence of a concrete floor slab. Notably, five  $M - \theta$  values are used to determine the stages at which each connection (i) experiences inelastic behavior due to bolt slip and concrete cracking ( $M_1, \theta_1$ ), (ii) attains its peak flexural capacity ( $M_2, \theta_2$ ), (iii) undergoes flexural strength degradation due to concrete crushing or steel reinforcement yielding ( $M_3, \theta_3$ ), (iv) attains its residual flexural resistance ( $M_4, \theta_4$ ), and (v) reaches its ultimate limit state, i.e. a zero flexural capacity ( $M_5, \theta_5$ ).

The flexural capacity ( $M_{\max}$ ) of each connection depends on the maximum force couple that can be resisted under positive and negative bending moment:

$$M_{\max} = \min\{F_T, F_C\} \cdot z \quad (3.1)$$

where  $F_T$  and  $F_C$  are the maximum tensile and compressive forces, respectively, that the connection can sustain under bending moment, and  $z$  is the lever arm between  $F_T$  and  $F_C$ . It is noteworthy that the magnitude of  $F_T$  and  $F_C$  is bounded by the capacity of the weakest component subjected to these forces. Figures 3.3b - 3.3e illustrate the force distributions for determining the flexural capacity of the four considered gravity connections. In all cases, the concrete floor slab is assumed to be a typical profiled steel deck with ribs running perpendicular to the beam profile. Referring to Figs. 3.3b-Fig. 3.3d, under negative bending moments ( $M^-$ ),  $F_T$  is merely limited by the tensile



**Figure 3.3** – (a) Definition of the backbone curve of gravity connections ( $M^+, \theta^+$ : values attained under positive bending moment;  $M^-, \theta^-$ : values attained under negative bending moment), (b)-(e) sketches of the force distribution considered to determine the flexural capacity  $M_{\max}$  of the (b) shear tab connection, (c) clip angle connection, (d) shear tab connection with T-stub, (e) flush end-plate connection

resistance of the reinforcing bars of the slab\*. Conversely,  $F_C$  assumes different values depending on the connection type. Notably, in the case of shear tab and clip angle connections,  $F_C$  acts on the bolts located on the lower part of the shear tab and clip angles respectively [198, 202] (see Fig. 3.3b and 3.3c). Therefore, its value is limited by shear/tensile resistance of the bolts, bearing failure of the bolt holes or net section fracture of the shear tab/clip angles<sup>†</sup> (see Section 3.2.1). Conversely, in a shear tab connection with a bottom T-stub,  $F_C$  is resisted by the T-stub [195] (see Fig. 3.3d). Hence, the magnitude of  $F_C$  is limited by the capacities of this element and the bolts used to connect it to the beam/column profiles (see Section 3.2.1). Similar considerations hold true when the clip angle and shear tab connections with/without T-stub are subjected to a positive bending moment ( $M^+$ ). However, in such a case,  $F_C$  is limited by the concrete crushing of the slab against the column profile [195, 198, 202]. Referring to Figs. 3.3b-Fig. 3.3d, it is noteworthy that the bolts located on the upper part of the shear tab and clip angles carry the design shear forces.

With regards to the flush end-plate connections, the force distributions illustrated in Fig. 3.3e under  $M^-$  and  $M^+$  correspond to the cases where the plastic neutral axis of

\*The tensile resistance of the concrete slab is neglected as well as the tensile resistance of the metal decking because it lies perpendicular to the steel beam [206]

<sup>†</sup>With regards to the shear tab and clip angle connections investigated in this study,  $F_C$  is limited by the bearing failure of their bolt holes.

the connection is located in the bottom and upper flange of the steel beam, respectively. Other case studies are discussed by Heong [206]. It is also noteworthy that as per EN 1993-1-8 [150], it is assumed that all the bolt-rows of the investigated flush end-plate connections develop their full plastic capacity under  $M^-$  and  $M^+$ . Referring to Fig. 3.3e, under negative bending moment,  $F_T$  is limited by the tensile resistance of the reinforcing bars of the slab and the bolts located on the upper part of the steel flush end-plate [206]. The additional bolts are used to carry the design shear forces, whereas  $F_C$  is resisted by the bottom flange of the beam profile [206]. Conversely, under positive bending moment,  $F_C$  is resisted by the concrete slab and top flange of the beam, whereas  $F_T$  is carried by the bolts located on the bottom part of the steel flush end-plate [206].

Referring to Fig. 3.3a, the bending moments  $M_2^+ = M_3^+$  and  $M_2^- = M_3^-$  equal the flexural capacity  $M_{\max}$  of each connection, which is determined based on the force distributions depicted in Figs. 3.3b - 3.3e. With regards the remaining parameters, their values are calibrated to the experiments listed in Table 3.1 (see Fig. 3.2). It is noteworthy that the parameters presented in this table are dependent on the connection and composite floor geometries. However, they represent typical ranges of steel beam depths (i.e., from 300 mm to 600 mm) and composite slab thicknesses (i.e., from 80 mm to 170 mm) seen in a conventional GFS. The experimental data [198, 202, 208, 209] that was employed for the calibration of the plastic deformation parameters presented herein are deemed representative for the above geometric ranges.

Referring to Table 3.1, the bending moments defining the backbone curve of each connection are reported as a function of  $M_{\max}$  so as their values can be readily adjusted according to the selected connection type. Furthermore, as Figs. 3.2a, 3.2b and 3.3a show, connection stiffening due to beam binding is not considered in the present study. The reason is that this phenomenon can be delayed if the distance between the beam flange-to-column face is appropriately designed (i.e., usually a minimum distance of about 10 mm suffice for steel beams with depths of 300 mm or less). For instance, for the case-study building discussed in Section 3.3, beam binding does not occur at chord rotations  $\theta < 0.08$  rads. Alternatively, the approach presented in Elkady and Lignos [159] may be used to explicitly consider binding, if necessary.

Figure 3.4 illustrates the moment-chord rotation backbone curve of the investigated connection types. Notably, each connection is characterized by an asymmetric  $M - \theta$  backbone curve due to the presence of the concrete floor slab. In particular, under positive and negative bending moments, bolt slip and concrete cracking occur at  $\theta_1$  rotations smaller than 0.1%. For  $\theta_2$  rotations larger than 1.2%, the connections reach their flexural capacity ( $M_{\max}$ ). Residual flexural moments larger than 35% of  $M_{\max}$  are

**Table 3.1** – Calibrated moment-chord rotation parameters of the backbone curve of the beam-to-column connections illustrated in Fig. 3.1

| Connection type    | Experimental study<br>(specimen ID) | Chord rotations <sup>a,d</sup> [rad] |                  |                  |                  | Moments <sup>b,e</sup>   |                        |                        |
|--------------------|-------------------------------------|--------------------------------------|------------------|------------------|------------------|--------------------------|------------------------|------------------------|
|                    |                                     | $\theta_1$                           | $\theta_2$       | $\theta_3$       | $\theta_4$       | $\frac{M_1}{M_{\max}^c}$ | $\frac{M_3}{M_{\max}}$ | $\frac{M_4}{M_{\max}}$ |
| Shear tab          | Liu et al. [198] (3A)               | 0.004<br>(0.003)                     | 0.020<br>(0.012) | 0.039<br>(0.030) | 0.040<br>(0.063) | 0.25<br>(0.30)           | 1.0<br>(1.0)           | 0.5<br>(0.5)           |
| Clip angle         | Donahue [202] (S-HA)                | 0.002<br>(0.002)                     | 0.014<br>(0.012) | 0.020<br>(0.025) | 0.033<br>(0.052) | 0.27<br>(0.33)           | 1.0<br>(1.0)           | 0.59<br>(0.75)         |
| Flush end-plate    | Shi et al. [208] (CJ4)              | 0.010<br>(0.007)                     | 0.017<br>(0.017) | 0.038<br>(0.034) | 0.08<br>(0.035)  | 0.90<br>(0.75)           | 1.0<br>(1.0)           | 0.59<br>(0.84)         |
| Shear tab & T-stub | Green et al. [209] (east beam)      | 0.008<br>(0.007)                     | 0.013<br>(0.013) | 0.015<br>(0.023) | 0.018<br>(0.027) | 0.70<br>(0.90)           | 1.0<br>(0.82)          | 0.76<br>(0.36)         |

<sup>a</sup> The values enclosed in brackets indicate the rotations defining the negative branch of the backbone curve (i.e.,  $\theta_1^-$ ,  $\theta_2^-$ ,  $\theta_3^-$  and  $\theta_4^-$ )

<sup>b</sup> The values enclosed in brackets indicate the moments defining the negative branch of the backbone curve (e.g.  $M_1^-/M_{\max}^-$ )

<sup>c</sup> Flexural capacity of the connection under positive ( $M_{\max}^+$ ) and negative ( $M_{\max}^-$ ) moment

<sup>d</sup> For each connection,  $\theta_5^+ = \theta_5^- = 0.08$

<sup>e</sup> For each connection,  $M_2^+/M_{\max}^+ = M_2^-/M_{\max}^- = 1.0$  and  $M_5 = M_4$

subsequently attained at  $\theta_4$  rotations, which vary considerably depending on the assumed connection type. The residual moment is sustained until the connection loses its load carrying capacity (i.e.,  $\theta_5 = 0.08$ ).

Referring to Fig. 3.4, the  $M$ - $\theta$  response of the shear tab connection is fairly similar to the one with clip angles. Under negative and positive bending moments, the flexural capacity of both connections is, respectively, on the order of 12 % and 18 % of the plastic resisting moment  $M_p$  of the bare steel beam of the GFS investigated in the present study. Interestingly, the shear tab connection with bottom T-stub attains a flexural capacity about 1.5 times higher than the two connections discussed earlier. Similarly, the flush end-plate connection attains  $M_{\max}^+$  and  $M_{\max}^-$  values between 25 % and 30 % of  $M_p$ . According to EN 1993-1-8 [150] provisions, this implies that the flush end-plate and shear tab connections with bottom T-stub can be categorised as partial-strength, whereas the other two may be classified as nominally pinned. Furthermore, the elastic rotational stiffness of each connection is at least  $0.8EI_{\text{beam}}/L_{\text{beam}}$ , where  $L_{\text{beam}}$  and  $I_{\text{beam}}$  are, respectively, the span and second moment of area of the steel beam of the GFS studied in Section 3.3. This suggests that all the investigated connections may be classified as semi-rigid [150] based on their rotational stiffness. In particular, the elastic rotational

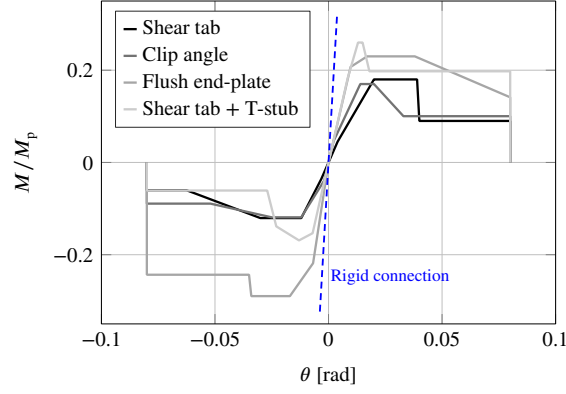


**Figure 3.4** – Moment-chord rotation backbone curve of the gravity connections normalized with respect to the plastic resisting moment ( $M_p$ ) of the steel IPE 270 beam (i.e., equivalent to W10x26 American wide flange beam) of the GFS under investigation

stiffness of the flush end-plate connection is between 1.5 to about 3 times higher than the one of the others.

Referring to Fig. 3.2, most of the gravity connections discussed herein exhibit pinching under cyclic loading. The flush end-plate connections exhibit a peak-oriented hysteretic response; hence, under cyclic loading, the moment-rotation behavior of all the examined connection types can be simulated accurately by using the Pinching4 material model [211], which is available in the Open System for Earthquake Engineering Simulation (OpenSees) Platform [153]. Six input model parameters should be defined in this case. Notably, the parameters  $rDisp/rForce$  define the ratio between the chord rotation/moment at which reloading begins and the maximum chord rotation/moment attained during the previous loading cycle. Similarly, the parameter  $uForce$  defines the ratio between the flexural strength developed upon unloading from negative/positive load and the maximum flexural strength attained under monotonic loading. Finally, the parameters  $gFLim$ ,  $gKLim$  and  $gDLim$  are used to control the cyclic degradation in flexural strength, reloading and unloading stiffness of each connection type, respectively.

Table 3.2 summarizes the parameters of the Pinching4 model after calibration to the respective experimental data (see Fig. 3.2). It is noteworthy that the  $rDisp/rForce$  parameters defined for the flush end-plate connection are set to 1.0 in both loading directions because a peak-oriented hysteretic response is more representative in this case (see Fig. 3.2). The examined test results suggest that the cyclic response of the connections does not exhibit in-cycle strength degradation for  $\theta < \theta_3$ . Therefore,  $gFLim$  is set to zero in all cases. With regards to the clip angle and shear tab connections with/without bottom T-stub, pinching is observed in both loading directions. This is mostly caused by

**Table 3.2** – Calibrated parameters of the Pinching4 model to simulate the strength and stiffness degradation of the gravity connections illustrated in Fig 3.1

| Connection type    | Experimental study<br>(specimen ID) | $rDisp^+$ | $rDisp^-$ | $rForce^+$ | $rForce^-$ | $uForce^+$ | $uForce^-$ | $gKLim$ | $gDLim$ | $gFLim$ |
|--------------------|-------------------------------------|-----------|-----------|------------|------------|------------|------------|---------|---------|---------|
| Shear tab          | Liu et al. [198]<br>(3A)            | 0.40      | 0.50      | 0.20       | 0.50       | 0.0        | 0.0        | 0.0     | 0.0     | 0.0     |
| Clip angle         | Donahue [202]<br>(S-HA)             | 0.62      | 0.85      | 0.42       | 0.40       | 0.20       | 0.25       | 0.0     | 0.08    | 0.0     |
| Flush end-plate    | Shi et al. [208]<br>(CJ4)           | 1.0       | 1.0       | 1.0        | 1.0        | 0.48       | 0.30       | 0.14    | 0.03    | 0.0     |
| Shear tab & T-stub | Green et al. [209]<br>(east beam)   | 0.65      | 0.65      | 0.70       | -0.05      | 0.50       | -0.90      | 0.30    | 0.10    | 0.0     |

(i) slippage between the steel components, and (ii) opening and closure of the concrete cracks in the slab. In the case of clip angle and shear tab connections with bottom T-stub, pinching may be also attributed to formation of a gap between the clip angles/T-stub and the column face during loading.

### 3.3 Case Study Building

#### 3.3.1 6-story steel Building with Friction Dampers as Dissipative Floor Connectors

Figure 3.5a illustrates the plan view of the 6-story steel building investigated in this study. It consists of 3-bay steel MRFs in the East-West (E-W) loading direction and two perimeter CBFs in the North-South (N-S) direction. In the N-S direction, the diaphragms of the GFS are connected to the steel columns of the CBFs through SFDs. Referring to Fig. 3.5c, such devices dissipate energy when they attain their activation force  $F_s$ . In addition to the SFDs, laminated rubber bearings (RBs) are installed between the columns of the CBF and the primary beams of the GFS (see Fig. 3.5d). The RBs are used to provide out-of-plane stability to the CBF as discussed by Tsampras et al. [67, 69]. In fact, the axial stiffness of the RBs is significantly higher than their shear stiffness ( $K_{RB}$ ). Hence, they enable in-plane relative motion between the CBF and the GFS. In particular, under shear deformation, the RBs exhibit a linear elastic response as schematically shown in Fig. 3.5d.

The prototype steel building is designed according to the European provisions [53, 149] for an importance class II and a behavior factor  $q = 2.0$  (i.e., equivalent to a strength

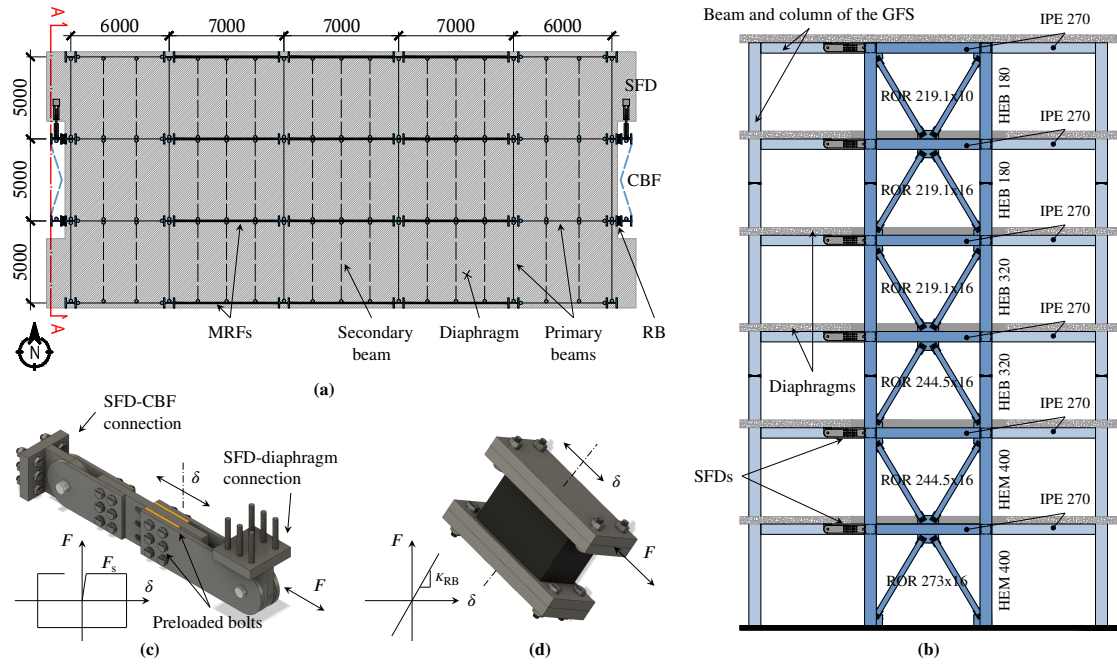


**Figure 3.5** – Configuration of the 6-story steel building equipped with floor SFDs in the N-S direction: (a) plan view, (b) elevation view (section A-A), (c) sliding friction damper, (d) rubber bearing

reduction factor in the US). According to EN 1998-1-1 [53], the CBF system may be designed without capacity design considerations. Paronesso and Lignos [85] demonstrated that the lack of capacity design does not compromise the seismic performance of the building because the activation forces of the floor SFDs are selected so as to prevent inelastic deformations in the CBF system. By assuming a relatively low behavior factor, higher activation forces may be used in the dampers, thereby limiting the SDR demands in the GFS [85].

The design location of the investigated building is situated in Sion (Switzerland), in a region characterized by a soil type D and a reference peak ground acceleration ( $a_{gR}$ ) of 0.22 g. The design seismic forces are determined through modal response spectrum analysis by assuming that the GFS and the CBFs are rigidly connected to each other. Figure 3.5b illustrates the elevation view of the steel CBF and its member sizes. All the members (e.g. columns, beams and braces) are fabricated from S355J2 steel (nominal yield stress,  $f_y = 355$  MPa). The floor diaphragms consist of profiled steel decks with ribs running in the E-W direction (i.e., perpendicular to the primary beams of the CBFs). Their reinforcement ratio is about 0.5 %.



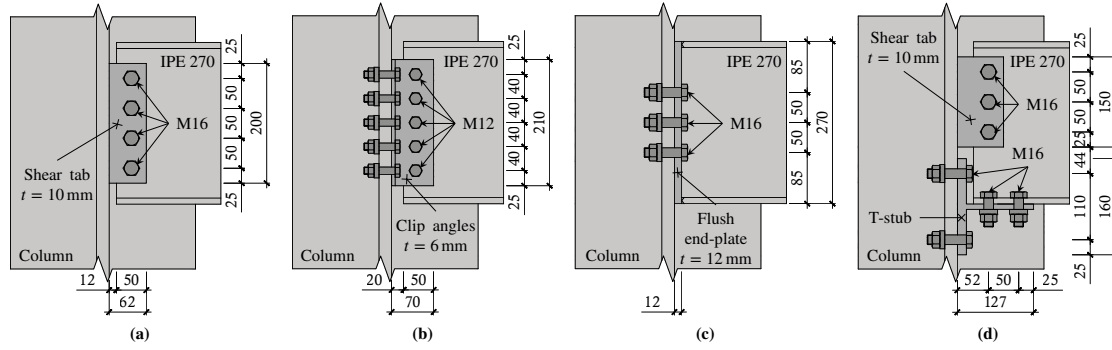


**Figure 3.6** – Beam-to-column connections designed for the GFS of the 6-story steel building: (a) shear tab connection, (b) clip angle connection, (c) flush end-plate connection, (d) shear tab connection with T-stub

Referring to Fig. 3.5a, columns are oriented around their weak axis in the N-S direction and they are spliced at stories 3 and 5. The MRFs in the E-W direction feature steel beams with stiffened end-plate connections. In the N-S direction, the CBF beams are connected to the column profiles through shear tab connections. With regards to the GFS, four different connection types are investigated as discussed in Section 3.2. A sketch of these connections is depicted in Fig. 3.6. Their design is compliant to the EN 1993-1-8 [150] provisions. In brief, these connections are designed against (i) yielding and net section fracture of any element connecting the beam web to the column face, (ii) bolt failure due to shear or combined tension and shear, (iii) bearing failure of the bolt holes, and (iv) block tearing. The bolted bracing-end connections shown in Fig. 3.5b are also designed according to EN 1993-1-8 [150]. Their design is mainly governed by local buckling of the gusset plate under compression and net section fracture of the gusset plate or the bracing member(s) under tension. Referring to Fig. 3.6a, a gap distance of 12 mm is left between the beam end and the column face in order to prevent beam binding under chord rotations smaller than 0.08 rads. Such a gap is increased to 20 mm for the clip angle connection.

Circular laminated RBs with  $K_{RB} = 0.8 \text{ kN/mm}$  and  $\delta_{RB} = 380 \text{ mm}$  are located at each floor of the building. According to the manufacturer specifications, these components consist of an elastomeric block made of natural rubber and reinforced with steel sheets bonded by vulcanising. Each RB has a diameter of 650 mm and a thickness of approximately 300 mm.

With regards to the SFDs, their activation forces are defined according to the methodology proposed by Paronesso and Lignos [85]. Notably, the  $F_s$  values are selected so as the structural components of the CBF as well as the floor diaphragms remain elastic

under both a design-basis (DBE, 10% probability of exceedance in 50 years) and a maximum considered earthquake event (MCE, 2% probability of exceedance in 50 years). For this purpose, a  $F_s$  distribution is defined along the height of the building as illustrated in Fig. 3.7. In brief, the activation force of the dampers located at floor  $i$  is determined as follows:

$$F_{s,1} = \frac{(1 - \alpha) \cdot \min\{V_{d,1}, V_{CBF,1}\}}{\sum_{i=1}^N 1/i} \quad (3.2)$$

$$F_{s,i} = \frac{F_{s,1}}{i} \quad (3.3)$$

Where  $N$  is the number of stories of the building,  $V_{CBF,i}$  and  $V_{d,i}$  are the story shear limits to prevent damage in the CBF and the floor diaphragms, respectively, and  $(1 - \alpha)$  is a reduction factor with  $0 < \alpha < 1.0$ . Such a factor is used to take into account the horizontal force demand  $\Delta F_{RB,i} = n_{RB} \cdot K_{RB,i} \cdot \delta_i$  that the RBs transfer to the steel CBFs under earthquake loading ( $n_{RB}$  is the number of RBs per floor and  $\delta_i$  is their horizontal displacement as shown in Fig. 3.5d). This implies that, under seismic action, the total horizontal force transferred to the CBF is equal to:

$$F_i = F_{s,i} + \Delta F_{RB,i} \quad (3.4)$$

As discussed by Paronesso and Lignos [85],  $\Delta F_{RB,i}$  can be taken equal to  $\alpha F_{s,i}$ . Hence, the activation force of each damper should be reduced by a factor of  $(1 - \alpha)$  so as to be smaller than the story shear limits  $V_{CBF,i}$  and  $V_{d,i}$ . Herein, a  $\alpha$  factor equal to 35 % is considered. This leads to activation forces ranging between 110 kN and 660 kN along the building height. This value is varied later on to evaluate the damper efficiency in achieving different seismic performance objectives.

### 3.3.2 Nonlinear Building Model

A two-dimensional (2D) numerical model of the 6-story steel building in the N-S direction is developed in OpenSees [153] (release version 2.5.0). Figure 3.8a illustrates the primary features of this model. The CBF columns and beams are modelled using force-based beam-column elements with 10 Gauss-Lobatto integration points along the length [154]. A 4x1 mesh is used to discretize the flange and web of each cross section according to Kostic et al. [155]. The Voce-Chaboche material model [156, 157] is adopted to simulate the stress-strain response of each fiber. The input parameters of this model are based on

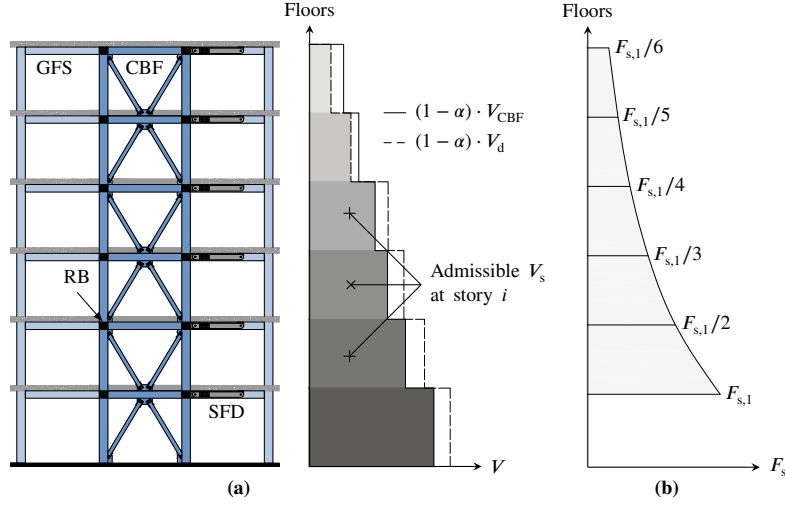


**Figure 3.7** – (a) Admissible story shear  $V_s$  in a 6-story steel CBF building, (b)  $\vec{F}_s$  pattern defined for a 6-story steel CBF building

the recommendations by de Castro e Sousa et al. [158] for S355J2 steel. The shear tab connections in the CBF beams are modelled with a zero-length spring, whose hysteretic moment-rotation response is defined according to Elkady and Lignos [159] at the even-numbered floors and according to Stoakes et al. [160] at the odd-numbered floors.

Steel braces are modelled according to Karamanci and Lignos [12]. In brief, cyclic brace buckling and fracture initiation due to low-cycle fatigue are explicitly considered in the 2D model. The in-plane and out-of-plane behavior of the bracing-end connections is modelled through an axial and rotational spring placed in series as discussed in Paronesso and Lignos [85].

The GFS of the buildings is modelled through a 1-bay equivalent gravity frame (EGF) as discussed in Elkady and Lignos [159]. At each story, the beams and columns of the EGF are modelled with an elastic element, whose properties are equivalent to half of the sum of those of the members that compose the GFS in the N-S direction. Plastic hinges at the column ends are idealized with a zero-length spring based on the modified Ibarra-Medina-Krawinkler (IMK) deterioration model [161] and the modelling procedures by Lignos and Krawinkler [212]. Similarly, at the EGF beams' extremities, the four connection types shown in Fig. 3.6 are modelled through rotational springs as discussed in Section 3.2.2.

Referring to Fig. 3.8a, each floor of the EGF is linked to the CBF through a truss element. Such element has a bilinear force-displacement response and it is employed to model both SFD and RBs as illustrated in Fig. 3.8b. Notably, at a given floor, the truss element becomes inelastic when it experiences an axial force equal to the activation force

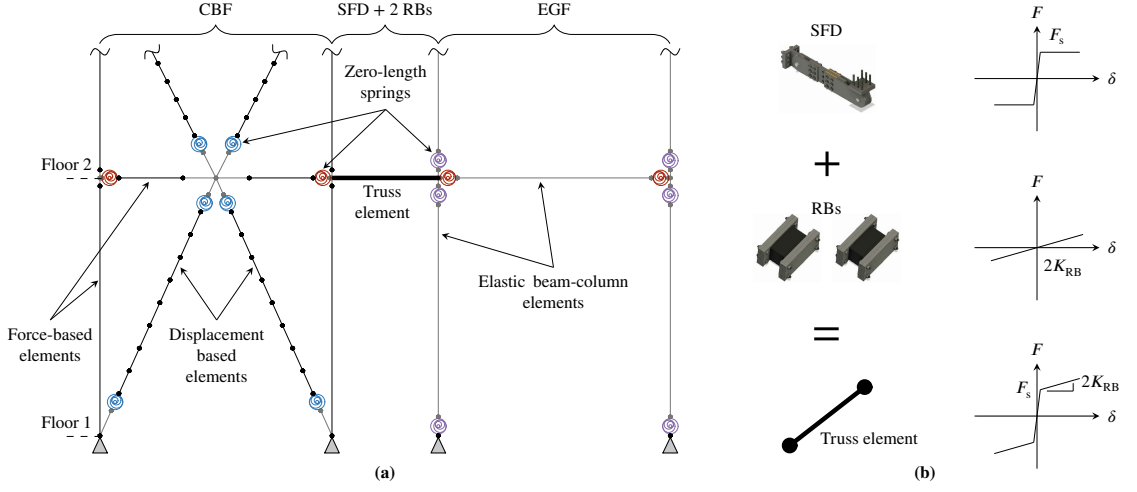


**Figure 3.8** – (a) 2D numerical model of the 6-story steel building in the N-S direction, (b) truss element used to model the SFD and the RBs at each story of the building

of the SFD located at that floor. Once the latter starts sliding, the RBs experience shear deformation, thereby exhibiting a post-elastic stiffness of  $2K_{RB}$  to the truss element. The elastic stiffness of the truss element corresponds to that of the SFD and is equal to 1000 kN/mm, which corresponds to the values from the experimental program by Paronesso and Lignos [84].

Finally, the base supports of the CBF and EGF are assumed to be pinned. Half of the gravity loads and seismic masses acting on the GFS are applied to the EGF columns. Second-order effects are considered through the corotational transformation. Furthermore, 2% damping ratio is assigned to the first and third vibration period of each numerical model. Damping is idealized with the Rayleigh model according to the procedures discussed in Karamanci and Lignos [12].

### 3.4 Nonlinear Response History Analysis

In this section, the seismic performance of the prototype building presented in Section 3.3 is investigated through nonlinear response history analysis (NRHA). In particular, the primary focus is on the seismic performance of the prototype and its GFS for comparative designs with alternative connection types (see Fig. 3.6). The response comparisons are based on the reported peak absolute acceleration demands (PFAs), peak story drift ratios (SDRs) and peak rotations of the beams ( $\theta_{\text{beam,peak}}$ ) and columns ( $\theta_{\text{col,peak}}$ ) of the GFS. A base case is also analysed where the gravity connections are assumed as ideally pinned (i.e., no contribution to lateral strength and stiffness).

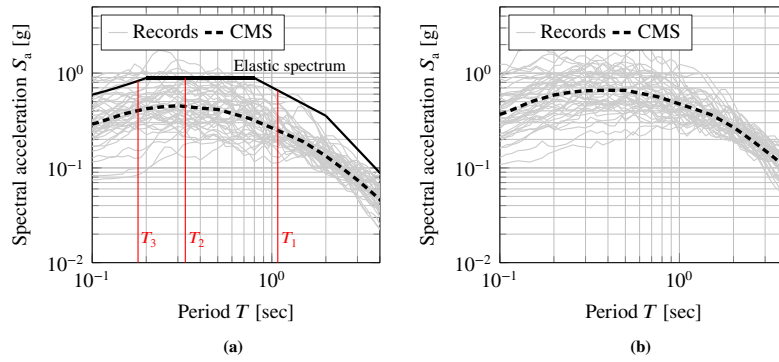


**Figure 3.9** – Acceleration spectra of the ground motions adjusted to the (a) DBE and (b) MCE seismic intensities respectively ( $T_1$ ,  $T_2$  and  $T_3$  are, respectively, the first, second and third fundamental period of the 6-story steel CBF building)

Nonlinear response history analysis is conducted by using two sets of 40 ground motions, which are selected from the PEER NGA-West database [169]. The first set is adjusted to the DBE seismic intensity, whereas the second one is adjusted to the MCE. The seismic records are selected based on the conditional mean spectrum [170] of Sion (see Figs. 3.9a and 3.9b). Such a spectrum is computed through probabilistic seismic hazard analysis as discussed in El Jisr et al. [213]. For comparison purposes, the elastic response spectrum of Sion is superimposed in Fig. 3.9a.

### 3.4.1 Peak Absolute Floor Acceleration Demands

Figure 3.10 depicts the PFAs at DBE and MCE along the height of the examined building for all four investigated gravity connections. In the same figure, the results for ideally pinned gravity connections are superimposed. In all cases, the PFAs are extracted from the GFS because it carries most of the seismic mass. The median response out of 40 ground motions is always considered in the reported results.

Referring to Fig. 3.10, the PFAs of the GFS are, on average, fairly insensitive to the considered gravity connection type, regardless of the seismic intensity of interest. Notably, PFA median values lower than 0.3 g and 0.4 g are obtained at DBE and MCE, respectively. In order to better interpret these findings, results from a single record of the 1999 Chi-Chi earthquake recorded at the CHY086 station are shown in Fig. 3.11 for the prototype building with shear tab and flush end-plate connections. In particular, this figure shows the hysteretic response of the two SFDs located at the 2<sup>nd</sup> floor (see Fig. 3.11a) and at the roof (see Fig. 3.11c) of the building. In Figs. 3.11b and Fig. 3.11d, the hysteretic behavior of the respective gravity connections is shown at the same floors.

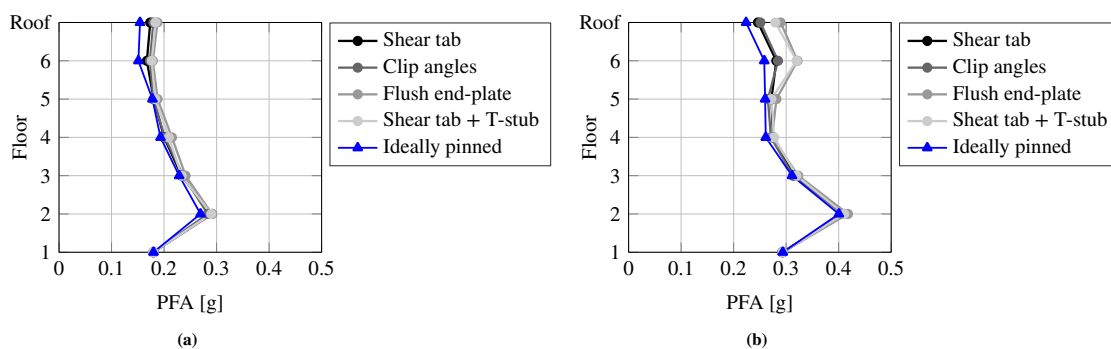


**Figure 3.10** – Median peak absolute floor acceleration demands obtained at (a) DBE and (b) MCE for different types of beam-to-column connections

Figure 3.11 suggests that the hysteretic energy dissipation of the SFDs is at least tenfold higher than that from the respective gravity connections. While flush end-plate connections are at least 1.5 to 3 times stiffer than their conventional shear tab counterparts, this does not practically influence the lateral drift demands of the GFS.

Referring to Fig. 3.10b, in the upper stories of the building, the GFS experiences slightly higher PFAs when flush end-plate or shear tab connections with T-stub are employed. Figure 3.11c suggests that the SFD located at the top story of the GFS undergoes smaller axial displacements when stiffer gravity connections are employed, thereby dissipating less seismic energy at that floor level than that in the other considered cases.

### 3.4.2 Peak Story Drift Ratio Demands

Figures 3.12a and 3.12b illustrate the peak SDRs along the height of the CBF at DBE and MCE, respectively. It is apparent that, the lateral drift demands of the CBF are insensitive to the gravity connection type. Indeed, a uniform peak SDR profile is achieved in all cases. Peak SDRs are consistently lower than 0.5%. As such, the steel CBF does not experience inelastic behavior in terms of brace flexural buckling and/or bracing end connection damage, which is consistent with the design approach that was proposed by Paronesso and Lignos [85].

Figures 3.12c and 3.12d depict the peak SDR profiles along the GFS system at DBE and MCE, respectively. Interestingly, the deflection of the GFS is not particularly influenced by the connection type of the GFS. This is consistent with what was shown in Section 3.4.1. Referring to Figs. 3.12c and 3.12d, at the top stories of the building, the GFS attains slightly smaller SDRs when stiffer connections (e.g., flush end-plate or

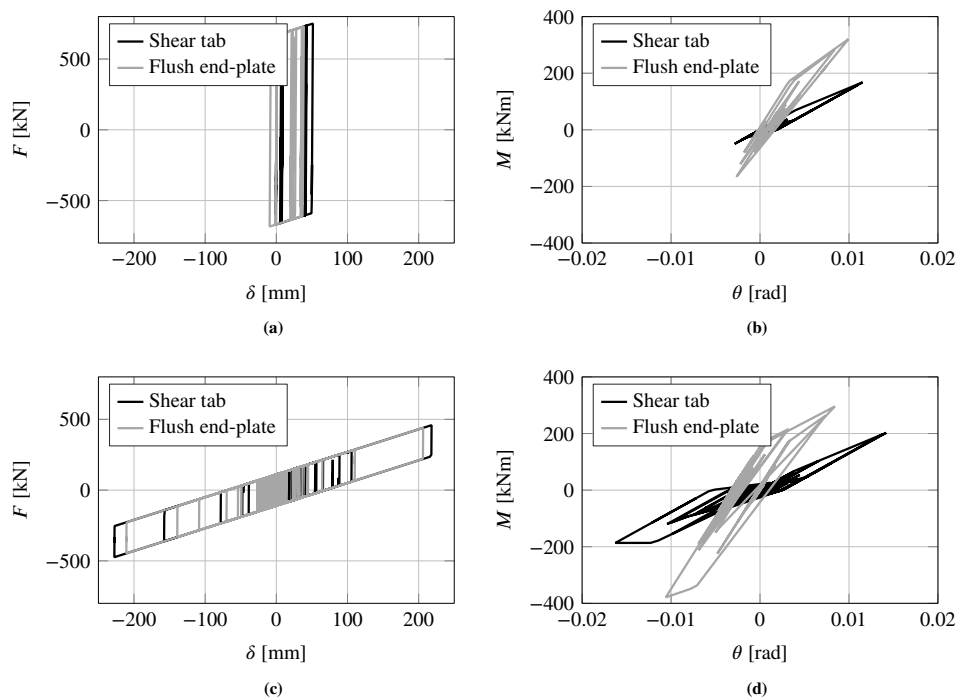


**Figure 3.11** – Results obtained at the (a)-(b) 2<sup>nd</sup> and (c)-(d) 7<sup>th</sup> floor of the 6-story building under the 1999 Chi-Chi earthquake recorded at the CHY086 station and scaled at the MCE seismic intensity: (a),(c) force-displacement response of the SFD, (b),(d) moment-rotation response of the shear tab and flush end-plate connections of the GFS

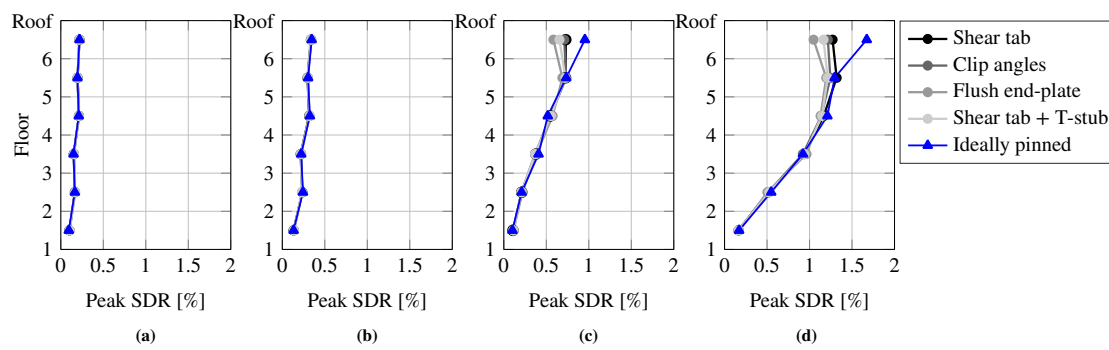


**Figure 3.12** – Median peak story drift ratios of the (a)-(b) CBF and (c)-(d) GFS for different gravity connections: (a),(c) at DBE, (b),(d) at MCE

shear tab connections with T-stub) are employed. This issue is further elaborated in Section 3.4.3.

Referring to Figs. 3.12c and 3.12d, the median peak SDRs along the height of the the GFS are about 1.0 % and 1.7 % at DBE and MCE, respectively. Miranda [144, 214] has found that partition walls of a building are severely damaged for the above lateral drift demands. While structural damage is prohibited (see Figs. 3.12a and 3.12b), the building functionality may still be lost in the aftermath of earthquakes with a return period of 2475 years. On the other hand, this shortcoming can be overcome by using sliding partition walls, which allow for their relative movement with respect to the structural elements they are attached to within a building [143–145]. For instance, recent developments [144] suggest that such partition walls accommodate lateral drift demands of about 1.5 % prior to damage. Similar developments may be adopted for the exterior cladding [215].

### 3.4.3 Peak Rotation Demands in the Members of the Gravity Framing System

Figures 3.13a and 3.13b illustrate the peak rotation demands in the steel beams of the GFS at DBE and MCE, respectively, for all the examined connection types. Interestingly, the smallest  $\theta_{\text{beam,peak}}$  values are attained when the GFS features stiff connections such as flush end-plate and shear tab connections with bottom T-stub. Indeed, these connections experience median  $\theta_{\text{beam,peak}}$  values slightly larger than  $\theta_1$  (see Table 3.1) merely at the upper floors of the GFS under seismic events with a 2475-years return period. Conversely, the shear tab and clip angle connections attain  $\theta_{\text{beam,peak}}$  median values between  $\theta_1$  and  $\theta_2$  at the two examined seismic intensities. However, none of the investigated gravity connections achieves  $\theta_{\text{beam,peak}}$  larger than  $\theta_2$ , i.e. they do not experience concrete crushing when the slab is in compression for all the analysed cases considered herein.

While locally the GFS connection type leads to variable rotational demands in the steel beams, the peak SDRs of the GFS are fairly insensitive to the connection type (see Figs. 3.13c and 3.13d). This can be explained by inspecting the rotational demands  $\theta_{\text{col,peak}}$  in the steel columns of the GFS for all the analysed cases. Figures 3.13c and 3.13d illustrate the  $\theta_{\text{col,peak}}$  values obtained at DBE and MCE, respectively. Interestingly, the steel columns of the GFS remain elastic regardless of the seismic intensity of interest. This is explained by the fact that their flexural capacity is at least two times larger than the maximum bending moment demands of the gravity connections under earthquake loading. Notably, among all cases, the largest  $\theta_{\text{col,peak}}$  values are attained by the pro-



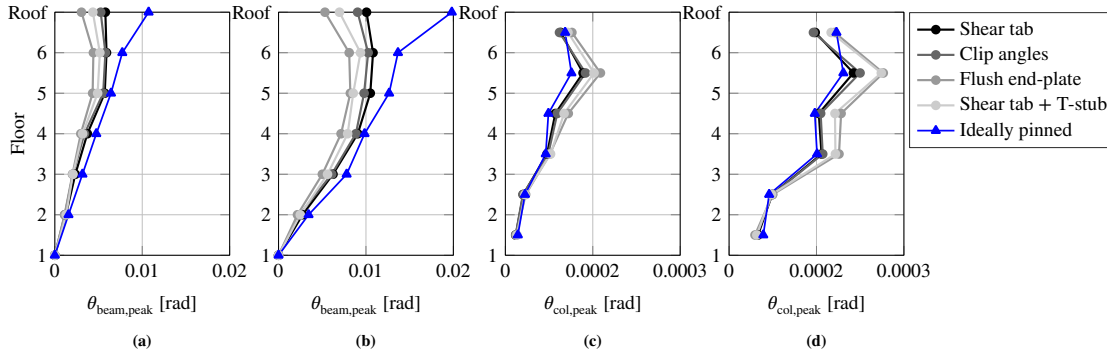


**Figure 3.13** – Median peak rotation demands of the (a)-(b) beams and (c)-(d) columns of the GFS at (a),(c) DBE and (b),(d) MCE

tototype with the stiffer gravity connections (i.e., flush end-plate or shear tab connections with bottom T-stub). Due to their high initial stiffness and flexural strength, these connections transfer higher flexural demands to the columns of the GFS under earthquake loading; hence, the elastic deformation of the gravity columns is relatively high in this case.

The simulation results in Figs. 3.10 to 3.13 reveal that the influence of the GFS connection type on the seismic behavior of steel CBF buildings equipped with floor SFDs is not dominant compared to that of the SFDs during a DBE or MCE seismic event. As discussed earlier, the damper activation forces were defined by considering a  $\alpha$  factor equal to 35% (see Section 3.3.1). Comparative studies for different  $\alpha$  factors should be employed so as to characterize the efficiency of the damper in terms of minimizing multiple story-based EDPs. While this iterative process may seem tedious, it is time consuming particularly in designs featuring a large number of dampers. As such, a simplified method should be developed for this purpose.

### 3.5 Proposed Simplified Method

In this section, a simplified method is proposed to investigate the influence of the damper activation forces on the relevant story-based EDPs of multi-story CBF buildings equipped with sliding friction dampers as dissipative floor connectors. Such a building is first transformed into an equivalent single-degree-of-freedom (SDF) system as discussed in Section 3.5.1. Subsequently, NRHA is conducted for different  $(1 - \alpha)$  factors. The obtained results are used to construct P-spectra for estimating the PFAs and peak/residual roof displacements ( $\delta_{\text{roof}}$ ) of the GFS as a function of the damper activation forces. As such, the ranges of  $(1 - \alpha)$  factors may be identified, which enable to limit insofar as pos-

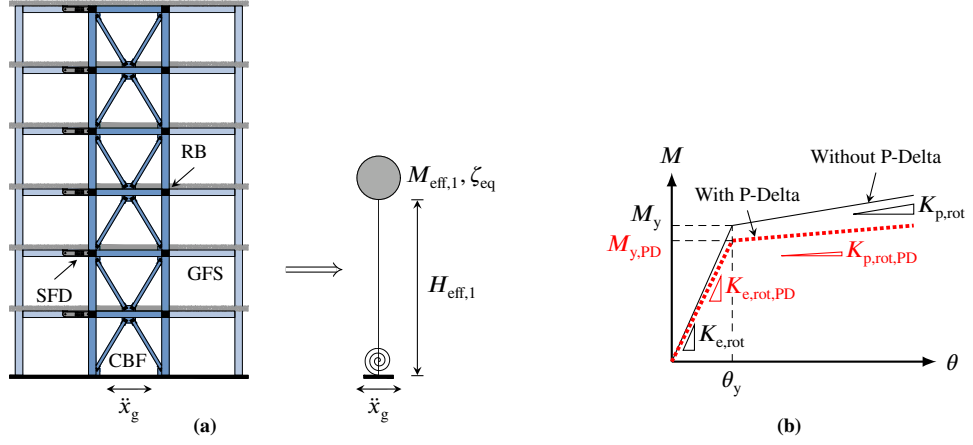


**Figure 3.14** – (a) 6-story steel CBF building equipped with floor SFDs transformed into an equivalent single-degree-of-freedom system, (b) moment-rotation response of the spring located at the base of the equivalent single-degree-of-freedom system

sible the absolute acceleration and displacement demands in the GFS under earthquake shaking. Accordingly, damage in the acceleration and drift-sensitive non-structural components of the building can be minimized. At the same time, the destabilizing effects of gravity loads are limited.

In the following sections, the proposed method is demonstrated through the prototype building discussed earlier. Its seismic performance is evaluated at the DBE and MCE seismic intensities for  $(1 - \alpha)$  factors ranging between 15 % and 100 %. The reliability of the simplified method is discussed in Section 3.5.3.

### 3.5.1 Equivalent Single Degree of Freedom System

Referring to Fig. 3.14a, the prototype building shown in Fig. 3.5 is transformed into an equivalent SDF system, whose effective modal mass and height are determined as follows [216]:

$$M_{\text{eff},1} = \frac{\left( \sum_{i=1}^N \phi_{i,1} \cdot m_i \right)^2}{\sum_{i=1}^N \phi_{i,1}^2 \cdot m_i} \quad (3.5)$$

$$H_{\text{eff},1} = \frac{\sum_{i=1}^N \phi_{i,1} \cdot m_i \cdot h_i}{\sum_{i=1}^N \phi_{i,1} \cdot m_i} \quad (3.6)$$

Where  $N$  is the number of stories of the building,  $h_i$  is the height of story  $i$ ,  $m_i$  is the mass at story  $i$  and  $\phi_{i,1}$  is the first mode shape of the building determined by considering that the GFS is rigidly connected to the CBF. The parameters  $M_{\text{eff},1}$  and  $H_{\text{eff},1}$  are determined as a function of the first mode  $\phi_1$  only. Indeed, Paronesso and Lignos [85] showed that the seismic performance of steel CBF buildings equipped with friction dampers as dissipative floor connectors is mostly dominated by the first mode of vibration.

Referring to Fig. 3.14b, the base support of the SDF system is modelled with a bilinear rotational spring, whose yield moment ( $M_y$ ), elastic rotational stiffness ( $K_{\text{e,rot}}$ ) and post-elastic rotational stiffness ( $K_{\text{p,rot}}$ ) are defined as follows:

$$M_y = H_{\text{eff},1} \cdot \frac{F_y}{\Gamma_1} \quad \text{where} \quad F_y = \sum_{i=1}^N F_{s,i} = (1 - \alpha) \cdot \min\{V_{d,1}, V_{\text{CBF},1}\}$$

$$\text{and} \quad \Gamma_1 = \frac{\sum_{i=1}^N \phi_{i,1} \cdot m_i}{\sum_{i=1}^N \phi_{i,1}^2 \cdot m_i} \quad (3.7)$$

$$K_{\text{e,rot}} = K_e \cdot H_{\text{eff},1}^2 \quad \text{where} \quad K_e = \frac{M_{\text{eff},1}}{(T_1/2\pi)^2} \quad (3.8)$$

$$K_{\text{p,rot}} = K_p \cdot H_{\text{eff},1}^2 \quad \text{where} \quad K_p = \frac{K_e \cdot K_{\text{RB,tot}}}{K_e + K_{\text{RB,tot}}}$$

$$\text{and} \quad K_{\text{RB,tot}} = n_{\text{RB}} \cdot \sum_{i=1}^N K_{\text{RB},i} \quad (3.9)$$

Where  $\Gamma_1$  is the modal participation factor of the first vibration mode of the prototype building and  $T_1$  is its fundamental period of vibration. Referring to Fig. 3.14b, for  $\theta < \theta_y$ , it is assumed that the SFDs act as rigid links between the CBF and the GFS. Therefore, the elastic rotational stiffness of the spring is determined as a function of the elastic stiffness of the CBF ( $K_e$ , see Eq. 3.8). For  $\theta = \theta_y$ , it is hypothesized that all the SFDs start sliding simultaneously by preventing the CBF from experiencing inelastic deformations. Consequently, for  $\theta > \theta_y$ , the post-elastic rotational stiffness of the spring is defined as a function of  $K_e$  and  $K_{\text{RB}}$  by assuming that the RBs are in series with the CBF (see Eq. 3.9). Second-order effects are considered by rotating the moment rotation diagram of the SDF system as a function of the corresponding stability coefficient  $\theta^*$  as

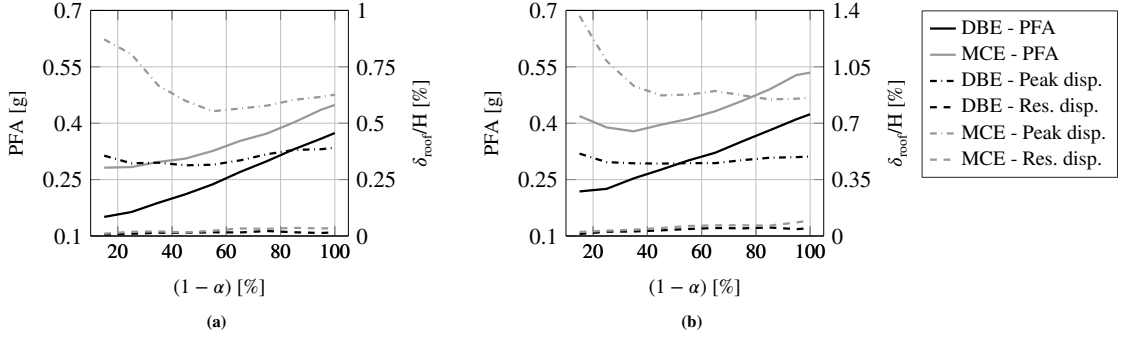


**Figure 3.15** – Performance spectra constructed for the 6-story CBF building equipped with floor SFDs: (a) median values, (b) 84<sup>th</sup> percentile

suggested by Ibarra [217] (see Fig. 3.14b):

$$\theta^* = \frac{M_{\text{eff},1} \cdot g}{K_e \cdot H_{\text{eff},1}} \quad \text{where} \quad g = 9.81 \text{ m/s}^2 \quad (3.10)$$

$$M_{y,\text{PD}} = M_y \cdot (1 - \theta^*) \quad (3.11)$$

$$K_{e,\text{rot},\text{PD}} = K_{e,\text{rot}} \cdot (1 - \theta^*) \quad (3.12)$$

$$K_{p,\text{rot},\text{PD}} = K_{e,\text{rot}} \cdot (b - \theta^*) \quad \text{where} \quad b = K_{p,\text{rot}}/K_{e,\text{rot}} \quad (3.13)$$

The equivalent SDF system is subjected to the same set of ground motions discussed in Section 3.4 (see Fig. 3.9).

### 3.5.2 Performance Spectra (P-Spectra)

Figure 3.15 shows the P-Spectra constructed for the prototype building presented in Section 3.3.1. The P-Spectra are dual graphics, which illustrate the earthquake-induced PFAs and peak/residual roof drift ratios  $\delta_{\text{roof}}$  of the GFS as a function of the  $(1 - \alpha)$  factor, which is used to determine the activation forces of the SFDs. These diagrams represent the median and 84<sup>th</sup> percentile responses in Figs. 3.15a and 3.15b, respectively, for  $(1 - \alpha)$  factors ranging between 15% and 100% and seismic events with a return period of 475 (i.e., DBE) and 2475 years (i.e., MCE). Figure 3.15 shows that, at both seismic intensities, the PFAs of the GFS increase proportionally with the magnitude of the damper activation forces. In particular, PFA median values lower than 0.45 g are obtained at MCE for  $(1 - \alpha) = 100\%$ . This suggests that damage on acceleration-sensitive non-structural components of the building is fairly minimal [177] regardless of the considered  $F_s$ .

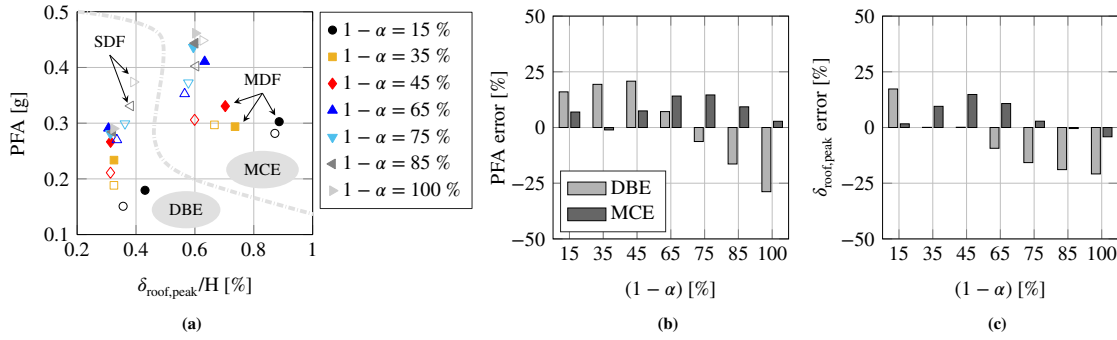


**Figure 3.16** – (a) Median values of the peak floor absolute acceleration demands and peak roof displacements of the GFS as predicted with the SDF (unfilled markers) and MDF systems (filled markers); relative error in predicting (b) the peak floor absolute acceleration demand and (c) the peak roof displacement of the GFS of the prototype building

Referring to Fig. 3.15, the residual roof displacements of the GFS are negligible (i.e., 0.05 %) regardless of the seismic intensity and damper activation force considered. Conversely, major variations of the peak roof displacements are observed at MCE for  $(1-\alpha) < 50$  %. Notably, as illustrated in Fig. 3.15a, median peak  $\delta_{\text{roof}}/H$  on the order of 0.9 % are attained at MCE for  $(1-\alpha) = 15$  %. Such values decrease to about 0.6 % when the activation forces of the SFDs are computed for  $(1-\alpha) \geq 50$  %. On the other hand, at DBE, median peak  $\delta_{\text{roof}}/H$  on the order of 0.35 % are obtained regardless of the considered damper activation force. Interestingly, similar trends are observed in Fig. 3.15b. This suggests that the use of  $(1-\alpha)$  factors larger than 50 % does not further limit the lateral deflections of the GFS. This simple example illustrates how the proposed method can provide, within seconds, the range at which the damper efficiency is optimal for a given seismic intensity of interest.

### 3.5.3 Estimated Errors in the Predictions

The reliability of the simplified method is evaluated by conducting NRHA on the 6-story CBF building with dissipative floor connectors presented in Section 3.3.2. The range of  $(1-\alpha)$  [%] considered in this study is [15, 35, 45, 65, 75, 85, 100]. Because in the first part of this investigation it was shown that the gravity connection type does not practically influence the seismic response of steel CBF buildings with dissipative floor connections, the analyses hereinafter are conducted with conventional shear tab connections (see Fig. 3.4) in the GFS.

Figure 3.16a illustrates the median PFAs and peak  $\delta_{\text{roof}}/H$  of the GFS computed with the SDF and multi-degree-of-freedom (MDF) systems. It is apparent that, at both seismic

intensities of interest, the equivalent SDF system predicts with reasonable accuracy both story-based EDPs. Notably, the MDF simulation results confirm that, at DBE, the peak  $\delta_{\text{roof}}/H$  of the GFS are slightly influenced by  $(1 - \alpha)$ , whereas its PFAs increase when  $(1 - \alpha)$  increases. Similarly, at MCE, the peak  $\delta_{\text{roof}}/H$  values suggest that the lateral deflection of the GFS increases when  $(1 - \alpha) < 50\%$ .

The relative error in predicting the median PFAs and the peak  $\delta_{\text{roof}}/H$  of the GFS with the equivalent SDF system are reported in Figs. 3.16b and 3.16c, respectively. Positive relative errors are attained when the equivalent SDF system underestimates the EDP demands of interest relative to its MDF counterpart. Referring to Figs. 3.16b and 3.16c, the median PFAs and peak  $\delta_{\text{roof}}/H$  values obtained with the equivalent SDF system differ by less than 30 % from those of the MDF system. This demonstrates the value of the simplified method so as to optimize the seismic performance of steel CBF buildings with dissipative floor connectors by selecting rational activation forces for the SFDs. Same findings hold true for the 84<sup>th</sup> percentile values of the examined EDPs. The results are not shown herein due to brevity. Furthermore, the total base shear computed with the equivalent SDF system is generally overestimated by about 1.5 times compared to that obtained with the MDF system. The reason is that the equivalent SDF system is constructed by assuming that all the SFDs are activated simultaneously under the seismic action. This assumption may be refined in future studies by considering different damping distribution methods [218]. However, this is outside the scope of the present study.

### 3.6 Conclusions

In this thesis chapter, it was investigated the role of the gravity connection type on the lateral drift demands of the gravity framing system (GFS) in multi-story steel CBF buildings equipped with sliding friction dampers as dissipative floor connectors. Four different types of gravity connections were considered for this purpose. These include (i) shear tab, (ii) clip angle, (iii) flush end-plate and (iv) shear tab connections with bottom T-stub. A general modelling approach was proposed to idealize both the monotonic and cyclic moment-rotation response of these connections. Subsequently, NRHA was conducted on a prototype 6-story steel CBF building with dissipative floor connectors.

The simulation results suggest that, on average, the PFA demands along the building height are practically insensitive to the gravity connection type. Particularly, PFA demands lower than 0.3 g and 0.4 g were obtained at DBE and MCE, respectively. The reason for this finding is that the energy dissipation from the friction dampers is superior

to that from the gravity framing connections. This also suggests that the GFS may be simply modelled with ideally pinned gravity connections for simplicity in the nonlinear building model.

Similarly, the lateral displacement demands of the GFS are insensitive to the gravity connection type for identical gravity column cross sections. Notably, maximum SDR median values of 1.0 % and 1.7 % were obtained at DBE and MCE, respectively. Unlike steel buildings with perimeter steel moment resisting frames, the lateral stiffness of the GFS is considerably smaller than that of a steel CBF system. Therefore, in frequently occurring seismic events (i.e., 50 % probability of occurrence over a 50 year life expectancy), and/or prior to the activation of the friction dampers, the CBF system mostly controls the lateral drift demands along the building height. Stiffer gravity connections, such as the flush end-plate and shear tab connections with bottom T-stub, are likely to experience smaller inelastic rotation demands compared to those in more flexible gravity connections. However, stiffer gravity connections impose high flexural demands on the adjoining gravity columns; therefore, their elastic contribution to the total drift demands of the GFS tends to increase in this case.

A simplified method was also proposed to evaluate the effectiveness of the sliding friction dampers in controlling the story-based EDPs of the GFS in steel CBF buildings. The simplified method was applied to a 6-story steel CBF building with sliding friction dampers as dissipative floor connectors. The building was first transformed into an equivalent nonlinear SDF system. Subsequently, NRHA was conducted in order to construct P-spectra for estimating PFAs and peak/residual roof displacements of the GFS as a function of the activation forces of the SFDs.

The PFAs of the GFS increase when the activation forces of the SFDs increase. However, on average, the PFAs do not exceed 0.45 g for the highest examined activation force. As such, damage in acceleration-sensitive non-structural components is anticipated to be fairly minimal regardless of the selected activation force. The simulation results suggest that the lateral drift demands in the GFS are minimized for  $(1 - \alpha)$  factors larger than 50 %. When  $(1 - \alpha) \geq 50 \%$ , the lateral drift demands of the GFS are fairly insensitive to the two examined seismic intensities; hence, an  $(1 - \alpha)$  factor close to 50 % should be adopted for optimal seismic performance of the examined prototype building.

The simulation results obtained with the simplified approach also revealed that residual displacements of the GFS are negligible and practically insensitive to the considered activation force of the friction dampers. For reference, values lower than 0.05 % were obtained in all examined cases.

The proposed simplified method predicts the story-based EDPs of interest with up to 30 % error. The general consensus is that, in a pre-design phase of a steel CBF building with SFDs as dissipative floor connectors, the proposed method can be reliably employed to identify the range of damper activation forces through which an optimal seismic performance may be anticipated.

Finally, it should be stated that the study features a number of limitations. Notably, the gravity columns were assumed to be the same in all examined cases. Designs with stiffer gravity columns are likely to experience reduced lateral drift demands in the GFS. In this case, the use of stiffer gravity connections (e.g., flush end-plate or shear tab with t-stubs) may be beneficial. With regard to the proposed method for evaluating the efficiency of the activation forces of the friction dampers on the overall building behavior, alternative damping distribution methods along the building height should be explored.



# Conclusions and Future Work

This doctoral thesis investigated the use of sliding friction dampers (SFDs) as dissipative floor connectors for enhancing the seismic performance of multi-story steel concentrically braced frame (CBF) buildings. The sliding friction dampers were assumed to be in a horizontal fashion and connected the steel CBF with the gravity framing system (GFS). A comprehensive experimental program was first conducted on five non-metallic composite friction pads in order to identify suitable pads to be employed in such dampers. A design methodology was subsequently developed to determine the damper activation forces so as to ensure damage-free seismic performance in the steel CBF and the diaphragms of the GFS. The efficiency of the proposed method was demonstrated through nonlinear response history simulations based on risk-targeted seismic performance at various levels of seismic intensities of interest to the engineering profession. Hazard curves of the maximum axial displacement of the SFDs and the peak story drift ratios of the GFS were developed to assess the seismic performance of multi-story steel CBF buildings within the framework of Performance-based Earthquake Engineering (PBEE) [219]. Additionally, it was explored the influence of four primary beam-to-column gravity connections on the seismic response of multi-story steel CBF buildings equipped with floor SFDs. Other contributions of this thesis involve the development of a simplified method to evaluate the effectiveness of the activation forces of the SFDs for controlling relevant engineering demand parameters (EDPs) of interest for damage control of steel frame buildings.

## Conclusions

### Experimental Investigation of Composite Materials for Sliding Friction Dampers

A comprehensive experimental program was conducted on five non-metallic friction pads, whose use had never been explored in supplemental damping devices. A full-scale sliding friction damper prototype was developed for this purpose. Parameters examined as part

of the experimental program included the applied pressure level to control the sliding force, the imposed loading protocol and the associated loading rate.

The tested pads are composed of fibres and organic and inorganic fillers bounded together by phenolic resins. Their selection was based on the following performance criteria: (i) their static friction coefficient should ideally be between 0.20 and 0.30 in order to limit wear on the friction pads under cyclic loading<sup>‡</sup>, (ii) their hardness shall be lower than the one of the steel plates so as the steel plates in contact with the pads experience minimal damage due to wear, (iii) the static and dynamic friction coefficients of the pads should be similar so as the friction damper exhibits a stable hysteretic response without slip force variations under cyclic loading, (iv) the pads should not be susceptible to galvanic corrosion when in contact with the steel plates of the damper.

The experimental campaign revealed that two out of the five tested pads (i.e., M1 and M4) are promising for exploitation in sliding friction dampers for seismic applications. Notably, the damper prototype exhibited a fairly stable axial force-axial displacement hysteretic response when such pads were employed because both materials are characterized by similar static and dynamic friction coefficients. Furthermore, it was found that their friction coefficient is fairly invariant at pressures higher than 7 to 8 MPa and under sliding velocities larger than 10 mm/s. Similarly, it was observed that the friction coefficient of one of the two pads (i.e., M4) is practically insensitive to temperature variations. On the contrary, the friction coefficient of the second material (i.e., M1) tends to slightly increase with the rise in temperature at the sliding interface. However, the experimental results obtained under the pulse-like and mainshock-aftershock loading protocols demonstrated that under conditions somewhat similar to those occurring during a seismic event, the temperature at the sliding interface does not increase sufficiently to cause major variations of its friction properties. Additionally, both pads provided consistent friction coefficients under consecutive events.

A number of shortcomings have been encountered with the remaining friction pads (i.e., M2, M3 and M5). These include (i) noise emissions above 80 dB, (ii) net section fracture of the pads after a few cycles conducted at a sliding force of 300 kN, and (iii) pressure-dependency of their friction coefficient. In particular, two of the examined friction pads (i.e., M2 and M3) demonstrated a significant loss of bolt pretension. This caused variation in contact between the pads and the inner slotted plate, which in turn led to non-uniform wear and an irreversible bending deformation of the pads. The observed loss of pretension was mainly attributable to the inadequate dry treatment carried out

---

<sup>‡</sup> $\mu_s$  values larger than 0.3 are endorsed if minor variations of the friction coefficient are attained due to wear under cyclic loading

on such pads after drilling the bolt holes with a water jet machine. Therefore, the performance of these two materials should be re-evaluated in the future, provided that a different manufacturing technique is employed for drilling the bolt holes.

During the experimental campaign, several tests were terminated due to fracture of at least one friction pad. It was observed that their fracture extended within the net section normal to the loading direction. During loading histories, the thickness of the pads progressively reduced due to the wear at the sliding interface. Concurrently, the damper axial force remained constant or increased with the number of loading cycles. As a result, the tensile stress demand, which was amplified by stress concentration near the bolt holes, exceeded the tensile stress resistance of the friction pad. Fracture occurred instantaneously in this case. However, this issue can be addressed by simply using thicker friction pads.

The experimental program conducted during this thesis featured a number of limitations. First, the pressure- and velocity-dependency of the pads' friction coefficient was investigated for a maximum pressure level of approximately 20 MPa and a maximum sliding velocity of 30 mm/s. These limits were imposed by the capacity of the existing laboratory equipment. Furthermore, time-dependent phenomena associated with force relaxations were not investigated within this framework.

## **Seismic Design and Performance of Steel Concentrically Braced Frame Buildings with Sliding Friction Dampers as Dissipative Floor Connectors**

Sliding friction dampers were employed as dissipative floor connectors in order to enhance the seismic response of multi-story steel CBF buildings. A design methodology was proposed for selecting their activation forces so that both the CBFs and the diaphragms of the GFS are protected from inelastic deformations under design-basis (DBE, 10% probability of exceedance in 50 years) and maximum considered earthquake events (MCE, 2% probability of exceedance in 50 years). The efficiency of the proposed method was demonstrated by evaluating the seismic performance of two 6-story steel CBF buildings with a capacity-designed and low ductility CBF system. It is noteworthy that under earthquake loading, the former is likely to become inelastic due to brace buckling. Conversely, in the latter, fracture of the bracing-end connections can potentially occur prior to brace buckling because, in this case, no specific rules for capacity design and detailing are imperative for the bracing-end connections.

Both buildings were design in Sion, Switzerland, which is considered to be a moderate seismicity zone in Europe. Their seismic performance was investigated through nonlinear response history analyses by using two sets of 40 ground motions, which were adjusted to the DBE and MCE seismic intensities, respectively, based on the conditional mean spectrum of Sion. Their seismic behavior were contrasted with that of steel CBF buildings equipped with rigid floor diaphragms.

Nonlinear response history simulations demonstrated that steel CBF buildings with rigid floor diaphragms are susceptible to drift concentrations. Furthermore, it was observed that their seismic response is subjected to high variability in the story drift ratios and peak absolute floor acceleration demands due to the strong influence of higher mode effects.

With regards to CBF buildings equipped with dissipative floor connectors, it was found that, regardless of the CBF-type employed, the activation forces determined according to the proposed methodology are effective in mitigating higher mode effects and in preventing the CBF and the floor diaphragms from experiencing inelastic behavior under earthquake loading. Notably, story drift demands smaller than 0.5 % were observed along the height of the CBFs even at seismic events with a return period of 2475 years. Furthermore, the associated variability in the story drift ratio demands was nearly zero regardless of the examined seismic intensities. This suggests that the lack of capacity design in the steel CBF system does not compromise the seismic performance of the building because the activation forces of the floor SFDs are selected so as to prevent inelastic deformations in such a system, i.e. capacity design is not imperative in this case.

Additionally, it was observed that, unlike steel CBF buildings with rigid diaphragms, those with dissipative floor connectors are subjected to a convex story shear force demand distribution along their height, which is characteristic of first-mode dominant seismic response. This suggests that the activation forces determined according to the proposed methodology are effective in mitigating higher mode effects. Therefore, in the pre-design phase of the building, the seismic design forces can be accurately estimated through the equivalent lateral force method by assuming a first mode lateral force pattern.

The simulation results also revealed that the floor SFDs allow to reduce by more than 50 % the earthquake-induced acceleration demands and their associated variability in the steel CBF buildings, thereby minimizing damage in the acceleration-sensitive non-structural components of the building. Furthermore, it was found that the GFS is subjected to smaller lateral drift demands when the steel CBF system is designed with low strength reduction factor. This suggests that steel CBF buildings equipped with

floor SFDs are less likely to experience damage to the drift-sensitive non-structural components when they are designed with low strength reduction factors. This confirms the fact that capacity design is not imperative in this case.

Finally, characteristic EDP hazard curves were developed to quantify the annualized maximum slot demand of the SFDs and the peak story drift ratios of the GFS at selected return periods of interest. The findings showed that at both DBE and MCE, the GFS of the low ductility CBF building with floor SFDs is likely to experience smaller peak story drift ratios compared to its rigid diaphragm counterpart. Conversely, during frequent seismic events, the GFS is prone to higher lateral drift demands when dissipative floor connectors are employed. Notably, in this case, peak story drift ratios close to 0.65 % were obtained. Past studies have highlighted that partition walls are susceptible to damage at these drift levels. However, this shortcoming can be overcome by using sliding partition walls, which allow for their relative movement with respect to the structural elements they are attached to within the building. On the other hand, it was found that structural damage in bracing-end connections and steel braces, which is likely to be observed at these drift amplitudes, is prevented.

### **Influence of Gravity Beam-to-Column Connections on the Seismic Behavior of Steel CBF Buildings with Dissipative Floor Connectors**

The influence of typical gravity connections on the seismic demands of multi-story steel CBF buildings equipped with floor SFDs was investigated. The examined connections included (i) shear tab, (ii) clip angle, (iii) flush end-plate and (iv) shear tab connections with bottom T-stub. A general modelling approach was first proposed to idealize both the monotonic and cyclic moment-rotation response of these connections. Notably, characteristic values were defined for each connection type in order to determine the stages at which the latter (i) experiences inelastic behavior due to bolt slip and concrete cracking, (ii) attains its peak flexural capacity, (iii) undergoes flexural strength degradation due to concrete crushing or steel reinforcement yielding, (iv) attains its residual flexural resistance, and (v) reaches its ultimate limit state, i.e. a zero flexural capacity. The flexural capacity of each connection was determined based on the maximum force couple that the latter could resist under positive and negative bending moment. With regards to the remaining parameters, their values were calibrated to prior experiments. The ranges of steel beam depths and (i.e., from 300 mm to 600 mm) and composite slab thicknesses (i.e., from 80 mm to 170 mm) that were used are similar to those seen in a conventional GFS. Similarly, the input model parameters of the Pinching4 material model adopted

to simulate the moment-rotation behavior of all the examined connection types were calibrated to the respective experimental data.

Nonlinear response history analysis was conducted on a prototype 6-story steel CBF building with SFDs as dissipative floor connectors. For this purpose, two sets of 40 ground motions were adjusted to the DBE and MCE seismic intensities based on the conditional mean spectrum of the design location of the investigated building (i.e., Sion, Switzerland). The GFS of such a building was composed of shallow steel beams (i.e., beam depth of 270 mm) and steel columns with a depth ranging between 300 mm and 400 mm. All the floor diaphragms consisted of concrete slab with a reinforcement ratio of about 0.5 % and featuring a profiled steel deck. According to EN 1993-1-8 [150] provisions, all the investigated connections were semi-rigid. In term of strength, the flush end-plate and shear tab connections with bottom T-stub represented partial-strength connections, whereas the other two were classified as nominally pinned.

The simulation results revealed that the peak floor absolute acceleration demands along the building height are practically insensitive to the gravity connection type. This is explained by the fact that the energy dissipation from the friction dampers is at least tenfold that from the gravity framing connections. Same findings hold true for the lateral displacement demands of the GFS. This is due to the fact that the lateral stiffness of the latter is considerably smaller compared to that of the steel CBF system. As a result, in frequently occurring seismic events (i.e., 50 % or higher probability of occurrence over a 50 year life expectancy), and/or prior to the activation of the friction dampers, the CBF system mostly controls the lateral drift demands along the building height. This implies that it is not required to accurately model the hysteretic moment-rotation response of the gravity connections when the seismic performance of steel CBF buildings equipped with dissipative floor connectors is investigated.

Finally, it was found that stiffer gravity connections, such as the flush end-plate and shear tab connections with bottom T-stub, are likely to experience smaller inelastic rotation demands compared to their more flexible counterparts. However, due to their high initial stiffness and flexural strength, they impose higher flexural demands on the adjoining gravity columns. Consequently, the elastic contribution of the gravity columns to the total drift demands of the gravity framing system tends to increase in this case.

## Performance Spectra Method for Pre-design of steel CBF Buildings with Dissipative Floor Connectors

A simplified method was proposed to evaluate the effectiveness of the SFDs in limiting the absolute floor acceleration and lateral drift demands in the GFS of steel CBF buildings. The simplified method was applied to a 6-story steel CBF building with floor SFDs. The building was first transformed into an equivalent single-degree-of-freedom (SDF) system. Its effective modal mass and height were defined as a function of the first mode of the building because, as demonstrated within the context of this thesis, the seismic performance of steel CBF buildings equipped with floor SFDs is mostly dominated by the first mode of vibration. Furthermore, the base support of the SDF system was modelled with a bilinear rotational spring, which properties were defined as a function of the elastic stiffness of the CBF system, the sum of the activation forces of the SFDs and the shear stiffness of the rubber bearings. Subsequently, dual graphics called P-spectra were generated through nonlinear response history analysis in order to estimate the peak floor absolute acceleration demands and peak/residual roof displacements of the GFS as a function of the activation forces of the SFDs. Such an investigation was conducted by using two sets of 40 ground motions, which were adjusted to the DBE and MCE seismic intensities based on the conditional mean spectrum of Sion (i.e., the design location of the investigated building).

The simulation results obtained with the SDF system highlighted that the peak absolute floor acceleration demands of the GFS increase when the activation forces of the dampers increase. Furthermore, it was found that, the lateral drift demands in the GFS are minimized when 50 % activation forces are employed, regardless of the seismic intensity investigated. The reliability of such results was evaluated by conducting nonlinear response history analysis on the 6-story CBF building equipped with floor SFDs. For this purpose, reduction factors between 15 % and 100 % were adopted to compute the activation forces of the SFDs. The results demonstrated that the proposed simplified method allows to predict the peak absolute floor acceleration demands and peak/residual roof displacements of the GFS by up to 30 % error. This suggests that, in a pre-design phase, the proposed method can be reliably employed to identify the range of damper activation forces through which an optimal performance of the steel CBF building may be anticipated.

## Recommendations for Future Research

In light of the work presented in this thesis, the following research topics are proposed for potential future research:

- Further experiments should be conducted on the two non-metallic composite pads that have been identified as promising for exploitation in sliding friction dampers for seismic applications. Notably, pressure levels higher than  $20 \text{ N/mm}^2$  and input velocities larger than  $30 \text{ mm/s}$  should be investigated in order to examine these pads under conditions similar to those encountered during real seismic events. Furthermore, time-dependent phenomena associated with force relaxation should be further evaluated;
- The collapse risk of mid- to high-rise steel CBF buildings equipped with floor sliding friction dampers should be benchmarked within the framework of FEMA P695 [182] in order to identify the range of applicability of the proposed design methodology for determining the damper activation forces;
- The seismic performance of multi-story steel CBF buildings equipped with floor sliding friction dampers should be investigated through nonlinear response history simulations that capture three dimensional effects in order to investigate the sensitive of the sliding friction dampers to potential torsional effects;
- Collapse vulnerability curves should be developed in order to further investigate the benefits of using sliding friction dampers as dissipative floor connectors;
- Further investigations should be conducted on the structural details to be employed to connect the sliding friction dampers to the CBF system as well as the floor diaphragms of the gravity framing system.





## Design Drawings of the Sliding Friction Damper Prototype

This appendix includes the design drawings of the sliding friction damper prototype developed and tested at the EPFL Structure Laboratory as part of this thesis (see Chapter [1](#)).

| Pos. | Elément                                   | Matériel    |
|------|---|-------------|
| 1    | Boulon SHV M24 totalement précontraint    | Classe 10.9 |
| 2    | Boulon SHV M24 partiellement précontraint | Classe 10.9 |
| 3    | Axe Ø 50 mm                               | ETG 100     |
| 4    | Plaque d'extrémité FLB 220.390.40         | S355 J2     |
| 5    | Plaque extérieure A-A FLB 220.440.20      | S355 J2     |
| 6    | Plaque extérieure B-B FLB 220.708.20      | S355 J2     |
| 7    | Plaque intérieure FLB 220.620.20          | S355 J2     |
| 8    | Plaque de frottement 220.200.15           | Variable    |

| Dispositif de frottement |    |                    |            |
|--------------------------|----|--------------------|------------|
| EPFL                     |    |                    |            |
| Assemblage               |    |                    |            |
| Inq.:                    | PM | Echelle:           | 1.4        |
| Ing.:                    |    | Messtab:           |            |
| Proj.:                   |    | Zugabezeichnung:   |            |
| Des.:                    |    | Plan d'alignement: |            |
| Dis.:                    |    | Date:              | 18.03.2019 |
|                          |    | Formet:            | A3         |
|                          |    | Format:            |            |
|                          |    | Formato:           |            |

**RESSLab**  
Resilient Steel Structures Laboratory

**EPFL**  
École Polytechnique Fédérale de Lausanne

Resilient Steel Structures Laboratory (RESSLab)  
School of Architecture, Civil, and Environmental Engineering, EPFL  
1915, Route de Saclay  
CH-1513, Lausanne, Switzerland  
Phone Number: +41 21 693 2427  
email: dimitrios.lignos@epfl.ch

## EPFL

## Vue transversale et longitudinale

[illegible]





**Resilient Steel Structures Laboratory (RES SLab)**  
School of Architecture, Civil, and Environmental Engineering, EPFL  
Attention to: Prof. Dimitrios Lignos  
Phone Number: +41 21 693 2427  
email: dimitrios.lignos@epfl.ch



## ELEMENTS

- 1 - BOULON SHV M24 10.9, L = 140 mm,  $F_{t,cal}$  = 226 kN  
2 - BOULON SHV M24 10.9, L = 160 mm,  $F_{t,cal}$  = variable  
3 - AXE Ø 50 x 150 mm  
4 - PLAQUE FLB 220.390.40  
5 - PLAQUE FLB 220.440.20  
6 - PLAQUE FLB 220.708.20  
7 - PLAQUE FLB 220.820.40  
8 - PLAQUE DE FROTTEMENT 220.200.15 (friction pad)  
9 - PALIER LISSE SKF PCM 505520 E Ø 55 x 20 x 2.5 mm

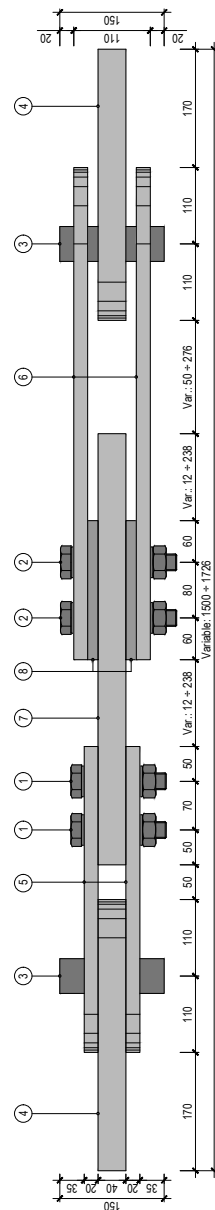
## LEGENDE

- |   |                                |
|---|--------------------------------|
|  | CHARPENTE METALLIQUE           |
|  | PLAQUE DE FROTTEMENT           |
|  | BOULON SHV M24                 |
|  | PAUVIER LISSE SKF PCM 505520 E |

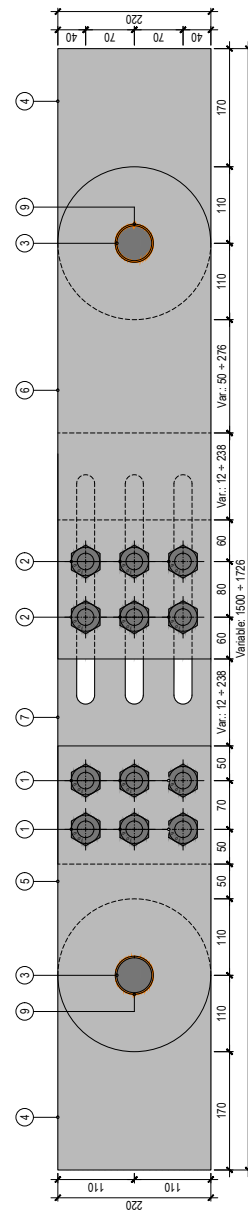
**MATERIAUX:**

- Plaques:  
Plaques de frottement:  
Boulons:  
Axes:
- Acier S35 J2  
Variable  
Classe d'acier 10.9,  $f_{t0} = 900 \text{ N/mm}^2$ ,  $f_{u0} = 1000 \text{ N/mm}^2$   
Acier ETG 100,  $f_t \geq 565 \text{ N/mm}^2$
- BOULONS:**  
Rondelles:  
Rondelles SCHNORR Ref. 701 600,  $\varnothing = 25 \text{ mm}$ ,  $\varnothing_s = 56$

VUE TRANSVERSALE 1:5




## VUE LONGITUDINALE 1:5



|                                 |    |           |     |  |
|---------------------------------|----|-----------|-----|--|
| <b>Dispositif de frottement</b> |    |           |     |  |
| <b>EPFL</b>                     |    |           |     |  |
| <b>Plaque d'extrémité</b>       |    |           |     | <b>Nombre du plan:</b><br>Plannummer:<br>Numero piano: <b>03</b> |
| Ing.:                           | PM | Echelle:  | 1:5 | Plans de référence:  |
| Ing.:                           |    | Massstab: |     | Zugehörige Pläne:  |
| Prog:                           |    | Scala:    |     | Piani di riferimento:  |
| Des.:                           | PM | Format:   | A4  | Date:  |
| Zeichn.:                        |    | Grösse:   |     | Datum:   |
| Dis.:                           |    | Formato:  |     | Data:  |
|                                 |    |           |     | 18.03.2019   |
|                                 |    |           |     | Liste matériaux:   |
|                                 |    |           |     | Materialliste: LM01 et LM02                                      |
|                                 |    |           |     | Lista materiali:   |

**Resilient Steel Structures Laboratory (RESSLab)**  
School of Architecture, Civil, and Environmental Engineering, EPFL  
Attention to: Prof. Dimitrios Lignos  
Phone Number: +41 21 693 2427  
email: dimitrios.lignos@epfl.ch



**LEGENDE**

CHARPENTE METALLIQUE

ROTULE GE 50 ESX-2LS

**ELEMENTS**

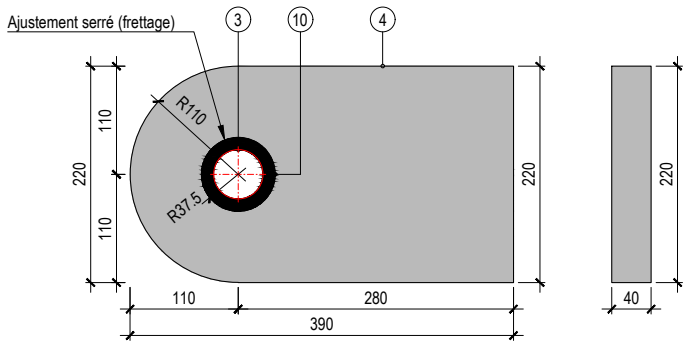
3 - AXE Ø 50 x 150 mm  
4 - PLAQUE FLB 220.390.40  
10 - ROTULE SKF GE 50 ESX-2LS Ø 75,  $F_{Rd,statique} = 780 \text{ kN}$

**MATERIAUX:**

Plaques: Acier S355 J2  
Axes: Acier ETG 100,  $f_y \geq 865 \text{ N/mm}^2$


**PLAQUE D'EXTREMITE 1:5**



|                                 |    |           |     |  |
|---------------------------------|----|-----------|-----|--|
| <b>Dispositif de frottement</b> |    |           |     |  |
| <b>EPFL</b>                     |    |           |     |  |
| <b>Plaque extérieure A-A</b>    |    |           |     | <b>Nombre du plan:</b><br>Plannummer:<br>Numero piano: <b>04</b> |
| Ing.:                           | PM | Echelle:  | 1:5 | Plans de référence:  |
| Ing.:                           |    | Massstab: |     | Zugehörige Pläne:  |
| Prog:                           |    | Scala:    |     | Piani di riferimento:  |
| Des.:                           | PM | Format:   | A4  | Date:  |
| Zeichn.:                        |    | Grösse:   |     | Datum:   |
| Dis.:                           |    | Formato:  |     | Data:  |
|                                 |    |           |     | 18.03.2019   |
|                                 |    |           |     | Liste matériaux:   |
|                                 |    |           |     | Materialliste: LM01 et LM02                                      |
|                                 |    |           |     | Lista materiali:   |

**Resilient Steel Structures Laboratory (RESSLab)**  
 School of Architecture, Civil, and Environmental Engineering, EPFL  
 Attention to: Prof. Dimitrios Lignos  
 Phone Number: +41 21 693 2427  
 email: dimitrios.lignos@epfl.ch



**LEGENDE**

CHARPENTE METALLIQUE

BOULON SHV M24

PALIER LISSE SKF PCM 505520 E

**ELEMENTS**

1 - BOULON SHV M24 10.9, L = 140 mm,  $F_{p,Cd} = 226$  kN  
 3 - AXE Ø 50 x 150 mm  
 5 - PLAQUE FLB 220.440.20  
 9 - PALIER LISSE SKF PCM 505520 E Ø 55 x 20 x 2.5 mm

**MATERIAUX:**

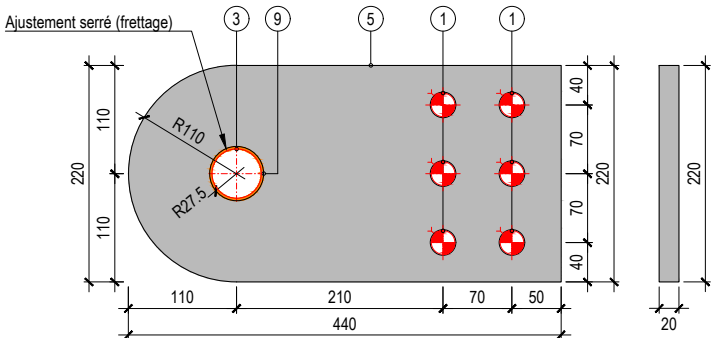
Plaques: Acier S355 J2  
 Plaques de frottement: Variable  
 Boulons: Classe d'acier 10.9,  $f_{yb} = 900$  N/mm<sup>2</sup>,  $f_{ub} = 1000$  N/mm<sup>2</sup>  
 Axes: Acier ETG 100,  $f_y \geq 865$  N/mm<sup>2</sup>

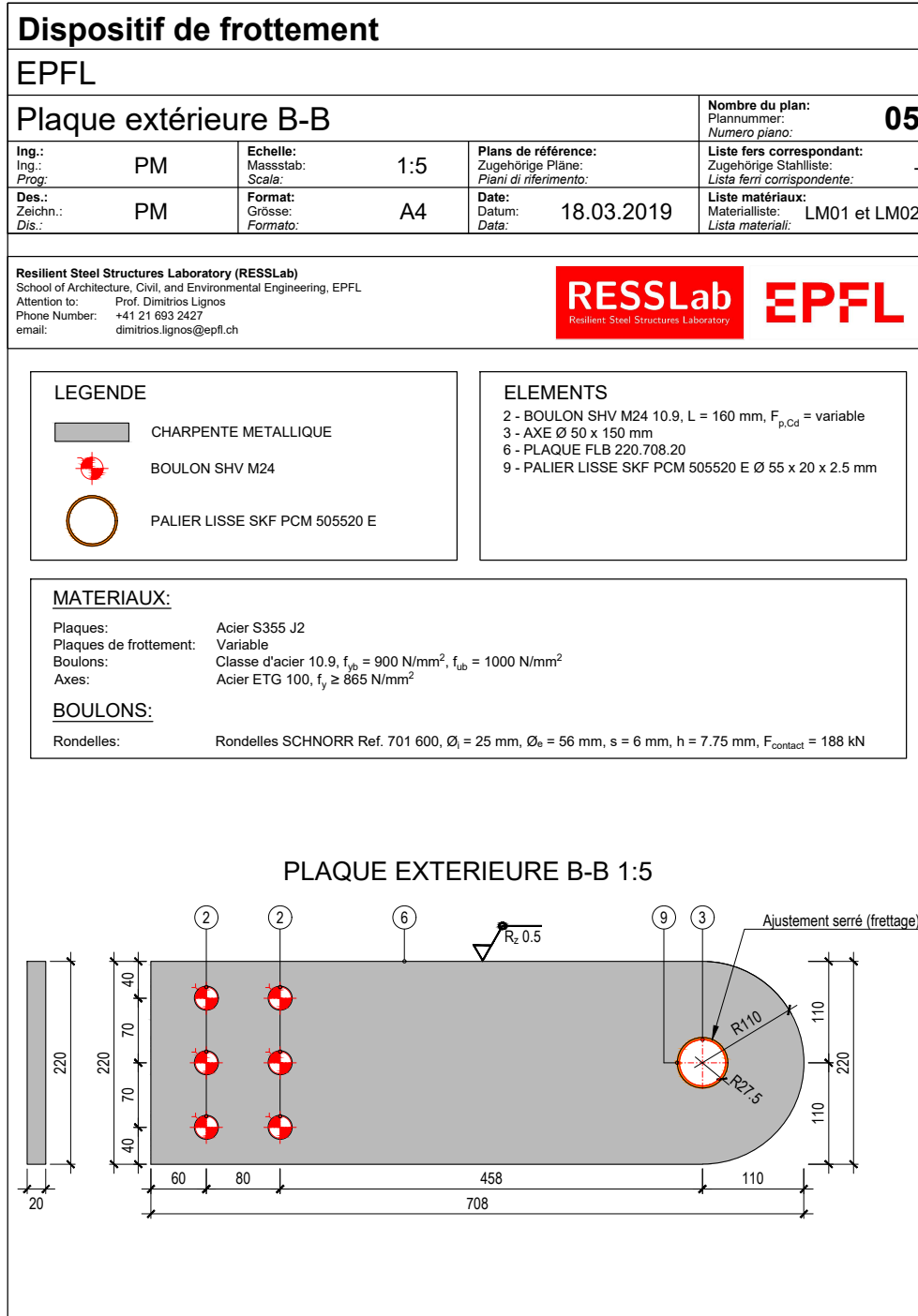
**BOULONS:**

Rondelles: Rondelles SCHNORR Ref. 701 600,  $\phi_i = 25$  mm,  $\phi_e = 56$  mm, s = 6 mm, h = 7.75 mm,  $F_{contact} = 188$  kN

**PLAQUE EXTERIEURE A-A 1:5**





|  |    |           |     |                             |
|--|----|-----------|-----|-----------------------------|
| <b>Dispositif de frottement</b>  |    |           |     |                             |
| <b>EPFL</b>  |    |           |     |                             |
| <b>Plaque intérieure</b>   |    |           |     | <b>Nombre du plan: 06</b>   |
| Ing.:  | PM | Echelle:  | 1:5 | Plans de référence:         |
| Ing.:  |    | Massstab: |     | Zugehörige Pläne:           |
| Prog.:   |    | Scala:    |     | Piani di riferimento:       |
| Des.:  |    | Format:   | A4  | Date:                       |
| Zeichn.:   | PM | Grösse:   |     | Datum:                      |
| Dis.:  |    | Formato:  |     | Data:                       |
|  |    |           |     | Liste fers correspondant:   |
|  |    |           |     | Zugehörige Stahlteile:      |
|  |    |           |     | Liste ferri corrispondente: |
|  |    |           |     | Liste matériaux:            |
|  |    |           |     | Materialliste:              |
|  |    |           |     | Liste materiali:            |
| <div style="display: flex; justify-content: space-between; align-items: center;"> <div> <p><b>Resilient Steel Structures Laboratory (RESSLab)</b><br/> School of Architecture, Civil, and Environmental Engineering, EPFL<br/> Attention to: Prof. Dimitrios Lignos<br/> Phone Number: +41 21 693 2427<br/> email: dimitrios.lignos@epfl.ch</p> </div> <div style="text-align: center;"> <br/> <b>RESSLab</b><br/> Resilient Steel Structures Laboratory </div> <div style="text-align: center;"> </div> </div>  |    |           |     |                             |
| <div style="display: flex; justify-content: space-between;"> <div style="width: 45%;"> <p><b>LEGENDE</b></p> <div style="display: flex; align-items: center; margin-bottom: 10px;"> <div style="width: 20px; height: 10px; background-color: gray; border: 1px solid black; margin-right: 5px;"></div> <span>CHARPENTE METALLIQUE</span> </div> <div style="display: flex; align-items: center;"> <span>BOULON SHV M24</span> </div> </div> <div style="width: 50%;"> <p><b>ELEMENTS</b></p> <p>1 - BOULON SHV M24 10.9, L = 140 mm, <math>F_{p,Cd} = 226</math> kN<br/> 2 - BOULON SHV M24 10.9, L = 160 mm, <math>F_{p,Cd} = \text{variable}</math><br/> 7 - PLAQUE FLB 220.620.40</p> </div> </div> |    |           |     |                             |
| <p><b>MATERIAUX:</b></p> <p>Plaques: Acier S355 J2<br/> Boulons: Classe d'acier 10.9, <math>f_{yb} = 900</math> N/mm<sup>2</sup>, <math>f_{ub} = 1000</math> N/mm<sup>2</sup></p> <p><b>BOULONS:</b></p> <p>Rondelles: Rondelles SCHNORR Ref. 701 600, <math>\varnothing_i = 25</math> mm, <math>\varnothing_e = 56</math> mm, s = 6 mm, h = 7.75 mm, <math>F_{contact} = 188</math> kN</p>  |    |           |     |                             |
| <p><b>PLAQUE INTERIEURE 1:5</b></p>  |    |           |     |                             |

|  |    |   |     |  |
|--|----|---|-----|--|
| <b>Dispositif de frottement</b>  |    |   |     |  |
| <b>EPFL</b>  |    |   |     |  |
| <b>Plaque de frottement</b>  |    |   |     | <b>Nombre du plan:</b><br>Plannummer:<br>Numero piano: <b>07</b> |
| Ing.:  | PM | Echelle:  | 1:5 | Plans de référence:  |
| Ing.:  |    | Massstab:   |     | Zugehörige Pläne:  |
| Prog.:   |    | Scala:  |     | Piani di riferimento:  |
| Des.:  | PM | Format:   | A4  | Date:  |
| Zeichn.:   |    | Grösse:   |     | Datum:   |
| Dis.:  |    | Formato:  |     | Data:  |
|  |    |   |     | 18.03.2019   |
|  |    |   |     | Liste des matériaux:   |
|  |    |   |     | Materialliste: LM02 + LM03                                       |
|  |    |   |     | Lista materiali:   |
| <b>Resilient Steel Structures Laboratory (RESSLab)</b><br>School of Architecture, Civil, and Environmental Engineering, EPFL<br>Attention to: Prof. Dimitrios Lignos<br>Phone Number: +41 21 693 2427<br>email: dimitrios.lignos@epfl.ch   |    |   |     |  |
| <b>LEGENDE</b><br><br>PLAQUE DE FROTTEMENT<br><br>BOULON SHV M24   |    | <b>ELEMENTS</b><br>2 - BOULON SHV M24 10.9, L = 160 mm, $F_{0.2}$ = variable<br>8 - PLAQUE DE FROTTEMENT 220.200.15 (friction pad)<br>8a - PLAQUE DE FROTTEMENT 200.200.15 (friction pad) |     |  |
| <b>MATERIAUX:</b><br>Plaques de frottement: Variable<br>Boulons: Classe d'acier 10.9, $f_{yb} = 900 \text{ N/mm}^2$ , $f_{ub} = 1000 \text{ N/mm}^2$<br><b>BOULONS:</b><br>Rondelles: Rondelles SCHNORR Ref. 701 600, $\varnothing_1 = 25 \text{ mm}$ , $\varnothing_e = 56 \text{ mm}$ , $s = 6 \text{ mm}$ , $h = 7.75 \text{ mm}$ , $F_{\text{contact}} = 188 \text{ kN}$ |    |   |     |  |
| <div style="display: flex; justify-content: space-around;"> <div style="text-align: center;"> <b>PLAQUE DE FROTTEMENT<br/>TYPE A 1:5</b><br/> </div> <div style="text-align: center;"> <b>PLAQUE DE FROTTEMENT<br/>TYPE B 1:5</b><br/> </div> </div>   |    |   |     |  |



EPFL

RESSLab

Resilient Steel Structures Laboratory (RESSLab)

School of Architecture, Civil, and Environmental Engineering, EPFL

Attention to: Prof. Dimitrios Lignos

Phone Number: +41 21 693 2427

email: dimitrios.lignos@epfl.ch

Liste : LM01 - Plaques en acier

Plan: 01 ÷ 06

Date: 14/03/2019

| Pos.    | Description           | Nombre pièces | Elément    | L [mm] | Poids unit. [kg/m] | Poids tot. [kg] | Matériel |
|---------|-----------------------|---------------|------------|--------|--------------------|-----------------|----------|
| pos. 4  | Plaque d'extrémité    | 2             | FLB 220.40 | 390    | 70.4               | 55              | S355 J2  |
| pos. 5  | Plaque extérieure A-A | 2             | FLB 220.20 | 440    | 35.2               | 31              | S355 J2  |
| pos. 6  | Plaque extérieure B-B | 2             | FLB 220.20 | 708    | 35.2               | 50              | S355 J2  |
| pos. 7  | Plaque intérieure     | 1             | FLB 220.40 | 620    | 70.4               | 44              | S355 J2  |
| Totale: |                       |               |            |        |                    | 179             |          |

EPFL

RESSLab

Resilient Steel Structures Laboratory (RESSLab)

School of Architecture, Civil, and Environmental Engineering, EPFL

Attention to: Prof. Dimitrios Lignos

Phone Number: +41 21 693 2427

email: dimitrios.lignos@epfl.ch

Liste : LM02 - Moyens d'assemblage

Plan: 01 ÷ 09

Date: 14/03/2019

| Pos.    | Description                               | Nombre pièces | Elément                   | $\Phi_{max}$ [mm] | L [mm] | Matériel            |
|---------|---|---------------|---------------------------|-------------------|--------|---------------------|
| pos. 1  | Boulon SHV M24 totalement précontraint    | 8             | SHV M24                   | 24                | 140°   | Classe d'acier 10.9 |
| pos. 2  | Boulon SHV M24 partiellement précontraint | 18            | SHV M24                   | 24                | 160°   | Classe d'acier 10.9 |
| pos. 3  | Axe                                       | 2             | Axe $\phi=50mm$           | 50                | 150    | ETG 100 round       |
| pos. 9  | Palier lisse                              | 4             | PCM 505520 E t=2.5mm      | 55                | 20     | -                   |
| pos. 10 | Rotule                                    | 2             | GE 50 ESX-2LS $\phi=50mm$ | 75                | 35     | -                   |

Longueur du boulon L selon Debrunner Acier

| <div>EPFL</div> <div>RESSLab</div> <div>Research in Earthquake Engineering and Structural Dynamics</div>  |                      |  |                  |           |           |           |                                    |                    |          |                                      |  |  |
|---|----------------------|--|------------------|-----------|-----------|-----------|------------------------------------|--------------------|----------|--------------------------------------|--|--|
| Resilient Steel Structures Laboratory (RESSLab)<br>School of Architecture, Civil, and Environmental Engineering, EPFL<br>Attention to: Prof. Dimitrios Lignos<br>Phone Number: +41 21 693 2427<br>email: dimitrios.lignos@epfl.ch |                      |  |                  |           |           |           |                                    |                    |          | Liste : LM03 - Plaques de frottement |  |  |
|   |                      |  |                  |           |           |           |                                    |                    |          | Plan: 01 et 07                       |  |  |
|   |                      |  |                  |           |           |           |                                    |                    |          | Date: 14/03/2019                     |  |  |
| Pos.  | Description          |  | Nombre<br>pièces | h<br>[mm] | t<br>[mm] | L<br>[mm] | Poids vol.<br>[kg/m <sup>3</sup> ] | Poids tot.<br>[kg] | Matériel |                                      |  |  |
| pos. 8a   | Plaque de frottement |  | 26               | 200       | 15        | 200       |                                    |                    | M1       |                                      |  |  |
| pos. 8  |                      |  | 26               | 220       | 15        | 200       | 2200                               | 1.5                | M2       |                                      |  |  |
| pos. 8  |                      |  | 26               | 220       | 15        | 200       | 2200                               | 1.5                | M3       |                                      |  |  |
| pos. 8  |                      |  | 26               | 220       | 15        | 200       | 1993                               | 1.3                | M4       |                                      |  |  |
| pos. 8a   |                      |  | 26               | 200       | 15        | 200       |                                    |                    | M5       |                                      |  |  |



## Instrumentation Plan

This appendix includes a detailed instrumentation plan of the sensors employed during the experimental campaign presented in Chapter 1. In particular, Table B.1 summarizes the instrumentation types used during the tests as well as their measurement range and function. In total, 15 sensors were utilized, including linear variable differential transformers, inclinometers, thermocouples and a washer load cell. Table B.2 describes their measured parameters and location, whereas Figure B.1 and B.2 show the instrumentation of the specimen. Furthermore, Table B.3 summarizes the sensors, which stopped working during several tests.

**Table B.1** – List of instrumentation type and measurement range

| Sensor ID                | Instrument type  | No. of units | Measurement range | Function                  |
|--------------------------|------------------|--------------|-------------------|---------------------------|
| WLC                      | Washer load cell | 1            | 400 kN            | Bolt preload              |
| LVDTh-WE                 | LVDT             | 1            | $\pm 10$ mm       | In-plane displacement     |
| LVDTh-W-NS<br>LVDTh-E-NS | LVDT             | 2            | $\pm 10$ mm       | Out-of-plane displacement |
| LVDTv-W<br>LVDTv-E       | LVDT             | 2            | $\pm 100$ mm      | Axial displacement        |
| INC-WE                   | Inclinometer     | 1            | $\pm 60^\circ$    | In-plane rotation         |
| INC-NS                   | Inclinometer     | 1            | $\pm 60^\circ$    | Out-of-plane rotation     |
| THbolt                   | Thermocouple     | 6            | 250 °C            | Inner temperature         |
| THout                    | Thermocouple     | 1            | 250 °C            | Surface temperature       |

**Table B.2** – List of instrumentation measurements and their notation

| Sensor ID  | Measured parameter        | Symbol              | Location   |
|------------|---------------------------|---------------------|--|
| WLC        | Bolt preload              | $P_{\text{bolt}}$   | Sliding preloaded bolt   |
| LVDTh-WE   | In-plane displacement     | $y_d$               | Inner slotted plate (West-East)                                  |
| LVDTh-W-NS | Out-of-plane displacement | $x_{d,W}$           | Fixed outer plate, west edge (North-South)                       |
| LVDTh-E-NS | Out-of-plane displacement | $x_{d,E}$           | Fixed outer plate, east edge (North-South)                       |
| LVDTv-W    | Axial displacement        | $z_{\text{slot},W}$ | From the sliding outer plate to the fixed outer plate, west edge |
| LVDTv-E    | Axial displacement        | $z_{\text{slot},E}$ | From the sliding outer plate to the fixed outer plate, east edge |
| INC-WE     | In-plane rotation         | $\theta_{WE}$       | Sliding outer plate (West-East)                                  |
| INC-NS     | Out-of-plane rotation     | $\theta_{NS}$       | Sliding outer plate (North-South)                                |
| THbolt     | Inner temperature         | $T_{\text{in}}$     | Sliding preloaded bolt   |
| THout      | Surface temperature       | $T_{\text{surf}}$   | Inner slotted plate  |

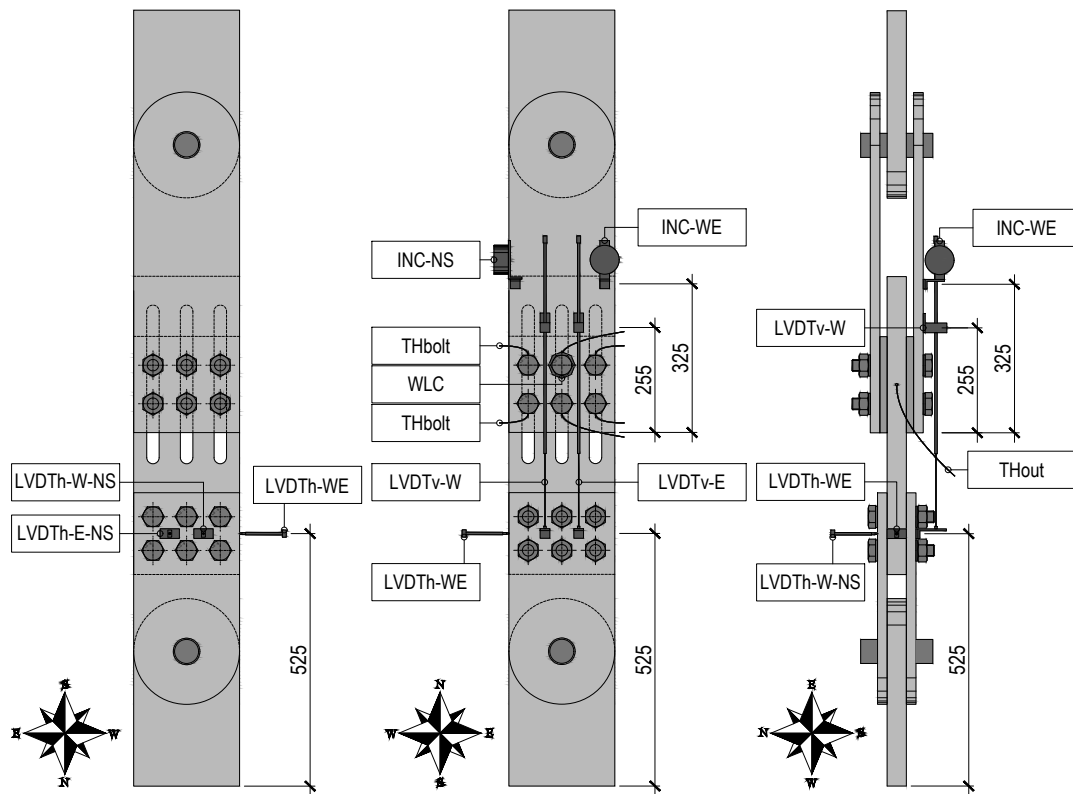


Figure B.1 – Instrumentation plan

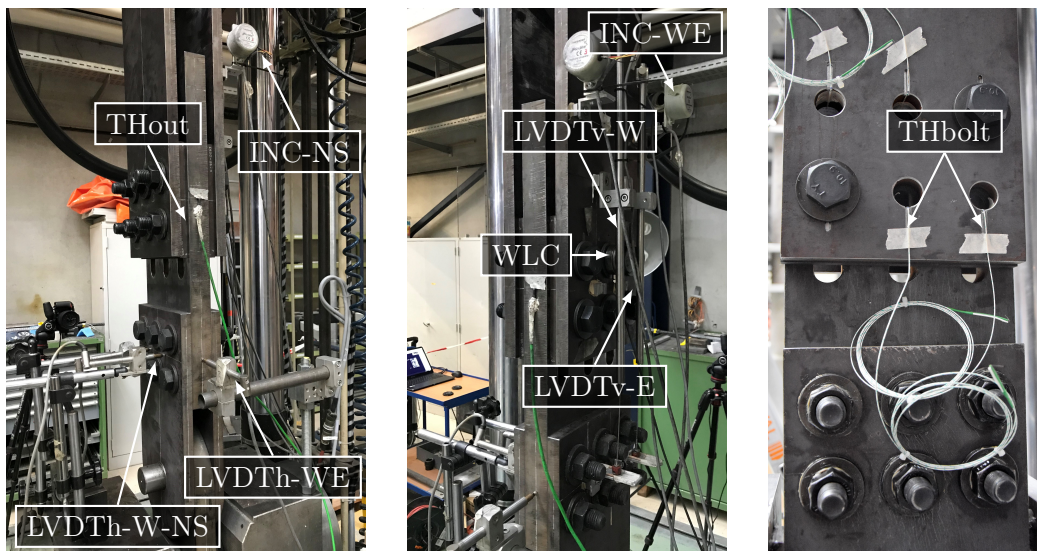
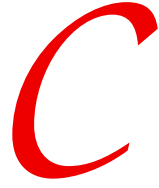


Figure B.2 – Instrumentation of the sliding friction damper

**Table B.3** – List of non-functional sensors

| Material ID | $F_{s,exp}$ [kN] | Loading protocol ID | Sensor  |
|-------------|------------------|---------------------|---------|
| M1          | 300              | IA-H                | LVDTv-W |
| M3          | 150              | M                   | LVDTv-E |
| M3          | 150              | CA                  | WLC     |
| M5          | 150              | DA                  | LVDTv-E |
| M5          | 150              | IA-H                | LVDTv-W |
| M5          | 300              | IA-H                | LVDTv-W |



## Deduced Quantities

This appendix presents the equations used to compute the experimental results discussed in Chapter 1 as a function of the measurements acquired with the sensors listed in Table B.1 and B.2.

### C.1 Average Slot Displacement

The average slot demand experienced by the sliding friction damper is determined as follows:

$$\delta = \frac{z_{\text{slot,W}} + z_{\text{slot,E}}}{2} \quad (\text{C.1})$$

where  $z_{\text{slot,W}}$  and  $z_{\text{slot,E}}$  are the axial displacements measured with LVDTv-W and LVDTv-E respectively (see Fig. B.1 and Table B.2). Referring to Table B.3, in the case that one of these sensors stopped working during a test,  $\delta$  is determined based on the data acquired with the functioning one (i.e.,  $\delta = z_{\text{slot,W}}$  or  $\delta = z_{\text{slot,E}}$ ).

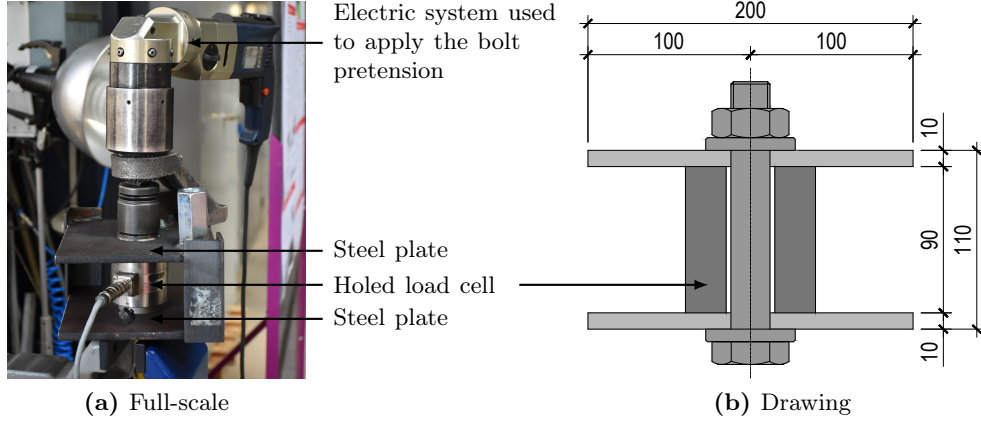


**Figure C.1** – Test setup used to define the relationship between the nominal bolt preload and the applied torque

## C.2 Nominal Bolt Preload

The normal force applied by the preload bolts on the friction pads is a function of the tightening torque  $T_{\text{bolt}}$ . The relationship between these two quantities is defined experimentally as illustrated in Figure C.1. The test setup consists of two squared S355 J2 steel plates and a holed load cell clamped together with a M24 bolt class 10.9 ( $f_{\text{ub}} = 1000 \text{ MPa}$ , see Figure C.1b). The experimental campaign is conducted on three lubricated bolts under three sequences of pretension. During each sequence, the bolts are progressively preloaded by applying five tightening torques (i.e., from 210 Nm to 830 Nm) with the electric system shown in Figure C.1a. The applied pretension is monitored with the holed load cell, which measured force capability is of 500 kN.

Referring to Figure C.2, the measured bolt preload ranges approximately from 40 kN to 210 kN. The dashed-dotted line highlighted in the plot represents the linear regression equation obtained for the prediction of the nominal bolt preload ( $R^2 = 0.93$ ):

$$N_{\text{nom,bolt}} = -1.57 + 0.22 \cdot T_{\text{bolt}} \quad \text{with } T_{\text{bolt}} > 0 \quad (\text{C.2})$$



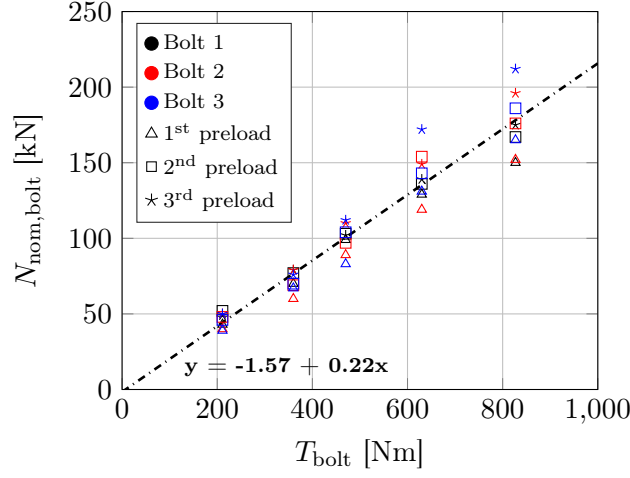


Figure C.2 – Bolt preload as a function of the applied torque ( $R^2 = 0.93$ )

### C.3 Bolt Preload Variation

The variation in bolt preload at instant  $i$  is determined as follows:

$$r_{\text{bolt},i} = \frac{P_{\text{bolt},in} - P_{\text{bolt},i}}{P_{\text{bolt},in}} \quad (\text{C.3})$$

where  $P_{\text{bolt},in}$  is the bolt preload measured with the washer load cell WLC (see Fig. B.1 and Table B.2) at the beginning of each test.

### C.4 Bolt Preload

The bolt preload is determined as follows:

$$N_{\text{bolt}} = N_{\text{nom,bolt}} \cdot (1 - r_{\text{bolt}}) \quad (\text{C.4})$$

where  $N_{\text{nom,bolt}}$  and  $r_{\text{bolt}}$  are computed according to Eq. C.2 and Eq. C.3 respectively.

### C.5 Total Normal Force

The total normal force applied through the preloaded bolts on the friction pads is determined as follows:

$$N_{\text{tot}} = n_{\text{bolt}} \cdot N_{\text{bolt}} \quad (\text{C.5})$$

where  $n_{\text{bolt}}$  is the total number of preloaded bolts (i.e.,  $n_{\text{bolt}} = 6$ ) and  $N_{\text{bolt}}$  is the bolt preload computed according to Eq. C.4.

## C.6 Cumulative Displacement

The cumulative displacement experienced by the sliding friction damper at instant  $i$  is determined as follows:

$$\sum \delta_i = \sum_{k=1}^{k \leq i} \delta_{m,k} \quad (\text{C.6})$$

where  $\delta$  is computed according to Eq. C.1.

## C.7 Cumulative Dissipated Energy

The cumulative energy dissipated by the sliding friction damper at instant  $i$  is computed as follows:

$$\sum E_i = \sum_{k=1}^{k \leq i} F_k \cdot \Delta \delta_k \quad (\text{C.7})$$

where  $F$  and  $\delta$  are, respectively, the axial force and axial displacement experienced by the sliding friction damper. The parameter  $\delta$  is computed according to Eq. C.1, whereas  $F$  is the slip load measured with the load cell of the Schenck machine.

## C.8 Tightening Torque

The tightening torque  $T_{\text{bolt}}$  applied to achieve the expected slip loads  $F_{\text{s,exp}} = 150 \text{ kN}$  and  $F_{\text{s,exp}} = 300 \text{ kN}$  is determined as follows:

$$\text{From Equation C.2:} \quad T_{\text{bolt}} = \frac{1.57 + N_{\text{nom,bolt}}}{0.22} \quad (\text{C.8})$$

$$\text{From Equation 2.2:} \quad N_{\text{tot}} = \frac{F_{\text{s,exp}}}{n_s \cdot \mu_s} \quad (\text{C.9})$$

For  $r_{\text{bolt}} = 0$ ,  $N_{\text{bolt}} = N_{\text{nom,bolt}}$  and  $N_{\text{tot}} = n_{\text{bolt}} \cdot N_{\text{nom,bolt}}$ . Consequently, Equation C.9 and C.8 becomes respectively:

$$N_{\text{nom,bolt}} = \frac{F_{\text{s,exp}}}{n_{\text{s}} \cdot \mu_{\text{s}} \cdot n_{\text{bolt}}} \quad (\text{C.10})$$

$$T_{\text{bolt}} = \frac{1}{0.22} \left( 1.57 + \frac{F_{\text{s,exp}}}{n_{\text{s}} \cdot \mu_{\text{s}} \cdot n_{\text{bolt}}} \right) \quad (\text{C.11})$$





## Supplementary Results from the Experimental Campaign

This appendix provides supplementary results from the experimental campaign conducted on the sliding friction damper prototype that are not included in Chapter 1.

### D.1 Friction Pad M1

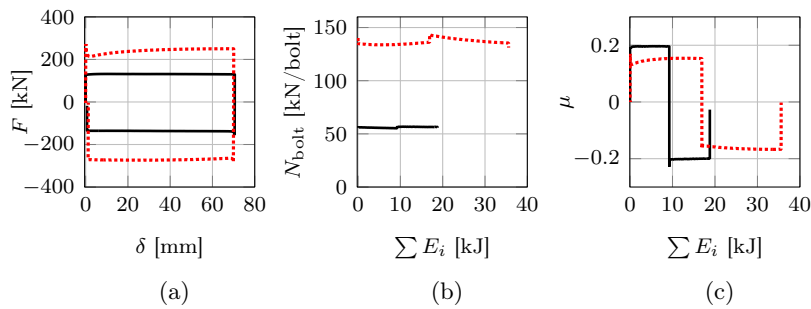


**Figure D.1** – Results obtained for the friction pad M1 under the linear static loading protocol ( $F_{s,exp} = 150$  kN: solid line,  $F_{s,exp} = 300$  kN: dotted line): (a) axial force as a function of the average slot displacement, (b) bolt preload as a function of the cumulative dissipated energy, (c) friction coefficient as a function of the cumulative dissipated energy

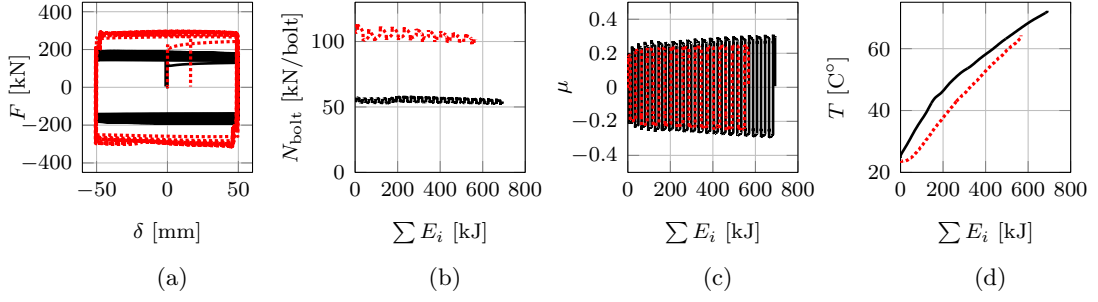


**Figure D.2** – Results obtained for the friction pad M1 under the cyclic loading protocol with constant amplitude ( $F_{s,exp} = 150$  kN: solid line,  $F_{s,exp} = 300$  kN: dotted line): (a) axial force as a function of the average slot displacement, (b) bolt preload as a function of the cumulative dissipated energy, (c) friction coefficient as a function of the cumulative dissipated energy, (d) temperature as a function of the cumulative dissipated energy

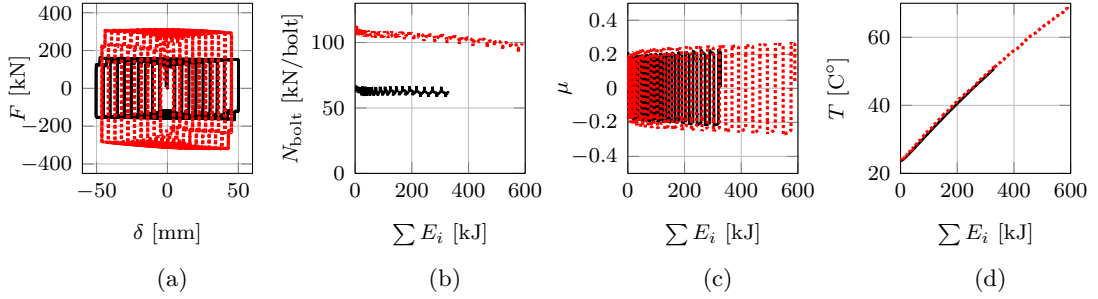


**Figure D.3** – Results obtained for the friction pad M1 under the cyclic loading protocol with increasing amplitude at low rate ( $F_{s,exp} = 150$  kN: solid line,  $F_{s,exp} = 300$  kN: dotted line): (a) axial force as a function of the average slot displacement, (b) bolt preload as a function of the cumulative dissipated energy, (c) friction coefficient as a function of the cumulative dissipated energy, (d) temperature as a function of the cumulative dissipated energy

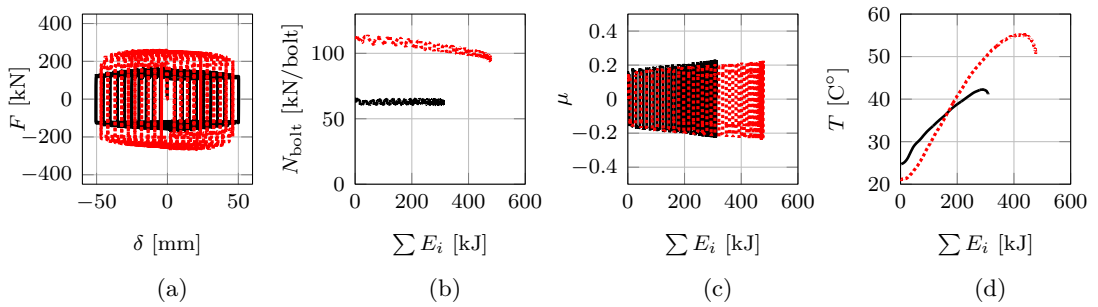


**Figure D.4** – Results obtained for the friction pad M1 under the cyclic loading protocol with decreasing amplitude at low rate ( $F_{s,exp} = 150$  kN: solid line,  $F_{s,exp} = 300$  kN: dotted line): (a) axial force as a function of the average slot displacement, (b) bolt preload as a function of the cumulative dissipated energy, (c) friction coefficient as a function of the cumulative dissipated energy, (d) temperature as a function of the cumulative dissipated energy

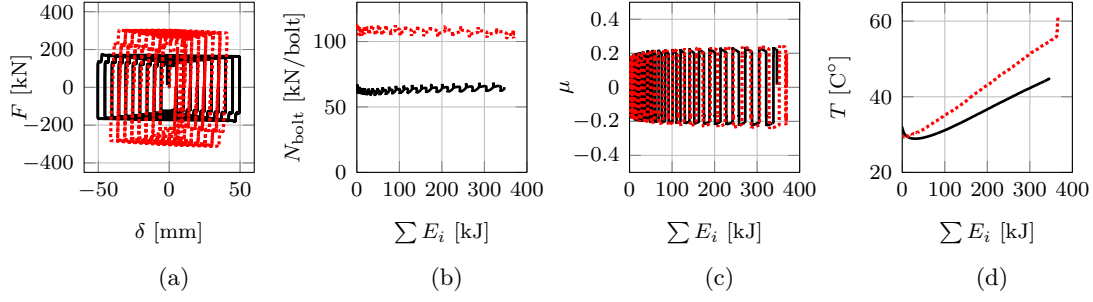


**Figure D.5** – Results obtained for the friction pad M1 under the cyclic loading protocol with increasing amplitude at moderate rate ( $F_{s,exp} = 150$  kN: solid line,  $F_{s,exp} = 300$  kN: dotted line): (a) axial force as a function of the average slot displacement, (b) bolt preload as a function of the cumulative dissipated energy, (c) friction coefficient as a function of the cumulative dissipated energy, (d) temperature as a function of the cumulative dissipated energy

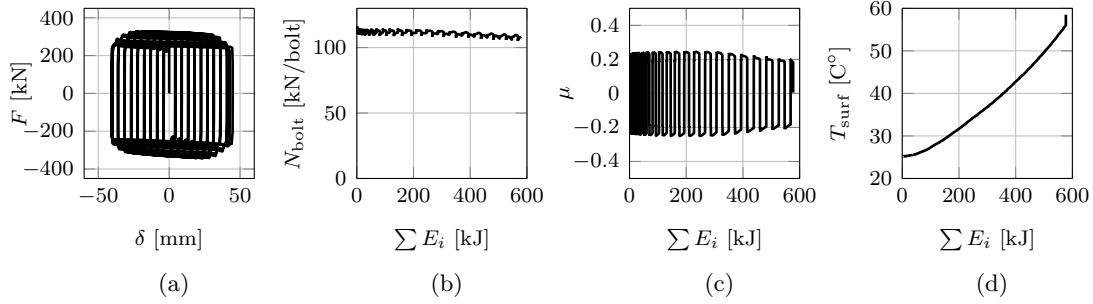


**Figure D.6** – Results obtained for the friction pad M1 under the cyclic loading protocol with increasing amplitude at high rate and  $F_{s,exp} = 300$  kN: (a) axial force as a function of the average slot displacement, (b) bolt preload as a function of the cumulative dissipated energy, (c) friction coefficient as a function of the cumulative dissipated energy, (d) temperature as a function of the cumulative dissipated energy

## D.2 Friction Pad M2

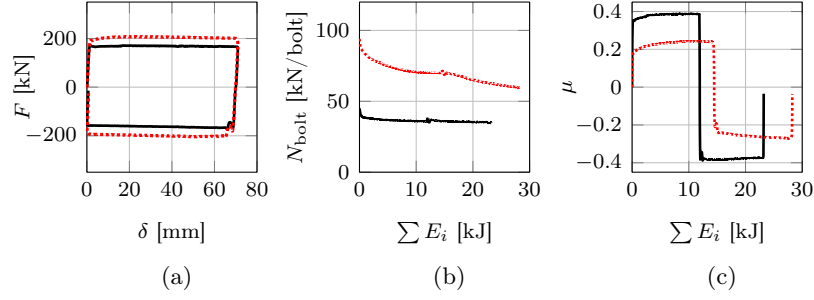


**Figure D.7** – Results obtained for the friction pad M2 under the linear static loading protocol ( $F_{s,exp} = 150$  kN: solid line,  $F_{s,exp} = 300$  kN: dotted line): (a) axial force as a function of the average slot displacement, (b) bolt preload as a function of the cumulative dissipated energy, (c) friction coefficient as a function of the cumulative dissipated energy

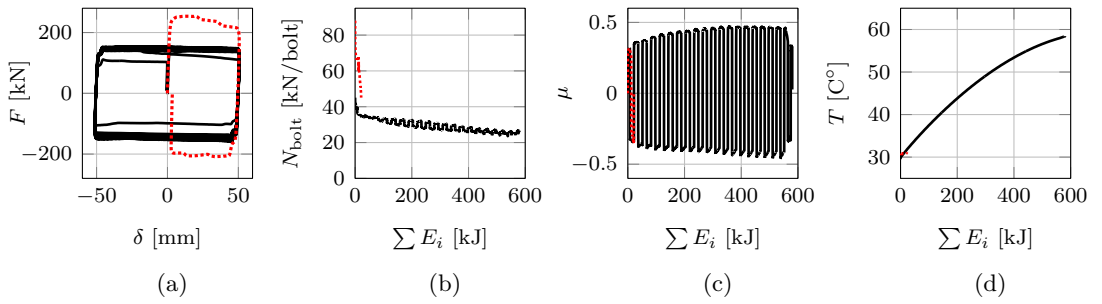


**Figure D.8** – Results obtained for the friction pad M2 under the cyclic loading protocol with constant amplitude ( $F_{s,exp} = 150$  kN: solid line,  $F_{s,exp} = 300$  kN: dotted line): (a) axial force as a function of the average slot displacement, (b) bolt preload as a function of the cumulative dissipated energy, (c) friction coefficient as a function of the cumulative dissipated energy, (d) temperature as a function of the cumulative dissipated energy



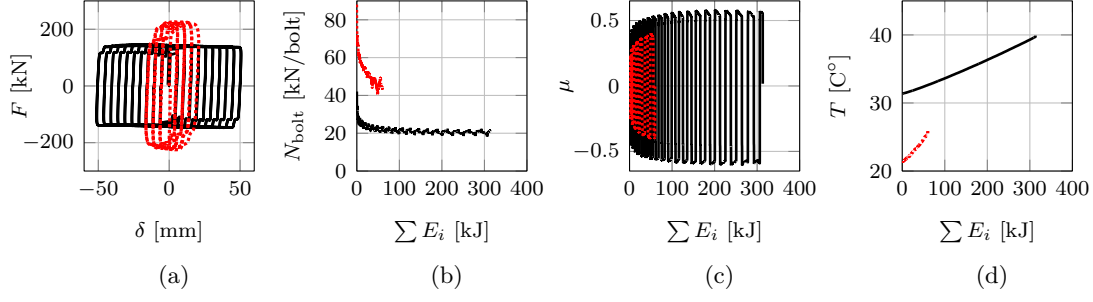


**Figure D.9** – Results obtained for the friction pad M2 under the cyclic loading protocol with increasing amplitude at low rate ( $F_{s,exp} = 150$  kN: solid line,  $F_{s,exp} = 300$  kN: dotted line): (a) axial force as a function of the average slot displacement, (b) bolt preload as a function of the cumulative dissipated energy, (c) friction coefficient as a function of the cumulative dissipated energy, (d) temperature as a function of the cumulative dissipated energy

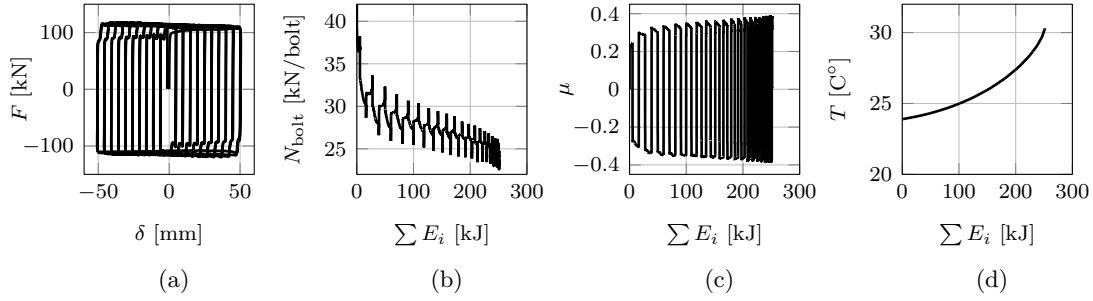


**Figure D.10** – Results obtained for the friction pad M2 under the cyclic loading protocol with decreasing amplitude at low rate and  $F_{s,exp} = 150$  kN: (a) axial force as a function of the average slot displacement, (b) bolt preload as a function of the cumulative dissipated energy, (c) friction coefficient as a function of the cumulative dissipated energy, (d) temperature as a function of the cumulative dissipated energy

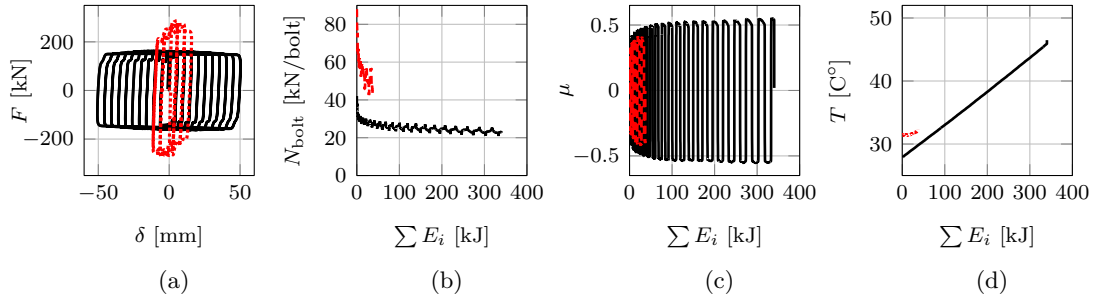


**Figure D.11** – Results obtained for the friction pad M2 under the cyclic loading protocol with increasing amplitude at moderate rate ( $F_{s,exp} = 150$  kN: solid line,  $F_{s,exp} = 300$  kN: dotted line): (a) axial force as a function of the average slot displacement, (b) bolt preload as a function of the cumulative dissipated energy, (c) friction coefficient as a function of the cumulative dissipated energy, (d) temperature as a function of the cumulative dissipated energy

### D.3 Friction Pad M3

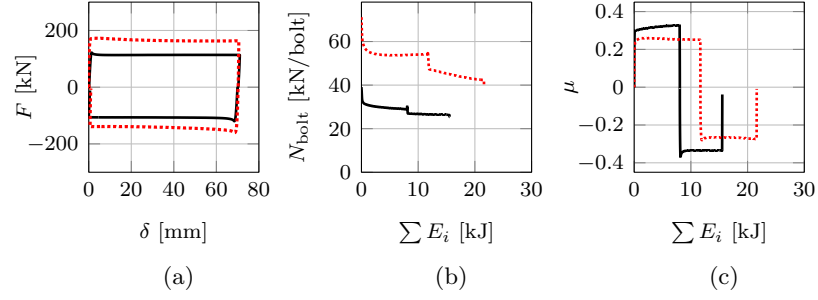


**Figure D.12** – Results obtained for the friction pad M3 under the linear static loading protocol ( $F_{s,exp} = 150$  kN: solid line,  $F_{s,exp} = 300$  kN: dotted line): (a) axial force as a function of the average slot displacement, (b) bolt preload as a function of the cumulative dissipated energy, (c) friction coefficient as a function of the cumulative dissipated energy

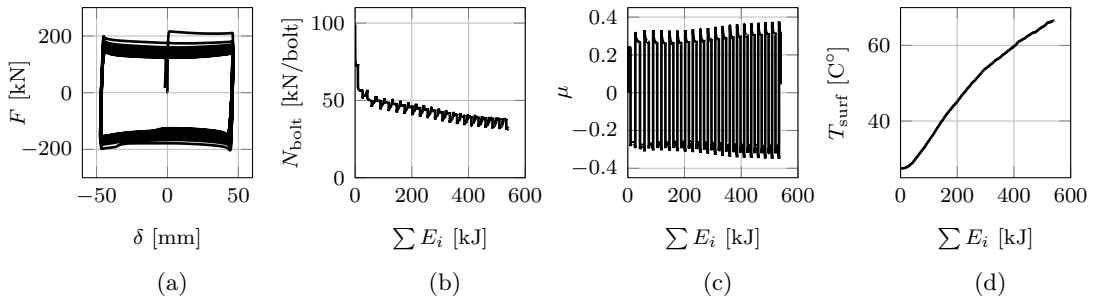


**Figure D.13** – Results obtained for the friction pad M3 under the cyclic loading protocol with constant amplitude and  $F_{s,exp} = 300$  kN: (a) axial force as a function of the average slot displacement, (b) bolt preload as a function of the cumulative dissipated energy, (c) friction coefficient as a function of the cumulative dissipated energy, (d) temperature as a function of the cumulative dissipated energy

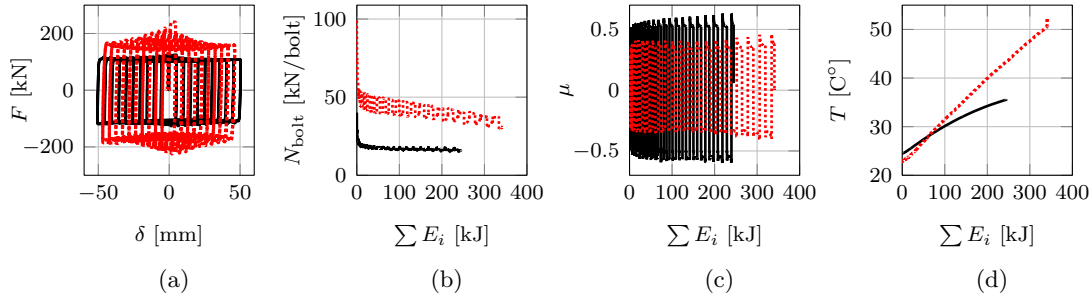


**Figure D.14** – Results obtained for the friction pad M3 under the cyclic loading protocol with increasing amplitude at low rate ( $F_{s,\text{exp}} = 150$  kN: solid line,  $F_{s,\text{exp}} = 300$  kN: dotted line): (a) axial force as a function of the average slot displacement, (b) bolt preload as a function of the cumulative dissipated energy, (c) friction coefficient as a function of the cumulative dissipated energy, (d) temperature as a function of the cumulative dissipated energy

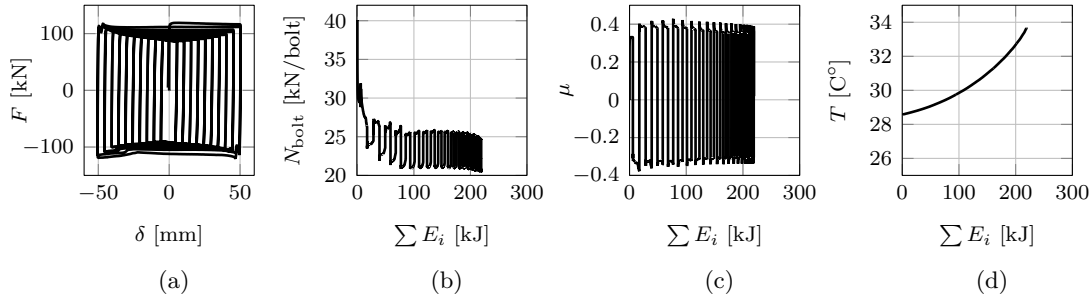


**Figure D.15** – Results obtained for the friction pad M3 under the cyclic loading protocol with decreasing amplitude at low rate and  $F_{s,\text{exp}} = 150$  kN: (a) axial force as a function of the average slot displacement, (b) bolt preload as a function of the cumulative dissipated energy, (c) friction coefficient as a function of the cumulative dissipated energy, (d) temperature as a function of the cumulative dissipated energy

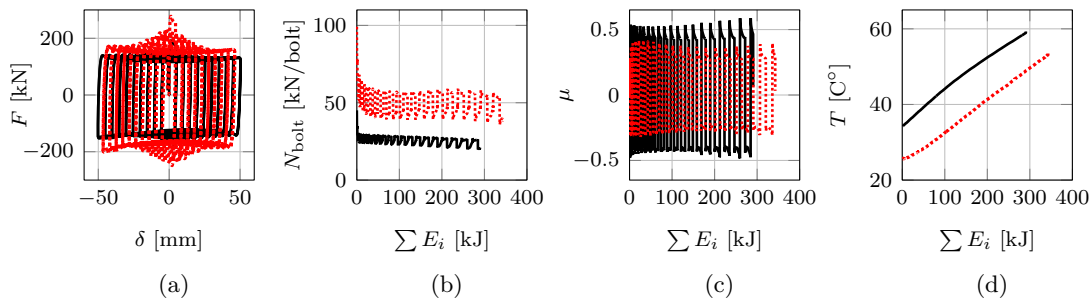


**Figure D.16** – Results obtained for the friction pad M3 under the cyclic loading protocol with increasing amplitude at moderate rate ( $F_{s,\text{exp}} = 150$  kN: solid line,  $F_{s,\text{exp}} = 300$  kN: dotted line): (a) axial force as a function of the average slot displacement, (b) bolt preload as a function of the cumulative dissipated energy, (c) friction coefficient as a function of the cumulative dissipated energy, (d) temperature as a function of the cumulative dissipated energy

## D.4 Friction Pad M4

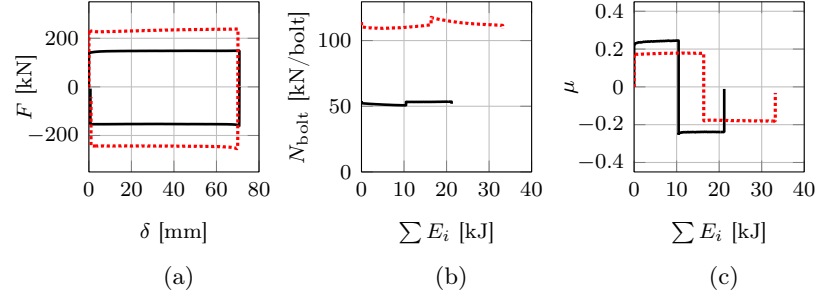


**Figure D.17** – Results obtained for the friction pad M4 under the linear static loading protocol ( $F_{s,exp} = 150$  kN: solid line,  $F_{s,exp} = 300$  kN: dotted line): (a) axial force as a function of the average slot displacement, (b) bolt preload as a function of the cumulative dissipated energy, (c) friction coefficient as a function of the cumulative dissipated energy

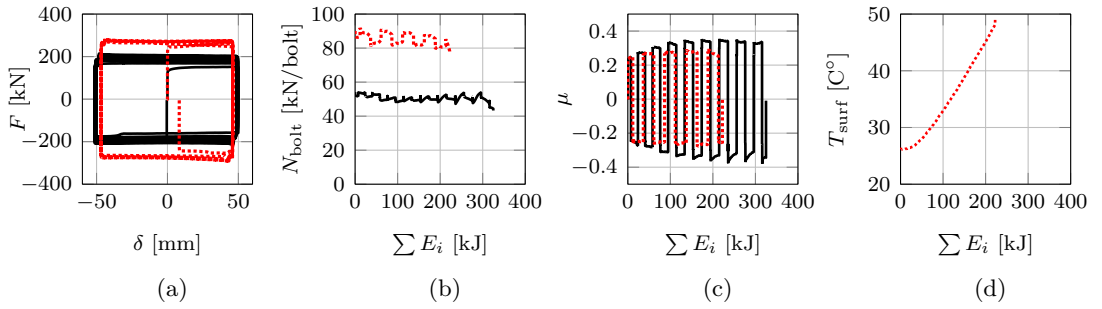


**Figure D.18** – Results obtained for the friction pad M4 under the cyclic loading protocol with constant amplitude ( $F_{s,exp} = 150$  kN: solid line,  $F_{s,exp} = 300$  kN: dotted line): (a) axial force as a function of the average slot displacement, (b) bolt preload as a function of the cumulative dissipated energy, (c) friction coefficient as a function of the cumulative dissipated energy, (d) temperature as a function of the cumulative dissipated energy

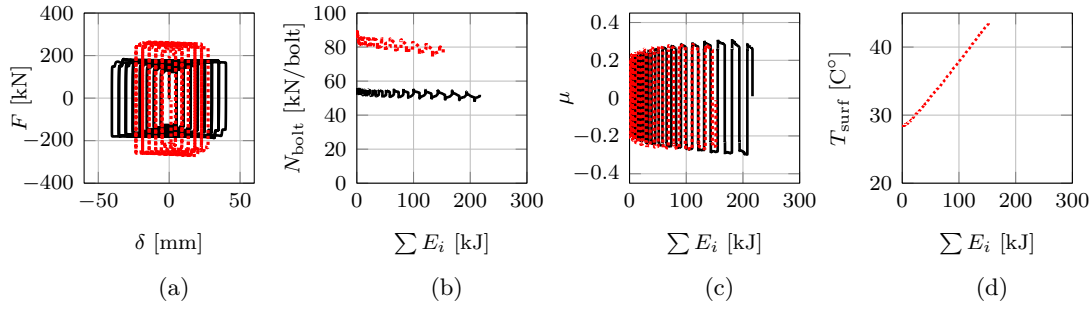


**Figure D.19** – Results obtained for the friction pad M4 under the cyclic loading protocol with increasing amplitude at low rate ( $F_{s,exp} = 150$  kN: solid line,  $F_{s,exp} = 300$  kN: dotted line): (a) axial force as a function of the average slot displacement, (b) bolt preload as a function of the cumulative dissipated energy, (c) friction coefficient as a function of the cumulative dissipated energy, (d) temperature as a function of the cumulative dissipated energy

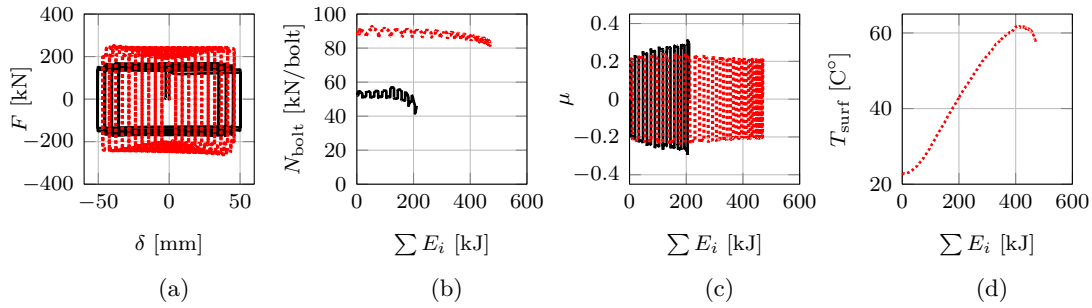


**Figure D.20** – Results obtained for the friction pad M4 under the cyclic loading protocol with decreasing amplitude at low rate ( $F_{s,exp} = 150$  kN: solid line,  $F_{s,exp} = 300$  kN: dotted line): (a) axial force as a function of the average slot displacement, (b) bolt preload as a function of the cumulative dissipated energy, (c) friction coefficient as a function of the cumulative dissipated energy, (d) temperature as a function of the cumulative dissipated energy

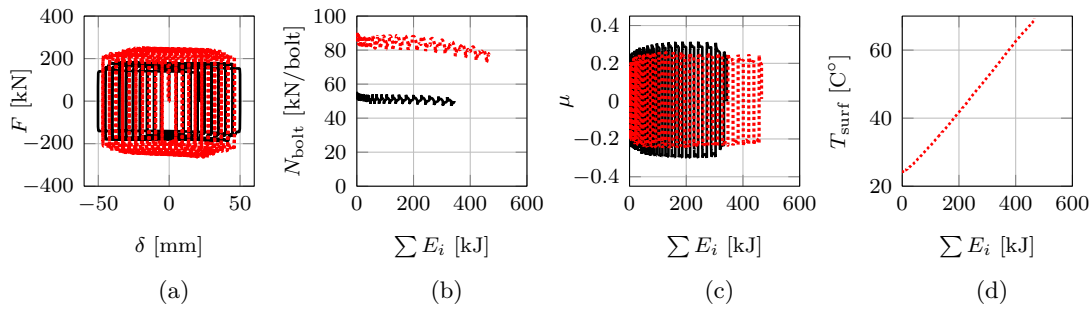


**Figure D.21** – Results obtained for the friction pad M4 under the cyclic loading protocol with increasing amplitude at moderate rate ( $F_{s,exp} = 150$  kN: solid line,  $F_{s,exp} = 300$  kN: dotted line): (a) axial force as a function of the average slot displacement, (b) bolt preload as a function of the cumulative dissipated energy, (c) friction coefficient as a function of the cumulative dissipated energy, (d) temperature as a function of the cumulative dissipated energy

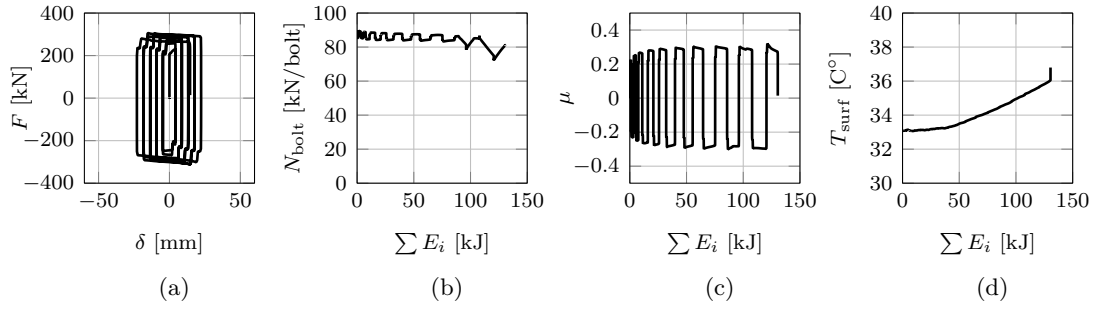


**Figure D.22** – Results obtained for the friction pad M4 under the cyclic loading protocol with increasing amplitude at high rate and  $F_{\text{s,exp}} = 300$  kN: (a) axial force as a function of the average slot displacement, (b) bolt preload as a function of the cumulative dissipated energy, (c) friction coefficient as a function of the cumulative dissipated energy, (d) temperature as a function of the cumulative dissipated energy

## D.5 Friction Pad M5

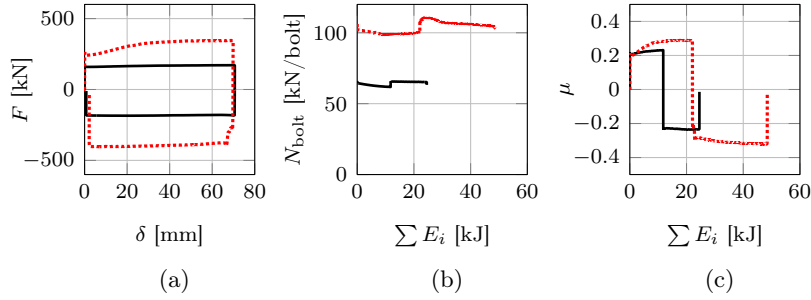


**Figure D.23** – Results obtained for the friction pad M5 under the linear static loading protocol ( $F_{s,exp} = 150$  kN: solid line,  $F_{s,exp} = 300$  kN: dotted line): (a) axial force as a function of the average slot displacement, (b) bolt preload as a function of the cumulative dissipated energy, (c) friction coefficient as a function of the cumulative dissipated energy

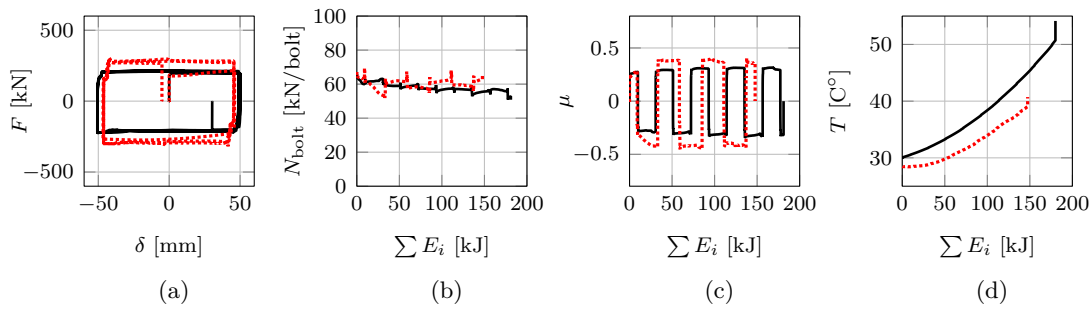


**Figure D.24** – Results obtained for the friction pad M5 under the cyclic loading protocol with constant amplitude ( $F_{s,exp} = 150$  kN: solid line,  $F_{s,exp} = 300$  kN: dotted line): (a) axial force as a function of the average slot displacement, (b) bolt preload as a function of the cumulative dissipated energy, (c) friction coefficient as a function of the cumulative dissipated energy, (d) temperature as a function of the cumulative dissipated energy

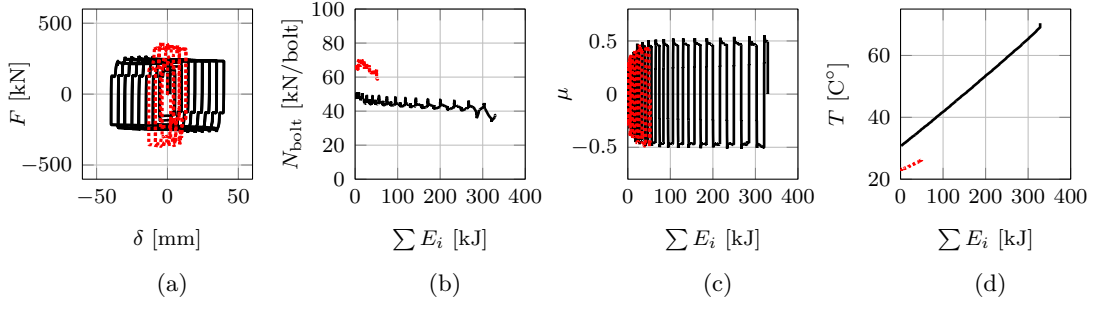


**Figure D.25** – Results obtained for the friction pad M5 under the cyclic loading protocol with increasing amplitude at low rate ( $F_{s,exp} = 150$  kN: solid line,  $F_{s,exp} = 300$  kN: dotted line): (a) axial force as a function of the average slot displacement, (b) bolt preload as a function of the cumulative dissipated energy, (c) friction coefficient as a function of the cumulative dissipated energy, (d) temperature as a function of the cumulative dissipated energy

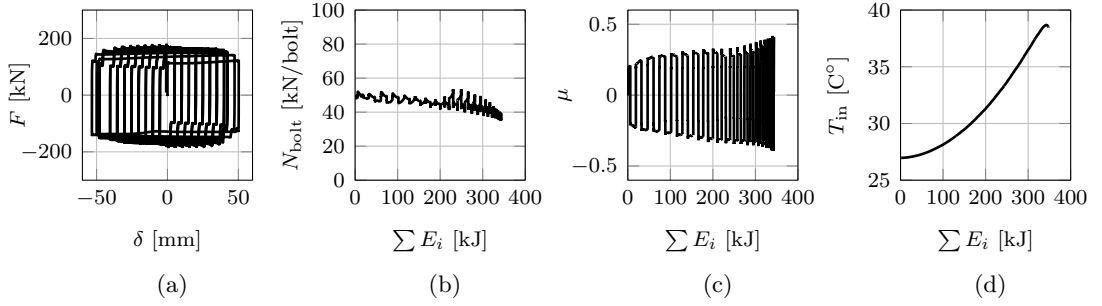


**Figure D.26** – Results obtained for the friction pad M5 under the cyclic loading protocol with decreasing amplitude at low rate and  $F_{s,exp} = 150$  kN: (a) axial force as a function of the average slot displacement, (b) bolt preload as a function of the cumulative dissipated energy, (c) friction coefficient as a function of the cumulative dissipated energy, (d) temperature as a function of the cumulative dissipated energy

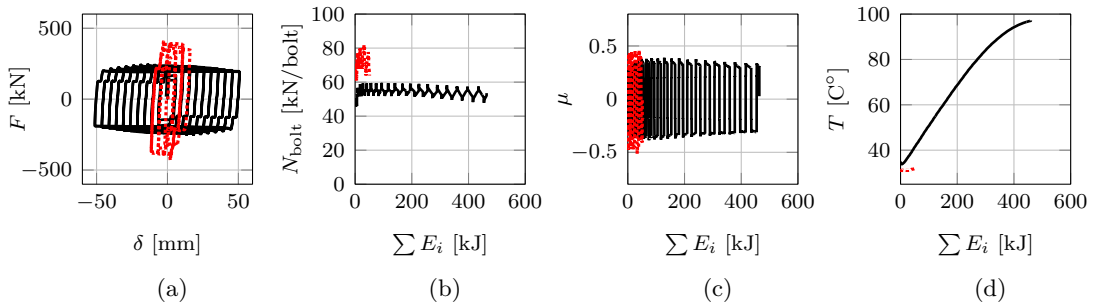


**Figure D.27** – Results obtained for the friction pad M5 under the cyclic loading protocol with increasing amplitude at moderate rate ( $F_{s,exp} = 150$  kN: solid line,  $F_{s,exp} = 300$  kN: dotted line): (a) axial force as a function of the average slot displacement, (b) bolt preload as a function of the cumulative dissipated energy, (c) friction coefficient as a function of the cumulative dissipated energy, (d) temperature as a function of the cumulative dissipated energy





# Design Summary of the 6-story Steel CBF Buildings

This appendix provides a design summary of the CBFs of the two 6-story steel buildings investigated in Chapters [2](#) and [3](#).

## E.1 Design standards

The investigated buildings are designed according to the following design standards:

- SZS C5/05 [\[220\]](#): Swiss steelwork manual used to define the cross-section properties of the structural members (i.e., beams, columns and braces);
- SZS C1/12 [\[221\]](#): Swiss steelwork manual used to define the properties of the profiled steel decks;
- EN 1990 [\[164\]](#): Eurocode used to define the combination of actions at the serviceability and ultimate limit states;
- EN 1991: Eurocodes used to define the permanent and variable loads acting on the buildings; these include EN 1991-1-1 [\[165\]](#) for self-weight and imposed loads, EN 1991-1-3 [\[222\]](#) for snow load and EN 1991-1-4 [\[223\]](#) for wind load;
- EN 1992-1-1 [\[224\]](#): Eurocode used to design the reinforced concrete slabs;

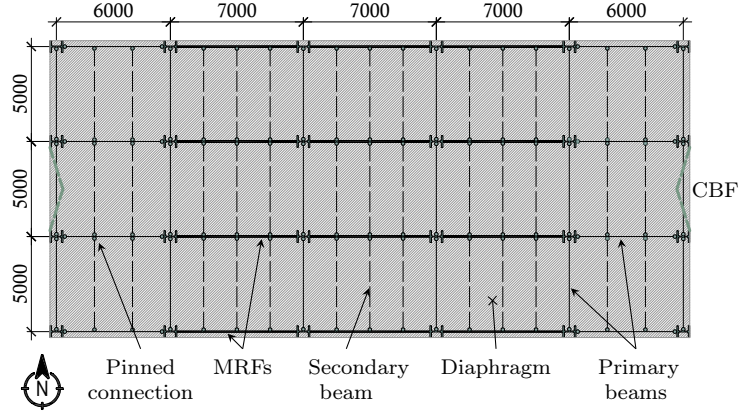


**Figure E.1** – Plan view of the buildings

- EN 1993: Eurocodes used to design the structural steel components; these includes EN 1993-1-1 [149] for the design of the steel beams, columns and braces, and EN 1993-1-8 [150] for the design of the joints;
- EN 1998-1-1 [53]: Eurocode used for the capacity design and detailing of the building components under the seismic load combination

## E.2 Basic Description of the Buildings

### E.2.1 Structural Type and Layout

The investigated buildings are two 6-story steel buildings of importance class II designed for  $q = 2.0$  and  $q = 3.0$  according to the European provisions listed in Section E.1. Their design location is situated in Sion (Switzerland), in a region characterized by a soil type D and a reference peak ground acceleration ( $a_{gR}$ ) of 0.22 g.

The two buildings have the same elevation and plan layout. As illustrated in Fig. E.1, they consist of four moment-resisting frames (MRFs) in the East-West (E-W) direction and two perimeter concentrically braced frames (CBFs) in the North-South (N-S) direction. The height of the first story is of 4.5 m, whereas that of the remaining stories is of 4.0 m. Columns are oriented around their weak axis in the N-S direction and they are spliced at story 3 and 5. Their base supports are fixed in the E-W direction and pinned in the N-S direction. In the E-W direction, the primary beams are connected to the columns with stiffened end-plate connections, whereas those in the N-S direction are pin-jointed at their ends. In addition, secondary beams with pin-jointed ends span in the N-S direction. The diaphragms consist of profiled steel decks with ribs running in the

**Table E.1** – Member cross sections of the CBFs and MRFs of the building designed for  $q = 2$ 

| Story | CBF <sup>a</sup> |         |              | MRF <sup>a</sup> |           |           |
|-------|------------------|---------|--------------|------------------|-----------|-----------|
|       | Beams            | Columns | Braces       | Beams            | Int. col. | Ext. col. |
| 6     | IPE 270          | HEB 180 | ROR 219.1x10 | HEB 300          | HEB 300   | HEB 300   |
| 5     | IPE 270          | HEB 180 | ROR 219.1x16 | HEB 300          | HEB 300   | HEB 300   |
| 4     | IPE 270          | HEB 320 | ROR 219.1x16 | HEB 450          | HEB 360   | HEB 360   |
| 3     | IPE 270          | HEB 320 | ROR 244.5x16 | HEB 450          | HEB 360   | HEB 360   |
| 2     | IPE 270          | HEM 400 | ROR 244.5x16 | HEB 450          | HEM 340   | HEM 340   |
| 1     | IPE 270          | HEM 400 | ROR 273x16   | HEB 450          | HEM 340   | HEM 340   |

<sup>a</sup> Column slices at the 3<sup>rd</sup> and 5<sup>th</sup> story

E-W direction. For  $q = 2$ , no composite action is considered to design the beams of the building. Conversely, for  $q = 3$ , the primary beams of the MRFs are sized by considering full composite action.

### E.2.2 Member Cross Sections

Figures E.2 and E.3 illustrate the elevation of the two buildings in the E-W and N-S direction. Tables E.1 and E.2 summarizes the member cross sections of the CBFs and MRFs designed for  $q = 2.0$  and  $q = 3.0$ , respectively.

At each floor, the diaphragms of the two buildings consist of profiled steel decks with rib oriented in the E-W direction (i.e. parallel to the primary beams of the MRFs). For  $q = 2.0$ , 110 mm deep slab featuring a 0.75 mm thick Cofrastra 56 deck is obtained from the Swiss C1/12 steelwork manual. Similarly, for  $q = 3.0$ , the deck configuration is constituted by a 130 mm deep slab featuring a 0.88 mm thick Cofrastra 56 deck. In such a case,  $\Phi 16$  mm headed shear stud connectors spaced at 200 mm are used to achieve full composite action in the composite steel beams of the MRFs.

### E.2.3 Material Properties

Tables E.3 and E.4 summarize the material properties of the primary structural components of the two buildings. Notably, all the steel members are fabricated from S355 J2 steel, whereas high-strength bolts 10.9 class are utilized for the steel connections. Referring to Table E.4, each diaphragm consists of a concrete slab C25/30 reinforced through B500B steel rebars and featuring a S350GD Cofrastra 56 deck.



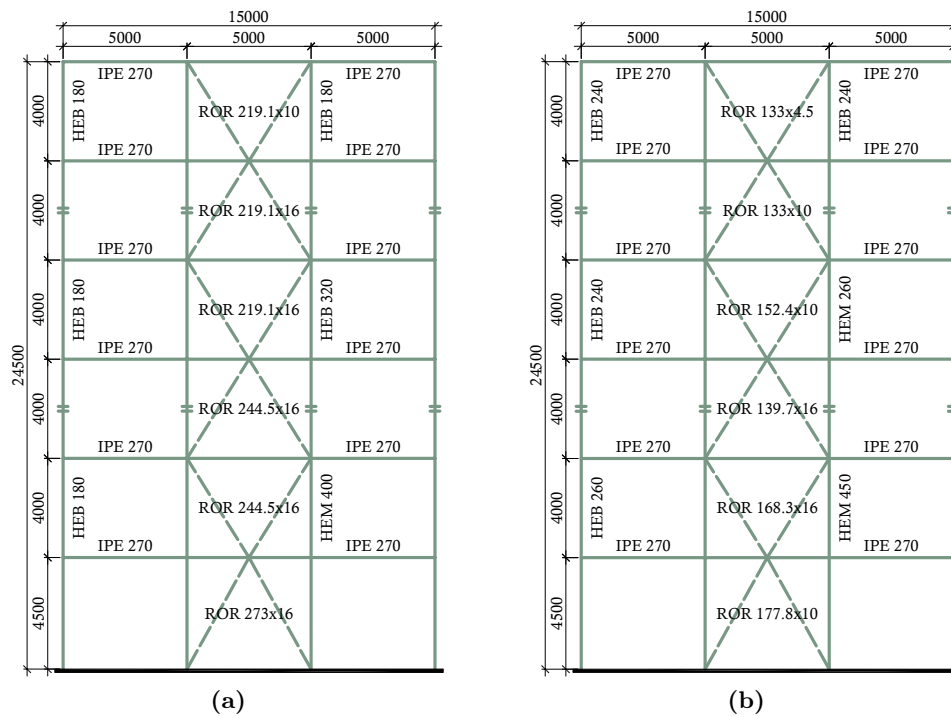


**Figure E.3** – Elevation view of the building designed for (a)  $q = 2$  and (b)  $q = 3$  in the N-S direction

**Table E.2** – Member cross sections of the CBFs and MRFs of the building designed for  $q = 3$

| Story | CBF <sup>a</sup> |         |              | MRF <sup>a</sup> |           |           |
|-------|------------------|---------|--------------|------------------|-----------|-----------|
|       | Beams            | Columns | Braces       | Beams            | Int. col. | Ext. col. |
| 6     | IPE 270          | HEB 240 | ROR 133x4.5  | IPE 270          | HEB 240   | HEB 280   |
| 5     | IPE 270          | HEB 240 | ROR 133x10   | IPE 270          | HEB 240   | HEB 280   |
| 4     | IPE 270          | HEB 260 | ROR 152.4x10 | IPE 400          | HEB 300   | HEB 340   |
| 3     | IPE 270          | HEB 260 | ROR 139.7x16 | IPE 400          | HEB 300   | HEB 340   |
| 2     | IPE 270          | HEM 450 | ROR 168.3x16 | IPE 400          | HEB 360   | HEB 550   |
| 1     | IPE 270          | HEM 450 | ROR 177.8x10 | IPE 400          | HEB 360   | HEB 550   |

<sup>a</sup> Column slices at the 3<sup>rd</sup> and 5<sup>th</sup> story

**Table E.3** – Material properties of the steel members

| Member  | Grade   | $f_y^a$<br>[N/mm <sup>2</sup> ] | $f_u^b$<br>[N/mm <sup>2</sup> ] | $E_s^c$<br>[N/mm <sup>2</sup> ] | $\nu^d$<br>[-] | $G^e$<br>[N/mm <sup>2</sup> ] |
|---------|---------|---------------------------------|---------------------------------|---------------------------------|----------------|-------------------------------|
| Beams   | S355 J2 | 355                             | 510                             | 210000                          | 0.3            | 80769                         |
| Columns | S355 J2 | 355                             | 510                             | 210000                          | 0.3            | 80769                         |
| Braces  | S355 J2 | 355                             | 510                             | 210000                          | 0.3            | 80769                         |

<sup>a</sup> Nominal value of yield strength according to EN 1993-1-1, Table 3.1

<sup>b</sup> Nominal value of ultimate tensile strength according to EN 1993-1-1, Table 3.1

<sup>c</sup> Steel Young's modulus according to EN 1993-1-1, Sec. 3.2.6

<sup>d</sup> Steel Poisson's ratio according to EN 1993-1-1, Sec. 3.2.6

<sup>e</sup> Steel shear modulus of elasticity according to EN 1993-1-1, Sec. 3.2.6

**Table E.4** – Material properties of the high-strength bolts and diaphragms

| Component          | Properties                           | Description   |
|--------------------|--------------------------------------|---|
| Bolts              | Grade: 10.9                          |   |
|                    | $f_{y,b} = 900$ MPa                  | Nominal value of the yield strength according to EN 1993-1-8, Table 3.1                     |
|                    | $f_{u,b} = 1000$ MPa                 | Nominal value of the ultimate tensile strength according to EN 1993-1-8, Table 3.1          |
| Steel deck         | Grade: S350GD<br>$f_{y,p} = 350$ MPa | Nominal value of the yield strength according to the Swiss C1/12 steelwork manual           |
| Slab reinforcement | Grade: B500B                         |   |
|                    | $f_{yk} = 500$ MPa                   | Characteristic yield strength according to EN 1992-1-1, Table C.1                           |
|                    | $E_s = 210\,000$ MPa                 | Design value of modulus of elasticity according to EN 1994-1-1, Clause 3.2                  |
| Concrete           | Grade: C25/30                        |   |
|                    | $f_{ck} = 25$ MPa                    | Characteristic compressive cylinder strength at 28 days according to EN 1992-1-1, Table 3.1 |
|                    | $f_{cm} = 33$ MPa                    | Mean value of cylinder compressive strength according to EN 1992-1-1, Table 3.1             |
|                    | $f_{ctm} = 2.6$ MPa                  | Mean value of axial tensile strength according to EN 1992-1-1, Table 3.1                    |
|                    | $E_{cm} = 31.5$ MPa                  | Secant modulus of elasticity according to EN 1992-1-1, Table 3.1                            |

**Table E.5** – Summary of the super-imposed dead loads

| Load description      | Load                  |
|-----------------------|-----------------------|
| Finishing             | 1.0 kN/m <sup>2</sup> |
| Partitions            | 1.2 kN/m <sup>2</sup> |
| Windows               | 0.5 kN/m <sup>2</sup> |
| Heating & ventilation | 0.5 kN/m <sup>2</sup> |

## E.3 Actions

### E.3.1 Permanent Action

The permanent loads considered to design the two buildings include:

- The self-weight of the structural steel components, which is determined according to SZS C5/05;
- The self-weight of the slabs (i.e., profiled steel deck + concrete), which is determined according to SZS C1/12;
- The super-imposed dead loads, which include finishing, partitions, windows as well as heating and ventilation (see Table E.5);

### E.3.2 Variable Actions

Referring to Table E.6, the variable loads considered to design the two buildings include:

- The imposed load, which is defined according to EN 1991-1-1, Table 6.2 and 6.10, for a Category B (i.e., office areas) and H (i.e., roofs not accessible);
- The snow load, which is defined according to EN 1991-1-3, Clause 5.2(3)P, based on the following assumptions:
  - The building site is located at an altitude of 500 m above the sea level;
  - The site location is characterized by a normal topography according to EN 1991-1-3, Table 5.1;
  - The building has a roof angle ranging between 0° and 30° according to EN 1991-1-3, Table 2;
  - The building site is located in an alpine climatic region according to EN 1991-1-3, Table C.1;

**Table E.6** – Summary of the variable loads

| Load description                  | Load                   |
|-----------------------------------|------------------------|
| Imposed load acting on the floors | 3.0 kN/m <sup>2</sup>  |
| Imposed load acting on the roof   | 0.0 kN/m <sup>2</sup>  |
| Snow load                         | 1.5 kN/m <sup>2</sup>  |
| Wind load on the windward side    | 0.55 kN/m <sup>2</sup> |
| Wind load on the leeward side     | 0.35 kN/m <sup>2</sup> |

- The wind load, which is defined according to EN 1991-1-4, Clause 5.3(3), based on the following assumptions:
  - Referring to EN 1991-1-4, Clause 4.2(1)P, a fundamental value of the basic wind velocity of 26 m/s is considered;
  - A terrain category IV is considered according to EN 1991-1-4, Table 4.1;
  - A structural factor of 0.90 and 0.96 is considered in the the N-S and E-W direction respectively according to EN 1991-1-4, Clause 5.3(2) and Fig. D.1.

### E.3.3 Seismic Action

#### E.3.3.1 Design Response Spectra

The investigated buildings are designed for  $q = 2.0$  and  $q = 3.0$ . According to EN 1998-1-1, Clause 2.2.2(2), the former is a low-dissipative structure, i.e. capacity design principles are not be employed contrary to the latter. In particular, for  $q = 3.0$ , a medium ductility class (DCM) is considered as stated in EN 1998-1-1, Table 5.1.

The horizontal design response spectra are defined according to EN 1998-1-1, Clause 3.2.2.5, by considering:

- A ground type D according to EN 1998-1-1, Table 3.1;
- A viscous damping of 2 %;
- An importance class II according to EN 1998-1-1, Table 4.3;
- A reference horizontal ground acceleration  $a_{gR} = 0.22$  g according to the European Facilities for Earthquake Hazard and Risk (EFEHR) website.

Figure E.4 illustrates the design response spectra computed for the two buildings.



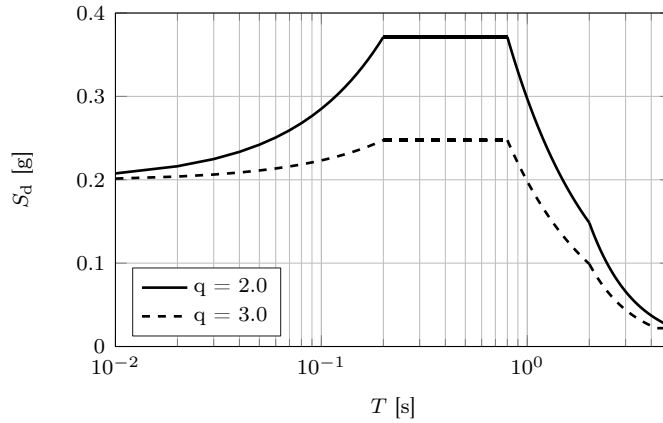


**Figure E.4** – Design response spectra

### E.3.3.2 Seismic Mass

The inertial effects of the design seismic action are determined by considering the presence of seismic masses at each floor of the buildings. The latter are calculated according to EN 1998-1-1, Clause 3.2.4(2)P:

$$\sum G_k + \sum \psi_{E,i} \cdot Q_{k,i} \quad (\text{E.1})$$

Where

- $\sum G_k$  is the total permanent load, which includes the self-weight of the structural components, the self-weight of the slabs and the super-imposed dead loads;
- $\psi_{E,i}$  is the combination coefficient for the accompanying variable action  $Q_{k,i}$ ;
- $Q_{k,i}$  is the design value of the accompanying variable action  $i$ .

The combination coefficient  $\psi_{E,i}$  is defined according to EN 1998-1-1, Clause 4.2.4(2)P:

$$\psi_{E,i} = \varphi \cdot \psi_{2,i} \quad (\text{E.2})$$

The values of  $\varphi$  and  $\psi_{2,i}$  are reported in Table E.7. The factor  $\varphi$  is computed according to EN 1998-1-1, Table 4.2, by assuming that the stories have a correlated occupancies.

The seismic masses acting at each floor of the buildings are summarized in Table E.8.

**Table E.7** –  $\varphi$  and  $\psi_{2,i}$  values used to compute the combination coefficient  $\psi_{E,i}$ 

| Variable action           | $\varphi^a$ | $\psi_{2,i}^b$ | $\psi_{E,i}^c$ |
|---------------------------|-------------|----------------|----------------|
| Imposed load - Category B | 0.8         | 0.3            | 0.24           |
| Imposed load - Category H | 1.0         | 0.0            | 0.0            |

<sup>a</sup> According to EN 1998-1-1, Table 4.2<sup>b</sup> According to EN 1990, Table A1.1<sup>c</sup> According to EN 1998-1-1, Clause 4.2.4(2)P**Table E.8** – Seismic mass acting at each floor of the buildings

| Floor | Seismic mass [kg] |           |
|-------|-------------------|-----------|
|       | $q = 2.0$         | $q = 3.0$ |
| Roof  | 319 772           | 268 111   |
| 6     | 356 832           | 382 606   |
| 5     | 364 181           | 388 712   |
| 4     | 364 439           | 389 413   |
| 3     | 373 287           | 391 703   |
| 2     | 376 293           | 395 430   |

### E.3.4 Combination of Actions at the Ultimate Limit States

#### E.3.4.1 Persistent or Transient Design Situations

The combinations of actions considered for a persistent or transient design situation are defined according to EN 1990, Clause 6.4.3.2:

$$\sum \gamma_G \cdot G_k + \gamma_{Q,1} \cdot Q_{k,1} + \sum \gamma_{Q,i} \cdot \psi_{0,i} \cdot Q_{k,i} \quad (\text{E.3})$$

Where

- $\gamma_G$  is the combination coefficient for permanent actions according to EN 1990, Table A1.2(B);
- $\gamma_{Q,1}$  is the combination coefficient for leading variable actions according to EN 1990, Table A1.2(B);
- $Q_{k,1}$  is the design value of the leading variable action;
- $\gamma_{Q,i}$  is the combination coefficient for accompanying variable actions according to EN 1990, Table A1.2(B);
- $\psi_{0,i}$  is the factor for accompanying variable actions according to EN 1990, Table A1.1;

**Table E.9** –  $\gamma_G$ ,  $\gamma_{Q,1}$  and  $\gamma_{Q,i}$  combination coefficients used for the persistent or transient design situation according to EN 1990, Table A1.2(B)

| Action                | Factor         | Action effect |            |
|-----------------------|----------------|---------------|------------|
|                       |                | Unfavourable  | Favourable |
| Permanent             | $\gamma_G$     | 1.35          | 1.00       |
| Leading variable      | $\gamma_{Q,1}$ | 1.50          | 0.00       |
| Accompanying variable | $\gamma_{Q,i}$ | 1.50          | 0.00       |

**Table E.10** –  $\psi_{0,i}$  factors used for the persistent or transient design situation according to EN 1990, Table A1.1

| Variable action           | $\psi_{0,i}$ |
|---------------------------|--------------|
| Imposed load - Category B | 0.7          |
| Imposed load - Category H | 0.0          |
| Snow                      | 0.5          |
| Wind                      | 0.6          |

The combination coefficients  $\gamma_G$ ,  $\gamma_{Q,1}$  and  $\gamma_{Q,i}$  are summarized in Table E.9, whereas the  $\psi_{0,i}$  values are reported in Table E.10.

#### E.3.4.2 Seismic Design Situation

The combinations of actions considered for a seismic design situation are defined according to EN 1990, Clause 6.4.3.4:

$$\sum G_k + \sum \psi_{2,i} \cdot Q_{k,i} + A_d \quad (\text{E.4})$$

Where  $\psi_{2,i}$  is the factor for accompanying variable actions according to EN 1990, Table A1.1, whereas  $A_d$  is the design value of the accidental action (e.g. seismic action). The factors  $\psi_{2,i}$  are summarized in Table E.11.

The effects due to the combination of the horizontal components of the seismic action are computed according to EN 1998-1-1, Clause 4.3.3.5.1:

$$A_d = E_{\text{Edx}} < + > 0.3 \cdot E_{\text{Edy}} \quad (\text{E.5})$$

$$A_d = E_{\text{Edy}} < + > 0.3 \cdot E_{\text{Edx}} \quad (\text{E.6})$$

Where  $< + >$  implies "to be combined with", and  $E_{\text{Edx}}$  and  $E_{\text{Edy}}$  represent the effects due to the application of the seismic action along the horizontal axis  $x$  and  $y$ , respectively,

**Table E.11** –  $\psi_{2,i}$  factors used for the seismic design situation according to EN 1990, Table A1.1

| Variable action           | $\psi_{2,i}$ |
|---------------------------|--------------|
| Imposed load - Category B | 0.3          |
| Imposed load - Category H | 0.0          |
| Snow                      | 0.0          |
| Wind                      | 0.0          |

**Table E.12** –  $\psi_{1,1}$  factors defined according to EN 1990, Table A1.1

| Variable action           | $\psi_{1,1}$ |
|---------------------------|--------------|
| Imposed load - Category B | 0.5          |
| Imposed load - Category H | 0.0          |
| Snow                      | 0.5          |
| Wind                      | 0.2          |

of the building. It is noteworthy that according to SIA 261, Clause 16.5,  $A_d = E_{Edx}$  and  $A_d = E_{Edy}$ , i.e. the effects due to the seismic action applied on the  $x$  direction are not combined with those due to the seismic action applied on the  $y$  direction.

### E.3.5 Combination of Actions at the Serviceability Limit States

The combinations of actions for serviceability limit states are defined according to EN 1990, Clause 6.5.3:

- Characteristic combination:

$$\sum G_k + Q_{k,1} + \sum \psi_{0,i} \cdot Q_{k,i} \quad (\text{E.7})$$

- Frequent combination:

$$\sum G_k + \psi_{1,1} \cdot Q_{k,1} + \sum \psi_{2,i} \cdot Q_{k,i} \quad (\text{E.8})$$

- Quasi-permanent combination:

$$\sum G_k + \sum \psi_{2,i} \cdot Q_{k,i} \quad (\text{E.9})$$

Where  $\psi_{1,1}$  is the factor for leading variable actions according to EN 1990, Table A1.1. The factors  $\psi_{1,1}$  are summarized in Table [E.12](#).

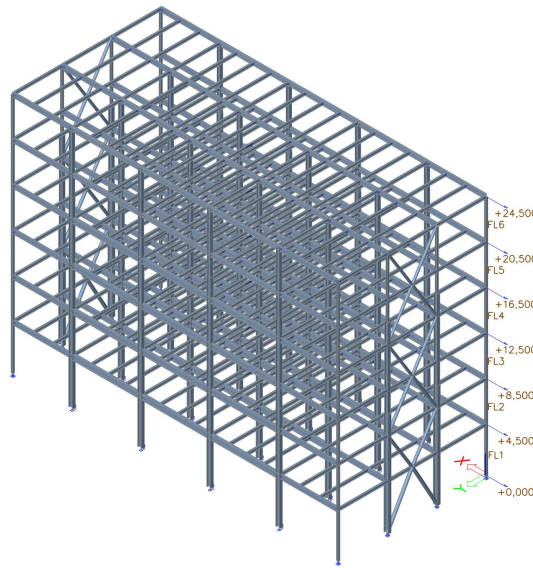


**Figure E.5** – 3D model developed in SCIA Engineer

## E.4 Structural Model

### E.4.1 Description of the Model

The building designed for  $q = 2$  is analysed through a 3D model developed in the structural analysis package SCIA Engineer version 20.0.3019 (see Fig. E.5). Similarly, SAP 200 v20.1.0 is used to investigate the building designed for  $q = 2$ . Due to brevity, only the model developed in SCIA Engineer is presented in this section.

In the N-S direction, the braces are modelled using 1D members, which work both in tension and compression. At each floor of the structure, rigid diaphragms (i.e., 2D members characterized by an infinite in-plane stiffness and a zero bending stiffness) are adopted in order to simulate the diaphragm action of the slabs. The floor loads (i.e., self-weight of the profiled steel deck, super-imposed dead load, imposed load and snow load) are applied to such diaphragms and transmitted to their supporting members based on the tributary area method. Similarly, load panels are used to apply the wind load to the structure. These elements allow to redistribute the applied surface load to nodes, edges and beams situated in their plane. However, they are entities not considered in the finite element model analysis (i.e., their stiffness is not taken into account in the calculations). Furthermore, global initial sway imperfections are considered in the N-S and E-W directions as per Clause 5.3.2(3)a in EN 1993-1-1.

**Table E.13** – Periods of vibration and effective modal masses

| Mode | $q = 2$   |                   |                   | $q = 3$ |                   |                   |
|------|-----------|-------------------|-------------------|---------|-------------------|-------------------|
|      | $T^a$ [s] | $M_{E-W}/M_{tot}$ | $M_{N-S}/M_{tot}$ | $T$ [s] | $M_{E-W}/M_{tot}$ | $M_{N-S}/M_{tot}$ |
| 1    | 1.39      | 0.80              | 0.00              | 1.77    | 0.77              | 0.00              |
| 2    | 1.11      | 0.00              | 0.70              | 1.29    | 0.00              | 0.76              |
| 3    | 0.69      | 0.00              | 0.00              | 0.80    | 0.00              | 0.00              |
| 4    | 0.53      | 0.12              | 0.00              | 0.66    | 0.13              | 0.00              |
| 5    | 0.34      | 0.00              | 0.22              | 0.46    | 0.00              | 0.19              |

<sup>a</sup> Period of vibration<sup>b</sup> Modal mass in the E-W direction<sup>c</sup> Total seismic mass<sup>d</sup> Modal mass in the N-S direction

*Note:* referring to EN 1998-1-1, Clause 4.3.3.3.2(1), the first 5 periods of vibration of both buildings suggest that their modes are well separated

Modal response spectrum analysis is used to determine the member efforts under seismic action as stated in EN 1998-1-1, Clause 4.3.3.1(2)P. Referring to EN 1998-1-1, Clause 4.3.2, accidental torsional effects are accounted for by assuming an eccentricity of the story mass of  $\pm 5\%$  of the floor-dimension perpendicular to the seismic action. Furthermore, the effects due to the combination of the horizontal components of the seismic action are considered as per Clause 4.3.3.5.1(3) in EN 1998-1-1.

#### E.4.2 Modal Response Spectrum Analysis

Modal analysis is used to identify the periods of vibration of the two buildings. Table E.13 summarizes the periods and the effective modal mass of the modes contributing to their global response. The latter are selected according to EN 1998-1-1, Clause 4.3.3.3(3). Notably, all modes with an effective mass larger or equal to 5% must be considered and the sum of the effective modal masses must be larger or equal to 90% of the total seismic mass.

Figure E.6 illustrates the modal shape of the first five periods of vibrations of the building designed for  $q = 2$ . Similar outcomes are obtained for the building designed for  $q = 3$ .

Referring to EN 1998-1-1, Clause 4.3.3.3.2(1), the periods of vibrations reported in Table E.13 can be considered as well-separated. Therefore, according to EN 1998-1-1, Clause 4.3.3.3.2(2), the Square-Root-of-Sum-of-Squares (SRSS) method can be used to compute the member efforts under seismic action.

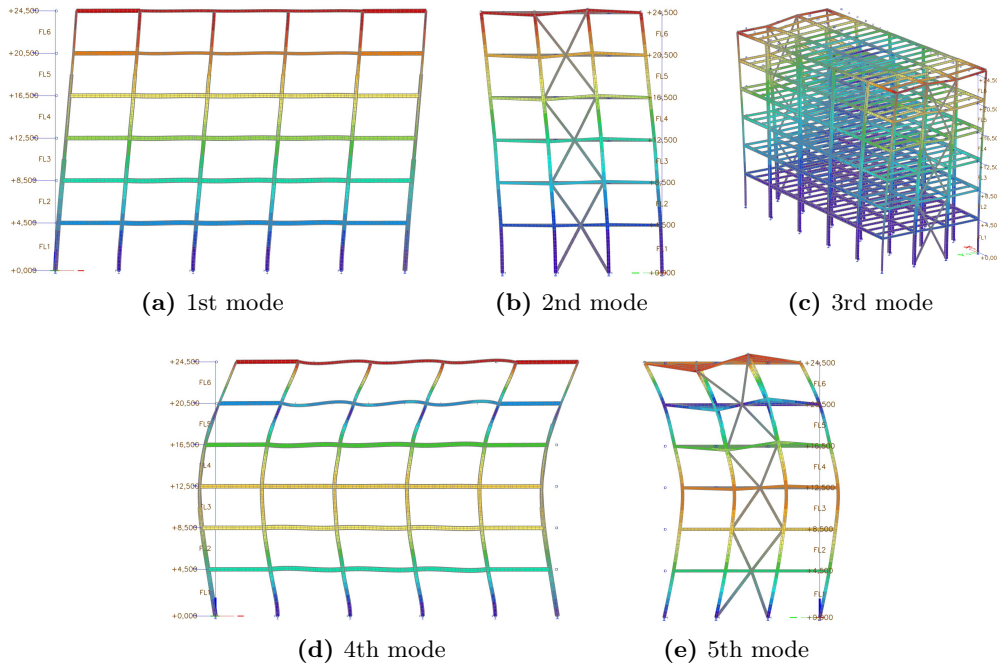


**Figure E.6** – Modal shapes of the first five periods of vibration of the building designed for  $q = 2$

## E.5 Design of the Concentrically Braced Frames

In this section, the verifications for the design of the CBFs for  $q = 2$  and  $q = 3$  are presented. In particular, summary tables for the design of the steel braces, beams and columns are included.

### E.5.1 Damage Limitation Verification

The damage limitation verification is computed according to EN 1998-1-1, Clause 4.4.3.2 for buildings having ductile non-structural elements:

$$d_r \cdot \nu \leq 0.0075 \cdot h \quad (\text{E.10})$$

Where

- $h$  is the story height;
- $\nu$  is the reduction factor, which takes into account the lower return period of the seismic action associated with the damage limitation requirement;  $\nu = 0.5$  for buildings with importance class II;

**Table E.14** – Damage limitation verification computed for the CBFs designed for  $q = 2$  and  $q = 3$ 

| Story | $h$  | $0.75\% \cdot h$ | $q = 2$ |       |                 | $q = 3$ |       |                 |
|-------|------|------------------|---------|-------|-----------------|---------|-------|-----------------|
|       |      |                  | $d_e$   | $d_r$ | $\nu \cdot d_r$ | $d_e$   | $d_r$ | $\nu \cdot d_r$ |
|       | [mm] | [mm]             | [mm]    | [mm]  | [mm]            | [mm]    | [mm]  | [mm]            |
| 6     | 4000 | 30               | 27.5    | 55.0  | 27.5            | 15.3    | 45.9  | 23.0            |
| 5     | 4000 | 30               | 24.2    | 48.4  | 24.2            | 15.5    | 46.5  | 23.3            |
| 4     | 4000 | 30               | 25.2    | 50.4  | 25.2            | 15.1    | 45.3  | 22.7            |
| 3     | 4000 | 30               | 17.4    | 34.8  | 17.4            | 11.9    | 35.7  | 17.9            |
| 2     | 4000 | 30               | 17.3    | 34.6  | 17.3            | 10.8    | 32.4  | 16.2            |
| 1     | 4500 | 34               | 9.0     | 18.0  | 9.0             | 11.7    | 35.1  | 17.6            |

- $d_r$  is the design inter-story drift defined according to EN 1998-1-1, Clause 4.4.2.2(2):

$$d_r = q \cdot d_e \quad (\text{E.11})$$

Where  $d_e$  is the inter-story drift determined through linear analysis based on the design response spectrum.

The damage limitation verification computed for the CBFs designed for  $q = 2$  and  $q = 3$  is summarized in Table E.14. Figure E.7 illustrates the maximum normalized floor displacements and maximum story drift ratios obtained along the height of the latter.

### E.5.2 Second-order Effects

According to EN 1998-1-1, Clause 4.4.2.2, second-order effects should not be taken into account if the following condition is fulfilled at each story of the building:

$$\theta = \frac{P_{\text{tot}} \cdot d_r}{V_{\text{tot}} \cdot h} \leq 0.10 \quad (\text{E.12})$$

Where  $\theta$  is the inter-story drift sensitivity coefficient,  $P_{\text{tot}}$  is the total gravity load at and above the story considered in the seismic design situation and  $V_{\text{tot}}$  is the total seismic story shear. The  $\theta$  coefficients computed in the N-S direction of the investigated buildings are summarized in Table E.15. Notably,  $\theta$  values lower than 0.10 are obtained at all stories.



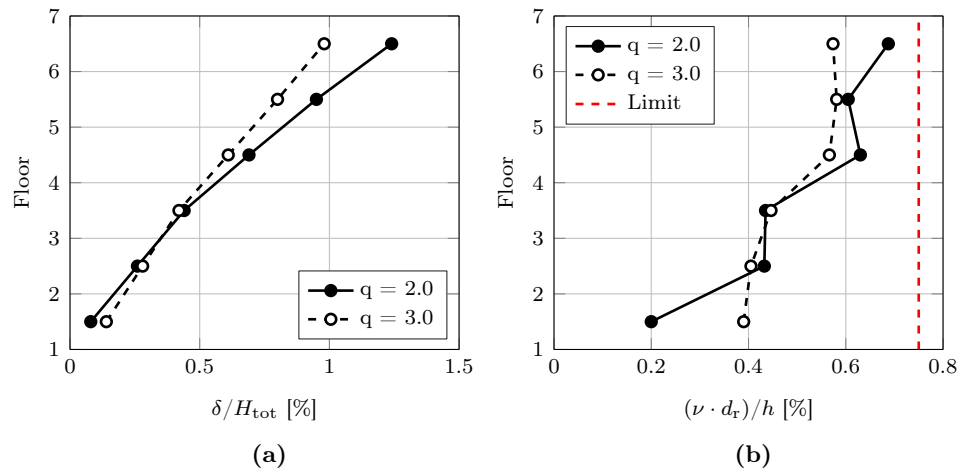


**Figure E.7** – (a) Maximum normalized floor displacements and (b) maximum story drift ratios along the height of the CBFs designed for  $q = 2$  and  $q = 3$

**Table E.15** – Second-order effects computed in the N-S direction of the investigated buildings

| Story | $h$  | $q = 2$ |           |           |          | $q = 3$ |           |           |          |
|-------|------|---------|-----------|-----------|----------|---------|-----------|-----------|----------|
|       |      | $d_r$   | $P_{tot}$ | $V_{tot}$ | $\theta$ | $d_r$   | $P_{tot}$ | $V_{tot}$ | $\theta$ |
|       | [mm] | [mm]    | [kN]      | [kN]      | [-]      | [mm]    | [kN]      | [kN]      | [-]      |
| 6     | 4000 | 55.0    | 3025      | 1422      | 0.03     | 45.9    | 2569      | 604       | 0.05     |
| 5     | 4000 | 48.4    | 6236      | 2377      | 0.03     | 46.5    | 6297      | 1107      | 0.07     |
| 4     | 4000 | 50.4    | 9522      | 3060      | 0.04     | 45.3    | 10 066    | 1464      | 0.08     |
| 3     | 4000 | 34.8    | 12 809    | 3585      | 0.03     | 35.7    | 13 859    | 1741      | 0.07     |
| 2     | 4000 | 34.6    | 16 183    | 4056      | 0.03     | 32.4    | 17 676    | 1984      | 0.07     |
| 1     | 4500 | 18.0    | 19 572    | 4302      | 0.02     | 35.1    | 21 510    | 2171      | 0.08     |

**Table E.16** – Summary of the design of the braces for  $q = 2$ 

| Story | Member       | Class <sup>a</sup> | $N_{Ed}/N_{b,Rd}$ <sup>b</sup> |
|-------|--------------|--------------------|--------------------------------|
| 6     | ROR 219.1x10 | 1                  | 0.71                           |
| 5     | ROR 219.1x16 | 1                  | 0.67                           |
| 4     | ROR 219.1x16 | 1                  | 0.66                           |
| 3     | ROR 244.5x16 | 1                  | 0.63                           |
| 2     | ROR 244.5x16 | 1                  | 0.52                           |
| 1     | ROR 273x16   | 1                  | 0.45                           |

<sup>a</sup> Cross section classification according to EN 1993-1-1, Table 5.2

<sup>b</sup> According to EN 1993-1-1, Clause 6.3.1

**Table E.17** – Summary of the design of the braces for  $q = 3$ 

| Story | Member       | Class <sup>a</sup> | $\bar{\lambda}$ <sup>b</sup> | $N_{Ed}/N_{b,Rd}$ <sup>c</sup> | $\Omega$ <sup>d</sup> | $(\Omega - \Omega_{min})/\Omega_{min}$ [%] |
|-------|--------------|--------------------|------------------------------|--------------------------------|-----------------------|--|
| 6     | ROR 133x4.5  | 1                  | 1.29                         | 0.94                           | 2.25                  | 1.2  |
| 5     | ROR 133x10   | 1                  | 1.35                         | 0.94                           | 2.38                  | 7.1  |
| 4     | ROR 152.4x10 | 1                  | 1.15                         | 0.80                           | 2.23                  | 0.0  |
| 3     | ROR 139.7x16 | 1                  | 1.32                         | 0.90                           | 2.41                  | 8.3  |
| 2     | ROR 168.3x16 | 1                  | 1.03                         | 0.57                           | 2.70                  | 21.5                                       |
| 1     | ROR 177.8x10 | 1                  | 1.27                         | 0.89                           | 2.33                  | 4.5  |

<sup>a</sup> Cross section classification according to EN 1993-1-1, Table 5.2

<sup>b</sup> According to EN 1993-1-1, Clause 6.3.1.2

<sup>c</sup> According to EN 1993-1-1, Clause 6.3.1

<sup>d</sup> According EN 1998-1-1, Clause 6.7.4

### E.5.3 Design of the Braces

The investigated CBFs consist of steel braces in a V-shaped configuration. Therefore, as per EN 1998-1-1, Clause 6.7.3, the compression diagonals are designed for the compression resistance in accordance with EN 1993-1-1, Clause 6.3.1. Tables E.16 and E.17 show a summary of the design of the braces for  $q = 2$  and  $q = 3$ , respectively. In Table E.17, the overstrength ratios computed as per EN 1998-1-1, Clause 6.7.4, are also reported. In particular, according to EN 1998-1-1, Clause 6.7.3, it is necessary to verify that the overstrength ratio computed at each story of the building do not differ from the minimum one by more than 25 %. Furthermore, the slenderness of each brace should be smaller or equal to 2.0.

**Table E.18** – Summary of the design of the primary and secondary beams for  $q = 2$  and  $q = 3$ 

| Behavior factor | Member  | Class <sup>a</sup> | $\frac{V_{Ed}^b}{V_{pl,Rd}}$ | $\frac{M_{Ed,y}^c}{M_{pl,y,Rd}}$ | $\frac{M_{Ed,y}^d}{M_{LT,Rd}}$ |
|-----------------|---------|--------------------|------------------------------|----------------------------------|--------------------------------|
| $q = 2.0$       | IPE 270 | 1                  | 0.16                         | 0.60                             | 0.70                           |
| $q = 3.0$       | IPE 270 | 1                  | 0.12                         | 0.57                             | 0.76                           |

<sup>a</sup> Cross section classification according to EN 1993-1-1, Table 5.2<sup>b</sup> According to EN 1993-1-1, Clause 6.2.6<sup>c</sup> According to EN 1993-1-1, Clause 6.2.5<sup>d</sup> According EN 1993-1-1, Clause 6.3.2**Table E.19** – Summary of the design of the CBF columns for  $q = 2$ 

| Story | Member  | Class <sup>a</sup> | $\frac{N_{Ed}^b}{N_{ky,Rd}}$ | $\frac{N_{Ed}^b}{N_{kz,Rd}}$ | $\frac{M_{Ed,y}^c}{M_{LT,Rd}}$ | $\frac{N_{Ed}^d}{N_{ky,Rd}} +$<br>$k_{yy} \cdot \frac{M_{Ed,y}}{M_{LT,Rd}} +$<br>$k_{yz} \cdot \frac{M_{Ed,z}}{M_{pl,z,Rd}}$ | $\frac{N_{Ed}^d}{N_{kz,Rd}} +$<br>$k_{zy} \cdot \frac{M_{Ed,y}}{M_{LT,Rd}} +$<br>$k_{zz} \cdot \frac{M_{Ed,z}}{M_{pl,z,Rd}}$ |
|-------|---------|--------------------|------------------------------|------------------------------|--------------------------------|--|--|
| 6     | HEB 180 | 1                  | 0.40                         | 0.69                         | 0.07                           | 0.40   | 0.69   |
| 5     | HEB 180 | 1                  | 0.40                         | 0.69                         | 0.07                           | 0.40   | 0.69   |
| 4     | HEB 320 | 1                  | 0.60                         | 0.77                         | 0.04                           | 0.62   | 0.80   |
| 3     | HEB 320 | 1                  | 0.60                         | 0.77                         | 0.04                           | 0.62   | 0.80   |
| 2     | HEM 400 | 1                  | 0.58                         | 0.72                         | 0.06                           | 0.65   | 0.81   |
| 1     | HEM 400 | 1                  | 0.57                         | 0.76                         | 0.06                           | 0.61   | 0.83   |

<sup>a</sup> Cross section classification according to EN 1993-1-1, Table 5.2<sup>b</sup> According to EN 1993-1-1, Clause 6.3.1<sup>c</sup> According to EN 1993-1-1, Clause 6.3.2<sup>d</sup> According EN 1993-1-1, Clause 6.3.3

#### E.5.4 Design of the Beams

In the N-S direction, the primary and secondary beams of the investigated buildings are designed according to EN 1993-1-1, Clause 6.2.5, 6.2.6 and 6.3.2. Table E.18 summarizes their design for both  $q = 2$  and  $q = 3$ .

#### E.5.5 Design of the Columns

The design of the CBF columns is governed by the stability checks provided by EN 1993-1-1, Clause 6.3.1, 6.3.2 and 6.3.3. Tables E.19 and E.20 summarizes their design for  $q = 2$  and  $q = 3$ , respectively.

**Table E.20** – Summary of the design of the CBF columns for  $q = 3$ 

| Story | Member  | Class <sup>a</sup> | $\frac{N_{Ed}^b}{N_{ky,Rd}}$ | $\frac{N_{Ed}^b}{N_{kz,Rd}}$ | $\frac{M_{Ed,y}^c}{M_{LT,Rd}}$ | $\frac{N_{Ed}^d}{N_{ky,Rd}} +$<br>$k_{yy} \cdot \frac{M_{Ed,y}}{M_{LT,Rd}} +$<br>$k_{yz} \cdot \frac{M_{Ed,z}}{M_{pl,z,Rd}}$ | $\frac{N_{Ed}^d}{N_{kz,Rd}} +$<br>$k_{zy} \cdot \frac{M_{Ed,y}}{M_{LT,Rd}} +$<br>$k_{zz} \cdot \frac{M_{Ed,z}}{M_{pl,z,Rd}}$ |
|-------|---------|--------------------|------------------------------|------------------------------|--------------------------------|--|--|
| 6     | HEB 240 | 1                  | 0.22                         | 0.33                         | 0.05                           | 0.25   | 0.38   |
| 5     | HEB 240 | 1                  | 0.24                         | 0.36                         | 0.06                           | 0.30   | 0.42   |
| 4     | HEM 260 | 1                  | 0.56                         | 0.72                         | 0.03                           | 0.58   | 0.74   |
| 3     | HEM 260 | 1                  | 0.57                         | 0.74                         | 0.03                           | 0.60   | 0.77   |
| 2     | HEM 450 | 1                  | 0.73                         | 0.89                         | 0.03                           | 0.76   | 0.92   |
| 1     | HEM 450 | 1                  | 0.75                         | 0.98                         | 0.03                           | 0.77   | 0.99   |

<sup>a</sup> Cross section classification according to EN 1993-1-1, Table 5.2<sup>b</sup> According to EN 1993-1-1, Clause 6.3.1<sup>c</sup> According to EN 1993-1-1, Clause 6.3.2<sup>d</sup> According EN 1993-1-1, Clause 6.3.3

## References

- [1] Minoru Wakabayashi, Takeshi Nakamura, and Nozomu Yoshida. “Experimental studies on the elastic-plastic behavior of braced frames under repeated horizontal loading. Part 1 experiments of braces with an H-shaped cross section in a frame”. In: *Bulletin of the Disaster Prevention Research Institute* 27.3 (1977), pp. 121–154.
- [2] Bunzo Tsuji and Takayoshi Nishino. “Elastic plastic deformation and collapse behavior of braced frames”. In: *Proceedings of Ninth World Conference on Earthquake Engineering* 6 (1988), pp. 3–7.
- [3] Robert Tremblay. “Inelastic seismic response of steel bracing members”. In: *Journal of Constructional Steel Research* 58.5-8 (2002), pp. 665–701.
- [4] Brad Shaback and Tom Brown. “Behaviour of square hollow structural steel braces with end connections under reversed cyclic axial loading”. In: *Canadian Journal of Civil Engineering* 30.4 (2003), pp. 745–753.
- [5] Benjamin V Fell, Amit M Kanvinde, Gregory G Deierlein, and Andrew T Myers. “Experimental investigation of inelastic cyclic buckling and fracture of steel braces”. In: *ASCE Journal of Structural Engineering* 135.1 (2009), pp. 19–32.
- [6] Charles W Roeder, Dawn E Lehman, Kelly Clark, Jacob Powell, Jung-Han Yoo, Keh-Chyuan Tsai, Chih-Han Lin, and Chih-Yu Wei. “Influence of gusset plate connections and braces on the seismic performance of X-braced frames”. In: *Earthquake Engineering & Structural Dynamics* 40.4 (2011), pp. 355–374.
- [7] Taichiro Okazaki, Dimitrios G Lignos, Tsuyoshi Hikino, and Koichi Kajiwara. “Dynamic response of a chevron concentrically braced frame”. In: *ASCE Journal of Structural Engineering* 139.4 (2013), pp. 515–525.
- [8] Jiun-Wei Lai and Stephen A Mahin. “Steel concentrically braced frames using tubular structural sections as bracing members: Design, full-scale testing and

- numerical simulation". In: *International Journal of Steel Structures* 14.1 (2014), pp. 43–58.
- [9] Patxi Uriz, Filip C Filippou, and Stephen A Mahin. "Model for cyclic inelastic buckling of steel braces". In: *ASCE Journal of Structural Engineering* 134.4 (2008), pp. 619–628.
  - [10] Yuli Huang. "Simulating the inelastic seismic behavior of steel braced frames including the effects of low-cycle fatigue". PhD thesis. Berkeley, CA, USA: University of California, 2009.
  - [11] Po-Chien Hsiao, Dawn E Lehman, and Charles W Roeder. "Improved analytical model for special concentrically braced frames". In: *Journal of Constructional Steel Research* 73 (2012), pp. 80–94.
  - [12] Emre Karamanci and Dimitrios G Lignos. "Computational approach for collapse assessment of concentrically braced frames in seismic regions". In: *ASCE Journal of Structural Engineering* 140.8 (2014), A4014019.
  - [13] Robert Tremblay and Nathalie Robert. "Seismic performance of low-and medium-rise chevron braced steel frames". In: *Canadian Journal of Civil Engineering* 28.4 (2001), pp. 699–714.
  - [14] Martin Lacerte and Robert Tremblay. "Making use of brace overstrength to improve the seismic response of multistorey split-X concentrically braced steel frames". In: *Canadian Journal of Civil Engineering* 33.8 (2006), pp. 1005–1021.
  - [15] *Tohoku Japan Earthquake & Tsunami Clearinghouse*. <http://learningfromearthquakes.org/2011-03-11-tohoku-japan/11-resources/48-effects-of-the-2011-tohoku-japan-earthquake-on-steel-structures>. Accessed: 2022-04-22.
  - [16] Hai Sang Lew, Edgar V Leyendecker, and Robert D Dikkers. *Engineering aspects of the 1971 San Fernando earthquake*. Vol. 40. US National Bureau of Standards, 1971.
  - [17] P. C. Jennings and G. W. Housner. "The San Fernando, California, earthquake of February 9, 1971". In: *Proceedings of the Fifth. World Conference on Earthquake Engineering*, Rome, Italy. 1973.
  - [18] Robert D Campbell, Matthew J Griffin, L J Bragagnolo, and Peter I Yanev. *The December 7, 1988 Armenia earthquake effects on selected power, industrial and commercial facilities*. Tech. rep. 1996.

- [19] Durgesh C Rai and Subhash C Goel. “Seismic evaluation and upgrading of chevron braced frames”. In: *Journal of Constructional Steel Research* 59.8 (2003), pp. 971–994.
- [20] Seong-Hoon Hwang and Dimitrios G Lignos. “Effect of modeling assumptions on the earthquake-induced losses and collapse risk of steel-frame buildings with special concentrically braced frames”. In: *ASCE Journal of Structural Engineering* 143.9 (2017), p. 04017116.
- [21] Trevor Edward Kelly. *Floor response of yielding structures*. Office of the Chief Structural Engineer, Ministry of Works and Development, 1978.
- [22] Mario E Rodriguez, José I Restrepo, and Athol J Carr. “Earthquake-induced floor horizontal accelerations in buildings”. In: *Earthquake Engineering & Structural Dynamics* 31.3 (2002), pp. 693–718.
- [23] Eduardo Miranda and Shahram Taghavi. “Approximate floor acceleration demands in multistory buildings. I: Formulation”. In: *ASCE Journal of Structural Engineering* 131.2 (2005), pp. 203–211.
- [24] Shahram Taghavi and Eduardo Miranda. “Approximate floor acceleration demands in multistory buildings. II: Applications”. In: *ASCE Journal of Structural Engineering* 131.2 (2005), pp. 212–220.
- [25] Samit Ray-Chaudhuri and Tara C Hutchinson. “Effect of nonlinearity of frame buildings on peak horizontal floor acceleration”. In: *Journal of Earthquake Engineering* 15.1 (2011), pp. 124–142.
- [26] Dimitrios G Lignos and Emre Karamanci. “Drift-based and dual-parameter fragility curves for concentrically braced frames in seismic regions”. In: *Journal of Constructional Steel Research* 90 (2013), pp. 209–220.
- [27] Ali Davaran, Alexandre Gélinas, and Robert Tremblay. “Experimental seismic response of slotted connections at the intersection of HSS braces in X-bracing systems”. In: *ASCE/SEI Structures Congress, Chicago IL, March. 2012*.
- [28] Taichiro Okazaki, Dimitrios G Lignos, Mitsumasa Midorikawa, James M Ricles, and Jay Love. “Damage to steel buildings observed after the 2011 Tohoku-Oki earthquake”. In: *Earthquake Spectra* 29.1\_suppl (2013), pp. 219–243.
- [29] Arvind K Jain, Richard G Redwood, and Feng Lu. “Seismic response of concentrically braced dual steel frames”. In: *Canadian Journal of Civil Engineering* 20.4 (1993), pp. 672–687.

- [30] Chui-Hsin Chen, Jiun-Wei Lai, and Stephen Mahin. “Seismic performance assessment of concentrically braced steel frame buildings”. In: *Proceedings of the 14th World Conference on Earthquake Engineering*. 2008.
- [31] Patxi Uriz and Stephen A. Mahin. *Towards earthquake resistant design of concentrically braced steel structures*. PEER Report 2008/08, University of California Berkeley, Berkeley, California, 2008.
- [32] James O Malley and Egor P Popov. “Shear links in eccentrically braced frames”. In: *ASCE Journal of Structural Engineering* 110.9 (1984), pp. 2275–2295.
- [33] Kazuhiko Kasai and Egor P Popov. “General behavior of WF steel shear link beams”. In: *ASCE Journal of Structural Engineering* 112.2 (1986), pp. 362–382.
- [34] Egor P Popov and Michael D Engelhardt. “Seismic eccentrically braced frames”. In: *Journal of Constructional Steel Research* 10 (1988), pp. 321–354.
- [35] K. Kimura, Y. Takeda, K. Yoshioka, N. Furuya, and Y. Takemoto. “An experimental study on braces encased in steel tube and mortar”. In: *Proceedings of the Architectural Institute of Japan Annual Meeting*. 1976.
- [36] Cameron J Black, Nicos Makris, and Ian D Aiken. “Component testing, seismic evaluation and characterization of buckling-restrained braces”. In: *ASCE Journal of Structural Engineering* 130.6 (2004), pp. 880–894.
- [37] Larry A Fahnestock, James M Ricles, and Richard Sause. “Experimental evaluation of a large-scale buckling-restrained braced frame”. In: *ASCE Journal of Structural Engineering* 133.9 (2007), pp. 1205–1214.
- [38] Mitsumasa Midorikawa, Tatsuya Azuhata, Tadashi Ishihara, Yutaka Matsuba, Yoshiyuki Matsushima, and Akira Wada. “Earthquake response reduction of buildings by rocking structural systems”. In: *Smart Structures and Materials 2002: Smart Systems for Bridges, Structures, and Highways*. Vol. 4696. International Society for Optics and Photonics. 2002, pp. 265–273.
- [39] David Roke, Richard Sause, James M Ricles, Choung-Yeol Seo, and Kyung-Sik Lee. “Self-centering seismic-resistant steel concentrically-braced frames”. In: *Proceedings of the 8th US National Conference on Earthquake Engineering*. San Francisco, CA, USA. 2006, pp. 18–22.
- [40] Lydell Wiebe and Constantin Christopoulos. “Mitigation of higher mode effects in base-rocking systems by using multiple rocking sections”. In: *Journal of Earthquake Engineering* 13.S1 (2009), pp. 83–108.



- [41] Matthew R Eatherton, Xiang Ma, Helmut Krawinkler, David Mar, Sarah Billington, Jerome F Hajjar, and Gregory G Deierlein. “Design concepts for controlled rocking of self-centering steel-braced frames”. In: *ASCE Journal of Structural Engineering* 140.11 (2014), p. 04014082.
- [42] Avtar S Pall and Cedric Marsh. “Response of friction damped braced frames”. In: *ASCE Journal of Structural Engineering* 108.9 (1982), pp. 1313–1323.
- [43] André Filiatrault and Sheldon Cherry. “Performance evaluation of friction damped braced steel frames under simulated earthquake loads”. In: *Earthquake Spectra* 3.1 (1987), pp. 57–78.
- [44] Ian D Aiken and James M Kelly. “Earthquake simulator testing and analytical studies of two energy-absorbing systems for multistory structures”. PhD thesis. Berkeley, CA, USA: University of California, 1990.
- [45] T. F. Fitzgerald, Thalia Anagnos, Mary Goodson, and Theodore Zsutty. “Slotted bolted connections in aseismic design for concentrically braced connections”. In: *Earthquake Spectra* 5.2 (1989), pp. 383–391.
- [46] Robert Tremblay. “Seismic behavior and design of friction concentrically braced frames for steel buildings”. PhD thesis. University of British Columbia, 1993.
- [47] Lucia Tirca, Ovidiu Serban, Robert Tremblay, Yan Jiang, and Liang Chen. “Seismic design, analysis and testing of a friction steel braced frame system for multi-storey buildings in Vancouver”. In: *Key Engineering Materials*. Vol. 763. Trans Tech Publications Ltd. 2018, pp. 1077–1086.
- [48] Andrew S Whittaker, Vitelmo V Bertero, Christopher L Thompson, and L Javier Alonso. “Seismic testing of steel plate energy dissipation devices”. In: *Earthquake Spectra* 7.4 (1991), pp. 563–604.
- [49] Ioannis Vayas and Pavlos Thanopoulos. “Innovative dissipative (INERD) pin connections for seismic resistant braced frames”. In: *International Journal of Steel Structures* 5.5 (2005), pp. 453–464.
- [50] Michael G Gray, Constantin Christopoulos, and Jeffrey A Packer. “Cast steel yielding brace system for concentrically braced frames: concept development and experimental validations”. In: *ASCE Journal of Structural Engineering* 140.4 (2014), p. 04013095.
- [51] Jack Wen Wei Guo and Constantin Christopoulos. “A procedure for generating performance spectra for structures equipped with passive supplemental dampers”. In: *Earthquake Engineering & Structural Dynamics* 42.9 (2013), pp. 1321–1338.

- [52] Nathan Brent Chancellor. “Seismic design and performance of self-centering concentrically-braced frames”. PhD thesis. PA, USA: Lehigh University, 2014.
- [53] European Committee for Standardization (CEN). *Eurocode 8: Design of structures for earthquake resistance - Part 1: General rules, specific actions and rules for buildings*. London: BSI, 2004.
- [54] Peter Dusicka, Ahmad M Itani, and Ian G Buckle. *Built-up shear links as energy dissipators for seismic protection of bridges*. Tech. rep. Technical Report MCEER-06-0003. University of Nevada-Reno: Multidisciplinary Center of Earthquake Engineering Research, 2006.
- [55] Ryan A Kersting, Larry A Fahnestock, and Walterio A López. “Seismic design of steel buckling-restrained braced frames”. In: *NIST GCR* (2015), pp. 15–917.
- [56] Avtar Pall and Tirca Pall. “Performance-based design using pall friction dampers—an economical design solution”. In: *Proceedings of the 13th World Conference on Earthquake Engineering, Vancouver, BC, Canada*. Vol. 71. 2004.
- [57] Andrew C Costley and Daniel Paul Abrams. *Dynamic response of unreinforced masonry buildings with flexible diaphragms*. National Center for Earthquake Engineering Research Buffalo, New York, 1996.
- [58] Gregory L Cohen, Richard E Klinger, John R Hayes Jr, and Steven C Sweeney. *Seismic response of low-rise masonry buildings with flexible roof diaphragms*. US Army Corps of Engineers, Engineer Research and Development Center, 2001.
- [59] Robert B Fleischman and Kenny T Farrow. “Dynamic behavior of perimeter lateral-system structures with flexible diaphragms”. In: *Earthquake Engineering & Structural Dynamics* 30.5 (2001), pp. 745–763.
- [60] Maria Koliou, Andre Filiatrault, Dominic J Kelly, and John Lawson. “Distributed yielding concept for improved seismic collapse performance of rigid wall-flexible diaphragm buildings”. In: *ASCE Journal of Structural Engineering* 142.2 (2016), p. 04015137.
- [61] Arturo Tena-Colunga and Daniel P Abrams. “Seismic behavior of structures with flexible diaphragms”. In: *ASCE Journal of Structural Engineering* 122.4 (1996), pp. 439–445.
- [62] Robert B Fleischman, Richard Sause, Stephen Pessiki, and Andrew B Rhodes. “Seismic behavior of precast parking structure diaphragms”. In: *PCI journal* 43.1 (1998), pp. 38–53.

- [63] David Key. “The seismic performance of energy absorbing dampers in building structures”. In: *Bulletin of the New Zealand Society for Earthquake Engineering* 17.1 (1984), pp. 38–46.
- [64] J Enrique Luco and Francisco CP De Barros. “Control of the seismic response of a composite tall building modelled by two interconnected shear beams”. In: *Earthquake Engineering & Structural Dynamics* 27.3 (1998), pp. 205–223.
- [65] David Mar and Steven Tipping. “Smart frame story isolation system: a new high-performance seismic technology”. In: *Proceedings of the Ninth US–Japan Workshop on the Improvement of Structural Design and Construction Practices*. British Columbia Canada. 2000, pp. 21–23.
- [66] Romis Vides and Stefano Pampanin. “Towards a performance-based design of pre-cast concrete diaphragms using jointed dissipative connectors: concept and feasibility study”. In: *New Zealand Conference of Earthquake Engineering, Rotorua, New Zealand*. Proceedings of the New Zealand Society of Earthquake Engineering (NZSEE) Annual Conference. 2015.
- [67] Georgios Tsampras, Richard Sause, Dichuan Zhang, Robert B Fleischman, Jose I Restrepo, David Mar, and Joseph Maffei. “Development of deformable connection for earthquake-resistant buildings to reduce floor accelerations and force responses”. In: *Earthquake Engineering & Structural Dynamics* 45.9 (2016), pp. 1473–1494.
- [68] Georgios Tsampras, Richard Sause, Robert B Fleischman, and Jose I Restrepo. “Experimental study of deformable connection consisting of buckling-restrained brace and rubber bearings to connect floor system to lateral force resisting system”. In: *Earthquake Engineering & Structural Dynamics* 46.8 (2017), pp. 1287–1305.
- [69] Georgios Tsampras, Richard Sause, Robert B Fleischman, and José I Restrepo. “Experimental study of deformable connection consisting of friction device and rubber bearings to connect floor system to lateral force resisting system”. In: *Earthquake Engineering & Structural Dynamics* 47.4 (2018), pp. 1032–1053.
- [70] Zhi Zhang, Robert B Fleischman, Jose I Restrepo, Gabriele Guerrini, Arpit Nema, Dichuan Zhang, Ulina Shakya, Georgios Tsampras, and Richard Sause. “Shake-table test performance of an inertial force-limiting floor anchorage system”. In: *Earthquake Engineering & Structural Dynamics* 47.10 (2018), pp. 1987–2011.

- [71] James M Kelly, Robert I Skinner, and Austin J Heine. “Mechanisms of energy absorption in special devices for use in earthquake resistant structures”. In: *Bulletin of NZ Society for Earthquake Engineering* 5.3 (1972), pp. 63–88.
- [72] Steve Merritt, Chia-Ming Uang, and Gianmario Benzoni. *Subassembly testing of star seismic buckling-restrained braces*. Tech. rep. TR-2003/04. Department of Structural Engineering, University of California, San Diego, California, USA, 2003.
- [73] Michalakis C Constantinou and Michael D Symans. *Experimental and analytical investigation of seismic response of structures with supplemental fluid viscous dampers*. Tech. rep. NCEER-92-0032. National Center for Earthquake Engineering Research, State University of New York at Buffalo, Buffalo, NY, 1992.
- [74] Nicos Makris, Yiannis Roussos, Andrew S Whittaker, and James M Kelly. *Viscous heating of fluid dampers during seismic and wind excitations: analytical solutions and design formulae*. Tech. rep. UCB/EERC-97/11. Earthquake Engineering Research Center, University of California, Berkeley, CA, USA, 1997.
- [75] Cameron J Black and Nicos Makris. *Viscous heating of fluid dampers under wind and seismic loading: experimental studies, mathematical modeling and design formulae*. Earthquake Engineering Resource Center, College of Engineering, the University of California, Berkeley, CA, USA, 2005.
- [76] Aldo A Ferri. “Friction damping and isolation systems”. In: *Journal of Vibration and Acoustics* 117(B) (1995), pp. 196–206.
- [77] Costantin Christopoulos and André Filiatrault. *Principles of passive supplemental damping and seismic isolation*. IUSS Press, 2005.
- [78] Avtar S Pall. “Limited slip bolted joints: a device to control the seismic response of large panel structures”. PhD thesis. Monreal, Quebec, Canada: Concordia University, 1979.
- [79] Carl E Grigorian, Tzong-Shuoh Yang, and Egor P Popov. “Slotted bolted connection energy dissipators”. In: *Earthquake Spectra* 9.3 (1993), pp. 491–504.
- [80] Satoko Ono, Kiichi Nakahira, Shigeharu Tsujioka, and Naoko Uno. “Energy absorption capacity of thermally sprayed aluminum friction dampers”. In: *Journal of Thermal Spray Technology* 5.3 (1996), pp. 303–309.
- [81] Eric Dane Wolff. “Frictional heating in sliding bearings and an experimental study of high friction materials”. PhD thesis. Buffalo, New York, USA: State University of New York at Buffalo, 1999.

- [82] J Chanchí Golondrino, Gregory A MacRae, and G Charles Clifton. “Behaviour of asymmetrical friction connections using different shim materials”. In: *Proceedings of the New Zealand Society for Earthquake Engineering Conference*. 2012.
- [83] Massimo Latour, Vincenzo Piluso, and Gianvittorio Rizzano. “Experimental analysis on friction materials for supplemental damping devices”. In: *Construction and Building Materials* 65 (2014), pp. 159–176.
- [84] Martina Paronesso and Dimitrios G. Lignos. “Experimental study of sliding friction damper with composite materials for earthquake resistant structures”. In: *Engineering Structures* 248 (2021), p. 113063.
- [85] Martina Paronesso and Dimitrios G Lignos. “Seismic Design and Performance of Steel Concentrically Braced Frame Buildings with Dissipative Floor Connectors”. In: *Earthquake Engineering and Structural Dynamics* (2022, under review).
- [86] Martina Paronesso and Dimitrios G Lignos. “Influence of gravity connections and damper activation forces on the seismic behavior of steel CBF buildings with dissipative floor connectors”. In: *Earthquake Engineering & Structural Dynamics* (2022, ready for submission).
- [87] Tsu T Soong and Billie Spencer. “Supplemental energy dissipation: state-of-the-art and state-of-the-practice”. In: *Engineering Structures - ENG STRUCT* 24 (Mar. 2002), pp. 243–259.
- [88] Micheal D Symans, Finley A Charney, Andrew S Whittaker, Michalakis C Constantinou, Charles A Kircher, M W Johnson, and Robert J McNamara. “Energy dissipation systems for seismic applications: current practice and recent developments”. In: *ASCE Journal of Structural Engineering* 134.1 (2008), pp. 3–21.
- [89] Shawn Kiggins and Chia-Ming Uang. “Reducing residual drift of buckling-restrained braced frames as a dual system”. In: *Engineering Structures* 28.11 (2006), pp. 1525–1532.
- [90] Jeffrey Erochko, Constantin Christopoulos, Robert Tremblay, and Hyunhoon Choi. “Residual drift response of SMRFs and BRB frames in steel buildings designed according to ASCE 7-05”. In: *ASCE Journal of Structural Engineering* 137.5 (2010), pp. 589–599.
- [91] André Filiatrault, Robert Tremblay, and Ramapada Kar. “Performance evaluation of friction spring seismic damper”. In: *ASCE Journal of Structural Engineering* 126.4 (2000), pp. 491–499.

- [92] Ian D Aiken, James M Kelly, and Avtar S Pall. “Seismic response of a nine-story steel frame with friction damped cross-bracing”. In: *Proceedings of the 9th world Conference on Earthquake Engineering, Tokyo and Kyoto, Japan*. 1988.
- [93] Ian D Aiken, Douglas K Nims, Andrew S Whittaker, and James M Kelly. “Testing of passive energy dissipation systems”. In: *Earthquake Spectra* 9.3 (1993), pp. 335–370.
- [94] Tzong-Shuoh Yang and Egor P. Popov. *Experimental and analytical studies of steel connections and energy dissipators*. Tech. rep. UCB/EERC-95/13. Berkeley, CA, USA: Earthquake Engineering Research Center, University of California, 1995.
- [95] Imad H Mualla and Borislav Belev. “Performance of steel frames with a new friction damper device under earthquake excitation”. In: *Engineering Structures* 24.3 (2002), pp. 365–371.
- [96] Wen-I Liao, Imad Mualla, and Chin-Hsiung Loh. “Shaking-table test of a friction-damped frame structure”. In: *The Structural Design of Tall and Special Buildings* 13.1 (2004), pp. 45–54.
- [97] Hoi Leung, G Charles Clifton, Hsen-Han Khoo, and Gregory A Macrae. “Experimental studies of eccentrically braced frame with rotational active links”. In: *Proceedings of the 8th International Conference on Behavior of Steel Structures in Seismic Areas, Shanghai, China*. 2015.
- [98] G Charles Clifton. “Semi-rigid joints for moment-resisting steel framed seismic-resisting systems”. PhD thesis. Auckland: ResearchSpace@, 2005.
- [99] Gregory A MacRae, G Charles Clifton, Hamish Mackinven, Nandor Mago, John Butterworth, and Stefano Pampanin. “The sliding hinge joint moment connection”. In: *Bulletin of the New Zealand Society for Earthquake Engineering* 43.3 (2010), pp. 202–212.
- [100] Massimo Latour, Vincenzo Piluso, and Gianvittorio Rizzano. “Free from damage beam-to-column joints: Testing and design of DST connections with friction pads”. In: *Engineering Structures* 85 (2015), pp. 219–233.
- [101] Brian Morgen. “A friction damper for post-tensioned precast concrete moment frames”. In: *PCI Journal* 49 (July 2004).
- [102] Hyung-Joon Kim and Constantin Christopoulos. “Friction damped posttensioned self-centering steel moment-resisting frames”. In: *ASCE Journal of Structural Engineering* 134.11 (2008), pp. 1768–1779.

- [103] Jun Iyama, Choungyeol Seo, James M Ricles, and Richard Sause. “Self-centering MRFs with bottom flange friction devices under earthquake loading”. In: *Journal of Constructional Steel Research* 65.2 (2009), pp. 314–325.
- [104] Jamaledin Borzouie, Gregory A MacRae, J Geoffrey Chase, Geoffrey W Rodgers, and G Charles Clifton. “Experimental studies on cyclic performance of column base strong axis-aligned asymmetric friction connections”. In: *ASCE Journal of Structural Engineering* 142.1 (2016), p. 04015078.
- [105] Fabio Freddi, Christoforos A Dimopoulos, and Theodore L Karavasilis. “Rocking damage-free steel column base with friction devices: design procedure and numerical evaluation”. In: *Earthquake Engineering & Structural Dynamics* 46.14 (2017), pp. 2281–2300.
- [106] Hsen-Han Khoo, G Charles Clifton, John Butterworth, Gregory A MacRae, and George Ferguson. “Influence of steel shim hardness on the Sliding Hinge Joint performance”. In: *Journal of Constructional Steel Research* 72 (2012), pp. 119–129.
- [107] P. Rojas, James M Ricles, and Richard Sause. “Seismic performance of post-tensioned steel moment resisting frames with friction devices”. In: *ASCE Journal of Structural Engineering* 131.4 (2005), pp. 529–540.
- [108] Michael Wolski, James M Ricles, and Richard Sause. “Experimental study of a self-centering beam-column connection with bottom flange friction device”. In: *ASCE Journal of Structural Engineering* 135.5 (2009), pp. 479–488.
- [109] Massimo Latour, Vincenzo Piluso, and Gianvittorio Rizzano. “Experimental analysis and design of friction joints equipped with sprayed aluminum dampers”. In: *Proceedings of the 8th International Workshop on Connections in Steel Structures, Boston, USA, May. 2016*, pp. 619–630.
- [110] Ernest Rabinowicz. *Friction and wear of materials*. 2nd ed. New York: Wiley & Sons, 1995.
- [111] Hyung-Joon Kim, Constantin Christopoulos, and Robert Tremblay. *Experimental characterization of boltstressed non asbestos organic (NAO) material-to-steel interfaces*. Tech. rep. 2004-01. Toronto, Canada: Civil Engineering Department, University of Toronto, 2004.

- [112] J Chanchí Golondrino, Gregory A MacRae, J Geoffrey Chase, Geoffrey W Rodgers, and G Charles Clifton. “Clamping force effects on the behaviour of asymmetrical friction connections (AFC)”. In: *Proceedings of the 15th World Conference on Earthquake Engineering (15WCEE), Lisbon, Portugal, September. 2012*, pp. 24–28.
- [113] Georgios Tsampras and Richard Sause. “Development and experimental validation of deformable connection for earthquake-resistant building systems with reduced floor accelerations”. In: *Network of Earthquake Engineering Simulation (NEES) Technical Report*, <https://nees.org/resources/13612> (2015).
- [114] SIA 263. *Steel structures*. Swiss Society of Engineers and Architects (SIA), Zurich, 2013.
- [115] Eurocode 3. *Design of steel structures*. British Standards Institution (BSI), London, 2005.
- [116] Bo NJ Persson. *Sliding friction: physical principles and applications*. Springer Science & Business Media, 2013.
- [117] Standard D639-14. *Standard test method for tensile properties of plastics*. West Conshohocken, PA, USA: American Society for Testing and Materials (ASTM), 2014.
- [118] Standard D695-15. *Standard test method for compressive properties of rigid plastics*. West Conshohocken, PA, USA: American Society for Testing and Materials (ASTM), 2015.
- [119] Standard D790-03. *Standard test method for flexural properties of unreinforced and reinforced plastics and electrical insulating materials*. West Conshohocken, PA, USA: American Society for Testing and Materials (ASTM), 2003.
- [120] European Committee for Standardization (CEN). *EN 15129: Anti-seismic devices*. London: BSI, 2018.
- [121] Babak Alavi and Helmut Krawinkler. “Behavior of moment-resisting frame structures subjected to near-fault ground motions”. In: *Earthquake Engineering & Structural Dynamics* 33.6 (2004), pp. 687–706.
- [122] Carlos Gordo-Monsó and Eduardo Miranda. “Significance of directivity effects during the 2011 Lorca earthquake in Spain”. In: *Bulletin of Earthquake Engineering* 16.7 (2018), pp. 2711–2728.



- [123] Jean Lemaitre. *Handbook of materials behavior models, three-volume set: nonlinear models and properties*. Elsevier, 2001.
- [124] Bharat Bhushan. *Modern tribology handbook, Two volume set*. CRC press, 2000.
- [125] Frank Philip Bowden and David Tabor. *Friction: an introduction to tribology*. RE Krieger Publishing Company, 1973.
- [126] Dominique François, André Pineau, and André Zaoui. *Mechanical behaviour of materials: Volume II: Viscoplasticity, Damage, Fracture and Contact Mechanics*. Springer Science & Business Media, 1998.
- [127] Po-Chien Hsiao, Kazuhiro Hayashi, Hiroyuki Inamasu, Yun-Biao Luo, and Masayoshi Nakashima. “Development and testing of naturally buckling steel braces”. In: *ASCE Journal of Structural Engineering* 142.1 (2016), p. 04015077.
- [128] Jiun-Wei Lai and Stephen A Mahin. “Strongback system: a way to reduce damage concentration in steel-braced frames”. In: *ASCE Journal of Structural Engineering* 141.9 (2014), p. 04014223.
- [129] Barbara G Simpson and Stephen A Mahin. “Experimental and numerical investigation of strongback braced frame system to mitigate weak story behavior”. In: *ASCE Journal of Structural Engineering* 144.2 (2017), p. 04017211.
- [130] Weng Y Kam, Stefano Pampanin, and Ken Elwood. “Seismic performance of reinforced concrete buildings in the 22 February Christchurch (Lyttleton) earthquake”. In: *Bulletin of the New Zealand Society for Earthquake Engineering* 44.2 (2011).
- [131] Robert I Skinner, James M Kelly, and Austin J Heine. “Hysteretic dampers for earthquake-resistant structures”. In: *Earthquake Engineering & Structural Dynamics* 3.3 (1974), pp. 287–296.
- [132] MJ Nigel Priestley, Sri Sritharan, James R Conley, and Stefano Pampanin. “Preliminary results and conclusions from the PRESSS five-story precast concrete test building”. In: *PCI journal* 44.6 (1999), pp. 42–67.
- [133] Alejandro Amaris, Stefano Pampanin, Desmond K Bull, and Athol Carr. “Development of a non-tearing floor solution for jointed precast frame systems”. In: *Proceedings of the New Zealand Society of Earthquake Engineering (NZSEE) Annual Conference*. 2007.

- [134] Matthew Roy Eatherton. “Large-scale cyclic and hybrid simulation testing and development of a controlled-rocking steel building system with replaceable fuses”. PhD thesis. Urbana, Illinois, USA: University of Illinois at Urbana-Champaign, 2010.
- [135] André Filiatrault and Bryan Folz. “Nonlinear earthquake response of structurally interconnected buildings”. In: *Canadian Journal of Civil Engineering* 19.4 (1992), pp. 560–572.
- [136] A. V. Bhaskararao and Radhey S Jangid. “Seismic analysis of structures connected with friction dampers”. In: *Engineering Structures* 28.5 (2006), pp. 690–703.
- [137] Yi Q Ni, Jinming Ko, and Zuguang Ying. “Random seismic response analysis of adjacent buildings coupled with non-linear hysteretic dampers”. In: *Journal of Sound and Vibration* 246.3 (2001), pp. 403–417.
- [138] Michela Basili and Maurizio De Angelis. “Optimal passive control of adjacent structures interconnected with nonlinear hysteretic devices”. In: *Journal of Sound and Vibration* 301.1-2 (2007), pp. 106–125.
- [139] Zhen Yang, You Lin Xu, and Xilin Lu. “Experimental seismic study of adjacent buildings with fluid dampers”. In: *ASCE Journal of Structural Engineering* 129.2 (2003), pp. 197–205.
- [140] Jinkoo Kim, Jingook Ryu, and Lan Chung. “Seismic performance of structures connected by viscoelastic dampers”. In: *Engineering Structures* 28.2 (2006), pp. 183–195.
- [141] C. C. Patel and Radhey S Jangid. “Seismic response of dynamically similar adjacent structures connected with viscous dampers”. In: *The IES Journal Part A: Civil & Structural Engineering* 3.1 (2010), pp. 1–13.
- [142] Xiao Huang and Hong-ping Zhu. “Optimal arrangement of viscoelastic dampers for seismic control of adjacent shear-type structures”. In: *Journal of Zhejiang University SCIENCE A* 14.1 (2013), pp. 47–60.
- [143] Ali Sahin Tasligedik, Stefano Pampanin, and Alessandro Palermo. “Low damage seismic solutions for non-structural drywall partitions”. In: *Bulletin of Earthquake Engineering* 13.4 (2015), pp. 1029–1050.
- [144] Gerardo Araya-Letelier, Eduardo Miranda, and Gregory Deierlein. “Development and testing of a friction/sliding connection to improve the seismic performance of gypsum partition walls”. In: *Earthquake Spectra* 35.2 (2019), pp. 653–677.

- [145] Simona Bianchi, Jonathan Ciurlanti, Daniele Perrone, André Filiatrault, Alfredo Campos Costa, Paulo X Candeias, António A Correia, and Stefano Pampanin. “Shake-table tests of innovative drift sensitive nonstructural elements in a low-damage structural system”. In: *Earthquake Engineering & Structural Dynamics* 50.9 (2021), pp. 2398–2420.
- [146] ASCE 7-16. *Minimum design loads and associated criteria for buildings and other structures*. ASCE/SEI 7-16, American Society of Civil Engineers, Structural Engineering Institute. Reston, Virginia, 2017.
- [147] ASCE 7-22. *Minimum design loads for buildings and other structures*. ASCE/SEI 7-22, American Society of Civil Engineers, Structural Engineering Institute. Reston, Virginia, 2022.
- [148] AASHTO. *Guide specifications for seismic isolation design*. Washington, USA: American Association of State Highway and Transportation Officials, 2014.
- [149] European Committee for Standardization (CEN). *Eurocode 3: Design of steel structure - Part 1-1: General rules and rules for buildings*. London: BSI, 2005.
- [150] European Committee for Standardization (CEN). *Eurocode 3: Design of steel structures - Part 1-8: Design of joints*. London: BSI, 2005.
- [151] Charles W Roeder, Eric J Lumpkin, and Dawn E Lehman. “A balanced design procedure for special concentrically braced frame connections”. In: *Journal of Constructional Steel Research* 67.11 (2011), pp. 1760–1772.
- [152] Dawn E Lehman, Charles w Roeder, David Herman, Shawn Johnson, and Brandon Kotulka. “Improved seismic performance of gusset plate connections”. In: *ASCE Journal of Structural Engineering* 134.6 (2008), pp. 890–901.
- [153] Francis Thomas Mckenna. “Object-oriented finite element programming: frameworks for analysis, algorithms and parallel computing”. PhD thesis. Berkeley, CA, USA: University of California, 1997.
- [154] Michele Barbato and Joel P Conte. “Finite element response sensitivity analysis: a comparison between force-based and displacement-based frame element models”. In: *Computer Methods in Applied Mechanics and Engineering* 194.12-16 (2005), pp. 1479–1512.
- [155] Svetlana M Kostic and Filip C Filippou. “Section discretization of fiber beam-column elements for cyclic inelastic response”. In: *ASCE Journal of Structural Engineering* 138.5 (2012), pp. 592–601.

- [156] E. Voce. “The relationship between stress and strain for homogeneous deformations”. In: *Journal of the Institute of Metals* 74 (1948), pp. 537–562.
- [157] Jean Lemaitre and Jean-Louis Chaboche. *Mechanics of solid materials*. Cambridge University Press, 1994.
- [158] Albano de Castro e Sousa, Yusuke Suzuki, and Dimitrios G Lignos. “Consistency in solving the inverse problem of the Voce-Chaboche constitutive model for plastic straining”. In: *Journal of Engineering Mechanics* 146.9 (2020), p. 04020097.
- [159] Ahmed Elkady and Dimitrios G Lignos. “Effect of gravity framing on the over-strength and collapse capacity of steel frame buildings with perimeter special moment frames”. In: *Earthquake Engineering & Structural Dynamics* 44.8 (2015), pp. 1289–1307.
- [160] Christopher D Stoakes and Larry A Fahnstock. “Cyclic flexural testing of concentrically braced frame beam-column connections”. In: *ASCE Journal of Structural Engineering* 137.7 (2011), pp. 739–747.
- [161] Luis F Ibarra, Ricardo A Medina, and Helmut Krawinkler. “Hysteretic models that incorporate strength and stiffness deterioration”. In: *Earthquake Engineering & Structural Dynamics* 34.12 (2005), pp. 1489–1511.
- [162] Dimitrios G Lignos, Alexander R Hartloper, Ahmed Elkady, Gregory G Deierlein, and Roland Hamburger. “Proposed updates to the ASCE 41 nonlinear modeling parameters for wide-flange steel columns in support of performance-based seismic engineering”. In: *ASCE Journal of Structural Engineering* 145.9 (2019), p. 04019083.
- [163] Constantin Christopoulos and André Filiatrault. *Principles of passive supplemental damping and seismic*. IUSS Press, Pavia, Italy, 2006.
- [164] European Committee for Standardization (CEN). *Eurocode 0 - Basis of structural design*. London: BSI, 2002.
- [165] European Committee for Standardization (CEN). *Eurocode 1: Actions on structures - Part 1-1: General actions - Densities, self-weight, imposed loads for buildings*. London: BSI, 2002.
- [166] Akshay Gupta and Helmut Krawinkler. *Seismic demands for performance evaluation of steel moment resisting frame structures*. Tech. rep. 132. Stanford University, California, United States: John A Blume Earthquake Engineering Center, 1999.

- [167] John Osteraas and Helmut Krawinkler. “The Mexico earthquake of September 19, 1985—Behavior of steel buildings”. In: *Earthquake Spectra* 5.1 (1989), pp. 51–88.
- [168] Lydik S Jacobsen. “Steady forced vibration as influenced by damping”. In: *Transactions of ASME* 5 (1930), pp. 169–181.
- [169] Timothy Ancheta, Yousef Bozorgnia, Robert Darragh, Walter J Silva, Brian Chiou, Jonathan P Stewart, David M Boore, Robert Graves, et al. “PEER NGA-West2 database: a database of ground motions recorded in shallow crustal earthquakes in active tectonic regions”. In: *Proceedings of the 15th World Conference on Earthquake Engineering*. 2012.
- [170] Jack W Baker. “Conditional mean spectrum: tool for ground-motion selection”. In: *ASCE Journal of Structural Engineering* 137.3 (2011), pp. 322–331.
- [171] Mohsen Kohrangi, Paolo Bazzurro, Dimitrios Vamvatsikos, and Andrea Spillatura. “Conditional spectrum-based ground motion record selection using average spectral acceleration”. In: *Earthquake Engineering & Structural Dynamics* 46.10 (2017), pp. 1667–1685.
- [172] Ting Lin, Stephen C Harmsen, Jack W Baker, and Nicolas Luco. “Conditional spectrum computation incorporating multiple causal earthquakes and ground-motion prediction models”. In: *Bulletin of the Seismological Society of America* 103.2A (2013), pp. 1103–1116.
- [173] Laura Eads, Eduardo Miranda, and Dimitrios G Lignos. “Average spectral acceleration as an intensity measure for collapse risk assessment”. In: *Earthquake Engineering & Structural Dynamics* 44.12 (2015), pp. 2057–2073.
- [174] Domenico Giardini, Jochen Wössner, and Laurentiu Danciu. “Mapping Europe’s seismic hazard”. In: *Eos, Transactions American Geophysical Union* 95.29 (2014), pp. 261–262.
- [175] Marco Pagani, Damiano Monelli, Graeme Weatherill, Laurentiu Danciu, Helen Crowley, V Silva, P Henshaw, L Butler, M Nastasi, L Panzeri, et al. “OpenQuake engine: An open hazard (and risk) software for the global earthquake model”. In: *Seismological Research Letters* 85.3 (2014), pp. 692–702.
- [176] José I Restrepo and Andrew M Bersofsky. “Performance characteristics of light gage steel stud partition walls”. In: *Thin-Walled Structures* 49.2 (2011), pp. 317–324.
- [177] FEMA. *Seismic performance assessment of buildings, Volume 1 — Methodology*. Rep. No. FEMA P-58-1. Washington, DC, 2012.

- [178] Rui Pinho, Mário Marques, Ricardo Monteiro, Chiara Casarotti, and Raimundo Delgado. “Evaluation of nonlinear static procedures in the assessment of building frames”. In: *Earthquake Spectra* 29.4 (2013), pp. 1459–1476.
- [179] Dimitrios G Lignos, Christopher Putman, and Helmut Krawinkler. “Application of simplified analysis procedures for performance-based earthquake evaluation of steel special moment frames”. In: *Earthquake Spectra* 31.4 (2015), pp. 1949–1968.
- [180] Fatemeh Jalayer and C Allin Cornell. *A technical framework for probability-based demand and capacity factor design (DCFD) seismic formats*. Tech. rep. PEER Report 2003/08. Berkeley, CA, USA: Pacific Earthquake Engineering Center, 2003.
- [181] Fatemeh Jalayer and C Allin Cornell. “Alternative non-linear demand estimation methods for probability-based seismic assessments”. In: *Earthquake Engineering & Structural Dynamics* 38.8 (2009), pp. 951–972.
- [182] NEHRP Consultants Joint Venture. “Evaluation of the FEMA p-695 methodology for quantification of building seismic performance factors (pp. 20899–28600)”. In: *Gaithersburg, MD: US Department of Commerce Engineering Laboratory, National Institute of Standards and Technology* (2010).
- [183] Douglas A Foutch and Seung-Yul Yun. “Modeling of steel moment frames for seismic loads”. In: *Journal of Constructional Steel Research* 58.5-8 (2002), pp. 529–564.
- [184] Francisco X Flores, Finley A Charney, and Diego Lopez-Garcia. “Influence of the gravity framing system on the collapse performance of special steel moment frames”. In: *Journal of Constructional Steel Research* 101 (2014), pp. 351–362.
- [185] Francisco X Flores, Finley A Charney, and Diego Lopez-Garcia. “The influence of gravity column continuity on the seismic performance of special steel moment frame structures”. In: *Journal of Constructional Steel Research* 118 (2016), pp. 217–230.
- [186] Pablo Torres-Rodas, Francisco Flores, Sebastian Pozo, and Bryam X Astudillo. “Seismic performance of steel moment frames considering the effects of column-base hysteretic behavior and gravity framing system”. In: *Soil Dynamics and Earthquake Engineering* 144 (2021), p. 106654.
- [187] Gregory A MacRae, Yoshihiro Kimura, and Charles Roeder. “Effect of column stiffness on braced frame seismic behavior”. In: *ASCE Journal of Structural Engineering* 130.3 (2004), pp. 381–391.

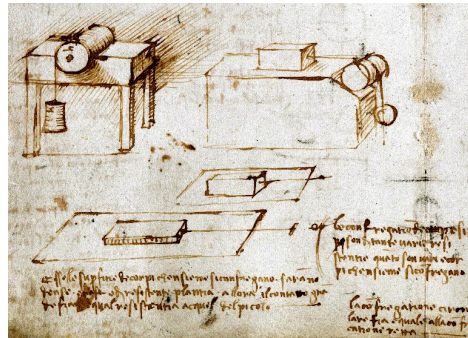
- [188] Xiaodong Ji, Mikiko Kato, Tao Wang, Toko Hitaka, and Masayoshi Nakashima. “Effect of gravity columns on mitigation of drift concentration for braced frames”. In: *Journal of Constructional Steel Research* 65.12 (2009), pp. 2148–2156.
- [189] R Maikol Del Carpio, Gilberto Mosqueda, and Dimitrios G Lignos. “Experimental investigation of steel building gravity framing systems under strong earthquake shaking”. In: *Soil Dynamics and Earthquake Engineering* 116 (2019), pp. 230–241.
- [190] ASCE/SEI41-17. *Seismic Evaluation and Retrofit of Existing Buildings*. American Society of Civil Engineers, Structural Engineering Institute. Virginia, 2017.
- [191] Seong-Hoon Hwang and Dimitrios G Lignos. “Earthquake-induced loss assessment of steel frame buildings with special moment frames designed in highly seismic regions”. In: *Earthquake Engineering & Structural Dynamics* 46.13 (2017), pp. 2141–2162.
- [192] Robert Tremblay, André Filiatrault, Peter Timler, and Michel Bruneau. “Performance of steel structures during the 1994 Northridge earthquake”. In: *Canadian Journal of Civil Engineering* 22.2 (1995), pp. 338–360.
- [193] Jack Wen Wei Guo and Constantin Christopoulos. “Performance spectra based method for the seismic design of structures equipped with passive supplemental damping systems”. In: *Earthquake Engineering & Structural Dynamics* 42.6 (2013), pp. 935–952.
- [194] Sarven Akcelyan, Dimitrios G Lignos, Tsuyoshi Hikino, and Masayoshi Nakashima. “Evaluation of simplified and state-of-the-art analysis procedures for steel frame buildings equipped with supplemental damping devices based on E-Defense full-scale shake table tests”. In: *ASCE Journal of Structural Engineering* 142.6 (2016), p. 04016024.
- [195] Roberto T Leon, Jerome F Hajjar, and Michael A Gustafson. “Seismic response of composite moment-resisting connections. I: Performance”. In: *ASCE Journal of Structural Engineering* 124.8 (1998), pp. 868–876.
- [196] Judy Liu and Abolhassan Astaneh-Asl. “Cyclic testing of simple connections including effects of slab”. In: *ASCE Journal of Structural Engineering* 126.1 (2000), pp. 32–39.
- [197] Abolhassan Astaneh-Asl, Judy Liu, and Kurt M McMullin. “Behavior and design of single plate shear connections”. In: *Journal of Constructional Steel Research* 58.5-8 (2002), pp. 1121–1141.

- [198] Judy Liu and Abolhassan Astaneh-Asl. “Moment–rotation parameters for composite shear tab connections”. In: *ASCE Journal of Structural Engineering* 130.9 (2004), pp. 1371–1380.
- [199] Abolhassan Astaneh, Marwan N Nader, and Lincoln Malik. “Cyclic behavior of double angle connections”. In: *ASCE Journal of Structural Engineering* 115.5 (1989), pp. 1101–1118.
- [200] Jiangang Shen and Abolhassan Astaneh-Asl. “Hysteretic behavior of bolted-angle connections”. In: *Journal of Constructional Steel Research* 51.3 (1999), pp. 201–218.
- [201] Maria M Garlock, James M Ricles, and Richard Sause. “Cyclic load tests and analysis of bolted top-and-seat angle connections”. In: *ASCE Journal of Structural Engineering* 129.12 (2003), pp. 1615–1625.
- [202] Sean Michael Donahue et al. “The role of the floor system in the seismic response of steel gravity framing”. PhD thesis. Austin, Texas, USA: The University of Texas at Austin, 2019.
- [203] Roberto T Leon. “Semi-rigid composite construction”. In: *Journal of Constructional Steel Research* 15.1-2 (1990), pp. 99–120.
- [204] Yan Xiao, Banseng Choo, and David A Nethercot. “Composite connections in steel and concrete. I. Experimental behaviour of composite beam—Column connections”. In: *Journal of Constructional Steel Research* 31.1 (1994), pp. 3–30.
- [205] N Derek Brown and David Anderson. “Structural properties of composite major axis end plate connections”. In: *Journal of Constructional Steel Research* 57.3 (2001), pp. 327–349.
- [206] Teo Teck Heong. “Design appraisal of steel-concrete composite joint”. PhD thesis. Singapore: National University of Singapore, 2003.
- [207] Anis Abidelah, AbdelHamid Bouchair, and Djamel Kerdal. “Experimental and analytical behavior of bolted end-plate connections with or without stiffeners”. In: *Journal of Constructional Steel Research* 76 (2012), pp. 13–27.
- [208] Wen-long Shi, Guo-qiang Li, Zhi-ming Ye, and R. Y. Xiao. “Cyclic loading tests on composite joints with flush end plate connections”. In: *International Journal of Steel Structures* 7.2 (2007), pp. 119–128.



- [209] Travis P Green, Roberto T Leon, and Gian A Rassati. “Bidirectional tests on partially restrained, composite beam-to-column connections”. In: *ASCE Journal of Structural Engineering* 130.2 (2004), pp. 320–327.
- [210] Roberto T Leon, Douglas J Ammerman, Jihshya Lin, and Robert D McCauley. “Semirigid composite steel frames”. In: *Engineering Journal - American Institute of Steel Construction INC* 24.4 (1987), pp. 147–155.
- [211] Laura N Lowes, Nilanjan Mitra, and Arash Altoontash. “A beam-column joint model for simulating the earthquake response of reinforced concrete frames”. In: *Pacific Earthquake Engineering Research Center* (2003).
- [212] Dimitrios G Lignos and Helmut Krawinkler. “Deterioration modeling of steel components in support of collapse prediction of steel moment frames under earthquake loading”. In: *ASCE Journal of Structural Engineering* 137.11 (2011), pp. 1291–1302.
- [213] Hammad El Jisr, Mohsen Kohrangi, and Dimitrios G Lignos. “Proposed nonlinear macro-model for seismic risk assessment of composite-steel moment resisting frames”. In: *Earthquake Engineering & Structural Dynamics* (2022).
- [214] Eduardo Miranda, Gilberto Mosqueda, Rodrigo Retamales, and Gokhan Pekcan. “Performance of nonstructural components during the 27 February 2010 Chile earthquake”. In: *Earthquake Spectra* 28.1\_suppl1 (2012), pp. 453–471.
- [215] Taichiro Okazaki, Masayoshi Nakashima, Keiichiro Suita, and Tomohiro Matus-miya. “Interaction between cladding and structural frame observed in a full-scale steel building test”. In: *Earthquake Engineering & Structural Dynamics* 36.1 (2007), pp. 35–53.
- [216] Anil K. Chopra. *Dynamics of structures: theory and applications to earthquake engineering*. 5th ed. Prentice Hall, 2012.
- [217] Luis F Ibarra. “Global collapse of frame structures under seismic excitations”. PhD thesis. Stanford, California, USA: Stanford University, 2004.
- [218] Sarven Akcelyan and Dimitrios G Lignos. “Seismic retrofit of steel tall buildings with bilinear oil dampers”. In: *Proceedings of the 16th European Conference on Earthquake Engineering*. 2018.
- [219] C Allin Cornell and Helmut Krawinkler. “Progress and challenges in seismic performance assessment”. In: *Pacific Earthquake Engineering Research Center Newsletter, Pacific Earthquake Engineering Research Center* (2000).

- [220] *C5/05 steelwork: Tables de construction*. Zurich, Switzerland: Centre Suisse de la Construction Métallique, 2016.
- [221] *C1/12 steelwork: Tables de dimensionnement pour la construction mixte*. Zurich, Switzerland: Centre Suisse de la Construction Métallique, 2012.
- [222] European Committee for Standardization (CEN). *Eurocode 1: Actions on structures - Part 1-3: General actions - Snow loads*. London: BSI, 2003.
- [223] European Committee for Standardization (CEN). *Eurocode 1: Actions on structures - Part 1-4: General actions - Wind actions*. London: BSI, 2005.
- [224] European Committee for Standardization (CEN). *Eurocode 2: Design of concrete structures - Part 1-1: General rules and rules for buildings*. London: BSI, 2004.



THIS THESIS WAS typeset in L<sup>A</sup>T<sub>E</sub>X by Martina Paronesso at the Swiss Federal Institute of Technology in Lausanne. The body text is set in 11 point Computer Modern. The figure above shows a free-hand sketch made by Leonardo da Vinci to illustrate the experimental setup developed to study friction [From Codex Arundel, British Library, London (Arundel folio 41r c. 1500–05)].

# Martina Paronesso

## *Curriculum Vitæ*



---

### PERSONAL DETAILS

Birth November 7, 1992  
Adresse Chemin de l'Ochettaz 16, 1025 St-Sulpice  
Mobile +41 76 406 41 69  
Mail [martina.paronesso@epfl.ch](mailto:martina.paronesso@epfl.ch)  
Nationality Swiss

---

### EDUCATION

- 2018–Present **PhD in Civil Engineering**, *Resilient Steel Structures Laboratory, Swiss Federal Institute of Technology in Lausanne, Lausanne, Switzerland.*  
PhD Dissertation Topic: Enhanced Life-Cycle Performance of Steel Braced Frame Buildings with Diaphragm Dissipative Connectors  
Supervisor: Professor Dimitrios G. Lignos
- 2015–2017 **M.Sc. in Civil Engineering with Specialisation in Structural Engineering**, *Swiss Federal Institute of Technology in Lausanne, Lausanne, Switzerland.*  
Master Thesis Topic: Seismic Performance Evaluation and Retrofit of Existing School Buildings (CROCS-System) in Switzerland  
Supervisor: Professor Dimitrios G. Lignos
- 2012–2015 **B.Sc. in Civil Engineering**, *Swiss Federal Institute of Technology in Lausanne, Lausanne, Switzerland.*

---

### AWARDS

- 2017 **SGEB Award**, *Swiss Federal Institute of Technology in Lausanne, Lausanne, Switzerland.*  
For a master project in the area of earthquake engineering or structural dynamics
- 2017 **Sarada M. et Raju A. Vinnakota**, *Swiss Federal Institute of Technology in Lausanne, Lausanne, Switzerland.*  
For a master student in civil engineering of EPFL who has demonstrated excellence in a master project with specialization in structural engineering

---

## PROFESSIONAL EXPERIENCE

### Practice

2017–2018 **Scientific Assistant**, *Resilient Steel Structures Laboratory, Swiss Federal Institute of Technology in Lausanne*, Lausanne, Switzerland.

2015 **Civil Engineering Internship**, *AR&PA Engineering Sagl*, Lugano, Switzerland.

### Teaching Assistantship

2018–2021 **Master Projects**, *Resilient Steel Structures Laboratory, Swiss Federal Institute of Technology in Lausanne*, Lausanne, Switzerland.

Master project at EPFL in civil engineering

2020–2021 **Semester Projects**, *Resilient Steel Structures Laboratory, Swiss Federal Institute of Technology in Lausanne*, Lausanne, Switzerland.

Master semester project at EPFL in civil engineering

2017, 2021 **Advanced Steel Design**, *Resilient Steel Structures Laboratory, Swiss Federal Institute of Technology in Lausanne*, Lausanne, Switzerland.

Master course at EPFL in civil engineering

2018 **Bridge Design**, *Resilient Steel Structures Laboratory, Swiss Federal Institute of Technology in Lausanne*, Lausanne, Switzerland.

Bachelor course at EPFL in civil engineering

2018 **Design of Steel Structures**, *Resilient Steel Structures Laboratory, Swiss Federal Institute of Technology in Lausanne*, Lausanne, Switzerland.

Bachelor course at EPFL in civil engineering

2016 **Dynamic Analysis of Structures**, *Applied Computing and Mechanics Laboratory, Swiss Federal Institute of Technology in Lausanne*, Lausanne, Switzerland.

Master course at EPFL in civil engineering

---

## COMPUTER SKILLS

ABAQUS, OPENSEES, SCIA ENGINEER, AUTOCAD, AUTODESK FUSION 360, L<sup>A</sup>T<sub>E</sub>X, MATLAB

---

## LANGUAGES

Italian **Native**

French **Fluent**

English **Intermediate**

German **Basic**

---

## PUBLICATIONS

### Conference Proceedings

- [1] Martina Paronesso and Dimitrios G Lignos. “Development and Experimental Verification of a Sliding Friction Damper for High-Performance Structures”. In: *Proceedings of 17. D-A-CH-Tagung 2021, SGEB, Zurich, Switzerland*. 2021.

- [2] Martina Paronesso and Dimitrios G Lignos. "Experimental Study of Sliding Friction Damper for High-Performance Steel Structures". In: *Proceedings of the 17th World Conference on Earthquake Engineering, Sendai, Japan*. 2020.

#### Journal Publications - Published or accepted

- [3] Dimitrios G Lignos and Martina Paronesso. "Low-damage steel structures for enhanced life-cycle seismic performance". In: *Stahlbau* 91.5 (2022), pp. 315–325.
- [4] Martina Paronesso and Dimitrios G Lignos. "Experimental study of sliding friction damper with composite materials for earthquake resistant structures". In: *Engineering Structures* 248 (2021), p. 113063.

#### Journal Publications - Under review

- [5] Martina Paronesso and Dimitrios G Lignos. "Influence of Gravity Connections and Damper Activation Forces on the Seismic Behavior of Steel CBF Buildings with Dissipative Floor Connectors". In: *Earthquake Engineering and Structural Dynamics* (2022, under review).
- [6] Martina Paronesso and Dimitrios G Lignos. "Seismic design and performance of steel concentrically braced frame buildings with dissipative floor connectors". In: *Earthquake Engineering and Structural Dynamics* (2022, under review).